PHYSICAL MODELLING OF COLLOIDAL SLURRY FLOWS

David Harbottle

Submitted in accordance with the requirements for the degree of

PhD

The University of Leeds

Institute of Particle Science and Engineering, School of Process, Environmental and Materials Engineering.

September 2008

The candidate confirms that the work submitted is his own work and that appropriate credit has been given where reference has been made to the work of others.

ACKNOWLEDGEMENTS

I would like to start by thanking the usual suspects for their guidance and support during my research. I would especially like to thank my supervisors Prof. Simon Biggs and Prof. Mike Fairweather for their insightful discussions and encouragement. They have allowed me to develop my own research interests and provided me with opportunities to travel, cementing my position within the research community.

I would also like to acknowledge the support of Dr Dominic Rhodes who as my industrial supervisor has continually reiterated the industrial relevance of this study. Nexia Solutions, now the National Nuclear Laboratory provided industrial sponsorship for the project which enabled me to build the slurry flow rig, as well as giving me a nice little top-up which made life a little more fun! So a big thank you for that.

As usual there are so many people that one would like to thank. During my PhD I have worked alongside several outstanding researchers who have played a role in making me the researcher I am today. I would like to thank Dr Grant Webber who at the start of my PhD helped me to get to grips with the world of colloid science, both at work and in the pub, obviously discussing the stability of foams! Associate Prof. George Franks, who supervised my visit to the University of Melbourne, where rheology and non-Newtonian fluid mechanics where the hot topics, the term "hot" being particularly appropriate! Prof. Paul Slatter at Cape Peninsula University of Technology, who supervised my visit to the research facility in Cape Town where I learnt the important facts about slurry pipe line design and instrumentation. A special thank you also has to be given to Dr Jeff Peakall and Dr Gareth Keevil who have so generously allowed me to use their rig facility and instrumentation to complete this study. Without them at the University of Leeds a study such as this could not have been undertaken.

Let me not forget the members of the Colloids and Polymer Engineering Research Group, some of whom I have had the pleasure of working alongside for a few years. Tim, Olivier, Gaelle, Jason, Qanita, Ken, Ishida, Chris, Jim, Amy and Rafiq, great times, many laughs wouldn't change a thing.

Finally a massive thank you has to be given to my parents and my sister. Without my parents funding my university education I wouldn't have been able to follow the career path I chose many years ago. Thanks for all the support and encouragement over the last 20 years. I'm possibly only a few years away from paying for that world cruise you wanted, but to be on the safe side you might want to book it anyway and I will try to pay you back in the future!

ABSTRACT

The study looks at the rheology and pipeline flow properties of colloidal suspensions dispersed in electrolytes of different concentration and type. Fuso silica spheres (0.8μm) form the dispersed phase of the suspension, and KNO_3, KCl electrolytes the continuous phase. The strength of the particle-particle interaction is significantly influenced by the electrolyte concentration. An increase in the electrolyte concentration from 10^{-4}M to 1M results in the formation of aggregates, thus influencing the sedimentation, sediment bed structure and pipeline transportation properties. Silica aggregates formed in 1M electrolytes are on average 5.75 times bigger than the primary particle. Pipeline transportation studies have shown the aggregated suspension to have a lower minimum transport velocity than the dispersed suspension. Such behaviour is believed to be related to interfloc flows within the aggregate, enhancing the level of fluid turbulence.

The centre-line and near wall turbulence intensities are enhanced in the presence of aggregates, while dispersed suspensions have negligible effect on modulating the fluid turbulence. Measurement of the streamwise RMS shows two critical Reynolds numbers with increasing flow velocity. The first critical Reynolds number (Re = 5500) occurs when the RMS profile of the aggregated suspension diverges (exceeds) from the RMS profiles of the dispersed and single phase flows. This enhancement is thought to be related to interfloc flows. A second critical Reynolds number (Re = 8000) is identified when the RMS profile of the aggregated suspension begins to converge with the dispersed and single phase RMS profiles. Convergence of the RMS profiles is related to the break-up of aggregates once a critical fluid shear stress is exceeded. Aggregate break-up data is verified with results collected using a Bohlin CVO-R rheometer.

CONTENTS

LIST OF FIGURES

LIST OF TABLES

Chapter 1

INTRODUCTION

NOMENCLATURE

C_D	Particle drag coefficient
D	Diameter of pipe
d_p	Diameter of particle
F_L	Flow parameter
g	Gravitational acceleration
i	Hydraulic gradient
V	Mean flow velocity
V_L	Limit deposit velocity
s	Density ratio of solid to liquid
m	constant
x	constant
ρ_s	Density of particle
ρ	Density of fluid
μ	Viscosity of fluid

Multiphase flow is a term commonly used to describe the transportation of solid particles in a carrier fluid. Multiphase flows occur in everyday life either in the natural environment such as rivers and oceans or in artificial systems where particles are transported along channels or pipelines. Process industries rely heavily upon pipeline transportation to maintain process optimisation. For example, the mineral and mining sector which can generate hundreds of millions of tonnes of solid material per day, achieves optimisation by continually removing solids from the site via pipelines. The other alternatives to industry are removal by rail road or road trucks. Both methods have huge economical and environmental issues when compared to pipeline transportation. An example where the installation of a pipeline has improved the economical output and overcome many environmental issues associated with mine operations is in Peru at the Antamina copper and

zinc mine. Solid material from the mine is transported to the harbour, a distance in excess of 300 km and down an elevation drop of 4155 metres. Up until 2001 solids from the mine were transported to the harbour by road trucks. Huge running costs were incurred in supporting the continuous removal of solids from the mine, along with environmental costs linked to atmospheric pollution and noise pollution, with trucks "rumbling" through local neighbourhoods 24 hours a day. In 2001, a slurry pipeline was installed from the mine down to the harbour, a total length of 301 km. The new pipeline has significantly improved the mine operation by increasing the mine output as well as reducing transportation costs by reducing labour and energy costs; the pipeline is designed such that the majority of the transportation energy is provided by gravity.

The transportation properties of slurries in horizontal pipelines have been studied in academic and industrial communities for over a century. Blatch[1] 1906, published the first study on the critical transport velocity of solids in horizontal pipelines. Blatch conducted a critical transport velocity study using sand-water slurries for the Washington Sewers Corp. The next significant step forward in understanding multiphase flows was made by Howard[2] in 1939. Howard combining the results from Blatch's earlier study with his own data, and from other sources (sand 0.3mm and gravel 3mm in a 4 inch pipe at solids concentrations up to 30% by volume), published a head loss equation that is related to the solids concentration and the mean slurry velocity, such an equation allowing for the energy requirements of the pipeline to be calculated (equation 1.0).

$$i_m = mV^x \qquad [1.0]$$

where m and x are constants that are related to the solids concentration, i is the hydraulic gradient and V the mean flow velocity. Since the publication of this equation there have been several improved versions accounting for more parameters, with an aim to produce a universal hydraulic gradient correlation.

One of the most significant contributions to the prediction of the minimum transport velocity of a slurry in a pipeline was made by Durand [3] , and Durand and Condolios [4] in the 1950's. Studying the flow properties of particles from 20 microns to 100mm (It should be noted that these particle sizes are not mean values, but are the upper and lower limits of the distribution. A typical distribution for one of the suspensions investigated is 0.2 –

25mm), in pipes ranging from 40mm to 700mm, at concentrations in excess of 50 wt %, they published the following correlation relating the minimum transport velocity (referred to as the limit deposit velocity in text) to the particle size, the solids concentration, the solid liquid densities and the pipe diameter:

$$F_L = \frac{V_L}{\sqrt{2gD\frac{\rho_s - \rho}{\rho}}} \qquad [1.1]$$

To this day, equation 1.1 is commonly used to determine the minimum transport velocity of a slurry pipeline. Equation 1.1 is frequently used due to its simplicity. However, due to a limited consideration for the physical parameters, a strong research programme has continued with an aim of providing a more accurate universal correlation. In 1987, Turian et al. [5] summarised the vast range of critical transport velocity correlations that had been published to date by recasting them in to a standard form. By considering over 800 experimental data sets and nearly 30 correlations, Turian's standard correlation took the form:

$$\frac{V_c}{[2gD(s-1)]^{0.5}} = f(C,s)C_D{}^h \left[\frac{D\rho[gD(s-1)]^{0.5}}{\mu}\right]^l \left(\frac{d_p}{D}\right)^m \qquad [1.2]$$

with constants *f(C,s)*, *h*, *l*, *m* provided in the original publication. The correlations that were considered by Turian showed developments on the earlier correlation published by Durand[4]. Newly published transport correlations considered the particle Reynolds numbers, particle size distribution, particle terminal settling velocity, drag coefficient, slurry density etc. When reviewing the literature a reader begins to understand the limitations of these correlations as a universal law. Many of the published correlations are based on fitting experimental data sets, with an approach of raising one or more of the experimental parameters to the power "n" so that the theoretical fit appears reasonable. In doing so, the correlation is only applicable over a limited range of experimental conditions. Wasp and Slatter [6] published a paper comparing the results of several minimum transport velocity correlations for 0.25mm sand in water at 1% volume as a function of the pipe diameter. Figure 1.0 which is redrawn from reference [6], illustrates the differences in the predicted minimum transport velocities when using different correlations.

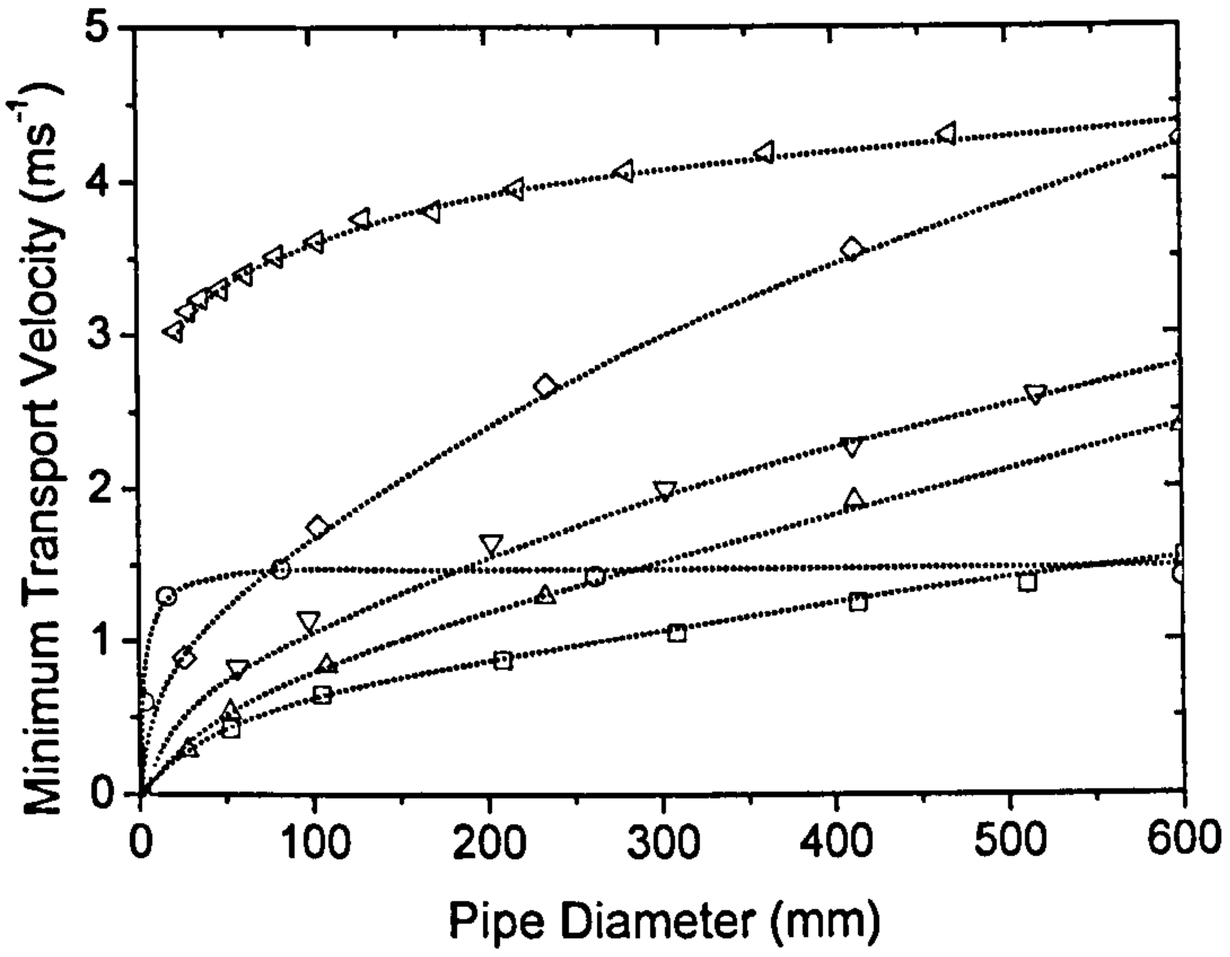

Figure 1.0 Comparison of six correlations to predict the minimum transport velocity of 0.25mm sand at 1% volume as a function of pipe diameter. Symbols: square – Condolios and Chapus [7], triangle – Spells [8], circle – Sinclair [9], inverted triangle – Hughmark [10], diamond – Durand [3], 90° triangle – Wasp [6].

The inaccuracies when predicting the minimum transport velocity of slurries using published correlations are frequently discussed in literature and at multiphase flow meetings. One of the main reasons for this inaccuracy is due to the lack of systematic and "well controlled" studies completed. Controlling accurately, all of the physical and process parameters in a flow loop that requires a hundred litres or more of slurry is difficult. In my opinion the only true way to develop a universal correlation is to derive a correlation theoretically from first principles.

The introduction so far has briefly considered what I frequently refer to as "classical" hydrotransport studies. That is to say, research in which the dispersed phase is commonly either, sand, coal, iron or nickel. These particles tend to be greater than a few hundred microns in diameter with a high solid density. Therefore, they exhibit high sedimentation velocities and are generally regarded as "settling" slurries. The term settling slurry can be rather misleading, as under no-flow conditions, even the finest particles (< 1 micron) will settle and deposit on a surface over time. The transition between a settling and a non-settling slurry is related to the flow regime at the normal pipeline operating velocity (typically 1-2ms^{-1}). For example, at a desired pipeline operating velocity, if a fraction of the sediment is transported on the pipe invert as a sliding bed, then slurry is considered as

settling, while if all the particles remain in suspension the slurry is then considered as non-settling.

Studies on the transportation properties of non-settling slurries have been rather limited in comparison to studies on settling slurries. Non-settling slurries contain fine particles which require significant time to sediment onto the pipe invert under gentle flow. However, the sedimentation and suspension rheological properties of fine particulate suspensions can be manipulated through changing the suspension chemistry and temperature; such changes possibly leading to a transition in the slurry behaviour. Suspension rheology is frequently studied, with the effects of changing the suspension pH and/or electrolyte concentration on suspension viscosity and sediment shear yield stress examined. Very fine particles used in suspension rheology studies are typically less than 1 micron and are described as being "colloidal". Theory developed during 20^{th} century showed that the interaction potential between two colloidal particles is given as the summation of the attractive van der Waals force and the electrical double layer repulsive force. An in-depth review of this topic is provided in chapter 2.

Over the last 20 years suspension rheology research has "boomed", a direct result of industrial needs. With advancing technologies and process operations, particles which are transported in pipelines are becoming finer and finer, to the point where colloidal forces can be manipulated to optimise pipeline transportation. To the authors knowledge, one of the first studies in which colloidal forces and suspension pipe flow were linked was by Horsley and Reizes [11] in 1978. They used silica with an average particle size of 17 microns (greater than colloidal, but interaction forces still present) and investigated the effect of suspension pH on the head loss gradient. By changing the pH of the suspension between pH 6 and pH 11 using HNO_3 and NaOH, the author's were able to change the interaction potential between neighbouring particles. For a constant flow velocity, Horsley and Reizes observed a decrease in the head loss gradient with a decrease in the zeta potential (-20mV to -70mV) for slurries containing 43wt. % solids. The author's makes no attempt to provide an explanation for this observation, with their only conclusion stressing that hydraulic gradient manipulation is only valid under laminar flow conditions, with all hydraulic curves "collapsing" onto one another in turbulent flow. Horsley and co-workers

have also looked at the use of viscosity modifiers [12, 13] and additives [14] to bring about similar effects.

In addition to the work of Horsley, there have also a handful of industrial examples where the use of additives can improve the pipeline performance of fine particulate suspensions [15, 16]. For example, the Samarco pipeline in Brazil is a 400 km pipeline used for the transportation of iron ore slurry. Trials with PolyDADMAC, a bridging flocculent, have been completed to identify improvements in operation by inducing floc formation. Trials have shown that the formation of flocs reduces the likelihood of obstructing the pipeline, prevents the formation of plugs in the pipeline on inclined sections, and prevents extreme densification of the sediment bed, thus, lowering the energy requirements on pump restart.

It should be noted that much of the research in this particular field (colloidal particles) has concentrated on the use of flocculants to modify the suspension rheology. To my knowledge there is little work other than the foremost study of Horsley and Reizes [11] where the effect of solution chemistry (pH change) has been investigated. The current study does not focus on the steric interactions between particles, but concentrates more closely on electrical double layer effects by controlling the suspension conductivity and pH.

Many of the multiphase pipeline studies with fine particles (20 – 40μm) are completed at concentrations where structuring in the suspension can occur, and the slurry exhibits non-Newtonian behaviour. The desires of the mineral industry who want to pump the most amount of material for the least amount of energy has driven this type of research. However, there are some industries which try to avoid pumping concentrated fine particulate slurries. For example, the nuclear industry avoids pumping concentrated suspensions due to the heat generating nature of the particles. If a pipeline blocks, the intense heat can lead to the creation of a hot-spot and increased corrosion of the pipe, thus cracks in the pipe can develop resulting in pipeline shutdown.

At present, the nuclear industry globally and within the UK is in a period of decommissioning and clean-up. In order for the nuclear sites to be returned to "green field", the sites need to be decommissioned and the waste packaged prior to ultimate disposal. Within the UK, a significant proportion of the clean up projects are associated with the large volumes of historical sludge waste which has been stored in ponds for over

50 years. The sludge contains particles with a broad size distribution from colloidal to granular, all dispersed in a fluid which contains virtually every element known to man! In order to treat the sludge, the sludge is to be pumped from existing storage facilities to newly built storage ponds before transferral to treatment plants for packaging. During transfer the slurry is to be pumped in stages with the pipeline flushed after every pumping cycle. With limited data available to the nuclear industry with regards to determining a suitable pipeline operating velocity for fine particulate suspensions in concentrated electrolytic solutions, the current study has therefore been commissioned by the National Nuclear Laboratory to investigate such systems.

At present the rheological and transportation properties of nuclear sludges are determined from data collected on simulants. These simulants tend to be over complicated, in such that there are too many variables. As a result, the experimental programmes tend to prove inconclusive or provide information which cannot be relied upon. A new approach when trying to understand the flow properties of such suspensions is required. The current project is designed to provide this new approach. Here we are investigating the flow properties of colloidal silica spheres in a fluid of known electrolyte type and concentration, and pH. By controlling the particle shape and size, as well as the solution chemistry we would expect to see clear differences in our results when adjusting one parameter. The reader should be aware that we are not trying to recreate the conditions in a sludge pond. The approach to this study is to work with a "model" simulant, a simulant where the continuous and dispersed properties are controlled and understood.

OBJECTIVES OF THE THESIS

The objective of the thesis is to provide a better understanding of the flow properties of colloidal suspensions in horizontal pipes. So far, colloidal suspensions have been extensively researched using analytical laboratory equipment, but there have been very few studies investigating such suspensions in pipelines. As previously mentioned in the introduction, industry is transporting finer and finer particles, and in order to optimise the pumping process, an understanding of the particle interaction and the strength of interaction is required. Of particular interest in this study is the measurement of the minimum transport velocity of a dispersed and aggregated colloidal suspension. These two suspensions provide contrasting rheological properties, thus there is an interest in whether or not these differences are significant enough to influence the transport velocity of a fine particulate suspension.

The turbulent properties of colloidal suspensions are also to be investigated. Turbulence provides the energy to keep particles in suspension and is therefore very important in pipeline transport. Turbulence modulation studies both experimentally and theoretically have not considered the effect of aggregates on the turbulence intensity, even though recent studies have shown that the flow fields through an aggregate are very "tortuous" and "complex" (see chapter 7). It is hoped that the study will show that these complex flow fields are capable of modulating the fluid turbulence.

Another objective of the study is to provide a methodology for a systematic flow study. For too many years researchers have used particles with a large polydispersity which are not fully characterised and dispersed in tap water. For colloidal suspensions such an approach can not be adopted and the whole system needs to be characterised and understood, from the single particle-particle interaction to the many body interactions in the suspension and sediment. By introducing a systematic and full characterisation study, the data can then be used by modellers to begin to predict the suspension flow properties from first principles.

THESIS STRUCTURE

Chapter 2

Chapter 2 is written to provide the reader with an overview on the theory of colloid stability. Silica particles which are used in the current study can be considered colloidal with a particle diameter less than 1 micron. Colloid theory is the fundamental science which underpins this project. This chapter reviews colloid theory, looking at how particles may acquire a surface charge when dispersed in a fluid medium, through to the electrical double layer models which were proposed throughout the last century, and finally the DLVO theory which can be used to suitably describe colloid stability. The chapter then concludes with a brief review on the different aggregation mechanisms for colloidal systems.

Chapter 3

A considerable amount of time during this project has been devoted to designing and constructing a horizontal flow loop for the transportation studies. Chapter 3 outlines the design equations which are used to ensure that the rig is "fit for purpose". The working principles of the instrumentation installed on the flow loop are discussed, along with the operating procedures for the minimum transport velocity and turbulence experiments.

Chapter 4

Prior to the flow loop experiments the silica suspensions and sediments are characterised using a variety of analytical laboratory instrumentation. Atomic force microscopy is used to measure the normal and lateral forces of interactions between two surfaces. A detailed description of the calibration procedures is provided, before a description of the methodology for both the normal and lateral force measurements. The techniques to determine the sedimentation properties of the dispersed and aggregated suspensions are also discussed, along with an overview of the working principles of a viscometer which is used regularly throughout the project to measure the shear yield stress of consolidated sediments. Finally, the instrumentation and the working principles of the two techniques used on the pipe loop, ultrasonic Doppler velocity profiling and particle imaging velocimetry are discussed.

Chapter 5

Chapter 5 is the first results chapter providing data on the particle-particle interaction force as a function of the electrolyte concentration and type. It should be brought to the reader's attention that in this chapter KBr is used as a background electrolyte in addition to KCl and KNO_3. KBr is only used to support the characteristic trends which are observed in the data throughout this chapter. A brief discussion on the complicated surface chemistry of silica is provided. Research with silica has produced many conflicting data sets, and the reader should be aware of the different silica surface properties. Ion-solvent, ion-ion and ion-surface interactions are also discussed with respect to altering the surface potential of the solid. The chapter includes zeta potential, shear yield stress, sedimentation, gel point and atomic force microscopy data.

Chapter 6

The minimum transport velocities of three colloidal suspensions are presented in this chapter. A review of the published correlations to determine the minimum transport velocity of fine particle suspensions is provided, along with a review on the physical and chemical approaches frequently adopted to modify the flow properties of such systems. The chapter includes further details on the novel approach which has been used in this study to determine the minimum transport velocity of fine particulate suspensions.

Chapter 7

Chapter 7 compares the turbulence intensity profiles of a sediment-free flow to a dispersed and an aggregated colloidal suspension. The effect of particles on the turbulent properties of a fluid are frequently discussed, but to my knowledge the introduction of aggregates and their effect on fluid turbulence has not been considered before. Pipe loop data comparing the turbulence intensities of three flows are presented.

Chapter 8

The conclusion and future work discussion chapter. The data collected throughout the project is related and summarised. Future work identifies the key gaps in the literature which need to be addressed to advance the research topics that have been considered in this study.

Appendix A

Results from a detailed characterisation study on several solid samples are presented in the appendix. From the characterisation study which included the measurement of the particle size, zeta potential and suspension pH stability, Fuso silica was chosen as the "model" simulant solid. Fuso silica is characterised by a narrow particle size distribution, particles with high sphericity, no nano aggregates and stable suspension pH. Further discussion on the characterisation tests and the reasons for selecting Fuso silica are provided in the appendix.

Samples studied:

1. Monospher 1000 – silica
2. Angstromsphere – silica
3. Calcium carbonate
4. Spheriglass – glass

Appendix B

Additional Fuso silica characterisation. Data includes:

1. Scanning electron micrographs
2. Particle size (aggregate)
3. pH stability
4. Settling – KNO_3 and KCl electrolytes
5. Critical coagulation concentration
6. Gel point – KNO_3 and KCl electrolytes

Appendix C

Atomic force microscopy – Lateral force raw data.

Appendix D

Slurry pipe loop design and dimensions.

Chapter References

1. Blatch, N.S., Transactions of the American Society of Civil Engineering, 1906. **LVII**: p. 400-408.
2. Howard, G.W., *Transportation of sand and gravel in a four-inch pipe.* Transactions of the American Society of Civil Engineering, 1939. **104**: p. 1334-1348.
3. Durand, R., *Basic relationships of the transportation of solids in pipes - experimental research.* Proc. Conf. Int. Assoc. Hydraulic Res., 1953: p. 89-103.
4. Durand, R. and E. Condolios, *The hydraulic transport of coal and solid material in pipes.* Proceedings of a Colloquium on the Hydraulic Transport of Coal, 1953(39-52).
5. Turian, R.M., F.L. Hsu, and T.W. Ma, *Estimation of the critical velocity in pipeline flow of slurries.* Powder Technology, 1987. **51**(1): p. 35-47.
6. Wasp, E.J. and P.T. Slatter, *Deposition velocities for small particles in large pipes.* 12th International Conference on the Transport and Sedimentation of Solid Particles, 2004: p. 671-680.
7. Condolios, E. and E.E. Chapus, *Designing solids handling pipelines.* Chemical Engineering 1963. **70**: p. 131-138.
8. Spells, K.E., *Correlations for use in transport of aqueous suspensions of fine solids in pipes.* Transactions of the Institution of Chemical Engineers, 1955. **33**: p. 79-82.
9. Sinclair, C.G., *The limit deposit velocity of heterogeneous suspensions.* Symposium on interaction between fluids and particles - London, 1962. **Insitution of Chemical Engineers**: p. 78-86.
10. Hughmark, G.A., *Aqueous transport of settling slurries.* Industrial and Engineering Chemistry, 1961. **53**(5): p. 389-390.
11. Horsley, R.R. and J.A. Reizes, *Variation in head loss gradient in laminar slurry pipe flow due to changes in zeta potential.* The South African Mechanical Engineer 1978. **28**: p. 307-311.
12. Jones, R.L. and R.R. Horsley, *Viscosity modifiers in the mining industry.* Mineral Processing and Extractive Metal, 1999. **20**: p. 215-224.
13. Farrow, J.B., et al., *The effect of alkali and alkaline earth cations on the rheology of concentrated quartz suspensions.* Journal of Rheology (New York, NY, United States), 1989. **33**(8): p. 1213-30.

14. Horsley, R.R., *Viscometer and pipe loop tests on gold slime slurry at very high concentrations by weight, with and without additives.* Hydrotransport 8 - 8th Internation Conference on the Hydraulic Transport of Solids in Pipes, 1982: p. 367-382.

15. Braganca, A.C. and T.A. Silva, *Alternative to lime as a rheology modifier in the transport of iron ore slurry by the Samarco pipeline.* Hydrotransport 17 - The 17th International Conference on the Hydraulic Transport of Solids, 2007: p. 29-38.

16. Alderman, N.J., N.I. Heywood, and D.J. Clowes, *Effect of comminuted flint on pumping chalk slurry in the 92km Kensworth - Rugby pipeline.* Hydrotransport 17 - The 17th International Conference on the Hydraulic Transport of Solids, 2007: p. 469-482.

Chapter 2

THEORY OF COLLOID INTERACTIONS

NOMENCLATURE

A	Hamaker constant
a	Particle radius
C_1	Stern layer capacitance
C_2	Diffuse layer capacitance
c	Ionic concentration
$c^{\cdot}$	φ^0
D_i	Diffusion coefficient of particle i
d_f	Fractal dimension
d_p	Diameter of particle
E	Collision efficiency
e	Electronic charge
G	Shear rate
g	Gravitational acceleration
h	Minimum surface-surface separation distance
J_{ij}	Collision frequency for particles of type i and j
k	Boltzmann constant
k_{ij}	Collision rate constant for particles of type i and j
m	Mass of aggregate
N_s	Adsorption site density
n	Ion concentration per unit volume
$n_i^{\cdot}$	Number concentration of particles of type i
T	Absolute temperature ^{o}K
u	Counter-ion specific adsorption potential
V_T	Total potential energy of interaction per unit area
V_A	Potential energy of attraction per unit area
V_R	Potential energy of repulsion per unit area
W	Stability ratio
x	Distance
y	Counter-ion mole fraction
z	Valency
ze	Ionic charge

φ	Potential
ε	Permittivity of the medium

κ	Debye-Huckel parameter
$\bar{p}$	Osmotic pressure difference
μ	Dynamic viscosity
ρ_s	Density of particle
ρ_l	Density of fluid
ρ_a	Density of aggregate
ρ	Charge density
$_0$	Distance x = 0 (surface)
$_\delta$	Distance of closest approach, ion-surface interaction
$_i$	Ion *i*
$_\infty$	Distance x = ∞ (bulk)

ABREVIATIONS

PZC	Point of zero charge
DLVO	Derjaguin, Landau, Verwey and Overbeek Theory
c.c.c.	Critical coagulation concentration
DLCA	Diffusion-limited cluster-cluster aggregation
RLCA	Reaction-limited cluster-cluster aggregation

Synopsis

A characteristic feature of a colloidal dispersion is the large interfacial area between the dispersed phase and the continuous medium. The dispersed phase, which is distributed more or less uniformly throughout the continuous medium, is in a higher energy state than that of the bulk material as a consequence of the proportionally large number of surface atoms. As a result, lyophobic colloids are thermodynamically unstable and have a tendency to aggregate. However, many colloidal systems appear stable over extended timescales. This apparent stability must be governed by some repulsive energy barrier. Destabilisation of the system can only be achieved in these cases when the kinetic energy of two approaching particles is sufficient to overcome this energy barrier. With an attractive van der Waals force always present between the particles, the collision efficiency (fraction of successful collisions resulting in aggregate formation) is controlled through altering the strength of the dispersive force which is a function of the surface properties and suspension chemistry.

The strength of the interparticle interaction energy can significantly influence the bulk behaviour of the dispersion. This chapter introduces several fundamental areas associated

with colloid science. First, the methods through which a surface can acquire a charge in solution are considered, before a brief discussion on the theories developed to represent charge and potential distribution. The theoretical approach to attractive and repulsive force determination is then discussed, and finally the overall influences of such forces on colloid stability and aggregation kinetics are considered.

2.1 Surface Charge

When a particle is dispersed within an aqueous electrolyte solution its surface will usually acquire a charge through one of several possible mechanisms: [1)] ionisation and [1a)]ion dissolution – when there is a greater tendency for one of the constituent surface chemical species to either dissociate[1] or dissolve[1a] into the aqueous medium; [2)] specific ion adsorption – preferential adsorption of ions onto the solid surface which results in a net charge; and [3)] isomorphous ion – substitution by a lower valency ion. For the relevant case in this study of an oxide mineral particle dispersed within an aqueous electrolyte solution, the ionisation of the hydroxylated oxide surface can yield either a net positive or negative surface charge through proton release or adsorption.

$$M - OH_2^+ \overset{K_1}{\leftrightharpoons} M - OH \overset{K_2}{\leftrightharpoons} M - O^- + H_2O$$

With the addition of a base (OH^-), the pH of the system is increased resulting in a greater tendency for the surface sites to lose protons. Hence the oxide surface becomes more negative. With the addition of an acid (H^+), the equilibrium is shifted in the opposite direction resulting in the protonation of the surface groups. The oxide surface becomes more positive. The equilibrium equation suggests that there is a characteristic pH where the surface exhibits a net zero charge. This value is called the point of zero charge (PZC), and can be determined through averaging pK_1 and pK_2.

2.2 Electrical Double Layer Models

The presence of a charged surface in solution promotes the redistribution of ions within the surrounding medium. The surface charge is balanced over a short distance into the

neighbouring aqueous environment by an excess of counter-ions and a deficit of co-ions. The uneven distribution of ions within the neutralisation region is commonly referred to as the 'electrical double layer'. Several simplifying assumptions have been applied to describe the redistribution of ions neighbouring a charged surface, with the assumptions modified in later revisions of the theory.

The earliest model to describe the ion distribution in the bulk was developed by Helmholtz in the 19th century. Helmholtz modelled the double layer as a simple capacitor, with the electric charge on the surface neutralised by an equal and opposite charge immediately adjacent to the solid surface. The simplicity of the model; a result of the single charged layer, falls someway short of describing many experimental observations.

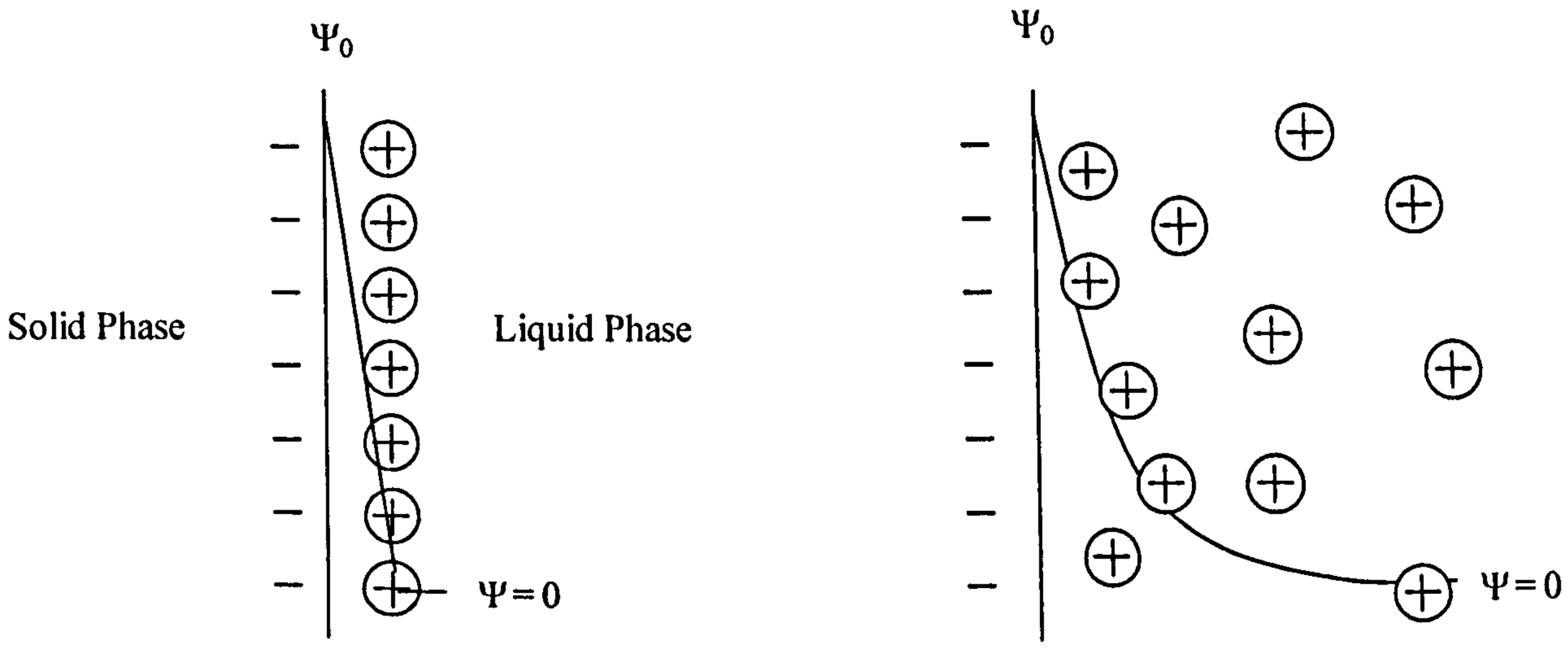

Figure 2.0 The Helmholtz model (L.H.S.), and the Gouy-Chapman model (R.H.S.) of the electrical double layer. Solid line represents the potential distribution.

The Gouy-Chapman model provided a significant refinement to the Helmholtz theory. Instead of treating the surface charge neutralisation with a single layer of counter-ions, the present model considered a charge distribution from the surface into the bulk solution; more consistent with entropy and thermal energy considerations. The potential (φ) distribution is related to the charge density (ρ), and is suitably described by the Poisson equation:

$$\frac{d^2\varphi}{dx^2} = -\frac{\rho}{\varepsilon} \qquad [2.0]$$

where ε is the permittivity of the medium. The overall charge density in an electrolyte solution is determined by the anion and cation concentrations. Ions of the same sign as the surface charge will be repelled from the surface, while ions of the opposite sign will be attracted towards the surface. The distribution of ions can be described by the Boltzmann equation:

$$n_i = n_i^{\infty} exp\left(-\frac{z_i e\varphi}{kT}\right) \qquad [2.1]$$

where n_i is the concentration of ion *i* per unit volume at a point where the potential is φ, n_i^{∞} is the concentration of ion *i* per unit volume in the bulk at a distance $x = \infty$, $z_i e$ is the ionic charge, *k* is the Boltzmann constant and T is the temperature given in unit Kelvin.

The charge volume density at a point from the interface is obtained through the summation of the anionic and cationic concentrations in a unit volume of the electrolyte solution.

$$\rho = \sum_i n_i^{\infty} z_i e \exp\left(-\frac{z_i e\varphi}{kT}\right) \qquad [2.2]$$

Combining both equations 2.1 and 2.2 with 2.0 yields the Poisson – Boltzmann equation. For a system where the electrical charge is small compared to the thermal energy, the Poisson – Boltzmann equation can be simplified by the Debye-Hückel approximation. Defining the boundary conditions as $\varphi = \varphi_0$ at $x = 0$ and $\varphi = 0$, $d\varphi/dx = 0$ at $x = \infty$, the Poisson – Boltzmann equation becomes:

$$\frac{d^2\varphi}{dx^2} = \left(\frac{\sum z_i^2 e^2 n_i^{\infty}}{\varepsilon kT}\right)\varphi \qquad [2.3]$$

with the second order differential solved to produce the Debye-Hückel approximation:

$$\varphi = c' \times \exp(-\kappa x) \qquad [2.4]$$

For a symmetrical, *z*:*z* electrolyte, *c'* is given as φ_0. Equation 2.4 shows that the potential decays exponentially as a function of length (*x*). $\kappa = \sqrt{\left(\frac{e^2 \sum z_i^2 n_i^{\infty}}{\varepsilon kT}\right)}$ with units m^{-1} is known as the 'Debye-Hückel parameter' with the reciprocal of κ often referred to as the 'diffuse layer'. The diffuse layer describes the region of varying potential from the interface; an important parameter in colloid stability, see Section 2.3 – Colloid Stability. At 25° C in water κ is simplified to:

$$\kappa = 0.329 \times 10^{10} \sqrt{c_i . z_i^2} \qquad [2.5]$$

where c_i is the ionic concentration and z_i is the valency.

The Gouy-Chapman theory also enables the surface charge density ρ_0 to be related to the surface potential. The surface charge density is opposed by the volume charge density through the diffuse layer and is given by:

$$\rho_0 = -\int_0^\infty -\varepsilon \left(\frac{d^2\varphi}{dx^2}\right) dx \qquad [2.6]$$

Applying the following boundary condition $\left(\frac{d\varphi}{dx}\right)_{x \to \infty} = 0$, and for a small potential $\frac{ze\varphi_0}{kT} < 1$ this integral can be solved as a linear relationship:

$$\rho_0 = \varepsilon \kappa \varphi_0 \qquad [2.7]$$

A fundamental assumption of the Gouy-Chapman model is the treatment of ions in solution as point charges, which can lead to an unreasonable counter-ion charge density at the interface for low surface potentials. The approach distance to the surface and the density of ions at the interface can be limited through treating the ions not as point charges, but as finite sized spheres with the charge located at the centre. Such behaviour was proposed by Stern in 1924.

The Stern model separates the diffuse layer of the Gouy-Chapman model into two regions. The inner region next to the surface known as the 'Stern layer' is defined separately from the diffuse layer which is suitably described by the Gouy-Chapman model. The two layers are separated by a Stern plane located at a distance δ; one hydrated counter-ion radius from the surface. δ identifies the closest distance an ion can approach without becoming specifically adsorbed. For the simplest case where there is no adsorption of the counter-ion, the surface charge is neutralised solely by the diffuse layer charge. In order to satisfy the limit $\left(\frac{d\varphi}{dx}\right)_{x \to \infty} = 0$, the surface potential drops over both the Stern and diffuse layers according to their capacitances. The capacitance over the Stern layer (C_1) and the capacitance over the diffuse layer (C_2) are given by:

$$C_1 = \frac{\rho_0}{\varphi_0 - \varphi_\delta} \qquad [2.8]$$

$$C_2 = \frac{\rho_0}{\varphi_\delta} \qquad [2.9]$$

The largest potential drop is over the region with the smallest capacitance. For example, in a high ionic solution where $C_1 < C_2$ the largest potential drop is over the Stern layer. While in a low ionic solution; $C_2 < C_1$, and the largest potential drop is over the diffuse layer.

The second case considers the affect of counter-ion adsorption on the charge distribution. The relationship between the charge densities at the surface and the Stern plane, for a non-adsorbing system, is no longer applicable. To achieve charge neutrality the summation of the Stern and diffuse charge densities must be equal and opposite to the surface charge density. The charge density of the Stern plane is defined as:

$$\rho_\delta = z_i e N_s y_i \exp\left[-\frac{(z_i e \varphi_\delta + u_i)}{kT}\right] \qquad [2.10]$$

where N_s gives the adsorption site density; y_i the counter-ion mole fraction and u_i the counter-ion specific adsorption potential. In some cases, such as polyvalent counter-ions, when the specific adsorption potential is large, charge reversal in the Stern plane may be observed as the charge density exceeds the charge density of the surface.

Grahame [1](1947) provided a further refinement to the electrical double layer model by modifying the Stern model through subdivision of the Stern layer into an inner layer and an outer layer. The Stern-Grahame model which remains the accepted model for describing the electrical double layer differentiates between the unhydrated ions that specifically adsorb to the surface, and the hydrated counter-ions in the Stern plane. The boundaries are defined as the Inner Helmholtz plane; one unhydrated ion radius from the surface, and the Outer Helmholtz plane located at a distance δ from the surface.

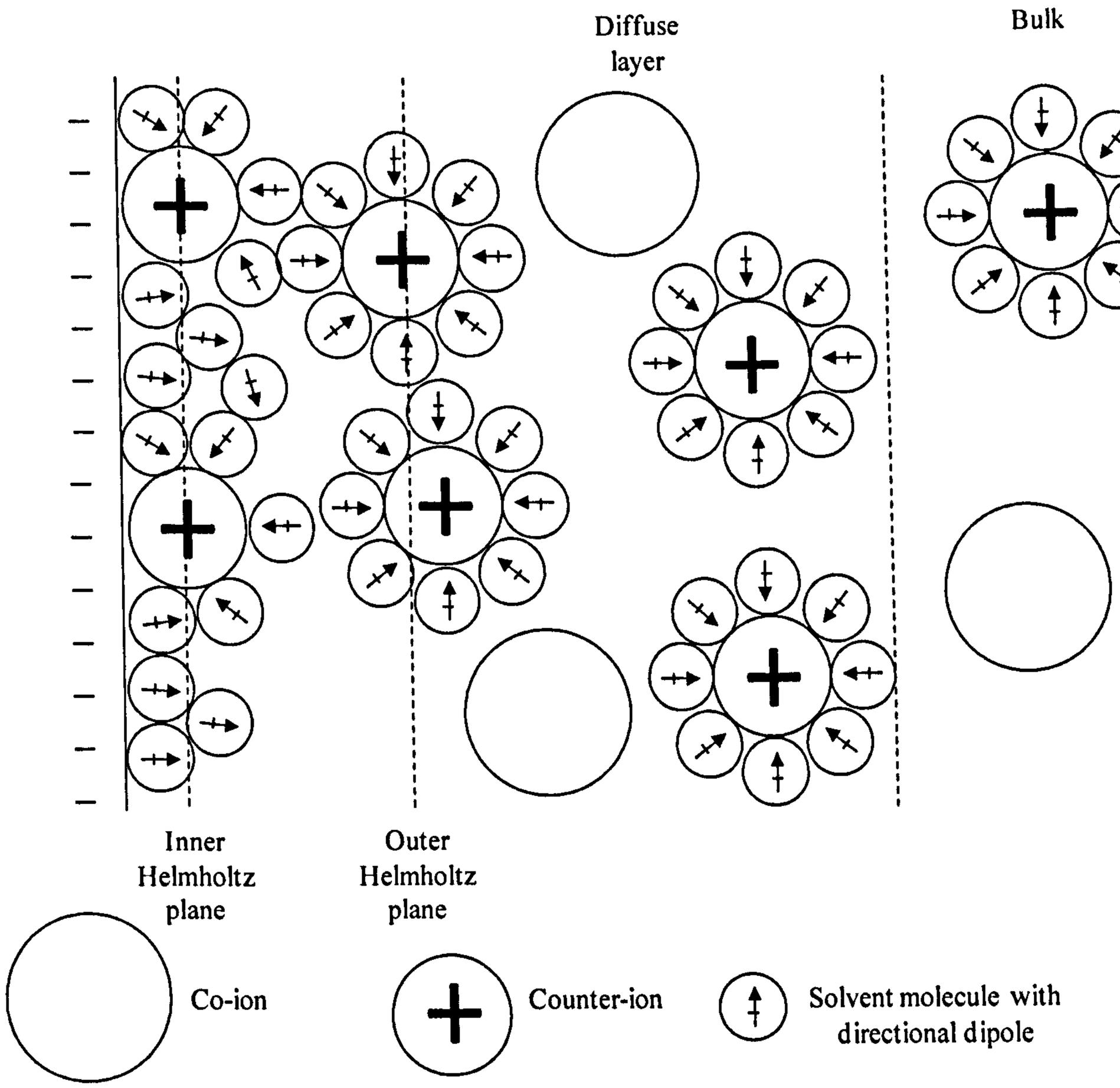

Figure 2.1 The Stern-Grahame model of the electrical double layer. Within the inner Helmholtz plane partially un-hydrated ions are adsorbed, with the hydrated ions at the outer Helmholtz plane. The surface of shear at which the electrokinetic potential is determined is at a distance just outside the outer Helmholtz plane.

2.3 Colloid Stability

The effective diameter of a charged sphere in solution is commonly considered to be equal to the solid sphere diameter (d_p) plus $2\kappa^{-1}$. When two equal spheres approach, the centre-centre separation distance may be less than the effective diameter of the sphere, resulting in electrical double layer overlap. The ionic concentration within this region is higher than the equilibrium concentration for that surface potential, and this drives an osmotic pressure gradient between the two surfaces. For a plate-plate interaction, the potential energy of repulsion per unit area V_R can be determined through calculating the work done in forcing the two plates together:

$$V_R = -\int_{\infty}^{h} \bar{p}\, dh \qquad [2.11]$$

where $\bar{p}$ is the osmotic pressure difference between the bulk and the overlapping double layer region, and h is the minimum surface-surface separation distance.

As two charged surfaces approach, the surface-chemical equilibrium is maintained by the interaction mechanics of the two double layers which can either be described by a constant charge or a constant potential approach. Assuming that the surface potential remains constant on approach, the equilibrium is maintained through both surfaces gradually discharging the potential-determining ion, reducing the magnitude of the surface charge. A constant potential approach is reasonable when the rate of double layer overlap between the two surfaces is extremely slow. However, the encounter time for a Brownian collision is typically in the order of 10^{-6} s [2], which is significantly greater than the discharge time of the potential determining ion from the surface. Here, a constant charge approach is postulated where the surface potential adjusts accordingly as a function of separation distance to maintain the surface-chemical equilibrium. The two approaches are rarely justified on their own in practice, with the real situation generally a combination of the two effects.

When describing the interaction potential between two charged surfaces, several expressions have been derived to account for both plate-plate and sphere-sphere interaction potentials. With the double layer interaction kinetics difficult to interpret due to the dynamic aspect of the system, the derived expressions for sphere-sphere interactions are usually based on plate-plate expressions using the Derjaguin's approximation, or the linear superposition approximation. Detailed analysis of these approximations employed when determining the interaction potential is outside the focus of this study. Readers are referred to the following references for a more in-depth interpretation of the approximations [3, 4].

For two identical spheres with radius $a_1 = a_2 = a$; Stern potentials $\varphi_{\delta 1} = \varphi_{\delta 2} = \varphi_{\delta}$, separated by a minimum distance h, in a symmetrical z-z electrolyte; the double layer interaction potential is given by:

$$V_R = 32\pi\varepsilon a(kT/ze)^2\gamma^2 \exp(-\kappa h) \qquad [2.12]$$

where e is the electronic charge

and $\gamma = \frac{\exp\left[\frac{ze\varphi_\delta}{2kT}\right]-1}{\exp\left[\frac{ze\varphi_\delta}{2kT}\right]+1}$, [2.13]

which can then be simplified further when the Stern potential is small to become:

$$V_R = 2\pi e a \varphi_\delta^2 \exp(-\kappa h) \quad [2.14]$$

Equation 2.14 summarises the influence of h and the inert ion concentration c_i (see equation 2.5) on V_R. As the separation distance increases the interaction potential decreases in an approximately exponential manner. While an increase in c_i results in an increase in κ, and a decrease in φ_δ; consequently reducing V_R.

The total potential energy of interaction is composed of a repulsive component and an attractive component. Hamaker [5] has shown that as two colloidal particles approach one another, the atoms in one particle interact with all the atoms in the neighbouring particle, and the resultant interaction potential V_A at close approach ($h << a$) is given by:

$$V_A = -A(a_1.a_2)/6(a_1 + a_2)h \quad [2.15]$$

with A defined as the Hamaker constant and subscripts $_1$ and $_2$ refer to particle 1 and particle 2.

The attraction potential is suitably described by London-van der Waals forces. Such forces result from the oscillation behaviour of the electron clouds around two non-polar molecules. These molecules are associated with fluctuating dipoles which align themselves with neighbouring dipoles when in close proximity; leading to a net intermolecular attraction. The Hamaker approach to evaluating the London-van der Waals attraction is based on the pair-wise summation of all intermolecular interactions between each body. The Hamaker constant in equation 2.16 is termed 'the effective Hamaker constant', which considers both the solid and dispersion medium properties. A modified constant accounts for a reduction in the attraction potential, compared to a system under vacuum. For a solid-liquid system where the two particles are of the same material, the effective Hamaker constant becomes:

$$A_{131} = (A_{11}^{\frac{1}{2}} - A_{33}^{\frac{1}{2}})^2 \quad [2.16]$$

where subscripts $_{11}$ and $_{33}$ represent the interaction between the particle-particle and the dispersion medium-dispersion medium respectively. Equation 2.16 concludes that the van der Waals interaction is always positive in a system when the two interacting bodies are composed of the same material. For the system under consideration in the present study, the Hamaker constants for water ($_{33}$) and silica ($_{11}$) are 5 and 50×10^{-20}J respectively [6].

One of the main disadvantages when applying the Hamaker approach is that it tends to over predict the inverse square force decay as the separation distance increases. The large separation distance between particles in a colloidal system introduces a time effect associated with the propagation of the electromagnetic radiation between the particles. Several studies [7, 8] have highlighted this error, which is considered negligible at short separation distances ($h \sim$ 10-20nm) when the interaction is strongest. The retardation effect can either be accounted for through applying an alternative approach to evaluating the London-van der Waals forces; the Liftshitz method, or through a simple modification of the Hamaker approach. Such approaches have been considered in detail in various textbooks [4, 6, 9]; with further discussion considered outside the scope of this study.

An explanation for the stability of colloids in aqueous media determined from the total potential energy of interaction between two approaching particles was first proposed in the 1940's by two independent research groups. The approach is commonly termed the 'DLVO theory' (Derjaguin and Landau [10], and Verwey and Overbeek [11]), and treats the total potential energy of interaction as linear superposition of the repulsive and attractive interaction potentials:

$$V_T = V_R + V_A \qquad [2.17]$$

The two interaction potentials can be determined theoretically from equations 2.14 and 2.15. Figure 2.2 below illustrates how both the repulsive potential and the attractive potential decays with separation distance. The summation of the two potentials results in the total interaction potential V_T which is plotted in the bottom figure of fig.2.2. The total interaction potential is determined theoretically for a 1:1 electrolyte at 298°K with a constant surface potential of -25mV.

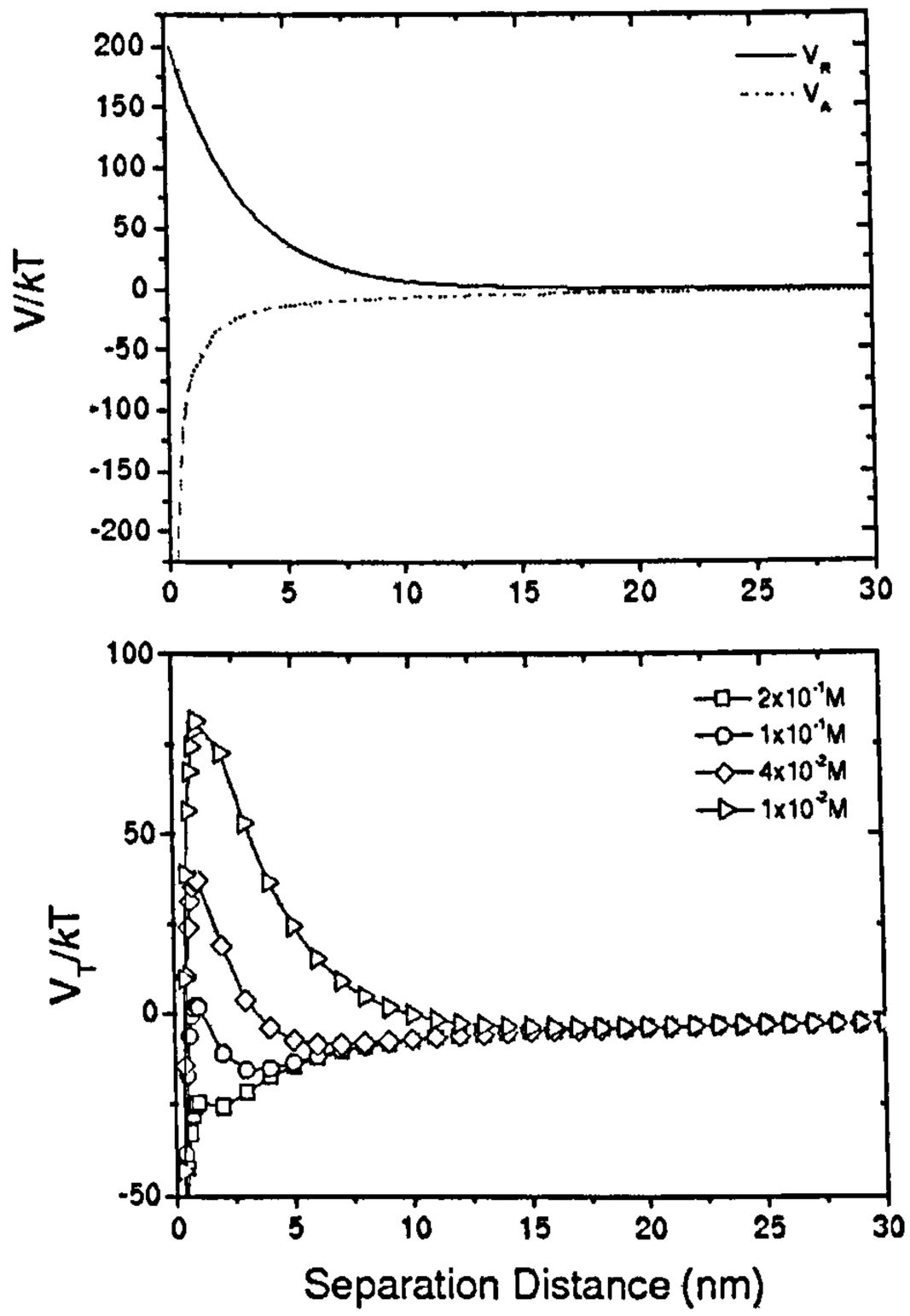

Figure 2.2 Top - The attractive and repulsive components as a function of separation distance. Bottom - Summation of the two potential energies resulting in the total potential energy of interaction. A lowering of the ionic concentration is observed to increase the repulsive barrier.

When considering the attractive potential (equation 2.15) it is clear that as the separation distance decreases the magnitude of the potential increases without limit, resulting in this potential always dominating at small separation distances. The inverse square decay behaviour also means that at large separation distances the attractive potential will dominate over the repulsive potential which decays exponentially – see figure 2.2 (top). This characteristic behaviour is clearly observed in figure 2.2 (bottom) for the 4×10^{-2}M electrolyte, which shows a shallow secondary minimum at 6nm and a deep primary minimum at a separation distance < 1nm. The secondary minimum may result in the formation of weak aggregates forming small clusters which can easily be re-dispersed. As the repulsive force is exceeded the particles are held by strong van der Waals attraction forces in the primary minimum, forming larger clusters that require a significant amount of energy to initiate aggregate break-up.

Depending upon the various physiochemical parameters of the system there may be a region over which the repulsion potential dominates. A repulsive energy barrier (kT) can be established which typically ranges $1/\kappa$, limiting the collision efficiency (E) of the colloidal particles. The energy barrier which is generally several kT, spanning several nanometres, ensures that the potential energy of a particle alone is insufficient to surmount the barrier and initiate doublet formation. Collision behaviours are explained by three mechanisms i) Perikinetic aggregation, ii) Othokinetic aggregation and iii) Differential sedimentation which incorporates a kinetic energy term to aid aggregation – see section 2.4. As the repulsive potential barrier is lowered (increase in c_i), the collision efficiency increases, until eventually a point is reached where the repulsive barrier diminishes and the total potential remains negative at all times; the collision efficiency in principle is then equal to 1.

The transition from a stable to an un-stable colloid suspension where rapid aggregation is observed typically occurs over a small range of electrolyte concentrations (see figure 2.3 – the clearing rates of Fuso silica used in this study are determined from the settling profiles collected using a LUMiFuge®). The clearing rate is measured as a function of the KNO_3 electrolyte concentration. The data shows a sharp transition in the clearing rate at the critical coagulation concentration). The concentration at which slow aggregation gives way to rapid aggregation is termed the 'critical coagulation concentration' (c.c.c.) and is theoretically described when $V_T = 0$ and $dV_T/dh = 0$. When the surface potential is large ($ze\varphi_\delta/4kT >> 1$) the c.c.c. as defined by equation 2.18 identifies an inverse sixth proportionality with the counter ion valency [9]:

$$c.c.c.(mol\ dm^{-3}) = \frac{88 \times 10^{-40}}{z^6 A^2} \qquad [2.18]$$

However, if the surface potential is small ($ze\varphi_\delta/4kT < 1$) the c.c.c. has a much weaker dependency on the counter-ion valency and is proportional to z^{-2}.

$$c.c.c.(mol\ dm^{-3}) = \left(\frac{3.65 \times 10^{35}}{A^2}\right).\left(\frac{\varphi_\delta^4}{z^2}\right) \qquad [2.19]$$

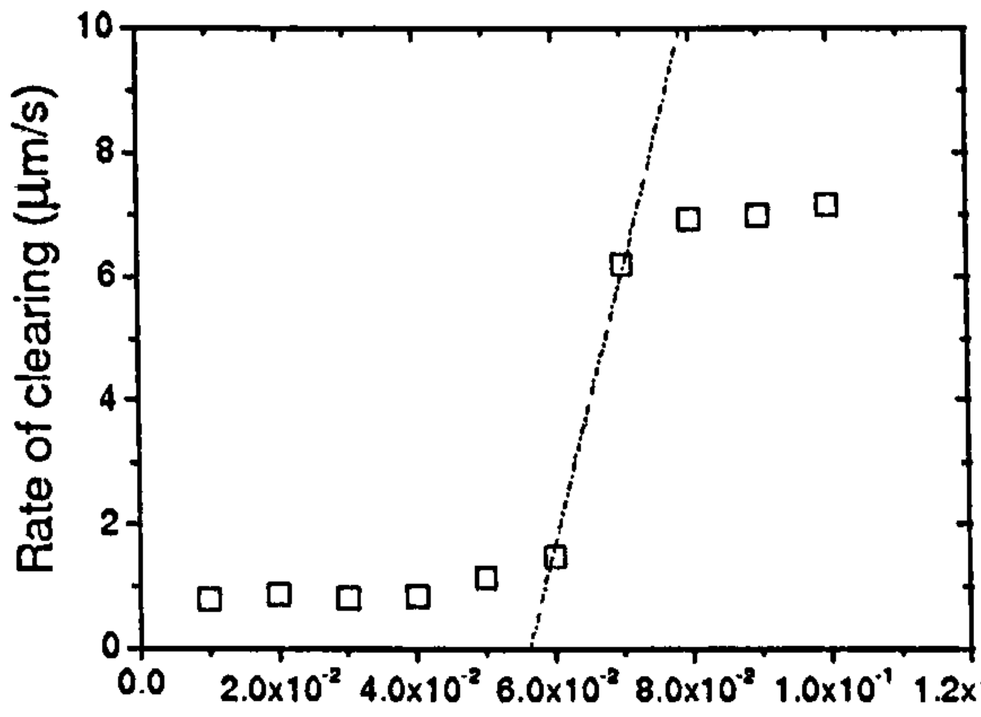

Figure 2.3 Critical coagulation concentration of Fuso silica determined experimentally by monitoring the clearing rate of the colloidal suspension; background electrolyte KNO_3. Rate of clearing determined through centrifugal sedimentation (LUMiFuge®).

Simple interpretation of the DLVO theory would suggest that at a small separation distance the two approaching surfaces would spring into contact. With the development of surface force apparatus in the 1970's, theory developed from studying the kinetics of coagulation could now be verified by directly measuring the interaction force as a function of separation distance. At large separation distances the double layer repulsive force was verified. While at small separation distances 'additional forces' not accounted for in the original theoretical interpretation provided some disparity. Large repulsion forces due to either hydration and/or osmotic pressure effects [12] are generally observed at high salt concentrations (> 10^{-3}M), preventing the direct contact between two approaching surfaces. The modified total potential energy curve exhibits a primary minimum, where the surface – surface separation distance typically approaches 0.3nm [4]. Surface hydration through the adsorption of hydrated cations prevents direct surface – surface contact. Dehydration of the surface sites and the expulsion of the hydrated ions from the gap involves work and hence an increase in the free energy of the system. Ion exclusion generally results from osmotic pressure which 'balances' the solution pressure between two approaching surfaces, preventing the influx of pure solvent from the bulk. With the overlapping of two double layers, the ionic concentration in the region increases generating an entropically unfavourable system. Pure solvent is then drawn into the gap to stabilise the system, with the increasing pressure providing a barrier of limiting approach.

2.4 Aggregation Kinetics

Brownian motion, gravitational forces and the kinetics of flow ensure that particles in a colloidal dispersion remain in constant motion. The random trajectory of a particle due to Brownian motion or displacement by a fluid eddy provides a source of energy for particle collisions. The physiochemical nature of the dispersion, the collision frequency, the collision efficiency, and the aggregate break-up rate under fluid shear are all factors that will influence the overall number and size distribution of aggregates formed in a suspension.

Formation of aggregates in a colloidal suspension and the rate at which these aggregates form can play a significant role in modifying suspension rheology, and therefore, process performance. For example, the relationship between the residence time and the characteristic time for aggregation is important in de-watering processes, where a short characteristic time for aggregation is favoured to induce rapid suspension separation [13]. In pipe flow the formation of open porous aggregates lead to an increase in the 'effective' solids volume fraction of the dispersed phase in the carrier fluid, influencing the transportation properties by modifying the slurry viscosity, the particle sedimentation rate and to be discussed in chapter 7 the turbulence intensities [14-16].

Aggregation processes can simply be described by the total number of collisions J_{ij} occurring between primary particles of size i and j in a unit volume and a unit time. The initial rate of aggregation (k_{ij}) is strongly dependent upon the particle diffusion coefficient which is influenced by several parameters such as particle size, temperature and transport mechanism.

$$J_{ij} = k_{ij} n_i' n_j' \qquad [2.20]$$

where n_x' is the number concentration of the different particles; k_{ij} the second order rate constant.

The rate constant for a colloidal dispersion in which the rate of aggregation is diffusion limited (Brownian motion) was first described by Smoluchowski [17], who calculated the rate of diffusion of spherical particles of type i to a fixed sphere of type j. As i particles attach themselves to the central sphere j and are removed from the suspension, a

concentration gradient is established in the radial direction from the fixed sphere. Eventually, a steady-state condition is reached where the number of *i-j* collisions in unit time can be described as:

$$J_i = 4\pi(a_i + a_j)D_i n_i' \qquad [2.21]$$

where D_i describes the diffusion coefficient of a spherical particle given by the Stokes-Einstein equation, and $a_i + a_j$, is the centre to centre separation distance when the particles are in contact.

If the central sphere is not held in a fixed position and experiences Brownian motion itself, a mutual diffusion coefficient D_{ij}, which is equal to the summation of both diffusion coefficients is to be substituted to replace D_i. In addition, the number of collisions is no longer solely dependent on the diffusion of *i*, but is dependent on both *i* and *j*; consequently, J_i is to be substituted with J_{ij}.

The initial rate constant for perikinetic collisions where both particles undergo Brownian diffusion is determined through relating the modified form of equation 2.21 to equation 2.20, substituting $\frac{kT}{6\pi\mu a}$ for the individual diffusion coefficients.

$$k_{ij} = \frac{2kT}{3\mu}\frac{(a_i + a_j)^2}{a_i a_j} \qquad [2.22]$$

Equation 2.22 shows the significance of the particle radius on the perikinetic rate constant. In a dispersion of equal spheres where the rate constant is a minimum, the diffusion coefficient of the particles and the collision radius effectively offset each other making the rate constant independent of particle size.

Smoluchowski [17] also considered the rate constant for a suspension where the particle collisions are significantly influenced by the fluid motion. The orthokinetic rate constant for aggregation was developed by considering a uniform laminar shear profile, where flowing particles a_i collide with a fixed sphere a_j. With particles a_i following straight streamlines and collisions justified when centre-to-centre separation distance satisfies $a_i + a_j$, the collision frequency can be subsequently determined from the total number of collisions J_{ij} in unit volume and unit time.

$$J_{ij} = \frac{4}{3} G n_i' n_j' (a_i + a_j)^3 \quad [2.23]$$

thus,

$$k_{ij} = \frac{4}{3} G (a_i + a_j)^3 \quad [2.24]$$

The diffusion coefficient in the perikinetic rate constant is now replaced by the dominant shear rate parameter G which accounts for the rate of particle displacement in a flow field. In a system of equal spheres, the orthokinetic rate constant shows a cube dependency of the collision radius. As the collision radius increases, the rate of aggregation increases with aggregate size, as the chance of capture increases. Unlike perikinetic aggregation, the rate of aggregation is no longer limited by a reduction in the diffusion coefficient.

In 'real' processes particle collisions are more likely to occur under turbulent flow conditions, with the aggregation rate equation under simple shear no longer valid. Saffman and Turner [18] for isotropic turbulence proposed the replacement of G with a mean shear rate parameter $\bar{G}$. The mean shear parameter is given as the power input per unit mass of fluid to the kinematic viscosity of the fluid ratio [19].

For a suspension within which the particles either have varying density or size, a third rate constant can be derived to account for differential sedimentation. The Stokes' equation which is dependent upon both particle size and density indicates that larger denser particles will sediment at a faster rate than smaller less dense particles. Assuming that the two particles are falling within the collision radius ($a_i + a_j$), it is expected that the velocity differential will result in contact between the large and small particle. The total number of collisions J_{ij} and the initial rate constant k_{ij} for particles of equal density are given by:

$$J_{ij} = \left(\frac{2\pi g}{9\mu}\right)(\rho_s - \rho_l)(a_i + a_j)^3 (a_i - a_j) n_i' n_j' \quad [2.25]$$

and

$$k_{ij} = \left(\frac{2\pi g}{9\mu}\right)(\rho_s - \rho_l)(a_i + a_j)^3 (a_i - a_j) \quad [2.26]$$

The three rate constants are independent of viscous and colloidal interaction effects. Viscous effects result from the work required to displace fluid from an ever decreasing gap

as two particles approach one another. The overall effect is a modification in the rate of aggregation. For perikinetic aggregation the viscous effect can be accounted for by a reduced diffusion coefficient, while a limiting collision efficiency parameter can be considered for orthokinetic aggregation. The effect of a stabilising force in a colloidal dispersion will also act to reduce the aggregation rate. This reduction can be accounted for by a stability ratio W; given as the ratio of the aggregation rate in the absence of colloidal interactions (theoretical) to the rate of aggregation influenced by colloidal interactions (experimental). A simple theoretical expression relating the interaction energy (V_T) to the stability ratio W was provided by Fuchs [20]: *$u = d/a$ for equal particles, where d is the collision radius and a the particle radius*

$$W = 2 \int_0^\infty \frac{\exp\left(\frac{V_T}{kT}\right)}{(u+2)^2} du \qquad [2.27]$$

An approximate solution to the integral was provided by Reerink and Overbeek [21] who derived an expression through approximating V_T to a Gaussian curve, resulting in a linear relationship between log$W$ and log$c$. The linear relationship for slow aggregation is valid until a critical electrolyte concentration is met. For fast aggregation satisfying the theoretical approach of Smoluchowski, W equals 1 and is independent of electrolyte concentration [21-23].

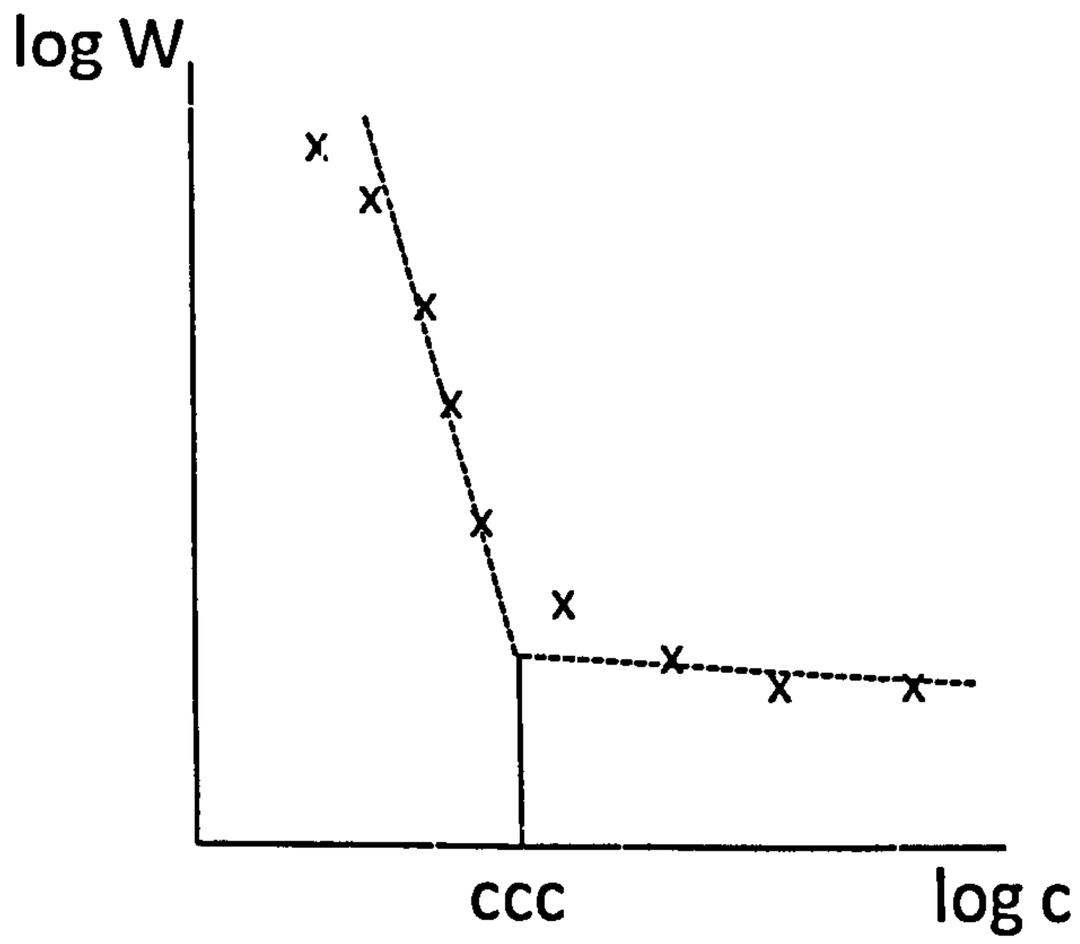

Figure 2.4 The influence of increased salt concentration on the stability ratio W. Figure redrawn from [24].

The structure of an aggregate (size and density) and the kinetics through which the aggregate is formed can be described by two irreversible aggregation mechanisms: [1] DLCA [25] (diffusion-limited cluster-cluster aggregation) and [2] RLCA [26] (reaction-limited cluster-cluster aggregation). DLCA occurs when the dispersive component for particle stability is negligible ($W = 1$) leading to a situation where all collisions result in a sticking event producing large open clusters, which are unlikely to undergo rearrangement to produce more compact clusters. With a small potential barrier to aggregation the probability of a sticking event when the particles come into close proximity is reduced. The aggregation kinetics is described by the RLCA model, where particles have an opportunity to diffuse into the core of the aggregate before they become attached. The mechanism which is limited by the reaction of the particle to the cluster produces smaller more compact aggregate structures.

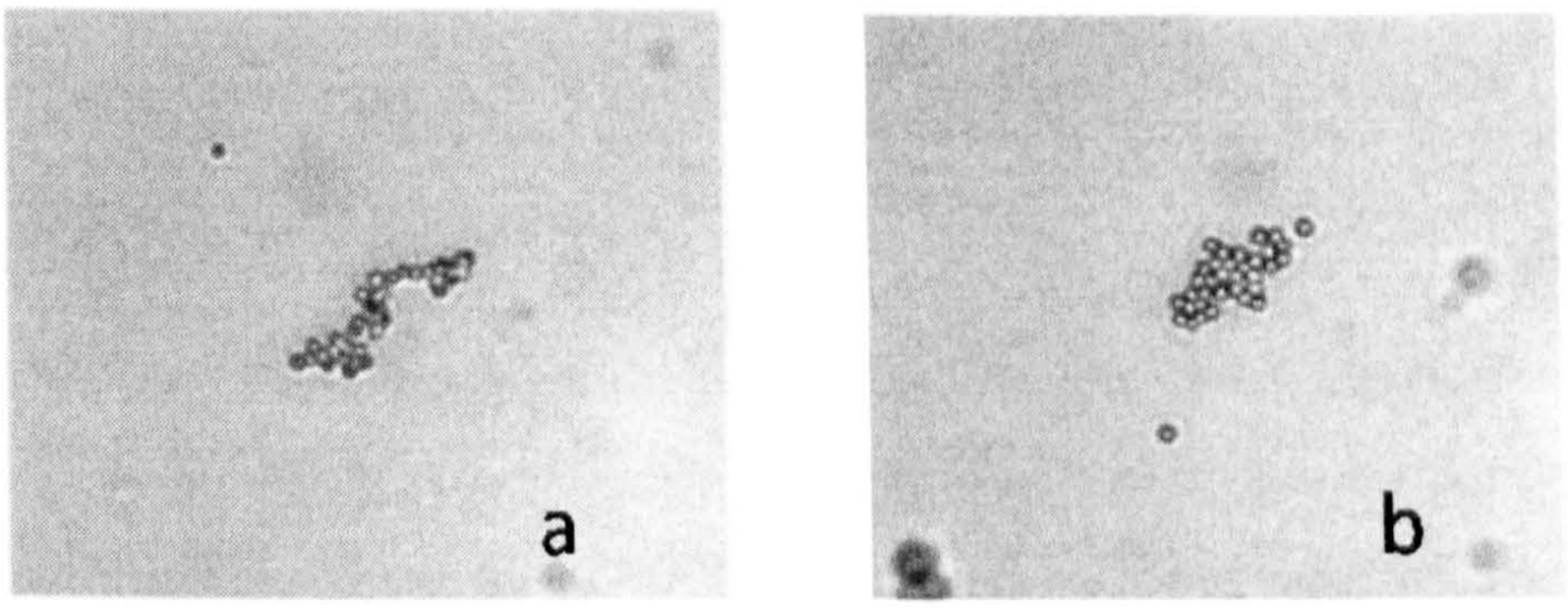

Figure 2.5[27]: Polystyrene latex aggregate structures prepared by diffusion-limited (a) and reaction-limited (b) colloid aggregation.

The spatial description of the random arrangement of particles in an aggregate can be suitably described by fractal mathematics. The mass fractal dimension d_f which is not limited to integer values can vary between 1 and 3 in a 3-D space, with 1 corresponding to a linear chain of particles and 3 a coalesced sphere, the densest possible configuration for a series of connected particles. d_f is frequently determined from static light scattering where the scattered intensity from the aggregate is correlated to the scattering angle. Both the mass and density of the aggregate are proportionally related to the fractal dimension, satisfying:

$$m(a) \propto a^{d_f} \qquad [2.28]$$

$$\rho_a(a) \propto a^{d_f - 3} \qquad [2.29]$$

Theory and experiment [28, 29] have shown that for DLCA, $d_f \approx 1.75 \pm 0.05$, and for RLCA, $d_f \approx 2.1 \pm 0.05$.

The strength of an aggregate is related to the aggregate density (number of particle-particle contacts) and the interparticle attraction component between neighbouring particles. Experiments have shown that exposing large length scale aggregates ($d_f = 1.75$) to mild shear, it is possible to bring about conformational change in the aggregate structure [27, 30]. An increasing aggregate fractal dimension correlates with an increasing shear, until a critical shear is reached where it may no longer be possible to quantify the structure of an aggregate by fractal dimensions. Breakage under orthokinetic conditions either by fragmentation or surface erosion of small components ultimately influences the overall size and density of the aggregate. In a perikinetic system the aggregate size and density is limited by the aggregate mass. As the aggregate grows a situation is reached where the mass force exceeds the buoyancy force, and the aggregate begins to settle. The displacement of fluid through and around the aggregate structure will provide a simple shear region to initiate surface erosion.

A unique behaviour of silica aggregates is associated with their ability to spontaneously restructure over time. Aubert and Cannell [31] using ~ 22nm silica spheres dispersed in 1M NaCl at different pHs and solids concentrations, observed the restructuring of unstable silica aggregates prepared by DLCA. The aggregates restructured within a period of minutes to hours, with the fractal dimensionality of the aggregate changing from 1.75 to 2.08. Schlomach [32] proposed a mechanism for this restructuring referring to a densification process of the outer aggregate, with diffusion of the primary particles towards the centre of mass of the aggregate. Further studies showing the restructuring phenomena of silica aggregates [33, 34] have considered the affect of either a hydration layer [35] or a surface gel layer [36, 37] between neighbouring particles which prevents direct contact (see chapter 5 for further discussion). This 'steric' barrier provides an opportunity for one particle to roll around another reconfiguring the structure to one which is thermodynamically more stable.

The spontaneous restructuring of silica aggregates is however an area which has not received much fundamental attention due to conflicting experimental observations. Subsequent research into silica clusters prepared by DLCA has also shown that spontaneous restructuring does not occur [29]. Martin et al.[29] studying the formation of

silica aggregates from 11nm primary particles observed no spontaneous rearrangement. The experiments completed under similar conditions to those specified by Aubert et al. [31] showed the fractal dimension of 1.84 to be independent of time. An increase in fractal dimension over several hours was observed, but this was associated to shear applied to the aggregates during re-suspension from the bottom of the scattering cell in order to obtain the measurement. The behaviour of a cluster prepared by DLCA is most likely to be associated with the surface properties of the silica which is determined from the manufacturing and preparation methods. Further discussion on the behaviour of colloidal silica in solution is covered in Chapter 5.

2.5 Conclusion

The present discussion has provided a brief overview on the long history associated with colloids and colloid stability. In the current environment of escalating fuel and energy prices many multiphase process operations can be optimised through a greater understanding of the particle-particle interactions. Such techniques have been applied in the water industry for many years to optimise sedimentation rates and water recovery. Only in recent years has the hydrotransport community begun to work with additives to control the particle-particle interaction behaviour and optimise the pipeline and pumping performance.

The discussion on colloids and colloid stability has been included in the thesis to provide a basis for interpretation of the data in the later chapters. The DLVO theory is strictly developed for pair interactions if only the double layer and Van der Waals forces are operative. Non-DLVO interactions such as steric or solvent interactions, thin film coalescence or multi particle contacts are beyond the theoretical confines [2]. However, over the years many researchers have found the DLVO theory to be a useful tool when interpreting non-colloidal particle-particle interactions and multi-particle suspension properties. For the results chapters later in the thesis, where particle-particle interactions and suspension rheological properties are investigated, the behaviour can be suitably interpreted and discussed using the DLVO theory; the theory being used only to provide a tool to supplement an understanding of the observed changes.

Chapter References

1. Grahame, D.C., Chemical Reviews (Washington, DC, United States), 1947. **41**.
2. Lyklema, J., H.P. van Leeuwen, and M. Minor, *DLVO-theory, a dynamic re-interpretation.* Advances in Colloid and Interface Science, 1999. **83**(1-3): p. 33-69.
3. Adamczyk, Z. and P. Weronski, *Application of the DLVO theory for particle deposition problems.* Advances in Colloid and Interface Science, 1999. **83**(1-3): p. 137-226.
4. Elimelech, M., et al., *Particle Deposition and Aggregation: Measurement, Modelling and Simulation.* Colloid and Surface Engineering Series, ed. R.A. Williams. 1995, Woburn, MA: Butterworth-Heinemann. 441.
5. Hamaker, H.C., Physica 1937. **4**: p. 1058-1072.
6. Shaw, D.J., *Introduction to Colloid & Surface Science.* Butterworth Heinemann, 1992.
7. Bevan, M.A. and D.C. Prieve, *Direct Measurement of Retarded van der Waals Attraction.* Langmuir, 1999. **15**(23): p. 7925-7936.
8. Gregory, J., *Approximate Expressions for Retarded van der Waals Interaction.* Journal of Colloid and Interface Science, 1981. **83**(1): p. 138-145.
9. Hunter, R.J., *Introduction to Modern Colloid Science.* Oxford University Press, 1993.
10. Derjaguin, B.V. and L. Landau, *Theory of the stability of strongly charged lyophobic sols and of the adhesion of strongly charged particles in solutions of electrolytes.* Acta Physicochim. URSS, 1941. **14**: p. 633-662.
11. Verwey, E.J.W. and J.T.G. Overbeek, *Theory of the stability of lyophobic colloids.* 1948, Amsterdam: Elsevier.
12. Israelachvili, J.N. and G.E. Adams, *Measurement of forces between two mica surfaces in aqueous electrolyte solutions in the range 0–100 nm.* Journal of the Chemical Society-Faraday Transactions I, 1978. **74**: p. 975-1001.
13. Franks, G.V., C.V. Sepulveda, and G.J. Jameson, *pH-sensitive flocculation: settling rates and sediment densities.* AIChE Journal, 2006. **52**(8): p. 2774-2782.
14. Huynh, L., P. Jenkins, and J. Ralston, *Modification of the rheological properties of concentrated slurries by control of mineral-solution interfacial chemistry.* International Journal of Mineral Processing, 2000. **59**(4): p. 305-325.

15. Heywood, N.I., *Slurry Mixing, Rheology and Handling Short Course.* Slurry Retrieval, Pipeline Transport & Plugging and Mixing Workshop, 2008.

16. Chhabra, R.P. and J.F. Richardson, *Non-Newtonian Flow in the process industries: Fundamentals and Engineering Applications.* Butterworth Heinemann, 1999(1).

17. Smoluchowski, M., Zeitschrift fuer Physik, 1917. **92**: p. 129.

18. Saffman, P.G. and J.S. Turner, *On the collision of drops in turbulent clouds.* Journal of Fluid Mechanics, 1956. **1**: p. 16-30.

19. Camp, T.R. and P.C. Stein, *Velocity gradients and internal work in fluid motion.* Journal of Boston Society of Civil Engineering, 1943. **30**: p. 219.

20. Fuchs, N., *Uber die Stabilitat und Aufladung der Aersole.* Zeitschrift fuer Physik, 1934. **89**: p. 736-743.

21. Reerink, H. and J.T.G. Overbeek, *The rate of coagulation as a measure of the stability of silver iodide sols.* Discussions of the Faraday Society, 1954. **18**: p. 74-84.

22. Holthoff, H., et al., *Coagulation rate measurements of colloidal particles by simultaneous static and dynamic light scattering.* Langmuir, 1996. **12**(23): p. 5541-5549.

23. Uricanu, V., J.R. Eastman, and B. Vincent, *Stability in colloidal mixtures containing particles with a large disparity in size.* Journal of Colloid and Interface Science, 2001. **233**(1): p. 1-11.

24. Elimelech, M., et al., *Particle Deposition & Aggregation - Measurement, Modelling and Simulation.* Colloid and Surface Science Engineering Series, 1995.

25. Lin, M.Y., et al., *Universal Diffusion-Limited Colloid Aggregation.* Journal of Physics-Condensed Matter, 1990. **2**(13): p. 3093-3113.

26. Lin, M.Y., et al., *Universal Reaction-Limited Colloid Aggregation.* Physical Review A, 1990. **41**(4): p. 2005-2020.

27. Tang, S., et al., *Fractal morphology and breakage of DLCA and RLCA aggregates.* Journal of Colloid and Interface Science, 2000. **221**(1): p. 114-123.

28. Burns, J.L., et al., *A Light Scattering Study of the Fractal Aggregation Behavior of a Model Colloidal System.* Langmuir, 1997. **13**(24): p. 6413-6420.

29. Martin, J.E., et al., *Fast aggregation of colloidal silica.* Physical Review A: Atomic, Molecular, and Optical Physics, 1990. **41**(8): p. 4379-91.

30. Hermawan, M., et al., *Characterisation of short-range structure of silica aggregates - implication to sediment compaction.* International Journal of Mineral Processing, 2004. **73**(2-4): p. 65-81.

31. Aubert, C. and D.S. Cannell, *Restructuring of colloidal silica aggregates.* Physical Review Letters, 1986. **56**(7): p. 738-41.

32. Schlomach, J. and M. Kind, *Theoretical Study of the Reorganization of Fractal Aggregates by Diffusion.* Particulate Science and Technology, 2007. **25**(6): p. 519-533.

33. Zhou, Z.K., P.Q. Wu, and B.J. Chu, *Cationic Surfactant Induced Fractal Silica Aggregates - a Light-Scattering Study.* Journal of Colloid and Interface Science, 1991. **146**(2): p. 541-555.

34. Zhou, Z.K. and B. Chu, *Fractal Study of Polystyrene Latex and Silica Particle Aggregates.* Physica A, 1991. **177**(1-3): p. 93-100.

35. Chapel, J.P., *History-Dependent Hydration Forces Measured between Silica Surfaces.* Journal of Colloid and Interface Science, 1994. **162**(2): p. 517-519.

36. Biggs, S. and A.D. Proud, *Forces between silica surfaces in aqueous solutions of a weak polyelectrolyte.* Langmuir, 1997. **13**(26): p. 7202-7210.

37. Taran, E., et al., *Nonlinear friction characteristics between silica surfaces in high pH solution.* Journal of Colloid and Interface Science, 2007. **307**(2): p. 425-432.

Chapter 3

SLURRY FLOW LOOP DESIGN AND ITS ASSOCIATED INSTRUMENTATION

NOMENCLATURE

B	Flux density
D	Diameter of impeller
d	Diameter of pipe
d_p	Diameter of particle
e	Voltage
g	Gravitational acceleration
l	Length of conductor
l'	Half loop length
M	Bending moment
m	Mass flow rate
N_{js}	Impeller speed required to just suspend the particles
P	Minimum power requirement
P_o	Dimensionless power number = 0.67
r	Radius of tube
S	6.8
U	Mean stream velocity
$\overline{U}$	Depth-averaged streamwise velocity
u''	Turbulence intensity
u'	RMS streamwise component of the flow
u	Instantaneous velocity
X	$100 \times \frac{Solid\ Mass}{Liquid\ Mass}$
x_{ent}	Entrance length
$\Delta\rho$	Solid liquid density difference
ρ_L	Density of fluid
ρ_m	Density of mixture
ν	Kinematic viscosity
v'	Relative velocities between the conductor and the field
ω	Angular rotation velocity

ABREVIATIONS

PIV	Particle imaging velocimetry
UDVP	Ultrasonic Doppler velocity profiling
Re	Reynolds number
EMF	Electromagnetic flow meter

Synopsis

The design criteria and design equations used to construct a horizontal slurry flow loop are outlined. Evaluation of the pipe loop and its individual components are initially made, before scrutinising the ancillary equipment and instrumentation required for the measurements. The slurry flow rig cleaning and operating procedures for the re-suspension and turbulence experiments are also outlined.

3.1 Pipe Loop Design

A century of multiphase flow research has highlighted the 'fit for purpose' philosophy that should be employed when designing a slurry flow loop. An extensive literature review by Gillies (1991) [1] illustrated the wide range of studies that can be completed using a slurry flow loop, thus stressing the importance of critical analysis design to deliver a system that allows for accurate and reliable data collection. Some of the slurry flow loop applications considered by Gillies[1] are:

- Solid loading limits of the system
- Minimum transport velocity
- Velocity and concentration profiling
- Calibration of meters and sensors
- Pumping characteristics and performance
- Particle degradation
- Erosion/corrosion
- Start up and shut down protocols

Figure 3.0 summarises the key steps that should be undertaken to ensure that a horizontal flow loop is 'fit for purpose'. The first step is to identify the application for the slurry flow loop which is generally governed by the project objectives, in our case, to investigate the re-suspension and turbulence properties of colloidal suspensions. The second step focuses on the material to be transported in the pipe loop. The research here was directed towards studying 'model' slurries; that is to say, slurries where the particle size, shape and density; and the solution chemistry can be sensitively controlled. An in-depth 'bench-top' experimental programme provided a comprehensive data set from which several slurries were chosen for further investigation in the pipe loop. Readers are referred to chapters 4 and 5 which report the experimental programme and the results in detail. The third step reports an early assessment of the possible technologies that can be installed on the pipe loop to collect the relevant experimental data, along with instrumentation that can be installed to continuously monitor the operating performance of the pipe loop. Imaging using PIV was chosen to study the re-suspension characteristics of the sediment beds, and UDVP was chosen to study the turbulence properties. The design of the pipe loop should then incorporate the key outcomes from steps 1-3. Our pipe loop design was greatly influenced by the cost of the raw materials for the slurry. Both the test loop length and the pipe diameter were suitably chosen in consideration of these raw material costs. The pipe material was influenced by cost, safety (pressure rating, chemical resistance) and its optical property (maintaining image clarity). Consideration was also given to access ports on the pipe loop, which allows for fluid/air drainage, as well as equally spaced fittings that enable the loop to be disassembled with ease to remove any sediment blockages. Finally, the subsidiary equipment such as pumps, mixers and flow meters were chosen based on design calculations which are a function of the slurry and the operating parameters.

Application	Investigate the influence of colloid interactions on: 1) Re-suspension behaviour of consolidated sediments 2) Minimum transport velocity of colloidal suspensions 3) Turbulence intensity of colloidal suspensions
Slurry properties	Discrete phase: 1) Size 2) Shape 3) Density 4) Concentration Continuous phase: 1) pH 2) Ionic concentration
Instrumentation	Selection criteria: 1) Suitability 2) Sensitivity 3) Safety 4) Cost
Piping	Selection criteria: 1) Pressure rating 2) Optical properties 3) Access ports
Ancillaries	1) Feed vessel 2) Pump 3) Data acquisition

Figure 3.0 Pipe loop design criteria

3.1.1 Experimental Pipe Loop

The pipe loop can be described as an open-loop, re-circulating system. Once-through and closed loop re-circulating systems were rejected on the basis of cost and ease of operation. Figure 3.1 shows a schematic layout of the experimental loop. The system consists of a 55 litre mixing tank supported 1.5m above the pump inlet. The fluid pulsations from the pump discharge are sufficiently dampened by a 2m coil of unreinforced PVC hose, pressure rating 5 bar (RS components, UK). A 5.5m long test section is constructed from clear PVC-U pipe, 26mm i.d., pressure rating 15 bar (International Plastic Systems, UK), and 26mm i.d. DURAN® glass tubing, pressure rating 8 bar (SCHOTT, UK). The test section is secured to a horizontally levelled bench, with an outbound and inbound length of 2.3m and 2.5m respectively.

Both test sections, UDVP on the outbound and PIV on the inbound are preceded by a disturbance free approach length. An air bleed valve is located on the outbound section and 4 pressure gauges are spaced at 0.75m intervals on the inbound section. An electro-magnetic flow meter is vertically positioned 0.75m along the feed line to the mixing tank.

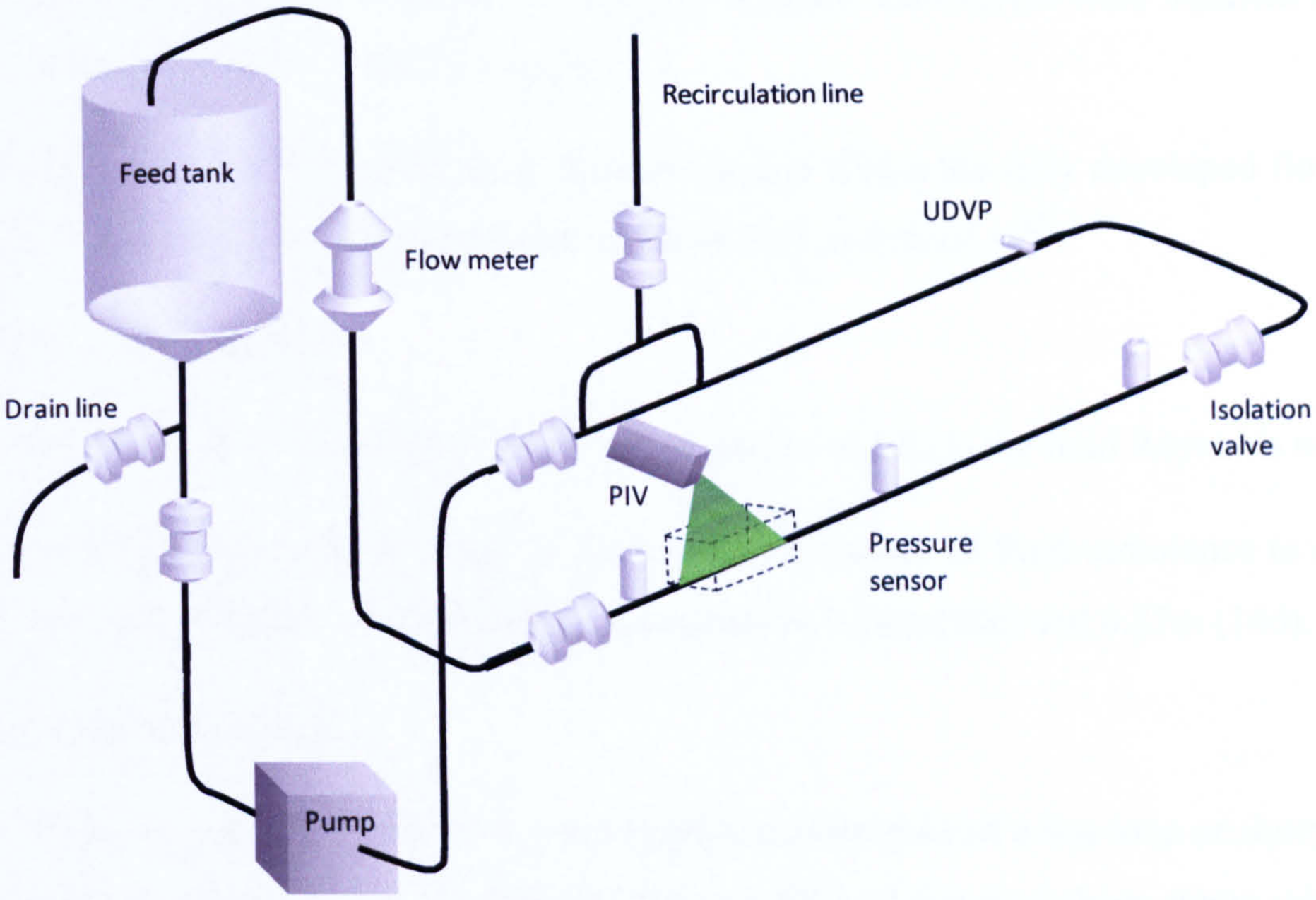

Figure 3.1 Schematic representation of the 26mm i.d. pipe loop

3.1.2 Pipe Selection

Three types of piping all with an internal diameter of 26mm were installed on the flow loop. The flexibility of PVC hosing enabled the flow lines to and from the pump to be connected with relative ease, and provided a suitable degree of pulsation dampening from the pump discharge. 80% of the rig is constructed using clear PVC-U tubing, chosen due to its rigidity, resistance to chemical attack and transparency. A 0.75m long DURAN® glass section installed beneath the illuminated laser sheet provides excellent optical properties, therefore, minimising adsorption and/or distortion of the light sheet. Due to the curvature of the pipe, a small water box (l: 250mm, w: 100mm, h: 120mm) was installed around the glass test section to improve image clarity by minimising the distortion of the laser light.

Economic limitations, laboratory floor space and measurement optimisation were all factors considered when selecting a suitable internal pipe diameter. The eventual pipe diameter was a compromise between minimising the rig volume and maintaining a sufficiently large pipe cross sectional area so that the two measurement techniques, PIV and UDVP could be applied.

The test length of the pipe loop included union sockets at 1m intervals which provided ease of access for pipeline cleaning and blockage removal. Ball valves were installed on the rig to be operated only as isolation valves.

Both PIV and UDVP instruments were positioned within the fully developed flow region. The entry length for fully developed turbulent flow is defined as[2]:

$$\frac{x_{ent}}{d} = 1.41 \times Re^{0.25} \qquad [3.0]$$

where x_{ent} is the entry length, d is the pipe diameter and Re is the fluid Reynolds number.

Over a Reynolds number range of 2500 to 11000 (on-set of fluid turbulence to maximum pump flow velocity), the entry lengths are given as 0.26m (10d) and 0.37m (14d).

3.1.3 Pump Selection

The choice of pump is crucial to the operating performance of a test loop or slurry pipeline. As can be seen in figure 3.2 there are several different types of slurry pump which reside under the headings of direct and fluid (in-direct) displacement. Indirect displacement defines the movement of a slurry using either air, water or oil as a motive fluid. Typical examples of indirect slurry pumps are: Jet, TORE, XAGO AtmosTras and Air Lift. Due to their limited applications, a brief description of the pumps operation will not be provided. However, readers are referred to the following references for further information [3, 4].

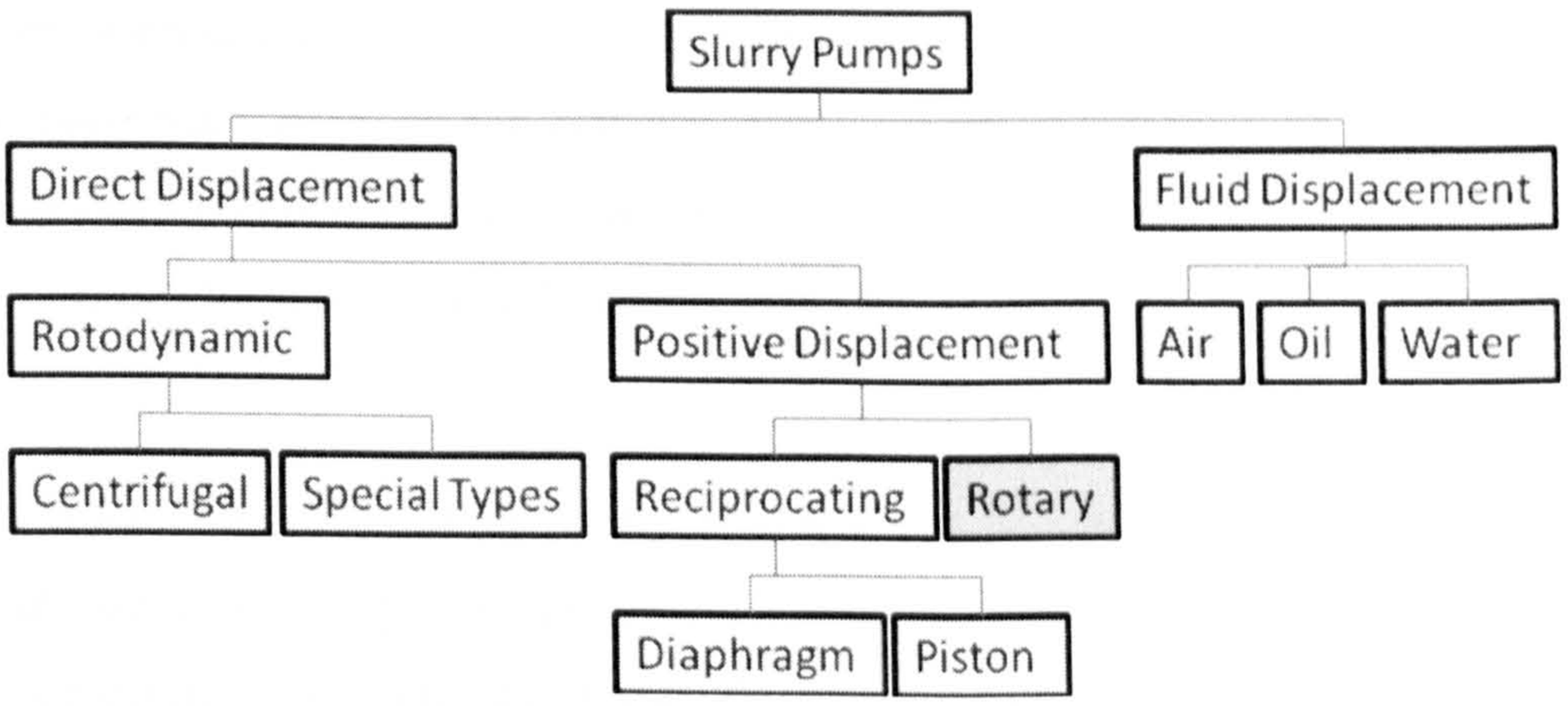

Figure 3.2 Types of slurry pump

Direct displacement pumps which are more commonly used in slurry applications describe a 'family' of pumps which convert mechanical energy into kinetic energy of the slurry. This group can be further sub-divided into two more categories; rotodynamic and positive displacement. A rotodynamic pump which generally describes the action of a centrifugal pump accelerates the slurry by means of a rotating element enclosed in a housing, generating a pulsation free slurry flow. Such pumps are portrayed as being the most durable, producing flow rates up to 17,000 m^3hr^{-1}, discharge pressures in excess of 200m water, operating temperatures ranging from -40 to 300°C and solids handling capabilities up to 200mm, with a solids loading approaching 80% by mass; dependent upon the rheological properties of the slurry. However, there are several disadvantages associated with running such a pump. Particles passing through the pump housing can be shattered on impact with the rotating disc, and conversely, the ribs on the rotating disc can be eroded away due to the abrasive nature of the particles in the suspension. Also, operating a centrifugal pump in extremely low flow rate conditions (tens of litres per hour) can cause the pump to continually stall, as it fails to generate a high enough suction or outlet pressure.

Positive displacement pumps can be categorised into reciprocating, further sub-divided into diaphragm or piston, and rotary pumps. Reciprocating pumps are characterised by high head, as well as low flow, low shear, low wear and low particle degradation rates, with a capability of pumping very viscous, abrasive slurries. The pump works on the principle of drawing a volume of slurry through a non-return valve into the pump housing on a suction stroke, before pressuring the slurry and expelling the slurry from the pump housing through a second non-return valve on the delivery stroke. Such systems can be single acting (one piston and one chamber) or double acting (one position and two chambers). Diaphragm pumps work on the same principle except that the slurry is not in direct contact with the piston.

There are a wide range of commercial pumps that can be categorised as 'rotary'. Only the two most common pumps, progressive cavity and peristaltic will be considered. A progressive cavity pump consists of a single start helical screw rotor which turns within a double interval helix stator, in a slightly eccentric motion. The pitch of the stator is twice that of the rotor and the movement of the two parts open and close a cavity which is passed from the suction to the delivery side of the pump. The rotor maintains a positive seal along

the length of the stator, and the seal progresses continuously through the pump, giving uniform positive displacement (little pulsation) [5]. Such pumps are typically used to pump highly viscous, shear sensitive materials, whilst achieving high flow rates and discharge pressures. However, one of the main disadvantages to running a progressive cavity pump is that it cannot be operated at extremely low flow rates, due to the high torques required to maintain the motion of the rotor and stator.

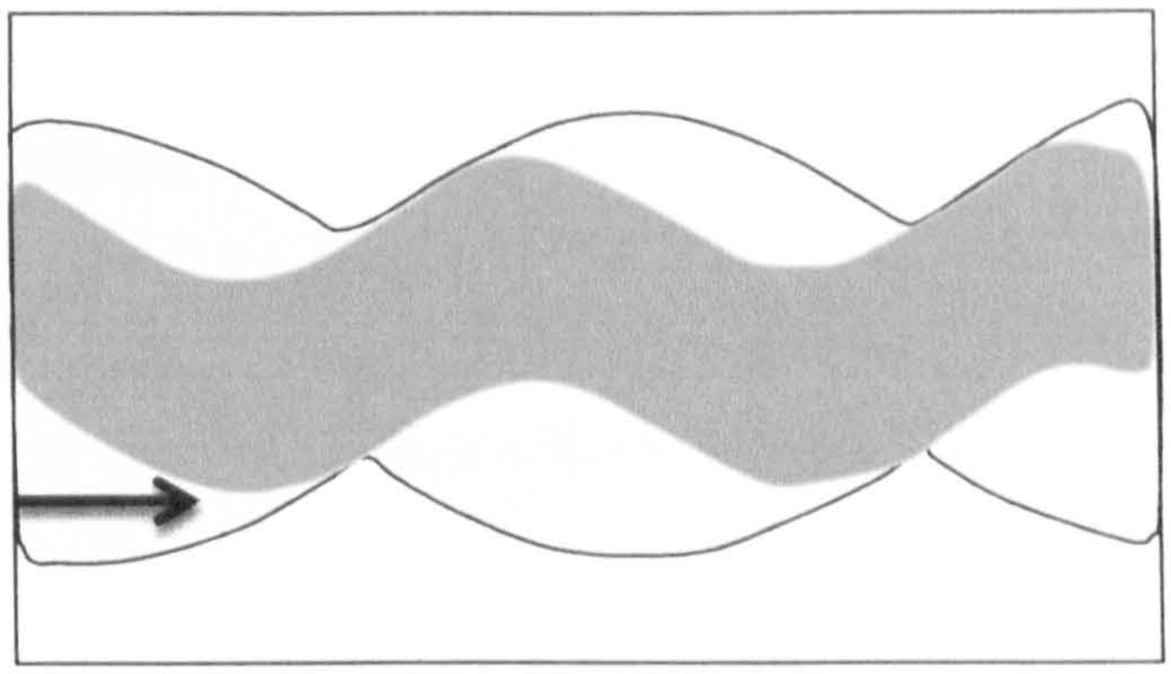

Figure 3.3 Operational diagram: Progressive cavity pump. Arrow indicates flow direction.

A peristaltic pump typically includes two, three or four bearing mounted rollers which rotate squeezing a flexible tube, inducing flow as it slides along the tube. As the roller compresses the tube driving the fluid before it, the tubing behind the roller returns to its original shape thus creating a vacuum, drawing in more fluid which in turn is driven forward by the next roller. Such action always results in pulsatile flow. Peristaltic pumps can provide sensitive flow control at extremely low flow rates, and are typically used to pump high viscosity, high solids content slurries.

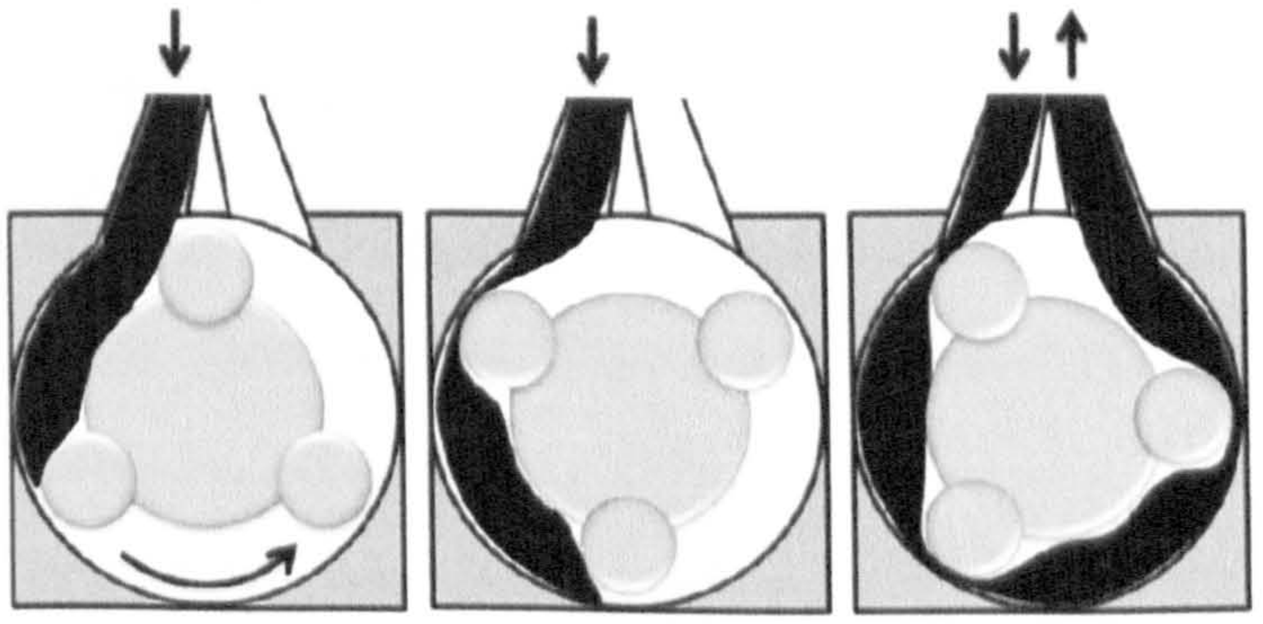

Figure 3.4 Operational diagram: Peristaltic pump. Arrows indicate flow direction.

An assessment of the available pumping technologies considering suitability, cost and reliability, concluded that a peristaltic pump should be installed on the slurry flow loop. A peristaltic pump is especially suited for this particular application due to its non-aggressive treatment of the suspension. With the study investigating the influence of aggregates on the minimum transport velocities and turbulence properties of colloidal suspensions, a view was taken that a centrifugal pump which could have been installed to operate at low flow rates, would most likely result in aggregate break-up through the pump housing, leading to a misrepresentation of the degree of aggregation. A 620 SN/RE (Watson-Marlow, UK), with a 17mm Marprene TM tubing element provided flow velocities up to 0.42ms^{-1} (Re = 11000) in full bore applications.

3.1.4 Feed Tank Design

Tank volume; impeller size, type and quantity; baffle size and quantity, and motor size are all to be considered in the design of the feed tank. In an open re-circulating slurry loop the feed tank provides sufficient time for dispersion of the solids, ensuring a homogenous feed to the test loop.

The volume of the tank is determined by the volume of the slurry loop (absolute minimum volume) plus a mixing volume and a safety factor. The mixing volume is based upon the required residency time in the tank, which for this particular application was chosen to be 90 seconds under maximum operating conditions, and a safety factor of 150-200mm above the fluid level. A 55 litre feed tank, with a height to diameter ratio of 1.25 was suitably designed for the application.

An axial flow JP3 impeller with a 0.28 ratio (impeller: tank diameter) was chosen for this particular application. The axial flow impeller draws fluid into the impeller from above, before discharging the fluid towards the base of the tank and the liquid surface.

Using Zweiterings' theory [6], the impeller speed required to just suspend the particles (no particle stationary on the vessel base for longer than 1 – 2 seconds) can be calculated. The theory is described by:

$$N_{JS} = S \cdot v^{0.1} \cdot d_p^{0.2} \cdot [g(\Delta\rho/\rho_L)]^{0.45} \cdot X^{0.13} / D^{0.85} \qquad [3.1]$$

where S = 6.8, a dimensionless parameter based on the system geometry, X is equal to $100 \times \frac{Solid\ Mass}{Liquid\ Mass}$, D corresponds to the impeller diameter, g is the gravitational constant, $\Delta\rho$ is the density difference between the solid and liquid mediums, ρ_L is the fluid density and υ is the kinematic viscosity. Based on a three blade axial impeller with a solid mass to liquid loading ratio of 0.25, the minimum rotational speed is calculated to be 6 revolutions per second. The dimensionless power number can then be applied to calculate the power requirement of the agitator motor. The dimensionless power number (Po) is defined as:

$$Po = \frac{P}{\rho_M . N_{JS}^3 . D^5} \qquad [3.2]$$

with ρ_m taken as 1000 kg/m^3, N_{JS} = 6, D = 0.112 m, the minimum power requirement of the agitator motor is then calculated to be 5W, when Po = 0.67 [7]. However, to induce turbulent flow conditions throughout the mixing vessel and to account for mechanical inefficiencies, a 0.25 kW DT agitator (Chemineer, UK) was installed. To prevent the build of a vortex in the mixing tank, a standard baffled configuration was used. Four equally spaced vertical baffles with lengths equal to the straight side of the tank, widths equal to one-twelfth of the tank diameter and offset to one-sixth of the baffle width from the tank wall were installed.

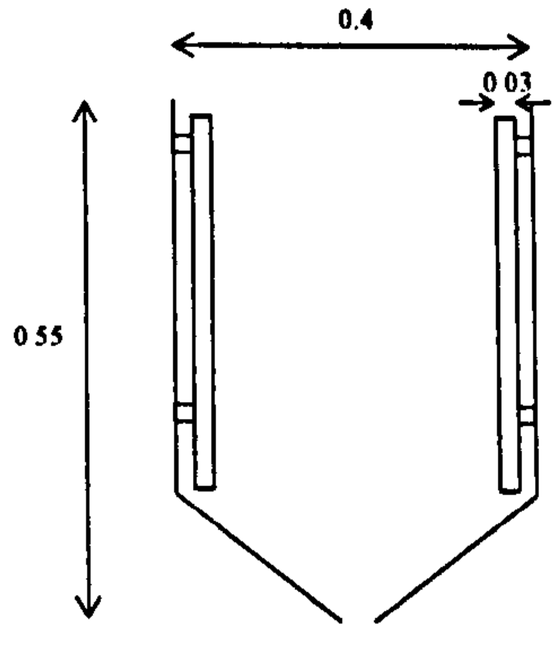

Figure 3.5 Feed tank dimensions. Units (m)

3.2 Instrumentation

The onset of particle re-suspension/deposition can be identified using a variety of techniques such as; visual assessment [8], measurement of the hydraulic gradient, conductivity measurements [9], voltage measurements in an applied transverse field [10] and electrical resistance tomography. All these techniques can provide a qualitative assessment of the flow regime. However, in order to quantitatively assess the flow, such techniques need to be combined with a measured flow rate.

3.2.1 Flow Meter

There are a wide variety of flow meters, mass or volumetric, invasive or non-invasive, which provide a range of operating specifications. However, many of the options available for gas and liquid flows are not suitable for slurry applications. With many invasive measurement techniques, the flow is squeezed through a fine clearance of known dimensions to determine the flow rate. With suspension flow, blockage and erosion of the flow channel geometry can result in significant measurement errors. Therefore, only non-invasive techniques are considered suitable for the slurry flow loop.

Electromagnetic flow meter (EMF): The working principle of the flow meter uses Faraday's law of electromagnetic induction. Faraday's law states that when a conductor of length l moves through a magnetic field of a given flux density B, a voltage e is produced in the conductor that is dependent on the relative velocities v' between the conductor and the field, such that:

$$e = Blv' \qquad [3.3]$$

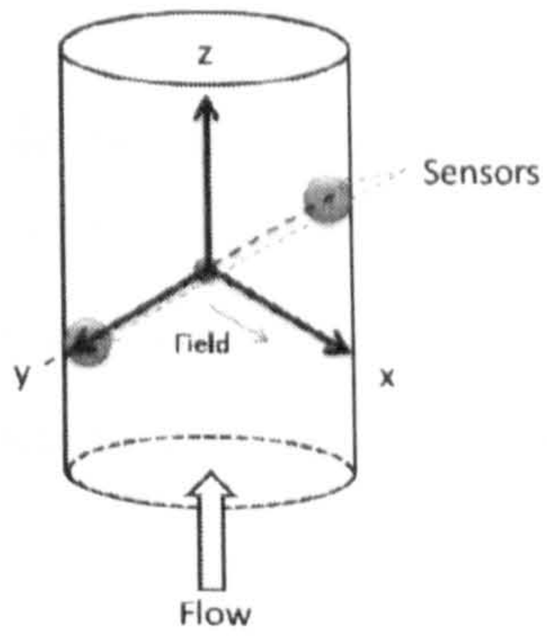

Figure 3.6 Sensors arrangement in an Electromagnetic flow meter

Figure 3.6 illustrates the working principle of an EMF. A magnetic field is generated in a plane that is perpendicular to the liquid (conductor) flow, and two sensors placed diametrically opposite one another on the same pipe section. As the conductive fluid flows down the longitudinal axis of the flow meter, the voltage induced in the liquid, is mutually perpendicular to both the velocity of the liquid and the magnetic field. Because the magnetic flux and the length of the conductor have fixed values, the magnitude of the induced voltage is directly proportional to the velocity of the liquid. With the sensors connected to an external circuit, the induced voltage causes a current *i* to flow which can then be converted into a flow rate.

Utilising a non-intrusive technique, with no moving parts and a choice of suitable liners (ceramics, fibreglass, neoprene) that enable the use of such an instrument in both chemical and physical testing environments, EMF's are extremely suited to slurry flow applications. Such instruments can typically operate from 0.04 to tens of thousands of litres per minute, depending upon the orifice size. The conductivity of the fluid should typically be greater than 0.05μS/cm to induce a measurable voltage.

Coriolis mass flow meter: A mass flowrate is determined through interpretation of a phase shift in the oscillating frequency of a tube loop. When empty, the tube is oscillated at its resonance frequency by a magnetic driver. As the slurry enters the tube, the harmonic vibrations impart an angular motion to the fluid, thus exerting a Coriolis force on the tube wall. The force causes the tube loop to twist with a bending moment M that is dependent upon; the angular rotation velocity ω, the tube loop radius r, the half loop length l and the mass flow rate m where:

$$M = 4\omega r l' m \qquad [3.4]$$

Typical operating conditions enable measurements to be made up to 9000 $kgmin^{-1}$, with the instrument accuracy independent of the slurry properties and flow regime. One of the main disadvantages associated with mass flow meters is that the fluid velocity can only be determined indirectly through combining the reading with an on-line density measurement.

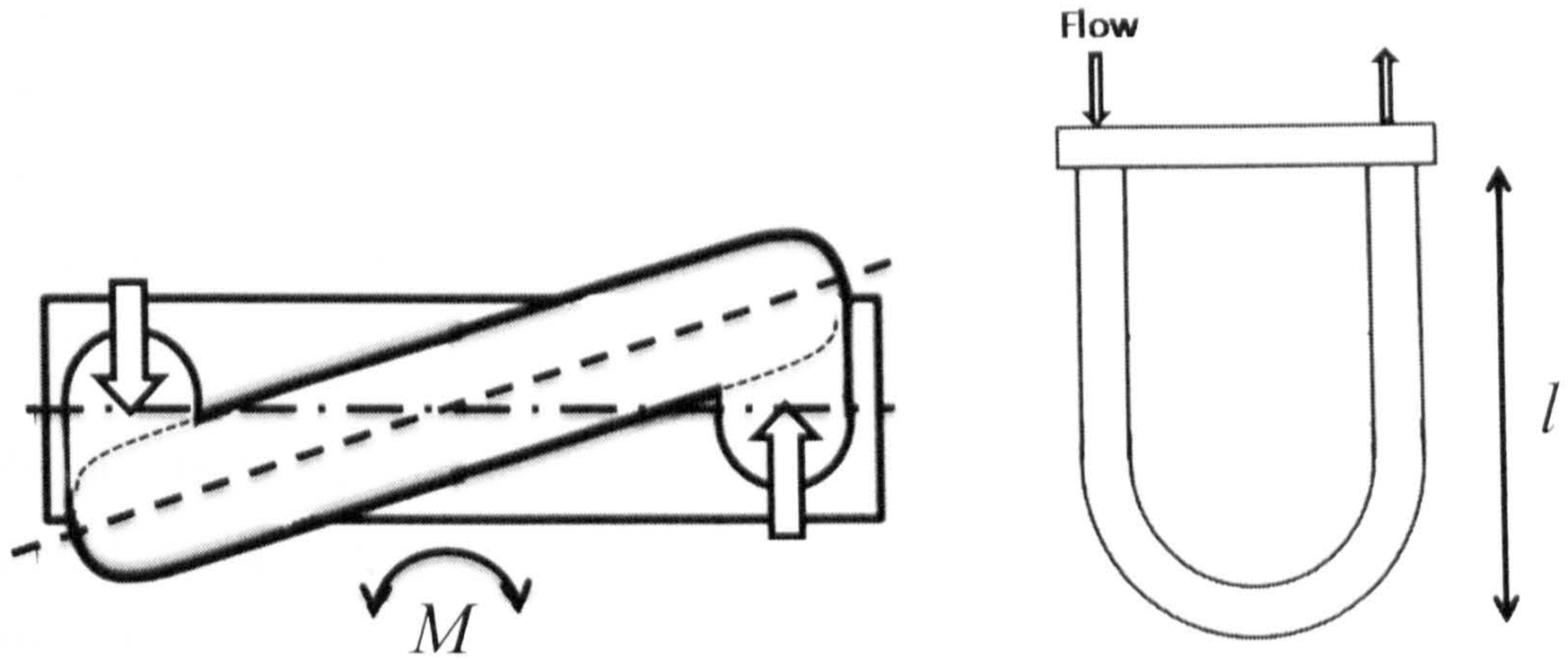

Figure 3.7 Coriolis mass flow meter sensor tube. Figure adapted from reference [11].

Cross correlation meter: At least two sensors are set at a known distance apart along the length of the pipeline. The sensors may detect changes in electrical conductivity, capacitance, or transmitted/reflected ultrasound [12]. The time of passage of individual eddies in turbulent flow between two sensors enables the average flow velocity to be calculated. The use of these techniques in industrial or research applications has been limited due to the high instrument costs, a direct result of the complexity of this approach.

Ultrasonic flow meter: Refer to chapter 4 Materials and Methods for measurement principle.

Through assessment of the available technology, a KROHNE OPTIFLUX 5300c magnetic inductive flow meter (KROHNE Ltd., Germany) was installed on the pipe loop. A 6mm measurement bore with a fused ceramic lining and platinum electrodes gives flow rate readings up to $7.5 \times 10^{-1} m^3 hr^{-1}$. The flow meter is installed vertically to reduce the risk of solids deposition on one of the electrodes and to avoid inaccuracies caused by asymmetric velocity profiles. The instrument accuracy supplied by the manufacturer is within ± 0.2% over the range 3.0×10^{-2} $m^3 hr^{-1}$ to 6.1×10^{-1} $m^3 hr^{-1}$. The calibration was confirmed through measuring the displaced volume as a function of time.

3.2.2 Pressure / Temperature Sensors

Flush diaphragm pressure sensors were installed on the pipe loop to provide information on the slurry flow regime, and to assist the early detection of pipe blocking. DMP 331-P sensors (Impress Sensors & Systems, UK) use strain gauges integrated within the

corrugated diaphragm to monitor the displacement of the element under loading. The sensors were individually calibrated up to 6 BarG, with a full scale deflection error of ± 0.35%. Two K-Type thermocouples (Cole-Parmer, USA) were installed on the pipe loop to monitor the slurry and atmospheric temperatures. Data was recorded using a TC-08 thermocouple data logger (Pico Technology Ltd., USA).

The 4-20mA output signal from both the pressure sensors and the flow meter were converted into the desired measured variables using scaling factors. An ADC-24 converter (Pico Technology Ltd., USA) provided up to 16 single-ended input channels.

3.3 Experimental Procedure

Slurries were prepared in 40 litre batches. The experimental programme was separated into a low and high solids concentration study. Three slurries, 1M KNO_3, 10^{-4}M KNO_3 and 10^{-4}M KCl were initially prepared to a solids concentration of around 6% by volume for the low concentration study, and 12% by volume for the high concentration study. The in-situ solids concentration for each experiment was determined through oven drying a one litre sample of slurry collected from the pipe loop discharge. All slurries were prepared 24 hours in advance of the pipe loop study, with the slurry pH monitored and adjusted to pH 6 using 5M complementary analytical grade acids (HNO_3 and HCl) and base (KOH). A paddle mixer was used to periodically agitate and disperse the solids in suspension prior to the slurry being transferred to the feed vessel. For all experiments, the impeller speed was set at 10 rev s^{-1}.

3.3.1 Sediment Bed Re-suspension and Minimum Transport Velocity Determination

Initially, the slurry was continuously circulated in the pipe loop at a flow rate of approximately 3.6×10^{-1} m^3hr^{-1} for 15 minutes, with the bleed valve repeatedly opened to remove air from the pipe loop. The flow rate was then increased to 7×10^{-1} m^3hr^{-1} for 5 minutes to remove any sediment from the pipe invert, thus, developing a homogenous concentration profile. The flow rate was then immediately reduced to 0 m^3hr^{-1}, and the two isolation valves at either end of the inbound test section were closed to prevent any disturbances such as back flow which may influence the compaction properties of the sediment. The remaining slurry in the feed tank was then drained into a holding tank.

A suitable sedimentation period that enabled a consolidated bed to form was determined from laboratory settling tests. Between each re-suspension experiment the sedimentation time for a 10^{-4} M and 1 M slurry was 24 hours and 3 hours respectively. Prior to each experiment, the associated slurry in the holding tank was re-mobilised, pH checked and then transferred to the feed vessel.

Several volumetric flow rates were chosen to investigate the re-suspension behaviour of the sediment, with the flow rates ranging from approximately 7×10^{-2} m^3hr^{-1} to 7×10^{-1} m^3hr^{-1}. Multiple re-suspension experiments were completed to ensure that a 'good' fit in the erosion rate versus slurry velocity data could be generated from which the minimum transport velocity would then be determined.

The rotational speed of the peristaltic pump was programmed prior to each experimental run to minimise the flow rate development time on start-up. The re-suspension behaviour of the sediment bed was determined from analysis of the image sequences collected using the PIV set-up. 450 frames from time t = 0 provided information on the sediment bed behaviour over the first 30 seconds of flow, while a second and third image sequence provided information on the level of sediment bed erosion after 4 minutes and 8 minutes of continuous flow. A thirty minute period where the flow rate is maintained at approximately $7 \times 10^{-1} m^3hr^{-1}$ followed each experiment to re-suspend any remaining sediment.

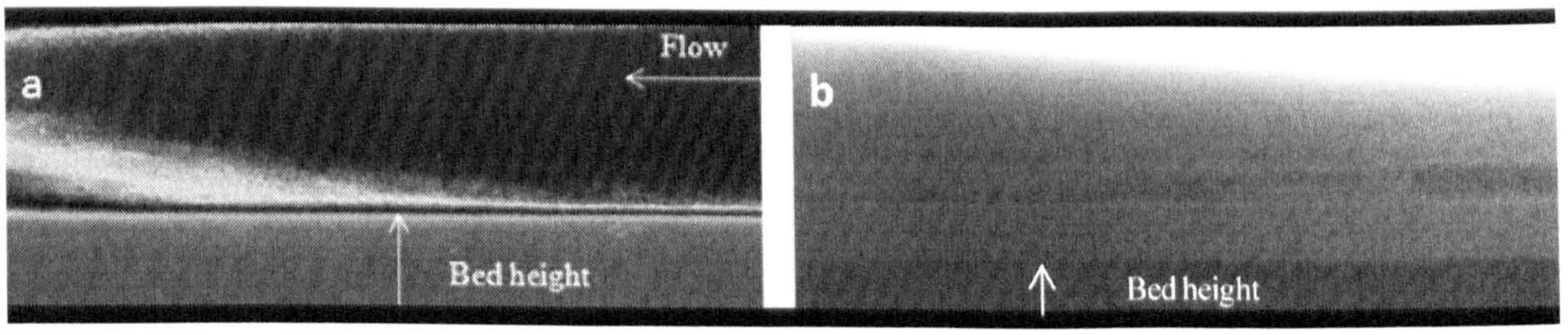

Figure 3.8 PIV images collected during re-suspension experiments, showing a decrease in the sediment bed height with time a) t = 10 seconds b) t = 240 seconds

Prior to initial slurry experiments in KNO_3 electrolytes, and then the transition to the KCl slurry, the pipe loop was cleaned with a 2% Decon solution and then washed through 5 times with de-ionised water. Each wash included 25 litres of de-ionised water that was circulated in the pipe loop for 1 hour at a flow rate of $3.6 \times 10^{-1} m^3hr^{-1}$. The wash was

necessary to remove any dirt from the pipe loop before a colloidal suspension was introduced, as well as eliminating any issues associated with cross contamination when the electrolyte is changed from KNO_3 to KCl.

By monitoring the sediment bed erosion rate with time as a function of the slurry flow velocity, it is possible to determine the minimum transport velocity of the colloidal suspensions. As previously mentioned in the introduction, and again to be discussed later in chapter 6 (see 6.4.2.), the current approaches and techniques used to determine the minimum transport velocity of a slurry could not be applied in this study. The techniques generally lack the resolution to identify particle deposition. As will be outlined in chapter 6, it is however possible to use the transition velocity (the flow velocity at the onset of sediment bed erosion) to determine the minimum transport velocity

Colloidal forces are sensitive to temperature changes, with the electrical double layer force dependent on the thermal energy (kT) of the particle (refer to chapter 2 – section 2.3). The slurry and atmospheric temperatures were recorded during all experiments. Typically, the temperature varied between 0.1°C and 0.2°C over a 10 minute period. For the re-suspension experiments, only the first 30 seconds of the bed erosion data was used in the study, therefore, the temperature change is considered negligible. For the turbulence intensity study, which is described below, each individual experiment at a given flowrate lasted 1.5 minutes. Therefore, only 3 experimental runs were completed before the pump was turned off for 10 minutes. This procedure prevented any significant temperature changes between data sets.

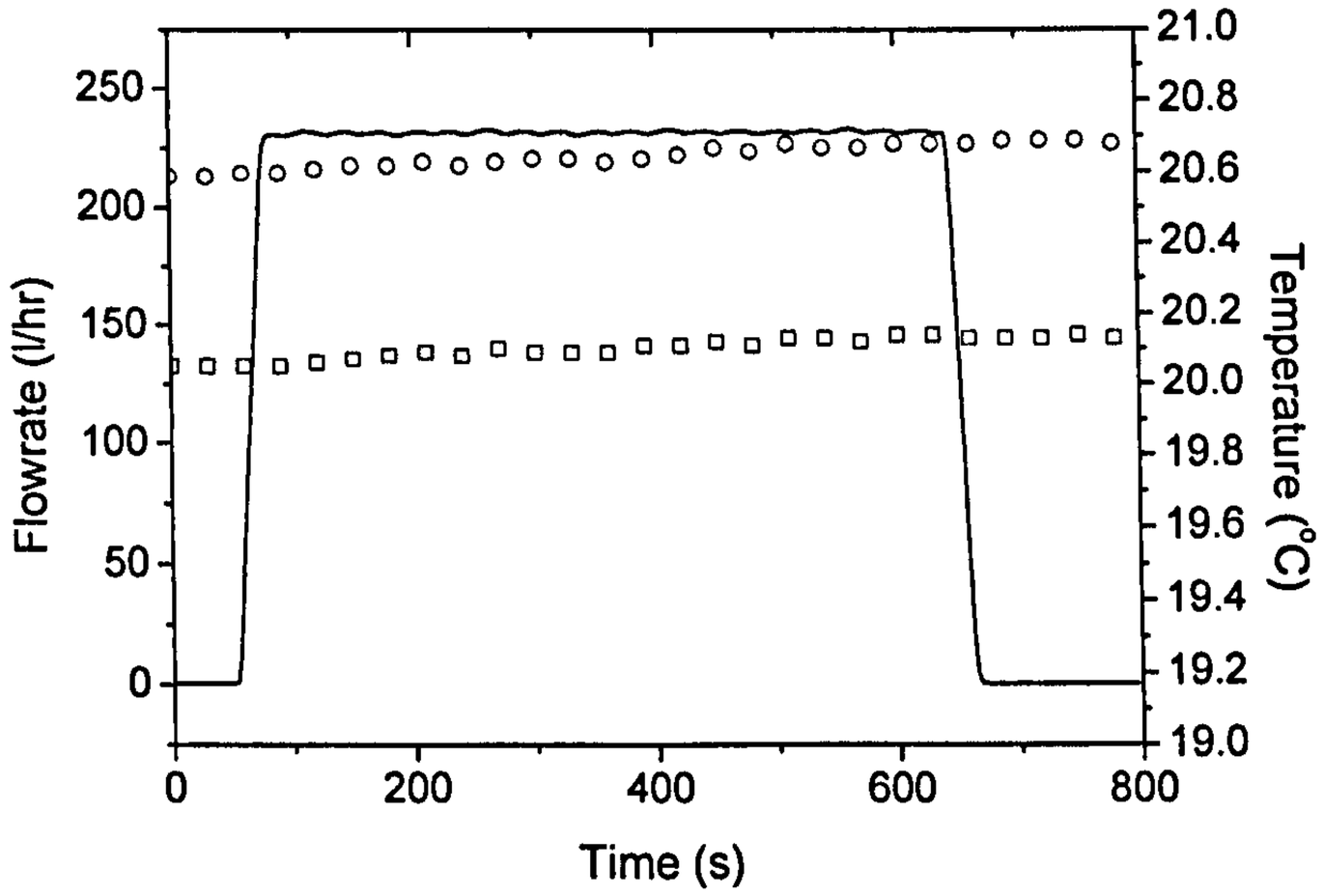

Figure 3.9 Atmospheric (o) and slurry (□) temperatures recorded during a typical re-suspension experiment. Solid line represents the slurry volumetric flowrate.

3.3.2 Turbulence Experiments

The ionic and the solids concentration effect on the suspension turbulence intensity in fully developed pipe flow was studied using UDVP. An ultrasonic probe positioned at 45° to the flow axis and submerged 1mm into the flow stream was used to collect 512 velocity profiles over a 30 second period. Flow profiles were collected at different flow rates between 7.5×10^{-1} m^3hr^{-1} and 5×10^{-2} m^3hr^{-1}, with each measurement collected after 1 minute of steady-state flow. The suspension turbulence intensity was determined from the root-mean square values (u') of the streamwise component of the flow, where the RMS is given as:

$$u' = \left[\frac{1}{n}\sum_{i=1}^{n}(u - U)^2\right]^{0.5} \qquad [3.5]$$

where u is the instantaneous velocity and U the mean stream velocity. Subsequently the turbulence intensity is then determined by:

$$u'' = \frac{u'}{\bar{U}} \qquad [3.6]$$

where $\bar{U}$ is the depth-averaged streamwise velocity.

The inclusion of sections 3.3.1 and 3.3.2 in the current chapter is only to describe the operating procedures for the minimum transport velocity and turbulence intensity experiments. The measurement principles of the two techniques used (PIV and UDVP) and the measurement parameters for each experiment are described in detail in chapter 4.

3.4 Conclusion

This chapter has highlighted the design equations that were used to construct a flow loop suitable for studying the flow properties of colloidal suspensions. One of the main drivers in the design was the raw material cost. With a project budget, the rig had to be of sufficient size to allow for the main measurement techniques, PIV and UDVP to be used on the pipe loop, while also minimising the slurry volume to reduce raw material costs. Figure 3.10 shows images of the slurry flow rig used in the current project. The black box is the laser shield for the PIV system which is used to illuminate the slurry during re-suspension experiments. The laser is mounted on a platform with a 90° optic guiding the laser sheet through the pipe. A camera is mounted on the traversing platform to collect the sediment height images during re-suspension.

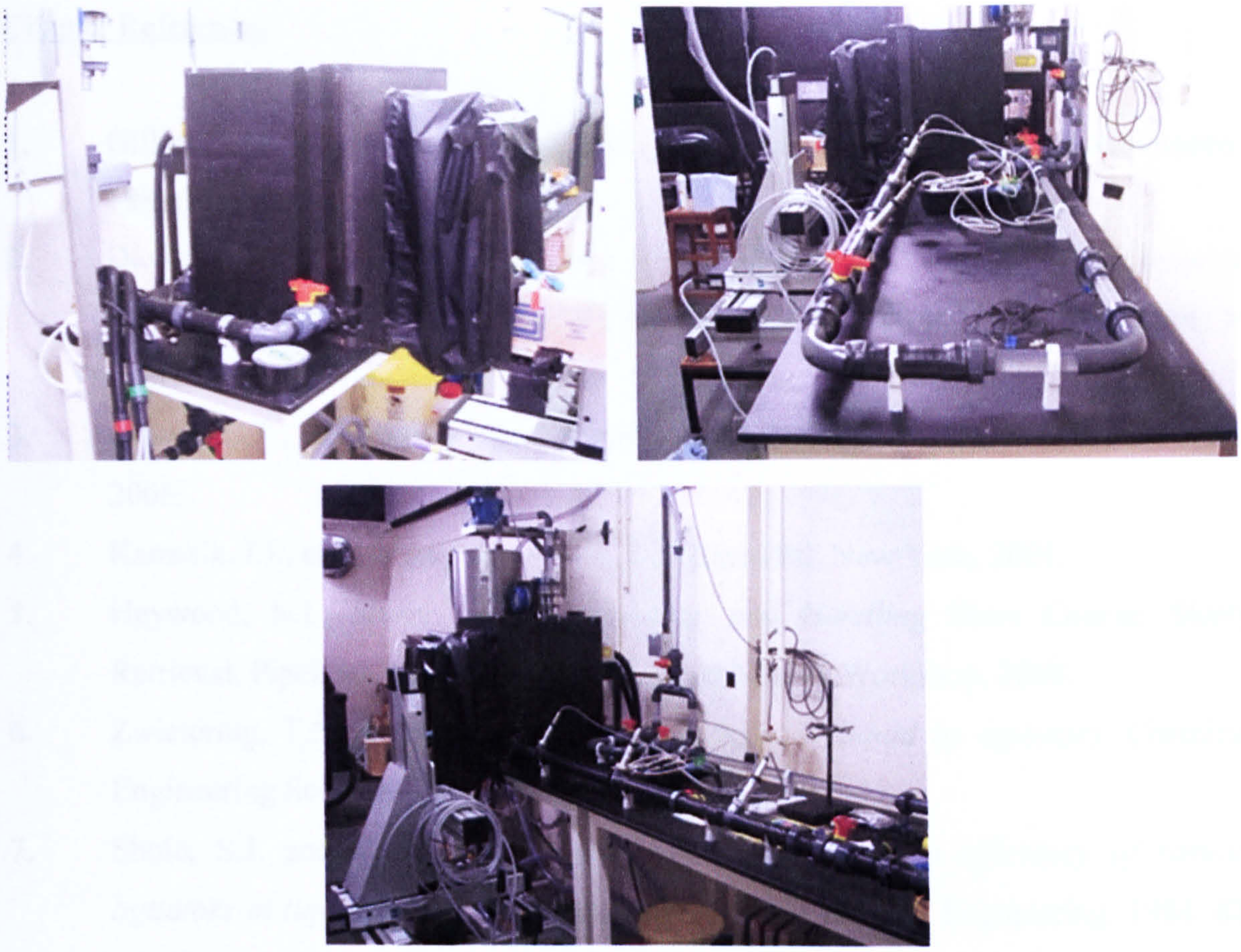

Figure 3.10 Images of the 26mm NB pipe loop constructed for the colloid suspension flow experiments.

Chapter References

1. Gillies, R.G., *Flow Loop Studies.* Slurry Handling: Design of Solid-liquid Systems, 1991(Elsevier Applied Science).
2. Davies, J.T., *Velcoities and Stresses in Turbulent Flows.* Turbulence Phenomena: An Introduction to the Eddy Transfer of Momentum, Mass, and Heat, Particularly at Interfaces, 1972.
3. Crowe, C.T., *Multiphase Flow Handbook.* CRC Press Taylor & Francis Group, 2006.
4. Karassik, I.J., et al., *Pump Handbook.* McGraw-Hill, New York, 2001.
5. Heywood, N.I., *Slurry Mixing, Rheology and Handling Short Course.* Slurry Retrieval, Pipeline Transport & Plugging and Mixing Workshop, 2008.
6. Zwietering, T.N., *Suspending of solid particles in liquid by agitators.* Chemical Engineering Science, 1958. **8**(3-4): p. 244-253.
7. Shuie, S.J. and C.W. Wong, *Stuides on homogenisation efficiency of various agitators in liquid blending.* Canadian Journal of Chemical Engineering, 1984. **62**: p. 602-609.
8. Thomas, D.G., *Transport characteristics of suspensions. VI. Minimum transport velocity for large particle size suspensions in round horizontal pipes.* AIChE Journal, 1962. **8**: p. 373-8.
9. Kazanskij, i., *Critical Velocity of depositions for fine slurries - new results.* In Proc. 6th International Conference on the Hydraulic Transport of Solids in Pipes, 1979: p. 43-56.
10. Brown, N.P., et al., *A probe for point velocities in slurry flows.* Canadian Journal of Chemical Engineering, 1983. **61**(4): p. 597-602.
11. McKetta, J. and W.A. Cunningham, *Encylopedia of chemcial processing design.* CRC Press 1992.
12. Brown, N.P. and N.I. Heywood, *The right instrumentation for slurries. Part 1.* Chemical Engineering (New York, NY, United States), 1992. **99**(9): p. 106-11, 113.

Chapter 4

MATERIALS AND EXPERIMENTAL METHODS

NOMENCLATURE

c	Speed of ultrasound in fluid
D	Diameter of active element
D_v	Diameter of vane
d_p	Diameter of particle
d	Distance from transducer
E	Elastic modulus
F_z	Normal force
F_y	Friction force
f_0	Transmitted frequency
f_i^D	Doppler frequency shift from position i
H	Length of vane
h	Suspension height
k_B	Boltzmann constant
k_y	Lateral stiffness of cantilever
k_z	Normal stiffness of cantilever
N	Characteristic length of near field region
q^2	Displacement of cantilever over time
T	Absolute temperature ^oK
T'	Maximum torsional moment
t	Cantilever thickness
t'	Time delay between transmitted and received signal
u_E	Electrophoretic mobility
u_x	Longitudinal velocity component
u	Longitudinal velocity vector
V	Poisson's ratio
V_i	Measured velocity vector
V_i'	Fluid velocity at distance i
v	Vertical velocity vector
w	Beam width
y	Lateral displacement of cantilever
z	Normal displacement of cantilever
α	Angle of inclination of ultrasonic probe
α'	Radius of particle
α''	½ the angle between the two adjoining beams

ε	Dielectric constant
κ	Debye-Huckel parameter
μ	Dynamic viscosity
τ_y	Yield stress
Φ	Solids volume fraction
Φ_{gel}	Solids volume fraction at suspension gel point
ξ	Zeta potential

ABREVIATIONS

UDVP	Ultrasonic Doppler velocity profiling
PIV	Particle imaging velocimetry
AFM	Atomic force microscope
STM	Scanning tunnelling microscopy
LDV	Laser Doppler velocimetry
M3PALS	Mixed Mode Measurement – Phase Analysis Light Scattering
SFR	Slow field reversal
FFR	Fast field reversal
ERT	Electrical resistance tomography
NB	Nominal bore

Synopsis

Chapter 4 discusses the apparatus and experimental methods employed throughout this research to characterise the individual particles, suspensions and sediments, along with techniques such as ultrasonic Doppler velocity profiling (UDVP) and particle imaging velocimetry (PIV) which are used to study the minimum transport velocities and turbulence intensities of the colloidal silica suspensions. The material properties of the colloidal silica are summarised in section 1. Atomic force microscopy a technique used to study particle-particle interactions is reviewed in section 2; sedimentation and viscometer techniques for characterising the suspension and sediment bulk properties are described in section 3, and section 4 discusses the techniques employed on the pipe loop to study the flow and turbulence properties of the concentrated silica slurries.

4.1 Material

An ultra high purity (> 99.5% SiO_2), near mono-disperse, silica sample (SP-1B) was obtained from Fuso Chemical Co., Ltd. (Osaka, Japan). This silica sample had a density of 2.26g/cm^3 (determined using a Micromeritics AccuPyc 1330 Pycnometer), and a mean particle diameter of 0.79µm, measured using a centrifugal sedimentation particle size analyser supplied by CPS Instruments Europe.

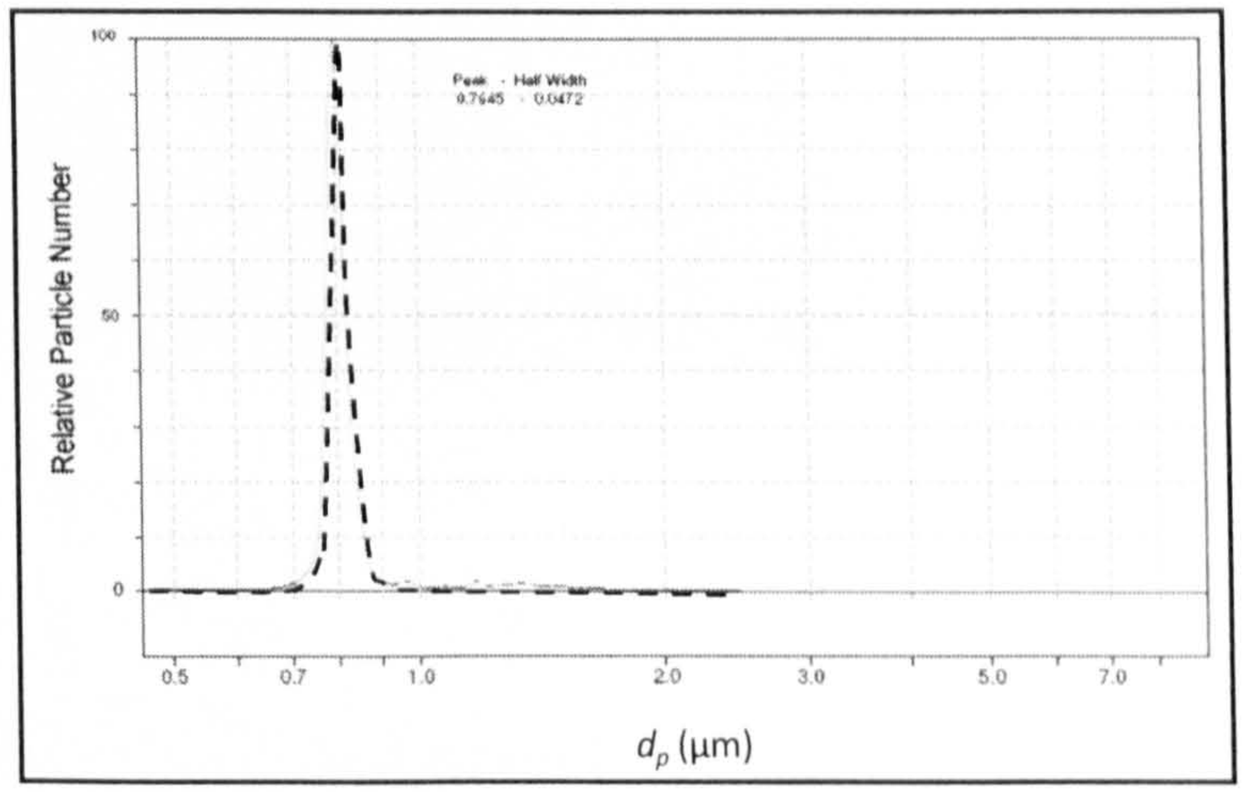

Figure 4.0 Fuso silica particle size distribution

All chemicals and other reagents were of analytical grade and were supplied by Aldrich Chemical Company, Inc (United Kingdom). The silica particles were dispersed in either KCl or KNO_3 (KBr – chapter 5 only, see chapter synopsis for details) electrolyte solutions (1M or 10^{-4}M) and all pH adjustments were made using complementary acids (HNO_3, HCl and HBr) and base (KOH). All water used throughout this study was Milli-Q® grade water with a conductivity of approximately 0.05µs/cm. Silica dispersions were either gently rotated or shaken for 24 hours in advance of any measurements to achieve full equilibrium, unless otherwise stated.

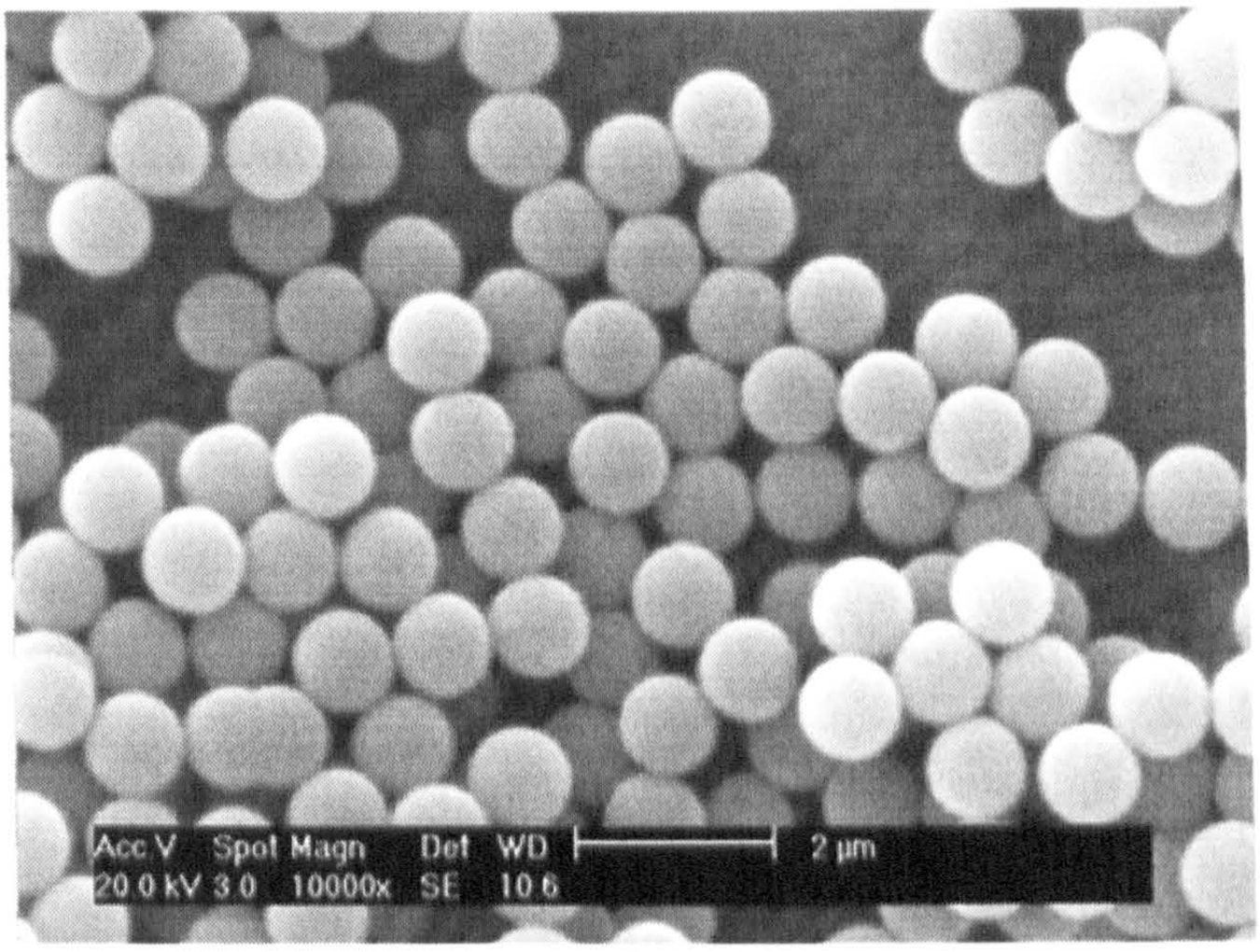

Figure 4.1 Scanning electron micrograph: Fuso silica

4.2 Atomic Force Microscopy

Atomic Force Microscopy was developed in the mid 1980s [1] to provide a level of sensitivity that would enable the measurement of interatomic forces, whilst overcoming the limitations associated with the more commonly applied technique - Scanning Tunnelling Microscopy (STM). STM is a technique that works on the principle of measuring a tunnelling current between two conducting surfaces, with the current continually being adjusted during the scan to maintain a constant applied voltage to the scanning tip. Consequently, the technique is restricted to use with only conductive or semi-conductive samples.

The AFM probe and sample may be constructed of almost any material since it is the force between the two that is being sensed. As a consequence most samples may be examined with this technique, either in gases or in liquids [2-5]. Development of the technique has provided the opportunity for researchers to study a greater variety of systems, assisting the advancement of knowledge in colloid science.

Classically, AFM is used as an imaging tool to study the topography of surfaces right down to the atomic level. In their simplest form, AFM's consist of a probe and a scanner (see figure 4.2). The probe which is located at the free end of a cantilever is brought in to contact or close proximity with the sample surface. The forces acting between the probe

and the sample cause the cantilever to bend or twist. Such cantilever movement is detected by observing the position of a laser beam that has been reflected off the back of the cantilever via a mirror onto a photo-sensitive photo-detector. The scanner allows movement of the tip relative to a stationary sample surface in the x,y and z directions due to independently operated piezo electrodes. The scanner electrodes are usually used in pairs on opposite sides of the scanner, so that the piezoelectric scanner movement can be controlled in any direction.

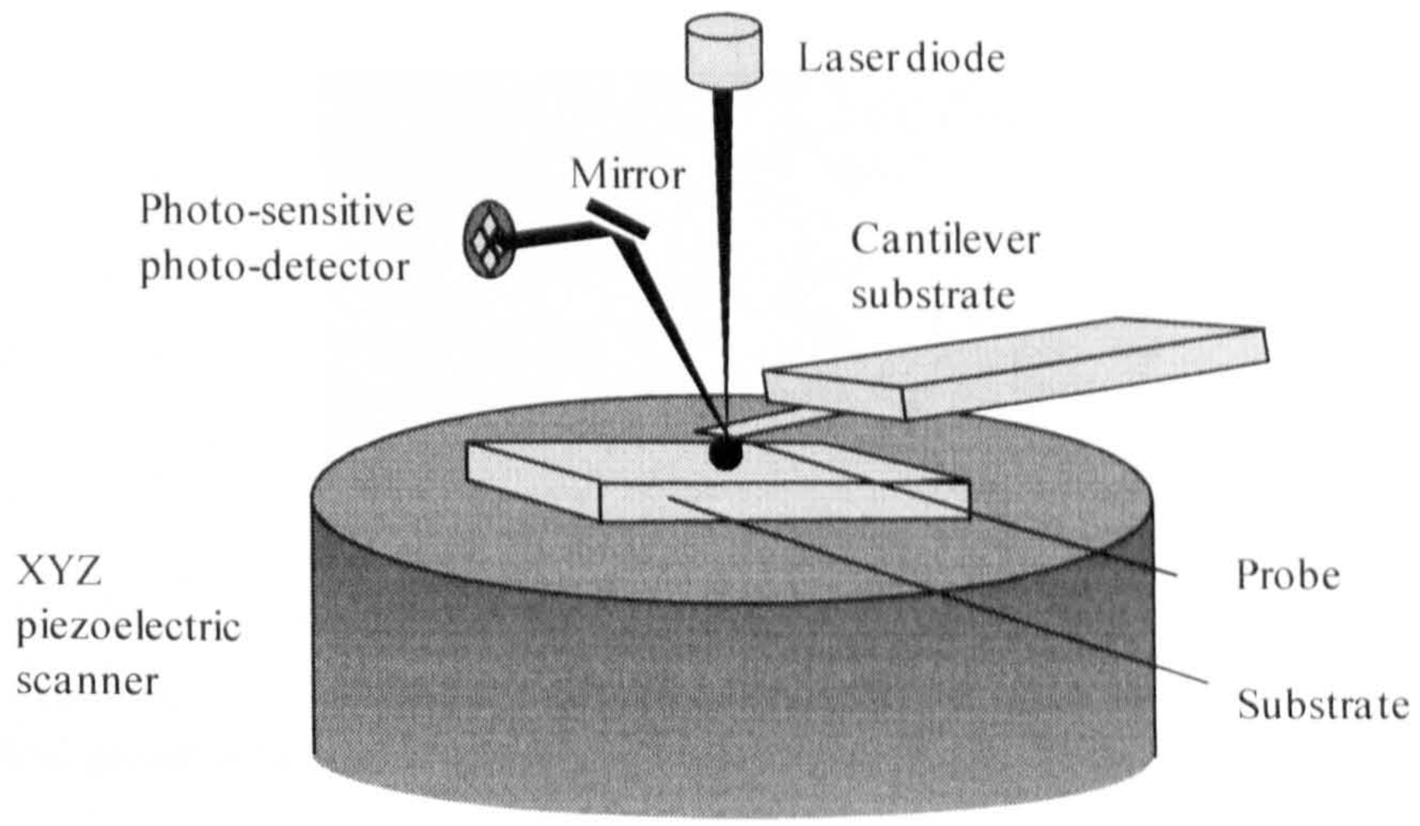

Figure 4.2 AFM operation

A Veeco Instruments (USA), Bioscope™ II AFM was used to investigate the normal and lateral forces of interaction acting between a single silica microsphere and a flat silica surface (Silicon Valley Microelectronics Inc., USA). The silica surface is prepared by the controlled oxidation of a silicon wafer at 1000°C in a pure oxygen environment, producing a surface oxide layer of approximately 100nm thick. Due to the extreme difficulty in mounting a 0.8μm sphere onto a tip-less cantilever, it was decided that a silica microsphere d_p = 29μm – Duke Scientific which is prepared using a sol gel process (Fuso silica spheres prepared using same process) and heat treated to 750°C to reduce the silica porosity, would instead provide a suitable representation of the interaction force acting between two silica surfaces. The force interaction is normalised by the particle radius so that the data is representative of the interaction force between two Fuso silica spheres. Measuring the

interaction force between two Fuso silica spheres is extremely difficult using the current approach. The forces measured provide an understanding of the level of interaction between two partially hydrophobic silica surfaces (Fuso silica considered partially hydrophobic, readers are referred to chapter 5 for more details). The data should not be relied upon to provide exact values of the interaction force between two Fuso silica spheres. The microsphere was mounted onto a wide-legged, V-shaped, tip-less silicon nitride cantilever (Veeco Instruments, USA) with a small quantity of Araldite®. The 3-dimensional traversing stage and the inverted optical microscope available on the Bioscope™ II were utilised in this work when preparing colloid probes.

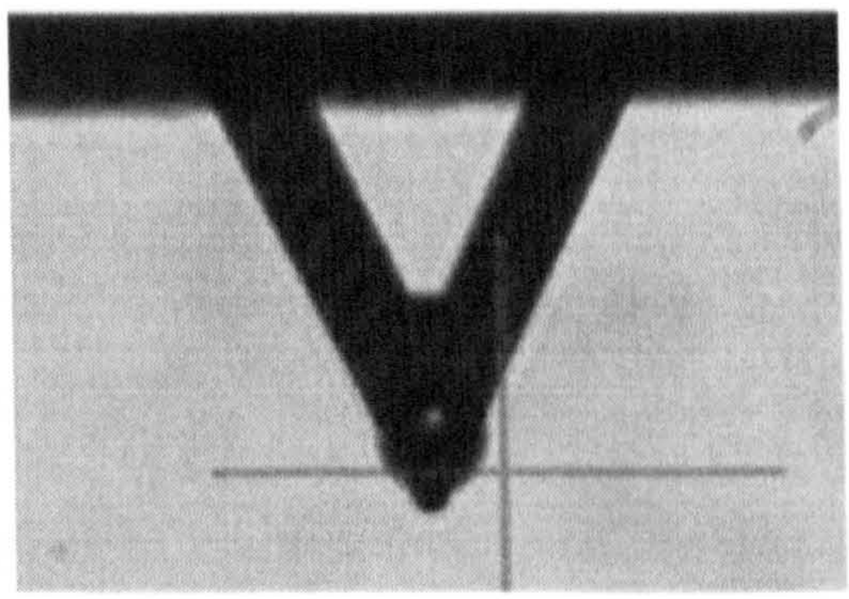

Figure 4.3 Colloid probe: 29μm silica sphere

4.2.1 Calibration

Accurate cantilever calibration is required to correctly interpret the output signal from the split-photodiode sensor into a force. The deflection and twisting behaviour of the cantilever is sensitive to the cantilever dimensions and its material properties. The normal force (F_z) is defined by Hooke's law using the cantilever deflection:

$$F_z = -k_z.z \qquad [4.0]$$

where, k_z is the normal stiffness and z the displacement of the cantilever's free end from the equilibrium position.

The friction force (F_y) is defined as the product of the lateral stiffness (k_y) and the lateral displacement (y) of the probe as it is scanned across the sample surface.

$$F_y = k_y . y \qquad [4.1]$$

Force spectroscopy was used to calculate the normal deflection sensitivity (nm/V) of the cantilever. Assuming that the sample experiences no deformation whilst in constant compliance, then the deflection of the cantilever equals the displacement of the piezo-actuator [6]. Thus, the slope of the photodiode detector voltage can be used to determine the normal deflection sensitivity, assuming that the motion of the piezo-actuator is correctly calibrated. The normal stiffness of the cantilever is calculated from an analysis of its oscillation behaviour caused by simple thermal fluctuations [7]. Such cantilever motion can be described in terms of a simple harmonic oscillator with only one degree of freedom. The normal stiffness can then be defined as:

$$k = \frac{T.k_B}{\langle q^2 \rangle} \qquad [4.2]$$

where, $T.k_B$ represents the temperature effect (T absolute temperature and k_B Boltzmann constant) and $\langle q^2 \rangle$ gives the average displacement of the cantilever over time, which is related to the oscillating mass and the resonant angular frequency of the cantilever.

The lateral sensitivity (nm/V) of the cantilever was also estimated from the raw voltage versus distance data. Initially, static friction resists the lateral motion of the probe over the sample surface, with the scanner movement in the y direction (scan angle 0 degrees) assisted by cantilever twist. The change in the photodiode detector voltage while the probe remains in a fixed position provides a sensible estimation for the lateral sensitivity. The lateral sensitivity of the cantilever was assessed as a function of normal load and solution chemistry. Within the range of conditions assessed, the cantilever sensitivity appeared not to be significantly affected (see figure 4.4b).

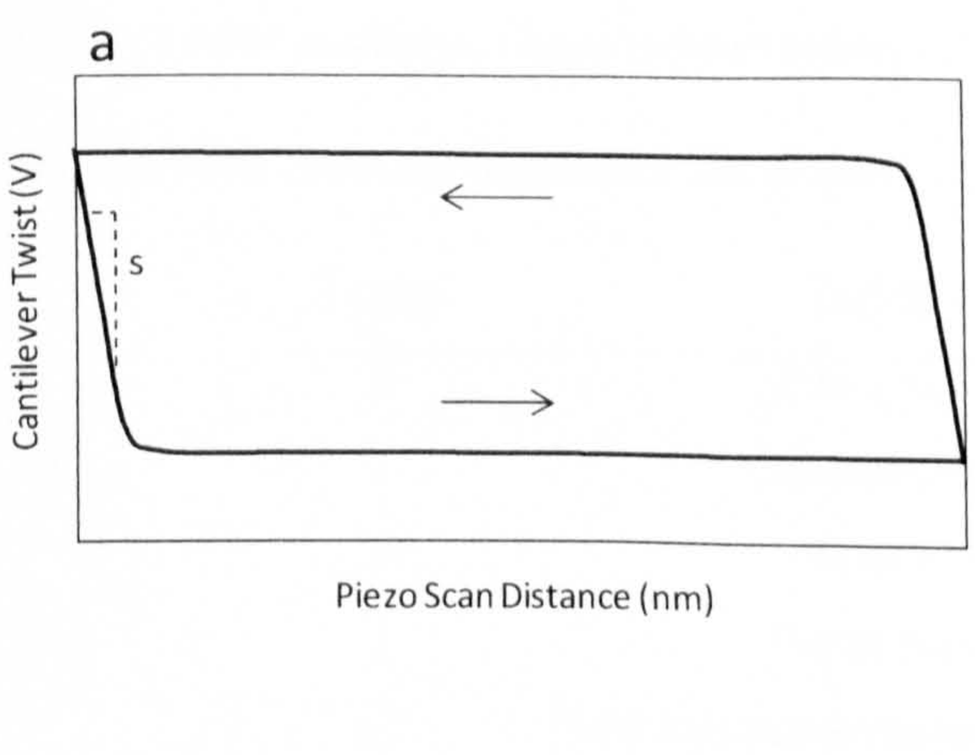

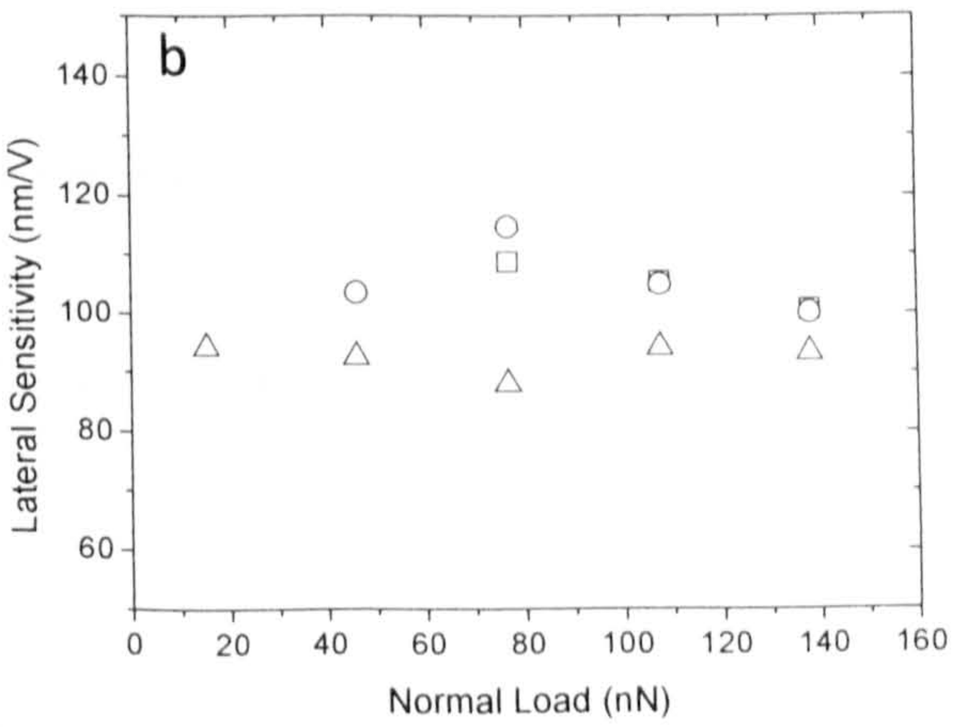

Figure 4.4 a) Lateral force measurement showing the characteristic friction loop and the slope, S, from which the lateral sensitivity of the cantilever is determined (cantilever twist under static friction conditions). b) Lateral sensitivity as a function of normal load. Symbols: triangle – 1M KNO_3, circle – 10^{-4}M KNO_3, square – 10^{-4}M KCl.

A theoretical method described by Neumeister & Ducker [8] was used to calculate the lateral stiffness (k_y) of a V-shaped cantilever (figure 4.5). To simplify the mathematical description of the deformation, Neumeister & Ducker treated the cantilever as two rectangular beams and a triangular plate, applying ordinary beam and rod theory to determine the deformation of the individual sections. The researchers validated their results against finite element analysis, demonstrating excellent agreement as a function of d.

$$k_y = \frac{E.t^3}{3(1+v)h^2}.\left(\frac{1}{tan\alpha}log\frac{w}{dsin\alpha}+\frac{Lcos\alpha}{w}-\frac{3sin2\alpha}{8}\right)^{-1} \qquad [4.3]$$

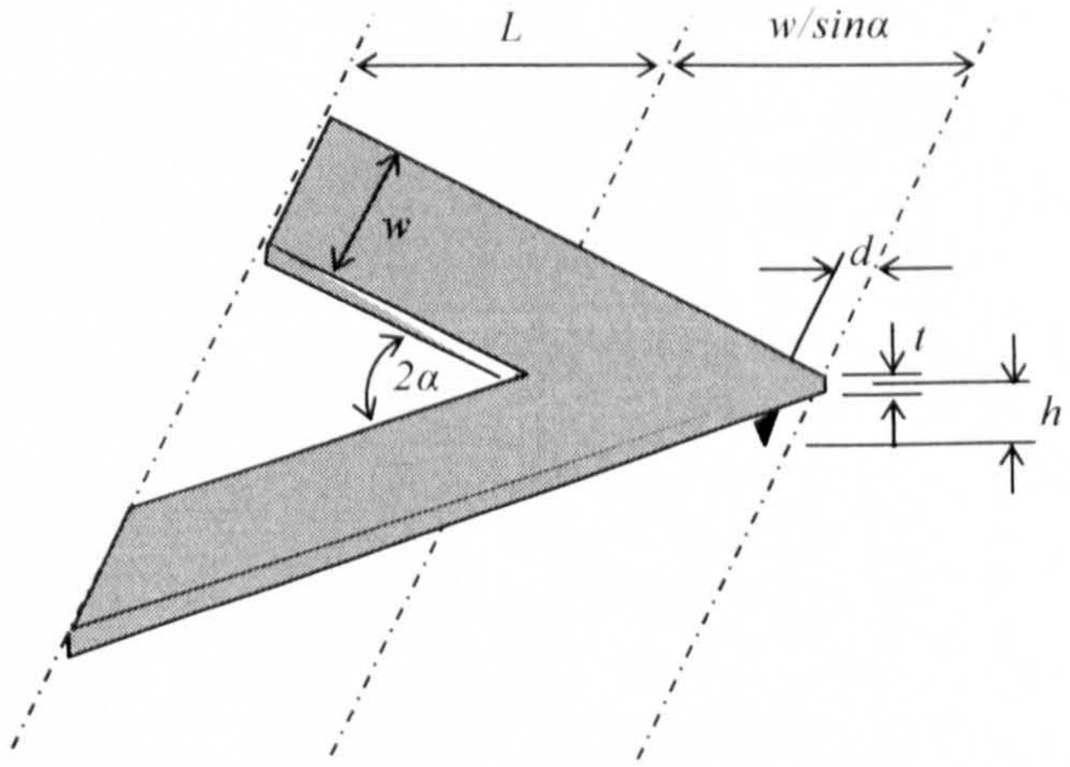

Figure 4.5 AFM cantilever. Figure redrawn reference [8]

Table 4.0 AFM cantilever dimensions and properties used in equation 4.3.

Symbol	Definition	Value	Units
E	Elastic modulus	3.04E+11	N/m^2
t	Cantilever thickness	0.6	µm
V	Poisson's ratio	0.24	
h	Particle diameter	29	µm
α''	½ the angle between the two adjoining beams	24.9	o

w	Beam width	34.8	μm
L	Distance from the clamping point to the intersection of the inner edges of the two beams	113.5	μm
d	Distance from the probe/cantilever contact point to the intersection of the outer edges of the two beams	10.3	μm

Table 4.1 provides a summary of the stiffness constants of the V-shaped cantilever used in the present study to provide quantitative normal and friction force data.

Table 4.1 Normal and lateral sensitivity and stiffness constants for the V-shaped cantilever used in the present study.

	Normal	Lateral
Sensitivity (nm/V)	31.77	101.11
Stiffness (N/m)	0.48	4.54

4.2.2 Force Measurement (Normal)

Force spectroscopy is a method widely employed to study tip-sample interaction forces and adhesion forces as the cantilever and surface approach and separate from one another. Figure 4.6 considers the simplest case, with two elastic solids displaying an adhesive interaction. The scanner is initially positioned at *a*, a distance far away from the sample surface such that no probe-sample interaction occurs and the cantilever shows no deflections from the baseline. The scanner is then extended in the z direction reducing the probe-sample gap (x and y voltages remain constant). At position *b*, attractive forces between the probe and the sample cause the cantilever to bend slightly towards the surface, before the probe jumps onto the surface due to the attractive forces exceeding the cantilever spring constant. Extending the scanner further the cantilever is deflected back through its original position (zero-line) as a result of compressive loading, position *c*. This region is characterised by a diagonal line and is referred to as the region of 'constant compliance' (contact-line). Once the scanner has extended a preset distance its motion is reversed and it retracts away from the surface unloading the cantilever. If the contact is adhesive, the cantilever will deform as the piezo-actuator retracts the surface. At a given point the elastic strain energy in the cantilever exceeds the adhesion, and the probe snaps out of contact

from the surface. The scanner continues to retract to its initial set point where the cantilever shows no deflection.

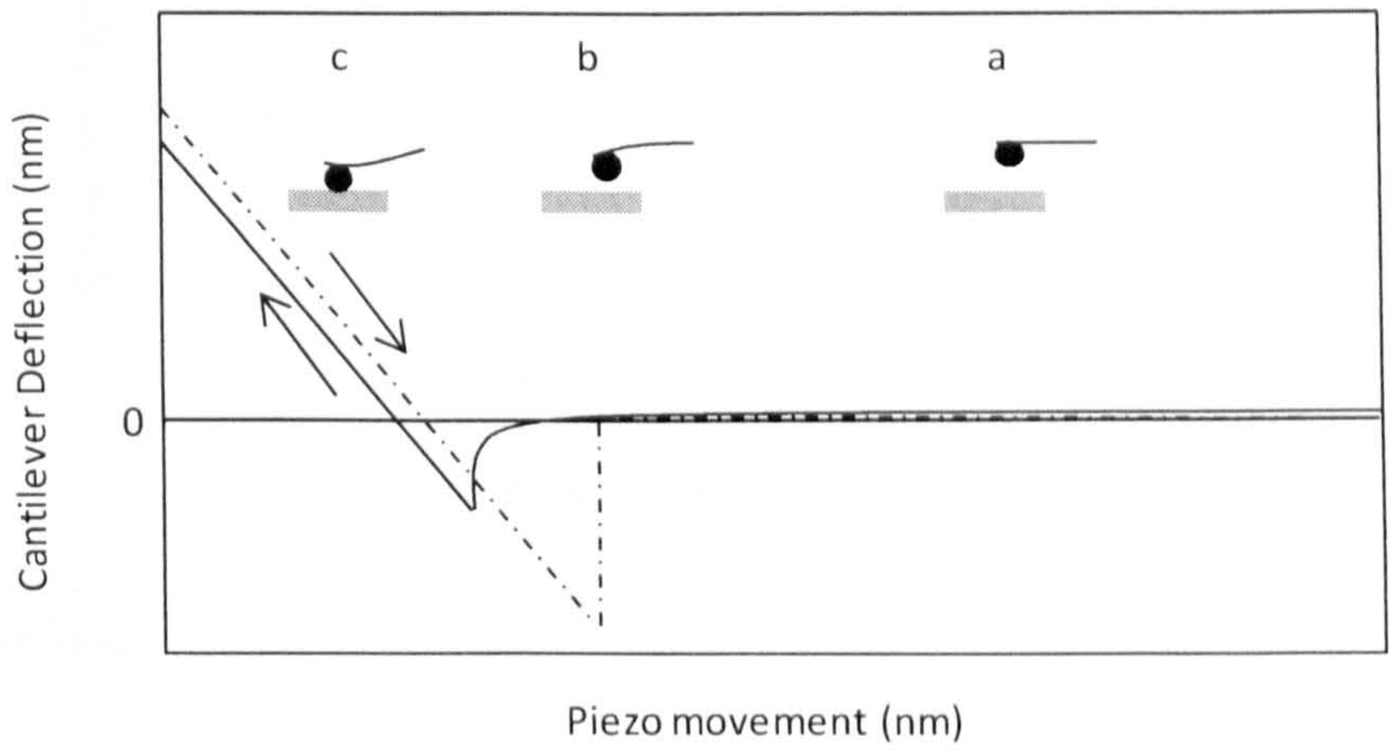

Figure 4.6 Normal force curve illustrating the probe-substrate interaction. Arrows indicate the advancing and retracting traces.

4.2.3 Force Measurement (Lateral)

Lateral force microscopy involves scanning the probe back and forth perpendicular to the long axis of the cantilever, while the probe is pressed against the surface with a constant applied load. As the scanner moves the probe over the surface, friction forces prevent the free motion of the cantilever which compensates for this by twisting. Initially, static friction between the two surfaces resists the shear force, causing the cantilever to twist in the direction to which the scanner is moving. Further movement of the scanner increases the elastic strain energy in the cantilever to the point where it eventually exceeds the static force initiating movement of the probe over the surface. Free motion of the cantilever is then prevented by a much smaller dynamic force, with the probe movement characterised by 'stick-slip' behaviour. Once the scanner has travelled the preset distance it then reverses its direction (retrace) to complete the friction loop. Figure 4.7 shows a typical friction loop with the lateral deflection in volts (a result of the repositioning of the reflected light beam off the back of the cantilever onto a photo-sensitive photo-detector), plotted against the scan distance in nanometres.

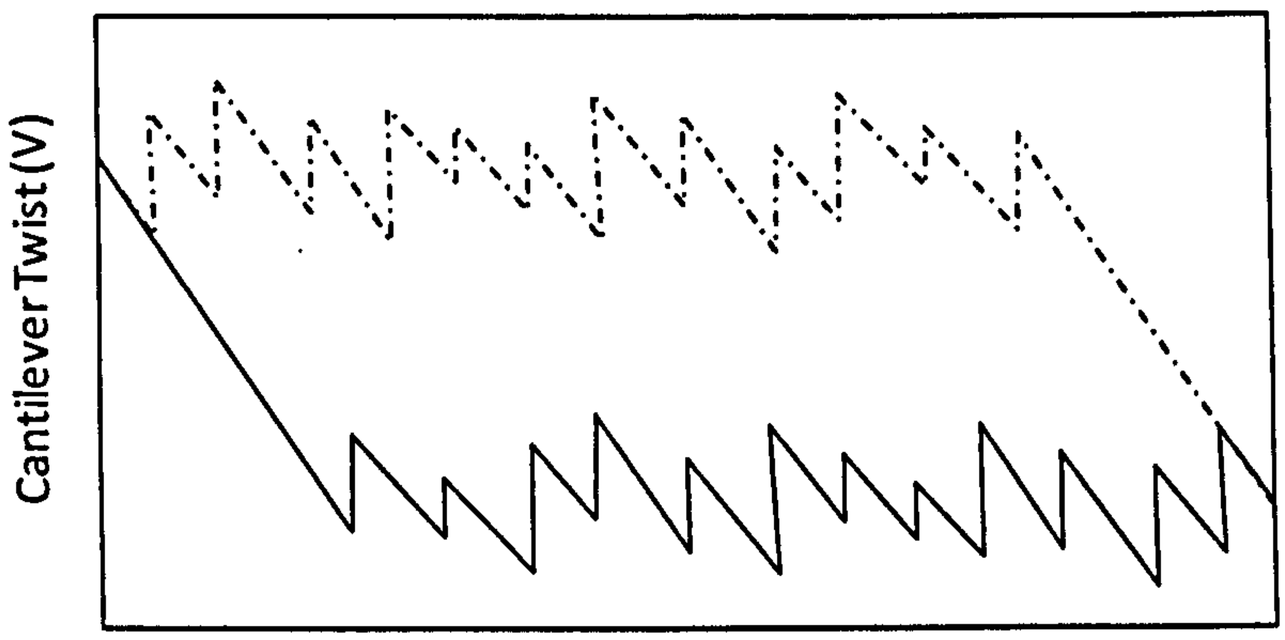

Figure 4.7 Friction loop

4.2.4 Experimental Procedure

The silica substrate underwent a rigorous cleaning procedure with, in sequence, a 2% Decon solution wash, a Milli-Q® water rinse, drying in a clean nitrogen stream and finally exposure to UV-ozone to remove any impurities from the surface, while the colloidal probe was exposed to UV-ozone. The substrate ($1cm^2$) was mounted in the centre of a plastic petri dish with a non-water soluble adhesive. The petri dish is secured to the BioScope™ II baseplate by the liquid sample holder, with the inlet and outlet ports of the holder connected to a small peristaltic pump (Materflex C/L, Cole Parmer, USA) to allow for fluid exchange. The cantilever is secured in the probe holder by a small spring loaded clip before the holder is positioned onto the z-scanner mount of the BioScope™ II head. The head is then lowered onto the mountings of the BioScope™ II EasyAlign module with the probe completely submerged in the sample fluid. The laser positioning controls are then used to locate the laser spot onto the tip of the cantilever, before using the x and y positioning controls to maximise the SUM signal (reflected energy from the cantilever), which indicates that the laser spot is "well" centred on the cantilever and will provide optimum sensitivity to any cantilever deflection. The y voltage is then offset to -2V compared to the deflection set point of 0V, which compensates for any disturbances associated with mechanical vibration or thermal oscillation experienced by the cantilever during engagement, that may result in a false feedback signal. The Bioscope™ II head is then mounted onto the baseplate encasing the liquid sample holder. The probe, fully submerged in the sample media is then subject to an equilibration period of 30 minutes before engagement with the substrate. Once the probe and substrate are in-contact (engaged) the

normal force of interaction is measured using the PicoForce® application, and the lateral force is measured using the scanning function of the diNanoscope® software v7.0.

All normal force interactions were completed within one experimental campaign, with the probe being withdrawn from the substrate during fluid transfer. Initially, force curves in pH 6 Milli-Q® water were collected and validated against existing data to ensure that the interaction forces were reasonable and not influenced by surface contaminants. A pH 6 10^{-4}M KNO_3 solution is then introduced into the fluid cell and a significant number (100-200) of force curves collected in a variety of different locations to enable statistical analysis of the data. A water wash was then completed for 30 minutes before introducing the pH6 1M KNO_3 solution. A second water wash of 2 hours was required to remove any impurities in the fluid cell associated with the 1M KNO_3 solution. Several water force curves were then obtained and validated once again against existing force curves collected in water, before introducing the final solution, pH 6 10^{-4}M KCl. A summary of the measurement parameters is provided in Table 4.2.

Table 4.2 Measurement parameters – Normal force

Ramp size	250nm
Scan rate	1Hz
Samples	512

Using the same methodology and validation procedures described above, all friction experiments were completed within one experimental campaign. A summary of the measurement parameters is provided in Table 4.3. Images of the cantilever were taken before and after each experimental campaign to ensure the colloid probe had not been removed from the cantilever surface.

Table 4.3 Measurement parameters – Lateral force

Integral gain	0.758
Proportional gain	0.733
Scan angle	0°

Scan rate	1Hz
Scan size	500nm

It should be noted that the cleaning procedure used on the colloid probe and silica substrate before measurement of the force interaction cannot be applied to the raw material used in the pipe loop studies Cleaning of the two surfaces removes any contamination, thus enabling the collection of repeatable and reliable data. It is then possible to relate the measured interaction force to the particle / aggregate structures which are observed in the suspensions.

Atomic force microscopy is a very sensitive tool to measure the nano forces present between surfaces. Contamination of either surface can result in extended pull-off profiles, multiple contact points and increased or decreased levels of adhesion. It is most probable that dirt between the two contacting surfaces will lead to significant variation in the approach and retraction curves. Dirt in the pipe loop suspensions will only affect a small percentage of the total number of interactions. For example, figure 4.8 below shows the size and shape of particles dispersed in a 10^{-4}M KNO_3 electrolyte (figure 4.8a - interaction remains purely repulsive) and a 1M KNO_3 electrolyte (figure_4.8b - strong attraction potential) suspension. In a 10^{-4}M electrolyte, the interaction force between the two surfaces is measured as being purely repulsive (see chapter 5) and one would therefore expect all particles to remain dispersed. However, the image below (figure 4.8a) shows that there are small number of doublets and triplets in the suspension which is most likely a result of dirt on the silica surface. Even though the cleaning procedure could not be applied to the raw material, small traces of dirt in the suspension does not appear to alter the vast majority of interactions, and can therefore be considered to have negligible affect in the pipe loop studies. Such behaviour is also supported by the zeta potential data in chapter 5 which shows that the silica surfaces are clean and not significantly contaminated by dirt; the iso-electric point for the silica in the absence of any specific ion absorption is measured in the region of pH 2-3 [9, 10].

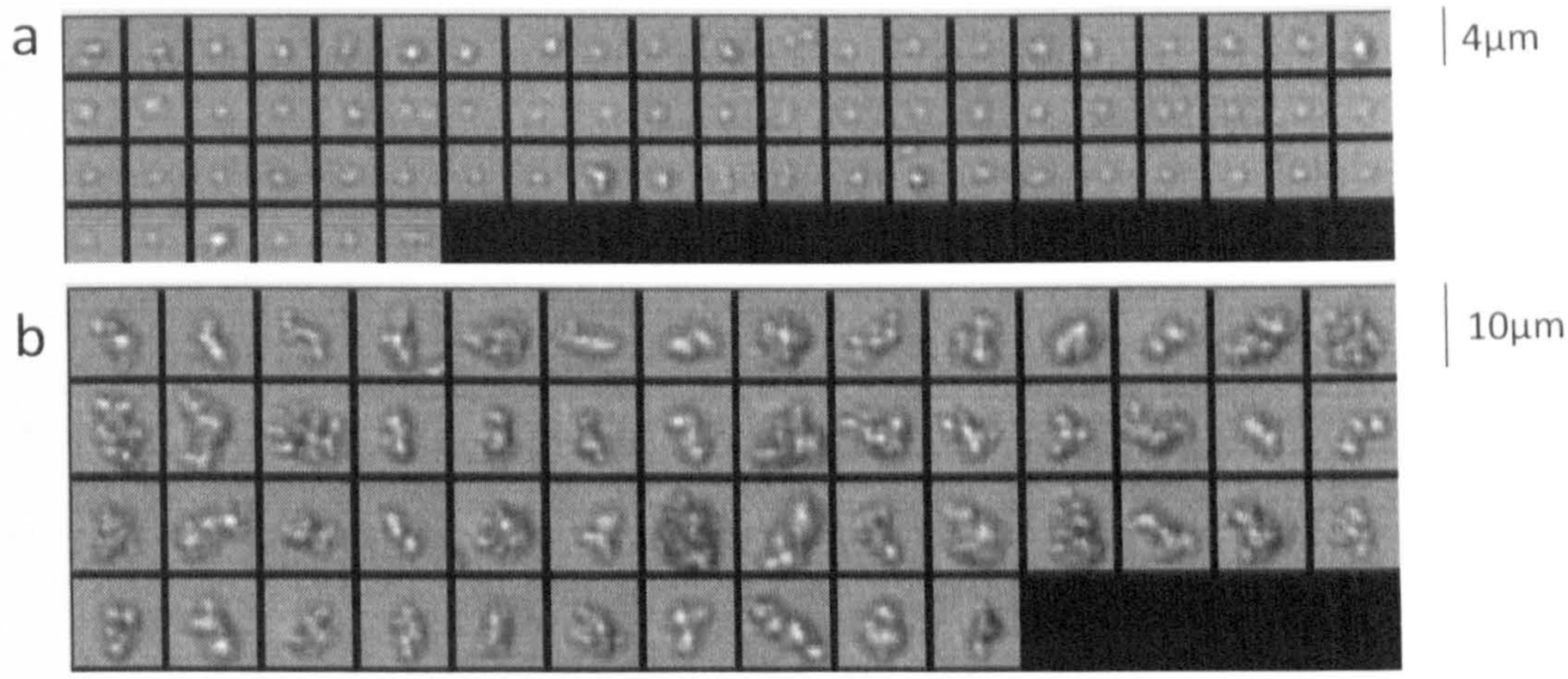

Figure 4.8 Particle images collected using a Sysmex particle sizer. a) Fuso silica dispersed in 10^{-4}M KNO_3, b) Fuso silica dispersed in 1M KNO_3

4.3 Zeta Potential

Particle surface charge was measured using a Malvern Instruments (UK) Zetasizer Nano. Briefly, the suspension within a measurement cell is excited by an electric field for a long enough period to initiate particle movement, a process called electrophoresis. The motion of the particles is then tracked using Laser Doppler Velocimetry (LDV) to determine the mobility of the particles. The mobility is then substituted into the Henry equation (equation 4.4) to calculate the zeta potential. For the systems under investigation, a value of 1.5 was used to define the Henry function *f(κa')* based on Smoluchowski's approximation.

$$u_E = \left(\frac{2\varepsilon\xi}{3\mu}\right) f(\kappa a') \qquad [4.4]$$

where u_E is the electrophoretic mobility; ε the dielectric constant; μ the fluid viscosity and ξ the zeta potential.

The Zetasizer Nano encompasses a technique called M3-PALS (Mixed Mode Measurement – Phase Analysis Light Scattering) that enables the mobility measurement to be completed at any position within the measurement cell, overcoming any issues associated with electro-osmosis. Electro-osmosis is a term given to describe liquid flow that is initiated by the movement of ions under the influence of an applied field. The true electrophoretic mobility of a particle is at a position where there is no net liquid flow. In a closed cell geometry, movement of fluid near the cell walls is replaced by returning fluid down the centre of the

cell. At a given position from the cell wall the two opposing flows produce a region of no flow, termed the stationary layer, where the electro-osmotic effect is nullified.

The M3 technology can eliminate the effect of electro-osmosis through a combination of reversing the applied electric field slowly (Slow Field Reversal – SFR) and rapidly (Fast Field Reversal –FFR). The FFR technique enables the particles to reach terminal migration velocity, while the fluid flow due to electro-osmosis is negligible. The technique produces reliable mean values, however, due to the short sampling period the resolution of the distribution is reduced. SFR which is sampled over a longer time period improves the resolution of the distribution, however, because of the longer sampling period the results are affected by electro-osmosis. The two techniques are combined to provide a mean (FFR) and distributed (SFR signal normalised to remove electro-osmotic effects) analysis of the zeta potential.

The PALS technology improves upon the sensitivity of the measurement compared to the traditional frequency shift analysis. A laser beam is split using a beam splitter with one of the beams reflected off a fixed mirror and the second off an oscillating mirror to produce a reference frequency. The beams are made to cross at the centre of the measurement cell creating alternating bands of high and low intensity illumination. As the particles pass through the high and low illumination bands the amount of light scattered fluctuates accordingly. The frequency of the scattered light is then compared to the frequency of the reference beam, and the phase shift analysed to determine the particle mobility rate.

4.3.1 Experimental Procedure

Silica suspensions were prepared to a concentration of 1000ppm to optimise the scattering intensity of the incident light beam (count rate greater than 20kcps, and zeta potential independent of concentration). All zeta potential measurements were made using the MPT-2 Autotitrator, with the pH of the suspension being adjusted from basic to acidic conditions using 0.1M and 0.01M complementary acids (HCl and HNO_3). The pH range of the measurement was a function of the electrolyte concentration, maintaining less than a 10% change in the ionic concentration of the solution.

The titration module and measurement cell were rigorously cleaned using 2% Decon and Milli-Q® water. To assess the sensitivity and purity of the measurement cell, a zeta

potential transfer standard is measured to ensure that the recorded zeta potential is -50mV ± 5mV. 15ml of the suspension is then transferred to the sample container with a magnetic stirrer in the base to prevent particle sedimentation. The measurement cell is then filled using the peristaltic pump within the titration module ensuring that no air bubbles are present in the system. Operating procedures were then selected within the Dispersion Technology Software (Malvern Instruments, UK).

4.4 Shear Yield Stress

A HB DV-II+ viscometer supplied by Brookfield Engineering Laboratories (USA) was used to study the shear yield stress of consolidated sediments. The apparatus measures the torque required to rotate an immersed element (vane) in a fluid. As the fluid resists the free motion of the vane (driven by a dc motor), a torsional moment acts on the vane introducing a phase shift between the angular position of the vane and the motor. The degree of off-set is interpreted as a value of torque.

A theory developed by Nguyen Quoc and Boger [11] was used to determine the shear yield stress of a material measured using the vane technique. To simplify the mathematical approach, the researchers assumed that the vane was to be considered as a cylinder of the same geometrical dimensions. Thus, the total torque acting on the element was a result of shearing at the cylinder wall and at the two end surfaces. For a small-diameter cylindrical element, a further assumption considered that the shear stress at the two end surfaces was uniformly distributed, and equal to the shear stress at the cylinder wall. In addition, it was considered that the shear stress at the cylinder wall is equal to the material yield stress at the maximum torsional moment. The yield stress (τ_y) is thus defined as:

$$\tau_y = \frac{T'}{\left(\frac{\pi . D_v^2}{2} . \left(\frac{H}{D_v} + \frac{1}{3}\right)\right)} \qquad [4.5]$$

where, T' is the maximum torsional moment; D_v the vane diameter and H the vane length.

4.4.1 Experimental Procedure

Suspensions (1M KNO_3, 10^{-4}M KNO_3 or 10^{-4}M KCl) were prepared to 12% by volume at pH 6 and tumbled gently for 48 hours. Initial experiments had shown that the suspension pH remained stable over a period of 10 days. Therefore, it is assumed that there is no pH

drift during the experiment. After 48 hours the slurry is transferred to a 250ml glass beaker (d: 60mm, h: 110mm), sealed with parafilm and left undisturbed for 7 days to form a fully consolidated sediment bed. Before the vane tool is attached to the viscometer, the instrument is calibrated and the sample beaker clamped in position. The vane tool is then attached to the viscometer and lowered gently to a known distance $\frac{d}{6}$ above the beaker base to eliminate end effects. Wall effects were assumed negligible due to the significant dimensional variation between the vane tool and the sample beaker. A standard operating procedure was created in the application software (Rheocalc v3.0) to record the torque as a function of constant spindle rotation (0.5rpm) over 120 seconds. Suitable vane tool geometries were chosen to ensure that the maximum torque recorded exceeded the 10% threshold (significant relative error), while not exceeding 100% torque. The torque is then converted into an energy, dyne-cm, with the maximum torque of a HB viscometer equal to 57,496 dyne-cm. Experimental repeats were completed through re-dispersing the compacted sediment, before following the same procedure as described above.

Table 4.4 Vane tool dimensions

	V72	V73
Diameter (cm)	2.167	1.267
Length (cm)	4.338	2.535

4.5 Sedimentation and Sediment Packing

4.5.1 Gravity Settling – visual assessment

The settling velocity of a suspension was determined through plotting the interface height between the suspension and the supernatant as a function of time. The interface height was recorded through visual assessment with the measurement intervals suitably chosen to account for the varying sedimentation rates observed. Data points were collected until the interface height remained unchanged over a minimum period of 20 hours. For suspension preparation see 4.5.3 Gel point.

4.5.2 Centrifuge Settling - LUMiFuge®

Due to errors associated with visual measurements, a more sensitive approach to determine the sedimentation velocities was made using a LUMiFuge® 114 stability analyser. The technique involves recording the light transmission (880 nm wavelength) through the measurement cell at set time intervals. A suitable transmission threshold is chosen (clear separation between profiles) from which information on the time interval and radial position at which the transmission threshold is sensed by each radial photo detector can then be interpreted as an interface versus time profile. The sedimentation velocity is then determined from the constant gradient proportion of the sediment height profile.

Samples were prepared to 0.5% by volume which maximised the optical sensitivity of the system. Polycarbonate measurement cells were filled with approximately 1ml of suspension, secured in the centrifuge and rotated at 300rpm (eleven times the force of gravity), recording a transmission profile every 10 seconds for 254 cycles.

4.5.3 Gel Point

The packing characteristics of a sediment bed can be suitably described by the gel point. The gel point can be thought of as the solids concentration of a networked suspension in the absence of any compressive force, or the minimum volume fraction needed to create an inter-connected network. The gel point is determined from the $\frac{d(\emptyset_0 . h_0)}{d(h_\infty)}$ gradient [12] where, $\emptyset$ is the solids volume fraction and h the suspension height. Subscripts $_0$ and $_\infty$ represent initial and final conditions respectively.

$$\emptyset_{gel} = \frac{d(\emptyset_0 . h_0)}{d(h_\infty)} \qquad [4.6]$$

12% by volume suspensions at pH 6 were prepared in the electrolytes of interest and tumbled for 48 hours. The suspensions were then poured into 150ml measuring cylinders to five different suspension heights between the range of 50mm and 250mm. Different suspension heights allow for the solids volume fraction of a bed to be determined in the absence of any consolidation pressure (gel point). For example, during sedimentation a bed will form with a varying sediment density, increasing from the minimum bed density at the surface to the maximum bed density at the base of the sedimentation column. The

densification of the sediment is a result of the static, bed load stress exceeding the compressive yield strength of the network (see chapter 5). In order to determine the suspension gel point which is a function of the particle-particle interaction and not the degree of sediment bed consolidation, the final sediment heights under different consolidation pressures are measured once the bed has fully consolidated (approximately 20 hours), with the gel point determined from equation 4.6.

4.6 Ultrasonic Doppler Velocity Profiling

Ultrasonic Doppler velocity profiling is a technique that has been widely used over the last 20 years to study the flow properties of opaque fluids [13-16]. An instantaneous velocity profile can be measured through detecting the Doppler shift frequency of echoed ultrasound as a function of time. A small piezoelectric transducer (typically 5mm in diameter) which emits and ultrasonic pulse is placed at an angle of inclination (α) to the flow direction to ensure a velocity component in the direction of the measurement line. The transmitted pulse interferes with the seeding (particles) in the fluid, scattering the energy which is then received as an echo by the transducer after a time delay. The position along the measurement line from where the echo is received is defined as:

$$d = \frac{c.t'}{2} \qquad [4.7]$$

where, d is given as the measurement distance from the transducer; c the speed of ultrasound in the liquid and t' the time delay between the transmitted and received signal.

The frequency of the echoed signal scattered from a particle that is travelling with a non-zero velocity is Doppler shifted. The received signal is then filtered to remove any frequencies that may have resulted from background noise, before comparison with the transmitted frequency to determine the velocity. At a specific measurement distance (equation 4.7), assuming that the seeding particles exhibit negligible phase slip with the fluid, the velocity at a distance i (V_i') is then defined as:

$$V_i' = \frac{c}{2.cos\alpha.f_0} f_i^D \qquad [4.8]$$

where, α is the angle of inclination of the ultrasonic probe to the flow direction; f_0 the transmitted frequency and f_i^D the Doppler frequency shift from position i. Both the distance

and velocity components are combined to produce a velocity profile along the measurement axis.

With the probe positioned at 45° to the flow, it is necessary to resolve the longitudinal and the vertical flow components. In a pipe flow it is sometimes reasonable to assume that $u\sin\alpha >> v\cos\alpha$ [17]. Therefore, only the longitudinal component is to be resolved and is given by:

$$u_x = \frac{V_i}{sina}$$

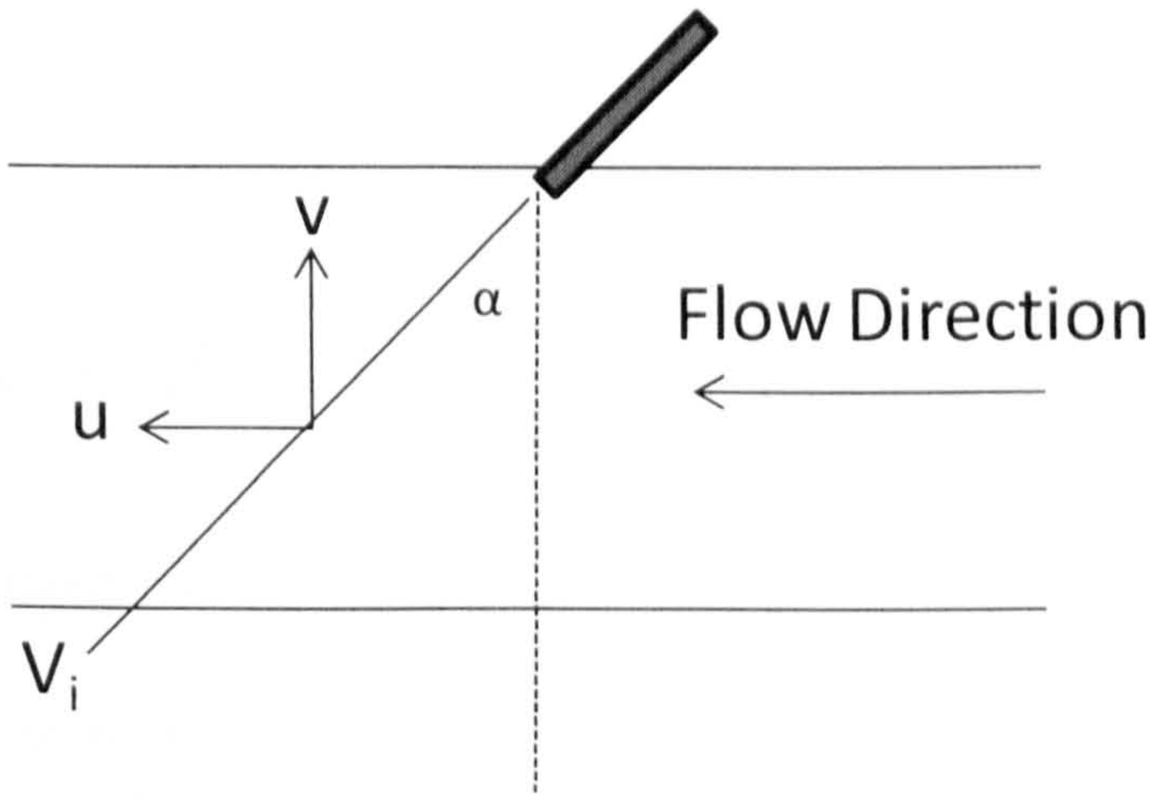

Figure 4.9 Transducer position through the pipe wall

Measurements made in a sediment free flow at Re = 3780 using particle imaging velocimetry confirmed the assumption that the vertical flow component in turbulence is negligible when compared to the longitudinal flow component. Figure 4.10 shows both the longitudinal and vertical velocity components. The vertical velocity component accounts for less than 1% of the total flow velocity.

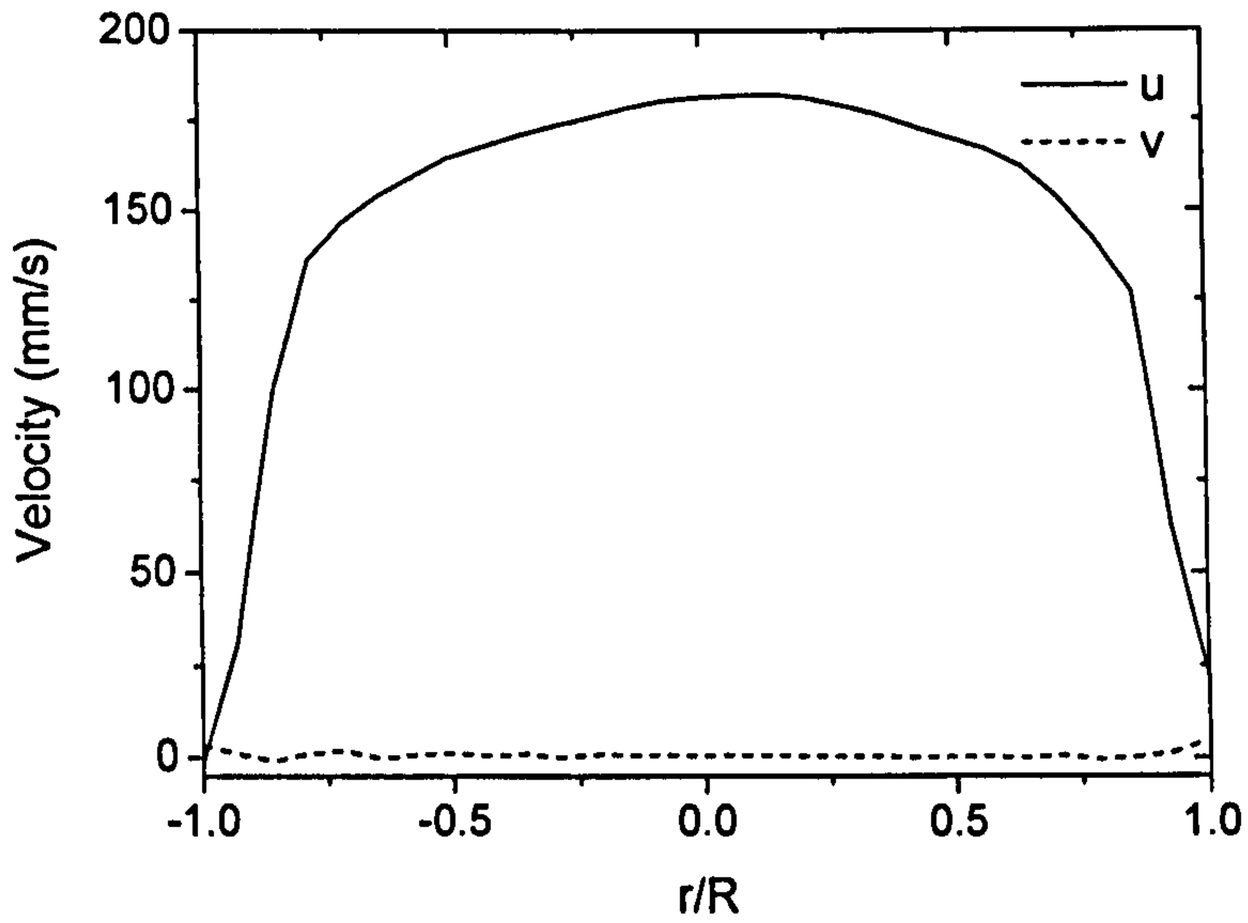

Figure 4.10 u velocity component and v velocity component for a sediment free flow (*Re* = 3780). Data collected using PIV.

4.6.1 Ultrasonic Transducer

The transducer acts as a 'source and sink' of ultrasonic energy. A thin piezo element transforms a high-frequency electrical signal into a high frequency mechanical vibration, generating longitudinal waves which propagate through the sample media. The sound field can be divided into "near field" and "far field" regions (see figure 4.11), with the transition taking place at a position where the pressure fluctuation is observed to pass through its final maxima. The "near field" region is characterised by chaotic pressure fluctuations that can interfere with both the flow trajectories of colloid particles as they pass through the measurement region [18], and the propagating sound beam itself (signal:noise). This region is described as the 'focusing region' or near field length of the signal, and has a characteristic length (N) of:

$$N = \frac{D^2 . f_0}{4c} \qquad [4.9]$$

where, D is the active element diameter.

The "far field" region is characterised by a diverging sound beam at a constant angle for a given pressure amplitude drop. In this region the signal:noise ratio can be assumed insignificant, while the trajectories of the transported particles go un-affected by the ever

decreasing acoustic pressure. This region is described as the 'measurement region', with the intensity of the ultrasonic beam decreasing with an associated increase in the beam divergence, thus reducing the spatial resolution of the measurement.

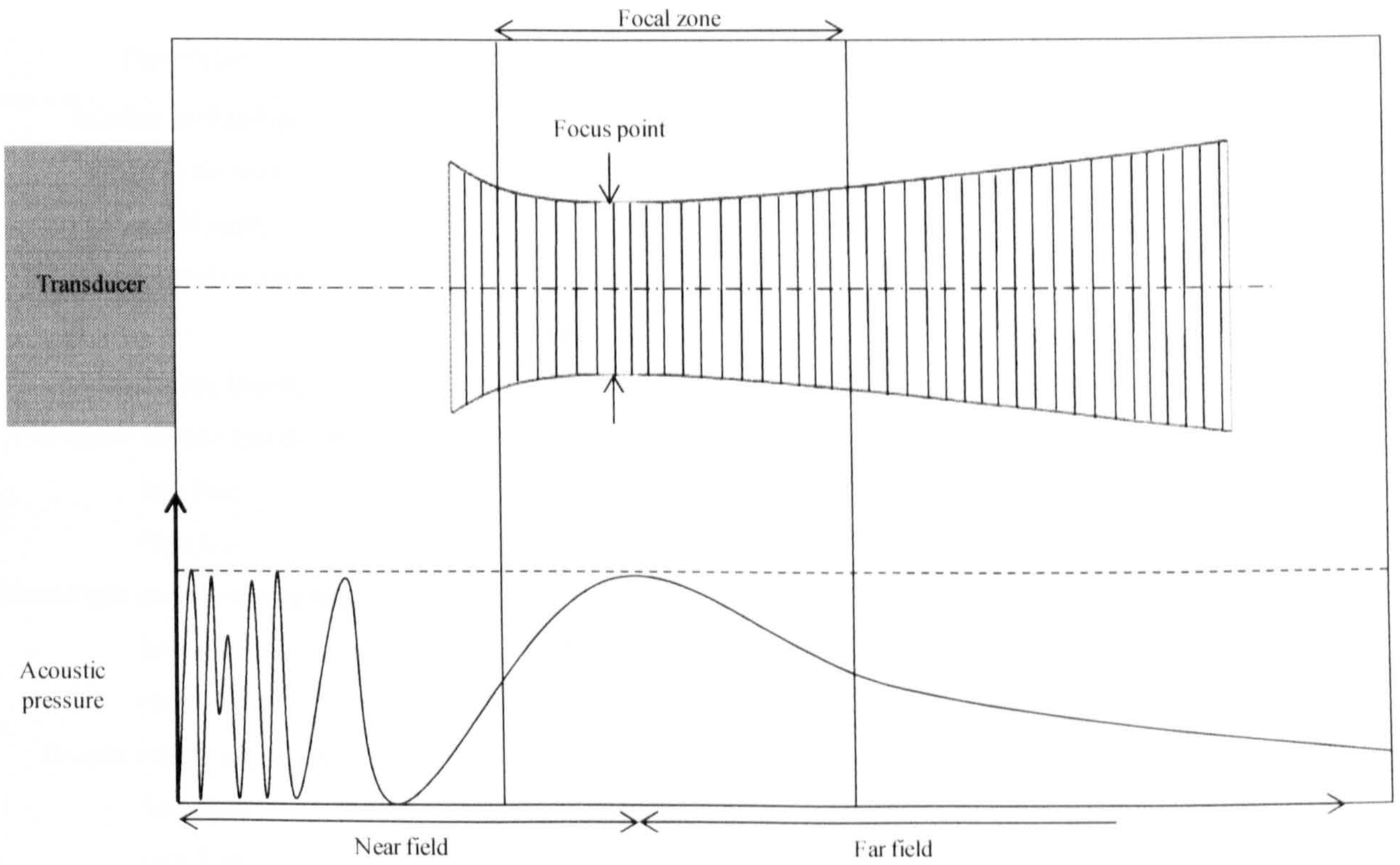

Figure 4.11 Transducer sound field. Figure redrawn from reference [19]

As the ultrasonic wave propagates along the measurement axis, the wave mode is transformed as the energy is absorbed/scattered in the medium or reflected/refracted at an interface. The resulting intensity of the reflected signal can be significantly lower than the transmitted signal. Between each pulse the transducer reverses into a sensory mode where the transducer generates an electrical signal that is proportional to the mechanical vibration of the active element which is excited by the reflected wave. The signal is then translated into an axial position and a fluid velocity.

Table 4.5 provides a summary of the UDVP set-up parameters used to measure the flow properties of the suspensions at low and high concentrations (6% and 12% by volume) within the velocity range being assessed (0.03 to 0.4 ms^{-1}).

Table 4.5 UDVP measurement parameters

Parameter	Low Concentration	High Concentration
Number of channels	94	94
Channel distance	0.37 (mm)	0.37 (mm)
Channel width	0.37 (mm)	0.93 (mm)
Measurement window	Start – 4.81 (mm)	Start – 4.81 (mm)
	End – 39.22 (mm)	End – 39.22 (mm)
Sound speed (water)	1480 (m/s)	1480 (m/s)
Maximum measurable depth:		
Low flow	270 (mm)	270 (mm)
High flow	110 (mm)	110 (mm)
Measurable on-axis velocity range:		
Low flow	-250 < x >250 (mm/s)	-250< x > 250 (mm/s)
High flow	-620 < x > 620 (mm/s)	-620 < x > 620 (mm/s)
On-axis velocity resolution:		
Low flow	2 (mm/s)	2 (mm/s)
High flow	5 (mm/s)	5 (mm/s)
Pulse rate:		
Low flow	2.7 (kHz)	2.7 (kHz)
High flow	6.7 (kHz)	6.7 (kHz)
Probe angle	45 (°)	45 (°)
Signal frequency	4 (MHz)	4 (MHz)
Cycles per pulse:	2	5
Repetitions	256	256
Noise level	4	4
Ultrasonic voltage	30 (V)	30 (V)
RF Gain	Start – 3	Start – 3
	End – 6	End – 6

For low concentration studies the measurement volume depth (channel width) is equal to the channel distance (distance between centres of two adjacent measurement volumes), resulting in a series of velocity bins with no overlap. However, at a higher solid concentration the received echo versus spatial resolution ratio for the measurement is

significantly reduced. To optimise the ratio, the number of cycles per pulse is increased from 2 to 5, extending the measurement volume depth to 0.93mm. This increase results in a substantial overlap of neighbouring velocity bins, with the echoed signal a result of information collected over effectively 2.5 velocity bins. Spatial averaging is made for each velocity bin, taking into account the velocities of neighbouring bins, therefore, resulting in an optimisation of the echo versus spatial resolution ratio and a smoothing of the velocity profile.

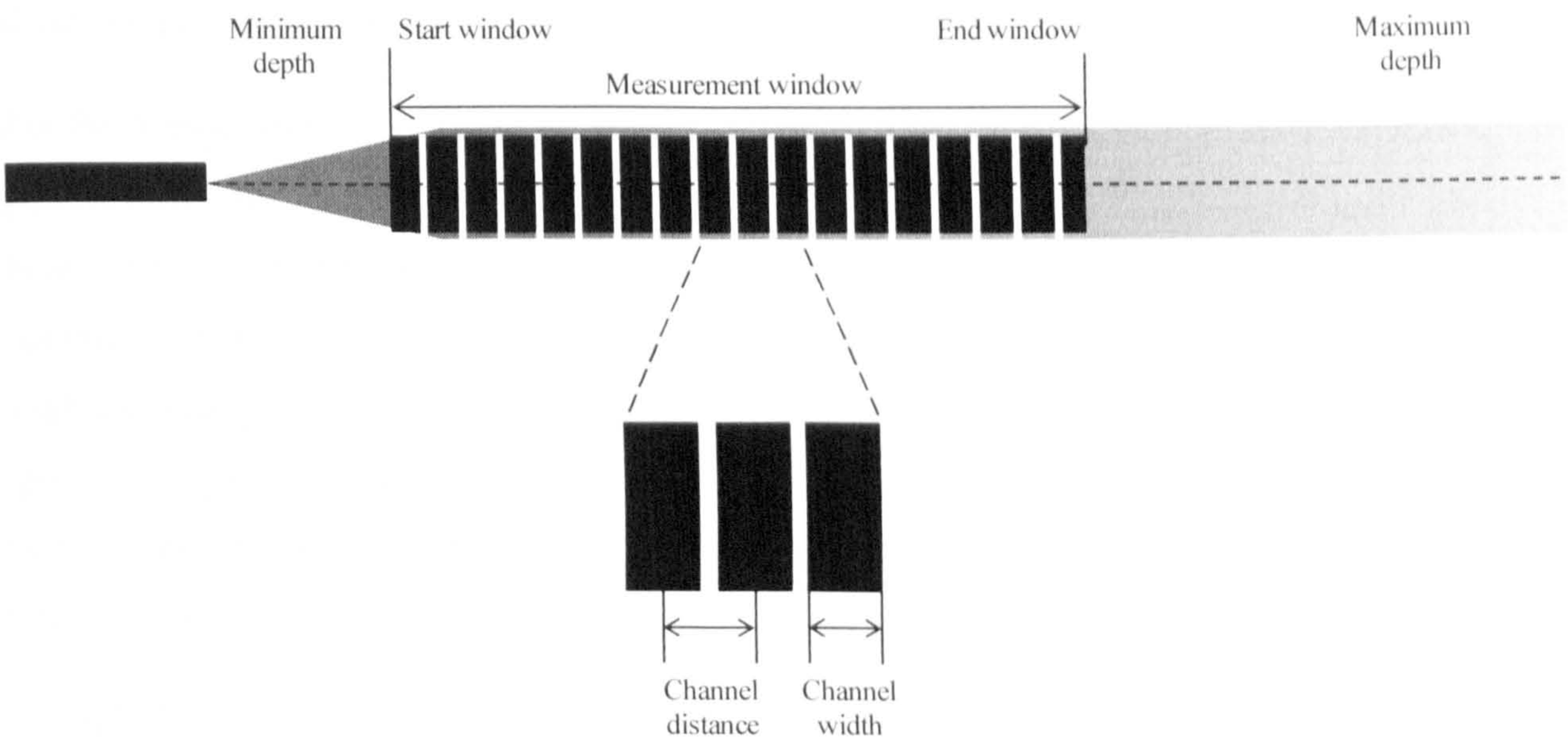

Figure 4.12 Illustration of signal breakdown.

4.7 Particle Imaging Velocimetry

Particle imaging velocimetry (PIV) is a non-intrusive technique for obtaining instantaneous whole field velocities. For the re-suspension study however, the PIV set-up was exploited only to measure the sediment height as a function of time. A brief description of a typical particle tracking application which was used to measure the velocity profiles in sediment-free flows is provided, describing how the three main components, illumination source, image capturing hardware and processing software of a PIV system are integrated to calculate displacement and velocity maps. A subsequent description defines how the technique is modified for the re-suspension application.

The flow field is illuminated by a thin sheet of laser light which is dual pulsed at a set frequency. Seeding particles which track the flow are illuminated, and their position within the flow field recorded using a digital camera which is aligned at right angles to the light sheet. Each dual pulse creates an image file containing two images, one from the first pulse and one from the second. The images are divided into rectangular regions called interrogation regions, where the processing software applies either a cross-correlation or auto correlation technique over each interrogation region to produce an average particle displacement vector. A vector map of the average particle displacement can be produced from analysis of all interrogation regions, and a raw velocity vector map can be formed by dividing the average particle displacement by the time interval between the dual pulses.

For the re-suspension study the PIV system is used to illuminate the sediment bed along the pipe invert. The intensity of the laser light sheet provides a useful light – dark contrast between the fluid and the sediment bed. With no interrogation method applied, the laser is operated in single pulse mode, collecting only one image per image file. OriginLab® data analysis and graphing software version 7.5 is used to analyse selected images. The 'profile/image' tool enables the user to calibrate the x, y scale of the image, from which the bed height can be measured. For typical re-suspension images collected, readers are referred to chapter 2, figure 3.8.

A 15Hz NewWave Solo PIV II-15, 30mJ, 532nm, Nd YAG laser (NewWave Research, USA), coupled with a MotionPro X5 digital camera (IDT, USA) was used in the study. The MotionPro X5 provided 1280 by 1040 resolution, with a 7 by 7 micron pixel size.

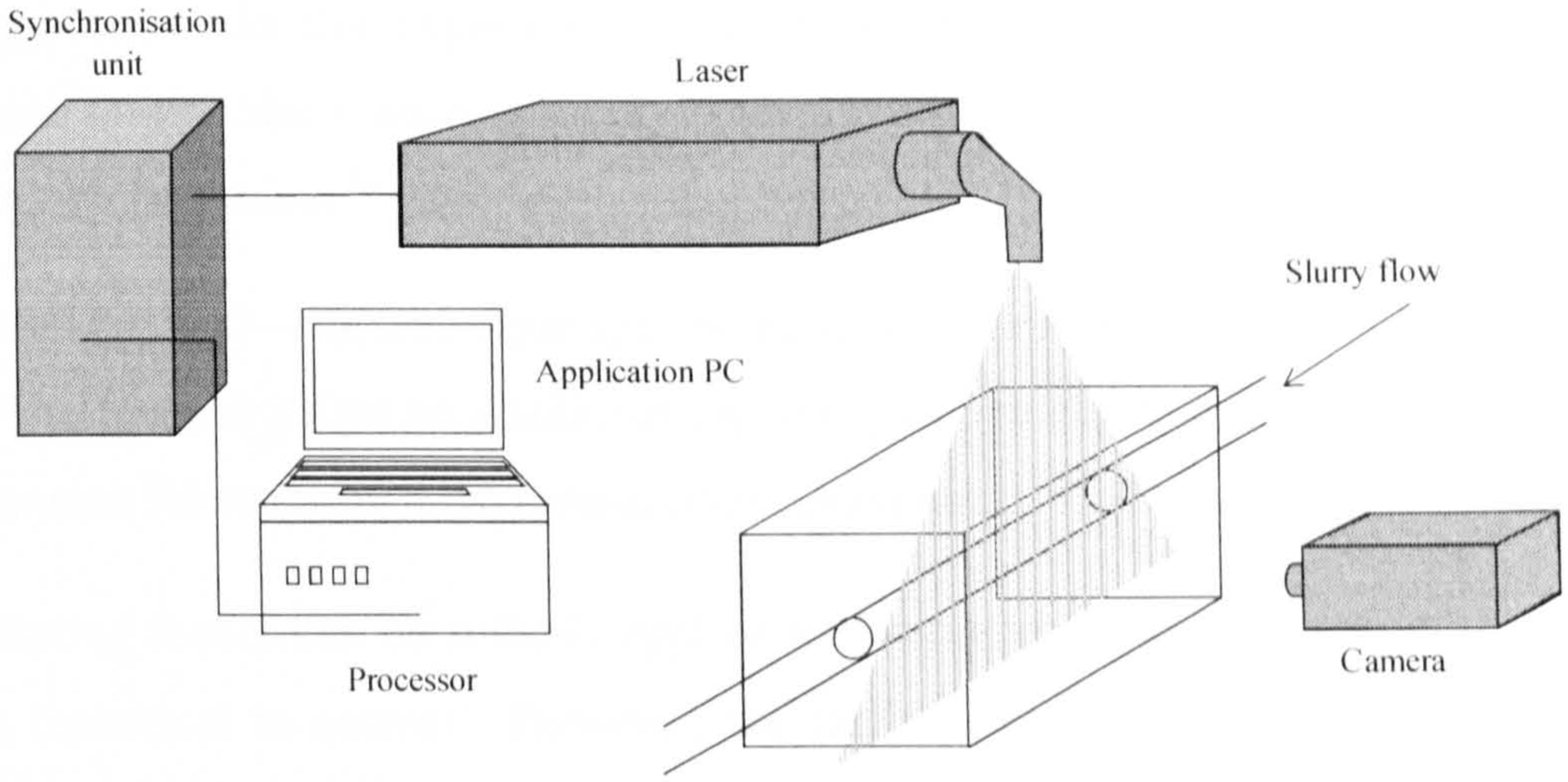

Figure 4.13 PIV set-up for the current experimental study. At the test section the slurry pipeline is passed through a water box. The water box reduces problems associated with light distortion due to pipe wall curvature.

4.8 Particle Size

Three different particle sizing techniques (two particle size distribution and one imaging) were used to measure the particle size of the primary particle and the aggregate. The instruments were not used extensively throughout the study, and therefore, only a brief description of their measurement technique will be provided.

CPS Disc Centrifuge - the technique works on the principle of calculating the particle size from the sedimentation rate. The particle suspension is injected into the centre of the centrifuge disc before diffusing outwards to the edge of the disc under centrifugal force. A sensor at the edge of the centrifuge disc detects the amount of light transmitted through the fluid. As particle pass in front of the sensor the light transmission reduces. From knowing the distance, time and fluid properties it is then possible to determine the particle size from Stokes' equation.

Malvern Mastersizer 2000 – the technique uses laser diffraction to measure the particle size. The particles in suspension are passed through a laser beam which is scattered, and the resultant scattering pattern is interpreted using Mie theory to produce a particle size distribution. The particle size distribution is determined by matching the observed

scattering pattern with that expected from spherical particles of different sizes. For further information on the Mie scattering theory readers are referred to the following texts which provide a concise review [20, 21].

Sysmex FPIA -2100 – the technique applies the same light scattering principle as described above. The Sysmex offers an additional capability of being able to image the particles as the suspension flows through the measurement chamber.

Mie scattering theory can be suitably applied to determine the particle size of the primary particles (spherical in nature). However, the larger fractal aggregates cannot always be considered spherical, with some of the aggregates forming chain like structures (large aspect ratio). Applying Mie scattering theory will introduce some error in the measurement of particle size distribution. However, when referring back to the images in figure 4.8 the majority of the aggregates formed appear spherical, thus the error in estimating the aggregate size using Mie theory is not believed to be significant. The particle size is not crucial to the outcome of the study. What is important is that fact that an increase in the electrolyte concentration from 10^{-4}M to 1M results in the formation of aggregates.

4.9 Rheology

A Bohlin CVO-R rheometer is used to measure the suspension properties as a function of shear rate. A 2ml cup and bob (measurement geometry) is used to determine the flow properties (viscosity versus shear rate) over the range, $10^{-3}s^{-1}$ to $500s^{-1}$, a range which greatly exceeds the pseudo-shear rate values in the pipe loop. The CVO-R applies a simple technique recording the torque applied to the sample and the resultant angular displacement induced in that sample. The viscosity is then simply determined by dividing the shear stress by the shear rate.

4.10 Electrical Resistance Tomography

Electrical resistance tomography is used on a 50mm NB pipe loop in South Africa. A short project conducted on the pipe loop enabled ERT images to be collected during the gradual re-suspension of kaolin sediments. As the technique is not considered as one of the main instruments used during the project, readers are referred to the following publications which outline the working principle of ERT [22, 23].

4.11 Conclusion

This chapter has introduced the many techniques which are used throughout this study to characterise the silica suspensions and sediments. As introduced in chapter 1, a more systematic approach is required when investigating the flow properties of particles in pipelines. The techniques identified in this chapter enable the single particle-particle interaction to be characterised and the many particle contact systems such as suspensions and sediments to be characterised. Gathering information using these techniques provides a basis for interpretation of the data collected in the pipe loop. It should be noted once again, that some of the techniques used in this study such as AFM are only used to provide data which is useful for interpreting other data sets. The exact values are not considered to be as important as the qualitative analysis.

Chapter References

1. Binnig, G., C.F. Quate, and C. Gerber, *Atomic Force Microscope.* Physical Review Letters, 1986. **56**(9): p. 930-933.
2. Ducker, W.A., T.J. Senden, and R.M. Pashley, *Measurement of Forces in Liquids Using a Force Microscope.* Langmuir, 1992. **8**(7): p. 1831-1836.
3. Biggs, S., et al., *Direct measurements of the adhesion between a glass particle and a glass surface in a humid atmosphere.* Journal of Adhesion Science and Technology, 2002. **16**(7): p. 869-885.
4. Biggs, S. and T.W. Healy, *Electrosteric Stabilization of Colloidal Zirconia with Low- Molecular-Weight Polyacrylic-Acid - an Atomic-Force Microscopy Study.* Journal of the Chemical Society-Faraday Transactions, 1994. **90**(22): p. 3415-3421.
5. Biggs, S. and P. Mulvaney, *Measurement of the Forces between Gold Surfaces in Water by Atomic-Force Microscopy.* Journal of Chemical Physics, 1994. **100**(11): p. 8501-8505.
6. Cappella, B. and G. Dietler, *Force-distance curves by atomic force microscopy.* Surface Science Reports, 1999. **34**(1-3): p. 1-104.
7. Hutter, J.L. and J. Bechhoefer, *Calibration of Atomic-Force Microscope Tips (Vol 64, Pg 1868, 1993).* Review of Scientific Instruments, 1993. **64**(11): p. 3342-3342.
8. Neumeister, J.M. and W.A. Ducker, *Lateral, normal, and longitudinal spring constants of atomic force microscopy cantilevers.* Review of Scientific Instruments, 1994. **65**(8): p. 2527-2531.
9. Kosmulski, M., *pH-dependent surface charging and points of zero charge. II. Update.* Journal of Colloid and Interface Science, 2004. **275**(1): p. 214-224.
10. Kosmulski, M., *pH-dependent surface charging and points of zero charge: III. Update.* Journal of Colloid and Interface Science, 2006. **298**(2): p. 730-741.
11. Nguyen Quoc, D. and D.V. Boger, *Yield stress measurement for concentrated suspensions.* Journal of Rheology (New York, NY, United States), 1983. **27**(4): p. 321-49.
12. Nasser, M.S. and A.E. James, *Settling and sediment bed behaviour of kaolinite in aqueous media.* Separation and Purification Technology, 2006. **51**(1): p. 10-17.

13. Ouriev, B. and E. Windhab, *Transient flow of highly concentrated suspensions investigated using the ultrasound velocity profiler-pressure difference method.* Measurement Science and Technology, 2003. **14**(11): p. 1963-1972.

14. Takeda, Y., *Velocity profile measurement by ultrasound Doppler shift method.* International Journal of Heat and Fluid Flow, 1986. 7(4): p. 313-18.

15. Ouriev, B. and E. Windhab, *Rheological study of concentrated suspensions in pressure-driven shear flow using a novel in-line ultrasound Doppler method.* Experiments in Fluids, 2002. **32**: p. 204-211.

16. Yamanaka, G., H. Kikura, and M. Aritomi, *Flow measurment on oscillating pipe flow near the entrance using the UVP method.* Experiments in Fluids, 2003. **34**: p. 307-315.

17. Bares, V., *UVP analysis of velocity field in circular pipe.* Fourth bi-annual Conference Wastewater 2001, 2001. **Mlada Boleslav, Czech Republic**: p. 365-368.

18. Lilliehorn, T., et al., *Trapping of microparticles in the near field of an ultrasonic transducer.* Ultrasonics, 2005. **43**(5): p. 293-303.

19. *UVP Monitor User's Guide.* Met Flow.

20. Hunter, R.J., *Introduction to Modern Colloid Science.* Oxford University Press, 1993.

21. Elimelech, M., et al., *Particle Deposition & Aggregation - Measurement, Modelling and Simulation.* Colloid and Surface Science Engineering Series, 1995.

22. Razzak, S.A., S. Barghi, and J.X. Zhu, *Electrical resistance tomography for flow characterisation of a gas-liquid-solid three-phase circulating fluidised bed.* Chemical Engineering Science, 2007. **62**: p. 7253-7263.

23. Stevenson, R., et al., *Examination of swirling flow using electrical resistance tomography.* Powder Technology, 2006. **162**(2): p. 157-165.

Chapter 5

CHARACTERISATION OF SILICA COLLOIDS AND SUSPENSONS

NOMENCLATURE

A_a Projected area of aggregate
C_D Drag coefficient
g Gravitational acceleration
h Suspension height
h_0 Initial suspension height
h_∞ Final sediment height
$K(\emptyset_0)$ Hindered mobility coefficient
P_y Compressive yield strength
P_s Vertical component of the static stress
r Radius of aggregate
U_t Terminal velocity
V_A Potential energy of attraction per unit area
V_R Potential energy of repulsion per unit area
V_a Volume of aggregate
v Volume fraction of a particle
γ Friction coefficient of a particle at infinite dilution
z_c Position of the moving boundary between the compression zone and the free settling zone

ε Porosity of aggregate
ρ_s Density of solid
ρ_l Density of fluid
$\Delta\rho$ Solid liquid density difference
$\emptyset_0$ Solids volume fraction in the settling column
Φ Mean coordination number
τ_y Yield stress
dh/dt Rate of descent of the suspension supernatant interface

ABREVIATIONS

DLVO Derjaguin, Landau, Verwey and Overbeek Theory
RH Relative humidity
AFM Atomic force microscopy
i.e.p. Iso-electric point
Re Reynolds number
c.c.c. Critical coagulation concentration

Synopsis

The surface chemistry of silica, along with the ion-ion, ion-solvent and ion-surface interactions plays an important role in determining the strength of a particle-particle contact. The rheological properties of a colloidal silica suspension or sediment are significantly influenced by the strength of this interaction. Particular attention in the current study is given to understanding the influence of both the electrolyte type and concentration on the strength of this interaction.

With many researchers observing two different kinds of silica-silica interaction; one that represents a DLVO type interaction and one that doesn't represent a DLVO interaction, this chapter opens with a brief introduction discussing the surface chemistry of silica. The reader should be aware that the information provided in the introduction is not all relevant to the silica used in the current study. However, it is important when working with silica that the researcher is aware of the different silica surface properties.

In this chapter KBr is introduced as a background electrolyte for the zeta potential and sediment shear yield stress measurements. KBr is not used in the pipe loop study but is only considered in the current chapter to aid interpretation of the observed trends in data.

5.1 Silica Surface Chemistry

Silica is by far the most abundant component of the earth's crust and has consequently been studied in great detail over many years. Silica appears in many forms; crystalline,

amorphous, soluble or chemically combined [1], all sharing the tetrahedral building block of four oxygen atoms surrounding a single silicon atom ($[SiO_4]^{-4}$).

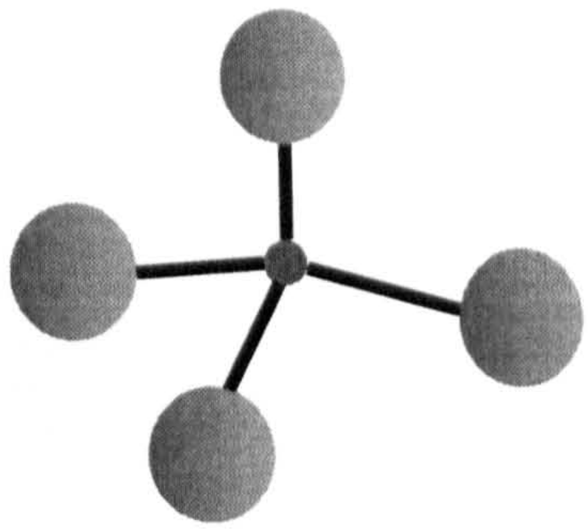

Figure 5.0 Schematic of the tetrahedral coordination of oxygen ions with silicon.

The surface of silica can be hydrophilic when silanol groups (Si-OH) are exposed or hydrophobic when the surface chemical groups are mainly siloxanes (Si-O-Si), see figure 5.1. The nature of the surface is reversible with a hydrophilic surface capable of undergoing dehydroxylation to form a hydrophobic surface, and a hydrophobic surface rehydrating to form a hydrophilic surface. The hydrophilic/hydrophobic nature of a silica surface is governed by the silanol group density (silanol number), which for a fully hydroxylated surface is within 4-8 OH groups per square nanometre[1, 2]; the variance a result of the manufacturing process and available surface area. Heat treatment of a fully hydroxylated surface leads to structure dehydration at relatively low temperatures, followed by the onset of dehydroxylation at higher temperatures (>200°C)[3]. With elevating temperatures the hydrophobicity of the silica surface increases as the silanol number diminishes to zero when pre-treatment temperatures are increased above 900°C. At these extremely high temperatures the siloxane bridges formed through condensing silanol groups are termed 'stable' compared to the 'strained' bridges that are formed under mild pre-treatment temperatures, with the strength of the bridge having a significant effect upon the time of rehydroxylation[3].

Rehydroxylation of the silica surface occurs when a dehydroxylated surface is exposed to water. Depending upon the degree of dehydroxylation and the conditions of rehydroxylation, the silica surface may never recover to its maximum hydroxylated state.

Studies have shown that for a silica surface exposed to very high pre-treatment temperatures (900-1000°C - silanol number < 1.0), a period of up to 5 years of surface contact with water at room temperature is required to rehydroxylate the surface to its initial state[3].

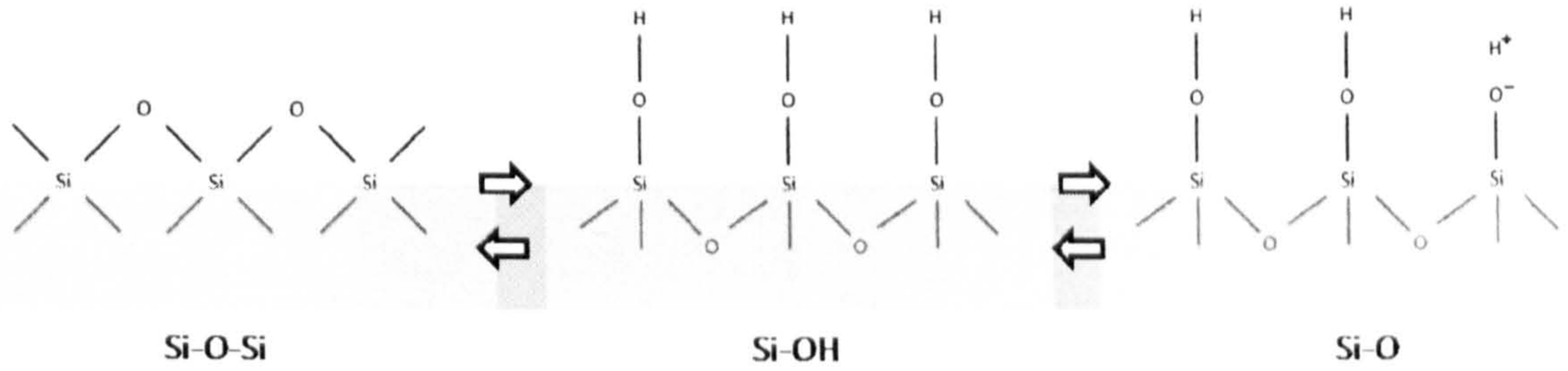

Figure 5.1 The three main silica surface chemical groups. Siloxane groups (Si-O-Si), Silanol groups (Si-OH) and Silicic acid groups ($Si\text{-}O^-$). Figure redrawn reference[4]

The behavioural characteristics of most mineral oxide colloidal dispersions except silica, can be readily described by the DLVO theory [5, 6]. In contrast, silica colloids are known to exhibit anomalous stability behaviour showing, for example; significant stability at the i.e.p. and in high salt concentrations at near-neutral pH, resisting both coagulation and sedimentation [7-10]. The unique behaviour of silica is believed to be associated with the surface chemical properties, which are dependent upon the preparation of the surface, and the nature of the solution. Many researchers have related this behaviour either to the formation of a gel layer on the surface, structuring of water at the solid-liquid interface, or a low Hamaker constant compared with other mineral oxides (see below).

5.1.1 Gel Layer

As water adsorbs on a hydrophilic silica surface (see figure 5.2), silanol and silicic acid groups (deprotonated silanol groups) form polymeric chains that protrude outwards from the silica surface. A three-dimensional network of cross-linking chains can encapsulate water from the bulk forming a surface gel layer, with the swelling of the gel layer controlled by the kinetics of the dissolution process, and the breaking probability of the chains. Vigil et al. [4] exposed hydrophilic surfaces to air of increasing relative humidity (RH) to demonstrate gel layer swelling. Force measurements on hydrophilic surfaces showed a gel layer increasing in size from 0Å at 0%RH to 15-20Å at 100%RH, while measurements on a hydrophobic surface showed no evidence of a gel layer even when the

surface was submerged in water. Typical force curves collected by Vigil et al. in 10^{-3}M salt between two hydrophilic and two hydrophobic surfaces are shown in figure 5.2, with the hydrophilic measurement showing an additional repulsion that is most likely associated to the formation of a silica gel layer.

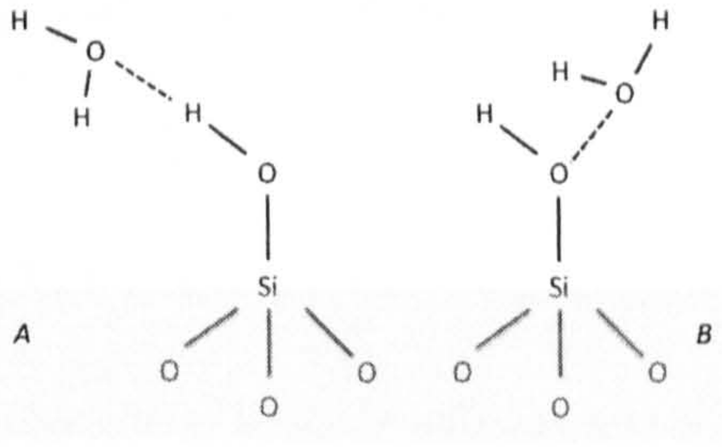

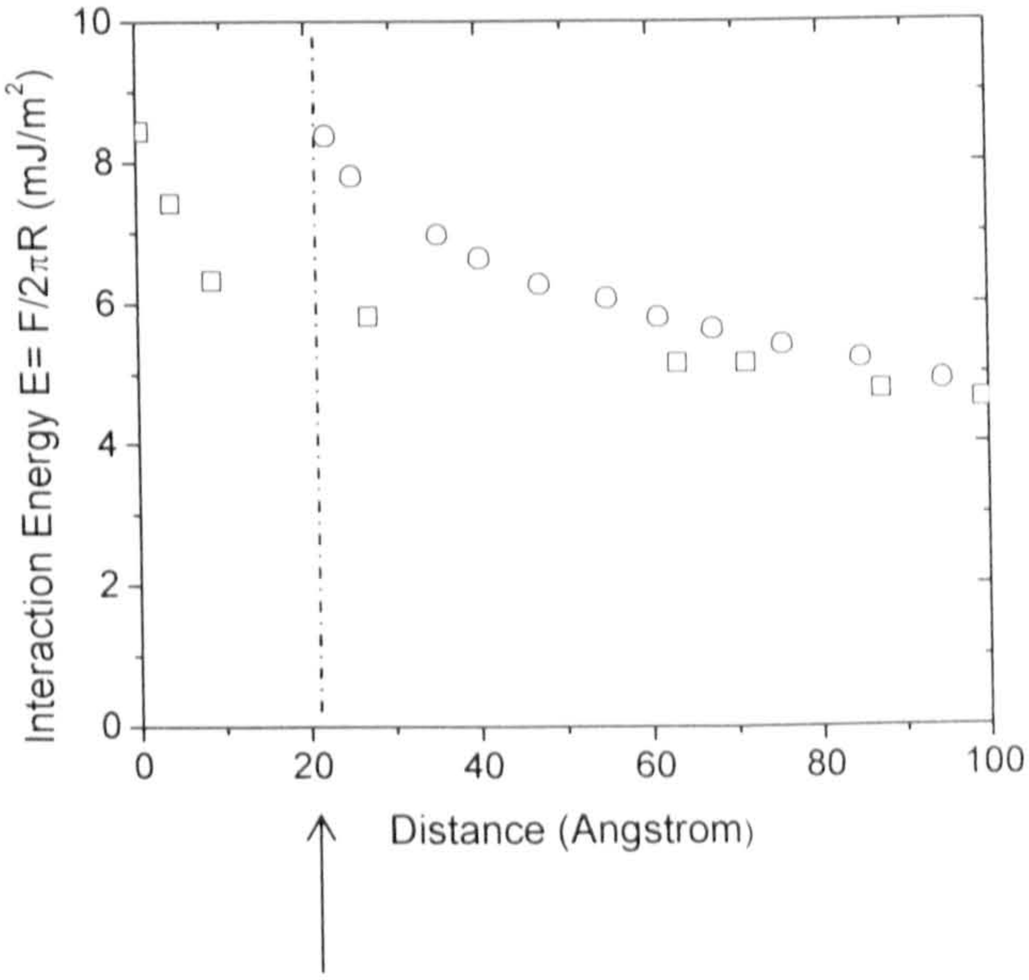

Figure 5.2 Left diagram: water molecule orientation with respect to the silanol group on the silica surface. A) Hydrogen atom in the water molecule bonded to the hydrogen atom of the $\equiv Si - OH$ group. B) Oxygen atom in the water molecule bonded to the hydrogen atom of the $\equiv Si - OH$ group. Figure redrawn reference [1]. Right diagram: Measured normal force of interaction between two hydrophilic and two hydrophobic surfaces. The presence of a gel layer on the silica surface adjusts the contact point. Symbols: circle – hydrophilic surface, square – hydrophobic surface. Data taken from [4].

5.1.2 Structured Water

The influence of structured water at the solid-liquid interface is a topic that has been disputed in literature for many years. The competition for surface silanol groups between water molecules and the cationic species in solution has been studied in detail by many researchers [10-12]. One study which shows the presence of a structured water layer and its effect on the short range repulsive force acting between silica particles is the study of Colic et al. [12]. Colic et al.[12] repeated the studies of Pashley and Israelachvili [11, 13] who investigated the influence of the hydrated ion size on the interaction potential between two mica surfaces. The secondary hydration layer theory proposed by Israelachvilli[11]

concluded that the short range repulsion force is determined by the size of the hydrated ion. Colic et al. [12] studied the same cation competition (Li^+, Na^+, K^+ and Cs^+) for the hydrated silica surface with the effect on the short range repulsive force determined from the suspension viscosity. The results contradicted the secondary hydration layer theory and concluded that the short range repulsion force is determined by the size of the unhydrated ion, not the hydrated ion. Colic et al. [12] showed that the smaller more hydrated ions produced suspensions with a higher viscosity. In high electrolyte concentrations (4M) the sequence of the deepest attractive potential well followed:

$$Li^+ > Na^+ > K^+ > Cs^+$$

which is the inverse of the sequence presented by Pashley [13].

Table 5.0 Un-hydrated and hydrated ion radii [14, 15].

Ion	Un-hydrated (Å)	Hydrated (Å)
Li^+	0.68	3.82
Na^+	0.97	3.58
K^+	1.33	3.31
Cs^+	1.67	3.30

The discussion presented by Colic et al. [12] focused on the ability of an ion to compete for water at the interface. The smaller Li^+ and Na^+ ions (see table 5.0) can be termed 'structure makers', having a greater affinity to reside within the surface hydration layer; while the larger 'structure breaker' ions K^+ and Cs^+ do not compete for water at the interface and remain on the periphery of the hydration layer. Structure maker ions therefore reduce the extent of the short range repulsion force enabling attractive networks to form, increasing the viscosity of the suspension. Figure 5.3 redrawn from reference [12] schematically illustrates the influence of the structure maker, structure breaker ions on the extent of the short range repulsion force.

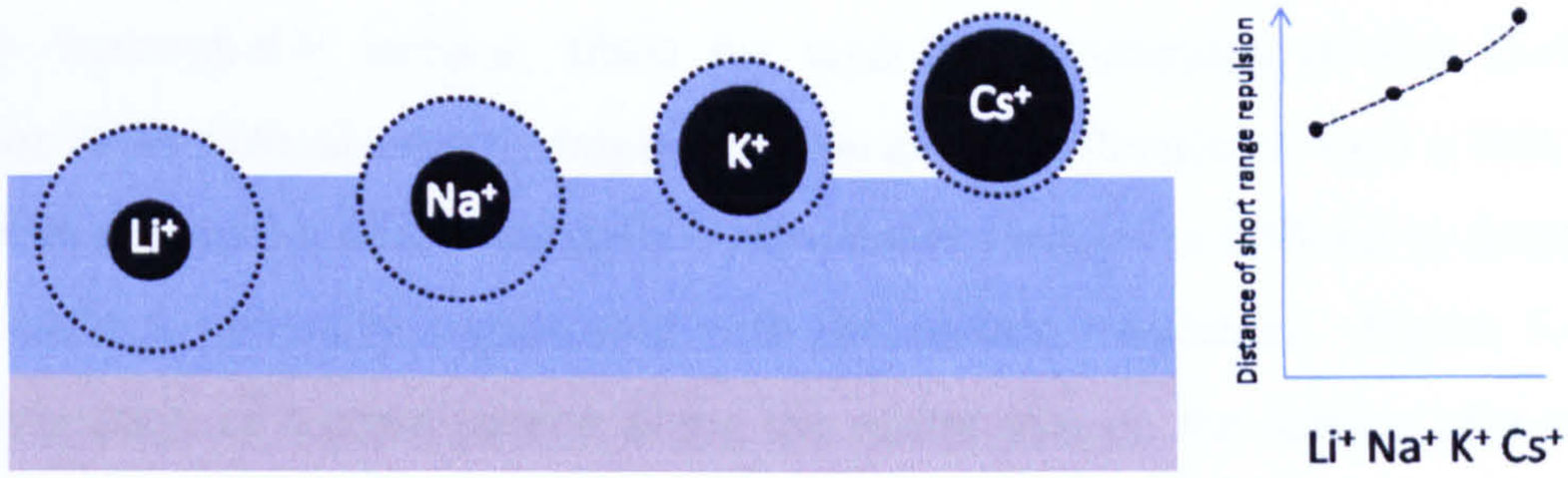

Figure 5.3 Schematic representation of the silica/water surface with a thick hydration layer with various counter-ions adsorbed to the surface. Most hydrated ions (structure maker) penetrate deeper into the hydration layer with the least hydrated ions (structure breaker) remaining on the periphery of the hydrated layer.

Although the author[12] interpreted the high concentration electrolyte results in terms of the structure-maker structure-breaker model, the results are unexpected. As will be discussed later, a silica surface with a low i.e.p. should behave as a structure breaker surface and not a structure maker surface. With a like-like affinity between an ion and a surface, it would be expected that the sequence of deepest attractive potential well would follow:

$$Cs^+ > K^+ > Na^+ > Li^+$$

Such behaviour is observed in the study[12] at pH 9 when the electrolyte concentration is reduced to 1M. It is most likely that the sequence observed in the high electrolyte concentrations is a result of other effects such as ion-ion and ion-solvent interactions; however, this has never been discussed in the literature since publication of the paper.

5.1.3 Hamaker Constant

The low Hamaker constant of silica in water compared with other mineral oxides has also been postulated when describing the unexpected stability at the i.e.p.. Dumont [16] provided a comparison between silica and titanium dioxide Hamaker constants in water, noting the silica Hamaker constant to be approximately 35 times smaller than that of titanium dioxide. It is therefore apparent that for spheres of equal size, the attraction energy between two silica particles is significantly lower than that between two titanium dioxide particles, and the effect of a structural stabilising force is therefore more evident.

The complicated surface properties of silica have been further scrutinized through surface force measurements [4, 8] which have suggested the formation of a hydration layer on a partially hydrophobic surface; albeit the layer is considerably thinner (5-15Å) than a hydration layer formed on a hydrophilic surface. The influence of such a thin layer on the interaction mechanics of two partially hydrophobic surfaces is difficult to determine, as the length scale is generally comparable with the surface roughness. Figure 5.4 shows the height variation of a cross section along the centre axis on the surface of a silica particle used in the current study, confirming that the variation in surface height is comparable with hydration layer thickness quoted in literature.

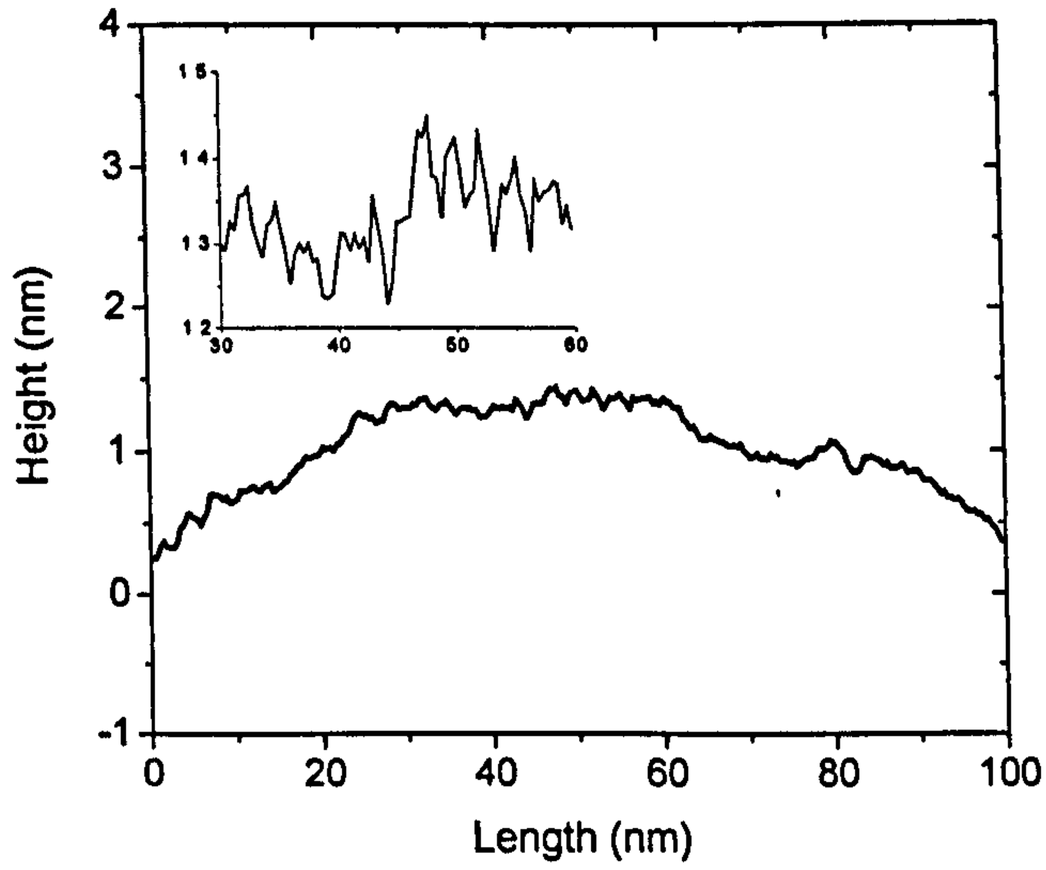

Figure 5.4 Typical height variations along the centre-line axis of a 0.8μm silica sphere. Height variation determined from contact mode imaging.

This brief introduction into the surface properties of silica has emphasised the potential complicated nature of the interaction. With the surface properties heavily dependent upon the manufacturing process (temperature), there are many contradicting studies which result from the hydrophilic/hydrophobic nature of the surface. With the particles used in the current study exposed to temperatures above 500°C in the manufacturing process (to reduce the solid porosity), and the surface roughness comparable to the hydration layer thickness measured on a partially hydrophobic surface, it is therefore reasonable to assume that the rheological properties of the silica suspensions studied, can be suitably characterised by

excluding any soft steric layer interaction, and can be treated as a surface which is representative of a DLVO interaction (see AFM results section 5.6)

5.2 Ion-Surface and Ion-Ion Effects

Ion-specific effects have been studied in detail for many years. The classic 'Hofmeister' series was first reported in 1888 and concerned the salting-out of proteins from solution. Ion competition for a surface, either by the specific adsorption onto a surface or surface charge screening by the electrical double layer, is commonly studied through observing shifts in either the iso-electric point (i.e.p.) [17], the absolute value of the zeta potential[18], the critical coagulation concentration [19, 20] and the shear or compressional yield stress of the material[21].

With a central i.e.p. and partial solubility at extreme pH's, titanium dioxide and zirconia are two model surfaces that have been readily used to investigate both anion and cation specific effects. The nature of the anion can be determined from the positive branch of the charging curve, and the nature of the cation can be determined from the negative branch of the charging curve. Kosmulski and Rosenholm [22] studied the absolute value of the negative and positive zeta potentials of both anatase and zirconia to determine individual ion effects. For a given anion the sequence of increased reduction in the negative zeta potential followed:

$$Li^+ > Na^+ > K^+ > Cs^+$$

whilst for a given cation the sequence of increased reduction in the positive zeta potential followed:

$$I^- > Br^- > ClO_4^- > NO_3^- > Cl^- > CH_3COO^-$$

With an iso-electric point around pH 2 [23], the cation specificity for the silica surface has received little attention. Franks et al. [17] investigated a wide range of monovalent electrolyte concentrations and observed that for a given anion (Cl^-), the sequence of increased reduction in the negative zeta potential followed:

$$Cs^+ > K^+ > Na^+ > Li^+$$

The same study also identified a shift in the i.e.p. at electrolyte concentrations above 0.1M. Specific adsorption of the monovalent ion shifted the i.e.p. to a higher pH, with the sequence of greatest i.e.p. shift to least i.e.p. shift following the same series as for the reduction in the negative zeta potential. The associated shift in the i.e.p. with increasing salt concentration was used to describe the abnormal yield stress behaviour observed in this study (see figure 5.5). The author observed a minimum in the yield stress at low pH (pH3) with the yield stress either passing through a maximum or continuing to increase as the pH was adjusted to pH 11. The inconsistent relationship between the i.e.p. and the maximum yield stress is difficult to interpret. The low yield stress in low pH environments can be justified in terms of the unexpected stability of silica at low pH's (see previous discussion on silica surface chemistry). The discrepancy between the i.e.p. and the maximum yield stress may be associated to measurement error (two different measurement techniques). However, this is unlikely as it would be expected that the error would translate through all data sets. With differences observed between the two structure maker ions and similar differences observed between the two structure breaker ions, there appears to be no obvious trend. The influence of ion-ion and ion-solvent interaction may provide an understanding for such observed behaviour.

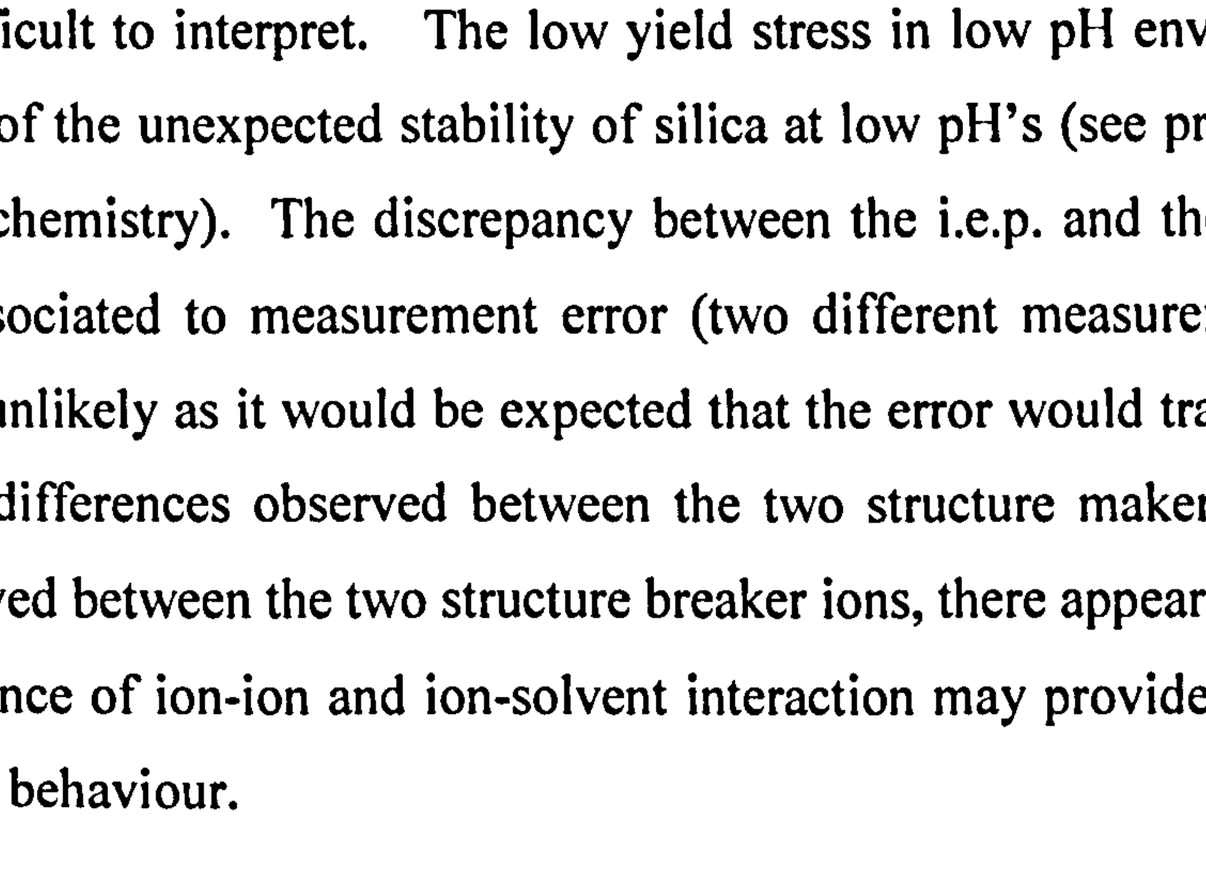

Figure 5.5 Silica shear yield stress data of 40 vol% in 1.0M CsCl (inverted triangles), KCl (triangles), NaCl (circles) and LiCl (squares). Silica i.e.p. ≈ pH4. Figure redrawn from reference [17].

The anion and cation series for a given surface can generally be explained by the relative abilities of both the ion and the surface to structure or de-structure water. As previously explained, the ability for an ion to structure water is related to the strength of the electric field at the surface, while the division between a structure making and a structure breaking surface is related to the nature/structure of the solid, and the surface i.e.p.. Dumont et al. [19] discussed the stability of metal oxides concluding that the structuring power of a surface bearing a positive electrical charge is always more structure maker than the same surface when negatively charged. More specifically, the transition from a structure maker to a structure breaker surface is associated with the surface heat of hydration. Theoretical and experimental results have validated the transition to arise for heats of immersion from 0.3 – 0.4 Jm^{-2}. Amorphous silica with a low heat of immersion ($\approx$ 0.1 Jm^{-2} [19]) and a low i.e.p. is a termed a 'structure breaker' surface, while titania (= 0.55 Jm^{-2} [19]) and alumina (= 0.773 Jm^{-2} [19]) having a high heat of immersion and a high i.e.p. are termed 'structure-maker' surfaces. With a low i.e.p. silica is classified as a structure breaker surface and will therefore preferentially adsorb structure breaker ions, while a structure maker surface such as anatase, zirconia or alumina, will preferentially adsorb structure maker ions. Such an effect is related to the secondary hydration layer theory and the structure maker – structure breaker theory previously discussed.

Kosmulski and Rosenholm have published an array of papers where the ion-ion interaction behaviour is shown to influence the specific binding behaviour of a counter-ion [24-26]. In a detailed study where they focused on the binding potential of monovalent ions in high ionic strength electrolytes, they discussed the differentiating effect of small cations and large anions, and the absence of this differentiating effect for large cations and small anions. The most negative zeta potentials of anatase in 0.4 mol dm^{-3} solutions were compared for $NaNO_3$ (ionic radius Na^+ 0.97Å, NO_3^- 2.97Å), NaI (I^- 2.20Å), $CsNO_3$ (Cs^+ 1.67Å) and CsI. For the differentiating case they observed a significant difference in the most negative zeta potential (11mV), while for the non-differentiating case the difference was considered insignificant. They concluded that the ion-ion interaction in solution governs the reduction in the negative zeta potential and the shift in the i.e.p. at high ionic strengths, with the specific ion-surface interaction playing only a secondary role.

A further theory proposed by many researchers when explaining the ion-surface specificity series, is the 'hard-soft' theory[24]. The approach is based upon the competition potential between the surface/counter-ion and the co-ion/counter-ion. A hard cation such as Li^+ or Na^+ has an enhanced affinity for a hard surface such as anatase, with the extent of surface interaction influenced by the hard-soft nature of the anion. A hard anion (Cl^-) in solution can successfully compete with the surface for the hard cation. Depending upon the degree of competition, the cation concentration within the interfacial region can be limited to prevent the formation of excess charge. For a structure breaker surface such as silica, the soft surface has an enhanced affinity to soft anions preventing excess charge when the cation is hard. However, when the cation is soft the competition mechanics change and the cation affinity for the surface increases.

Individual ion activity coefficients should also be considered when discussing ion-surface specificity. Vera et al. [27] looked at the individual anionic and cationic activity coefficients in aqueous electrolyte solutions of LiBr, LiCl, KCl and NaCl, by measuring the electromagnetic field of the ion selective electrode against a single junction reference electrode. The study verified previous conclusions that the activity coefficient of an ion depends on its counter-ion, and the activity coefficient of the cation is different from the activity coefficient of the anion. Measuring the activity coefficients in electrolyte solutions up to 3M, the results showed the coefficient for Li^+ to be consistently higher than the anion coefficient. With an increase in the electrolyte concentration the cation coefficient showed a threefold increase while the anion coefficient halved in value.

The activity coefficient reflects the potential for ion-solvent interaction and therefore the degree of ion hydration. In low concentration electrolyte solutions (common anion Cl^-) the activity coefficients of Li^+, Na^+ and K^+ were compared. The order of the highest to the lowest activity coefficient followed:

$$Li^+ > Na^+ > K^+$$

Interestingly, the activity coefficient of lithium increased with an increase in the electrolyte concentration, while the sodium coefficient remained unchanged and the potassium coefficient decreased. In terms of the structure-maker structure-breaker approach this is significant, as the ion affinity for its corresponding surface would increase for both Li^+ and

K^+ ions, with an increase in electrolyte concentration, while the ion affinity of the structure maker Na^+ ion would remain unchanged as the electrolyte concentration is increased. The anion activity coefficients in solution showed a similarity in behaviour, with the only significant difference in the activity coefficient associated with a change in the counter-ion.

5.3 Zeta Potential

The relationship between rheology and zeta potential has been subjected to extensive research [17, 18, 21, 28-33]. As previously discussed in chapter 2 the strength and the nature of an interaction between two colloidal particles is primarily influenced by the ionic concentration. As the ionic concentration is increased the degree of surface charge screening also increases, reducing the potential energy barrier for the interaction.

Initial characterisation of the silica in this study was completed through investigating the affect of both the electrolyte strength and type on the zeta potential. Unlike previous silica studies [10, 12, 17] where cationic effects were investigated, here the focus has been on the influence of the anion (Cl^-, Br^-, NO_3^-) with a similar cation (K^+). All three figures, 5.6a (NO_3^-), b (Cl^-) and c (Br^-) show the characteristic reduction in the absolute silica zeta potential as more surface sites become protonated at lower pH's. Ion effects are observed when monitoring the $pH_{i.e.p.}$ and the absolute value of the negative zeta potential. For KNO_3 the i.e.p. is measured at approximately pH 3 and shows no deviation with an increase in the electrolyte concentration. Over the concentration range investigated (10^{-4} M – 1M) the electrolyte can be described as being 'inert'. The i.e.p. for silica in KCl solution is also measured at approximately pH 3, with the data suggesting a slight shift in the i.e.p. to a higher pH when the electrolyte concentration is increased to 1 M, thus indicating specific adsorption of the cation [17]. However, it should be acknowledged that as the zeta potential approaches zero it becomes increasingly more difficult to initiate particle movement in an electric field and therefore measure the 'true' zeta potential (refer to chapter 4 on measurement principles of zeta potential). Without several experimental repeats the observed shift could be considered within experimental error. For silica in KBr solution there is no measurable difference in the $pH_{i.e.p.}$ over the concentration range studied (10^{-1}M to 10^{-4}M), which agrees with the general consensus that specific ion adsorption effects are only observed when the electrolyte concentration exceeds 0.1M [26, 34].

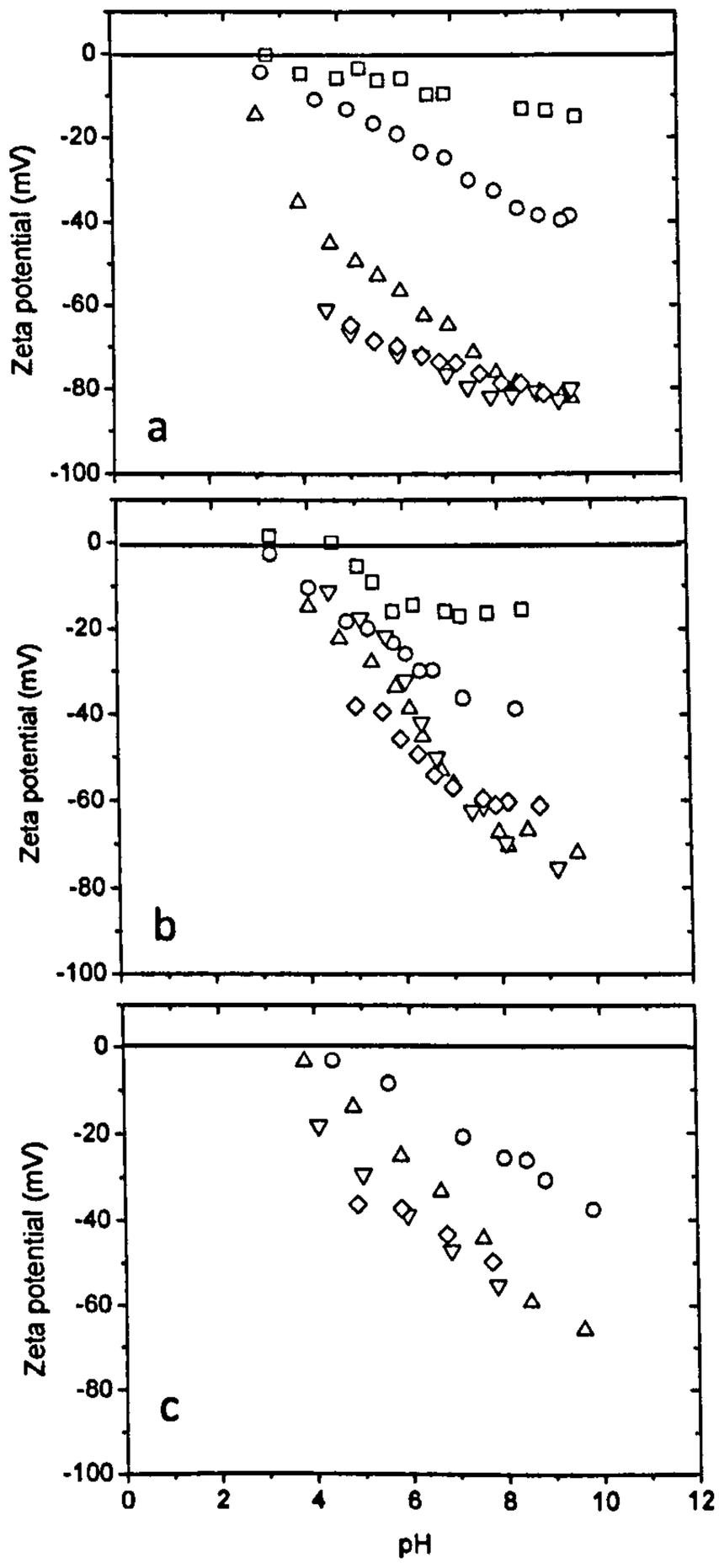

Figure 5.6 Zeta potential of Fuso silica dispersed in a) KNO_3 b) KCl and c) KBr electrolytes. Symbols: square – 1M, circle – 10^{-1}M, traingle – 10^{-2}M, inverted triangle – 10^{-3}M and diamond – 10^{-4}M.

Kosmulski [34] published the first study investigating anion effects on the electrokinetic mobility of silica colloids. Titrating fumed silica with three different acids; HCl, $HClO_4$ and HNO_3, Kosmulski[34] observed differences in the electrokinetic mobility at very low pHs. With an increase in the suspension pH, there was no detectable difference in the electrokinetic mobility of the silica; the author concluding such an affect to be a result of anion depletion from the interfacial region due to electrostatic repulsion. Such behaviour contradicts the results of this current study where the affect of the anion is clearly observed at low salt concentrations and at high pH values away from the i.e.p..

Kosmulski's study briefly evaluates the anion effects of different salts. Comparing 0.1M $CsNO_3$ and 0.1M CsCl, there is no measurable difference in the silica electrokinetic mobility with pH. The result is somewhat inconclusive as the Cs^+ ion greatly influences the electrokinetic mobility of silica [17], the ion preferentially adsorbing relative to the more hydrated ions where the ion-ion interaction would play a more significant role in determining the electrokinetic mobility. It is therefore expected in this instance that the electrokinetic mobility is affected only by the dominant cation with the effects of the anion screened. With a brief study and limited conclusive data for different salts, the conclusion that the anion specificity observed through acid titrations is expected to be similar for salts, is difficult to acknowledge.

Figure 5.7 provides a comparison of the negative zeta potential at pH 9 for all three electrolytes used in this study as a function of increasing electrolyte concentration. There is an observed shift in the negative zeta potential which is associated with the anion. Repeat experiments have shown the measurement error at pH 9 to be within 3%. The sequence of increased reduction in the negative zeta potential follows:

$Br^- > Cl^- > NO_3^-$

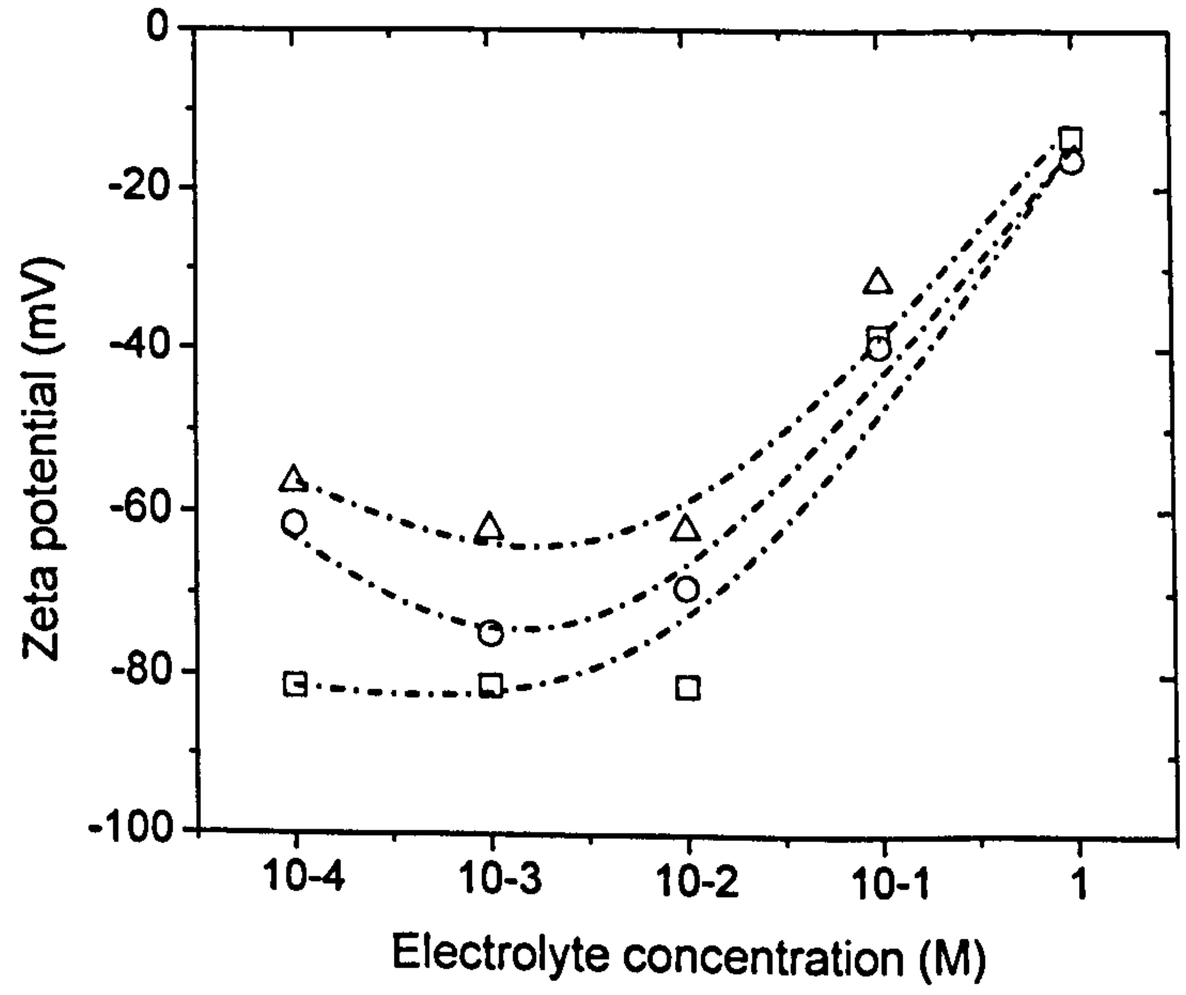

Figure 5.7 Zeta potential comparisons as a function of electrolyte type and concentration. All data points determined at pH 9. Symbols: square – KNO_3, circle – KCl and triangle – KBr. Lines to guide the eye.

With all three anions having similar hydration enthalpies and activity coefficients, the discussion around the hard-soft approach and/or the structure-maker structure-breaker approach is rather limited. However, with subtle differences in the anion properties, ion-solvent and ion-surface interactions may provide an explanation for such behaviour. Additionally, the behaviour could be related to the ion-ion interaction and the dissociation energy of the salt (see table 5.1). The sequence $Br^- > Cl^- > NO_3^-$ (increased reduction in the negative zeta potential) is more evident at low salt concentrations with the effect diminishing as the salt concentration is increased. This behaviour complements the idea of incomplete dissociation of the electrolyte. In high ionic strength electrolyte solutions, small changes in the electrolyte dissociation energy are compensated for by the high ion density in solution. However, when the ion density in solution is low (10^{-4}M), such variances in the dissociation energy become more significant. With the electrolyte dissociation energy decreasing in the order (see table 5.1):

KCl > KBr

it is expected under conditions of incomplete dissociation that the concentration of K^+ ions in the interfacial region decreases following:

KBr > KCl

The sequence shows that for incomplete dissociation of the electrolyte, the K^+ ion concentration in solution from a KBr electrolyte should exceed the K^+ ion concentration from a KCl electrolyte. The resulting change in the concentration of free K^+ ions in solution will affect the degree of surface charge screening, and therefore the electrokinetic mobility of the silica. With an increase in the K^+ ion concentration there is an associated increase in the shielding of the silica surface charge, reducing the magnitude of the negative zeta potential. With no dissociation data for KNO_3 available, a direct comparison of all three electrolytes cannot be made. However, subsequent data (sections 5.4, 5.5 and 5.6) to be discussed, provides validation of the zeta potential measurements with the same trends observed using alternative measurement techniques. The brief discussion on the possibility that the ion dissociation energy influences the zeta potential in low concentration electrolytes provides a reasonable assessment of the electrokinetic mobility data collected for silica in different potassium salts.

Table 5.1 Ion dissociation energies. Values taken from reference[35].

Molecule	Dissociation Energy (eV)
KBr	3.97
KCl	4.43
KNO_3	-

Three suspensions were selected for further characterisation and investigation in the pipe loop. Selection of the electrolyte concentration and type was made in view of producing sediments with different rheological properties. One approach would be to select an appropriate electrolyte concentration that would generate significantly different zeta potentials as a function of the suspension pH. Analysis of the data suggests that a 10^{-2}M electrolyte would be suitable, with zeta potential values spanning 70mV. However, Franks [17] presented data which showed for the same electrolyte concentration (10^{-2}M) and at a solids (silica) concentration above the gel-point, a shift of 70mV may only vary the yield stress by 20-30Pa. The same data also showed that a much larger variation in the shear yield stress was possible at the same pH and electrolyte concentration, when the type of electrolyte was altered. Based on these observations and the conclusions drawn from the electrokinetic mobility data, three electrolytes, 1M KNO_3, 10^{-4}M KNO_3 and 10^{-4}KCl at pH 6 (natural pH of suspension ≈ pH6) were chosen for further investigation.

5.4 Shear Yield Stress

The topic of a 'true' yield stress has been debated in literature for many years [36, 37], with discussion centring on the accepted definition and time scale for material deformation. From an engineering perspective the yield stress is typically defined as the minimum stress that must be applied to a material in order to initiate flow within a time scale suitable for the application. In multiphase pumping applications the time scale is usually of the order of seconds to minutes, depending upon the length of pipe, the angle of inclination, and the physical properties of the sediment.

One of the more accurate and more commonly used techniques when measuring the yield stress of a concentrated colloidal suspension, is the single point vane technique developed

by Boger et al. [38]. The vane tool causes little destruction of the particle network when lowered into the sample and minimises wall slip and wall depletion effects during the measurement; effects commonly encountered when using Couette or cone and plate techniques. The single point method determines the yield stress through interpretation of the maximum torque (refer to chapter 4), unlike in-direct yield stress determination where the reliability of the result is dependent upon the quality of the data collected in the low shear rate range. Several parameters including particle size, particle size distribution and shape; solids volume fraction and the interaction potential between individual particles have all been shown to influence the material yield stress [17, 28, 32, 39-41]. Of interest in this study is the affect of the particle surface chemistry on the yield stress of a consolidated sediment bed. Surface chemistry effects on the shear yield stress of a material have been studied in detail, with the classical 'bell-shaped' yield stress curve continually reproduced for materials that exhibit a central i.e.p (see figure 5.8). Johnson et al. [32] provide an excellent paper looking at the effect of DLVO and non-DLVO forces on the yield stress of zirconia and alumina based suspensions. The authors showed that for a suspension influenced by DLVO forces, a maximum in the shear yield stress of the material is observed when the zeta potential is zero and the interaction is dominated by the strongly attractive van der Waals force (see chapter 2). While, a shift in the pH away from the i.e.p. results in the gradual reduction of the shear yield stress until a pH is reached where the material freely flows and no longer exhibits a yielding point. The reduction in the yield stress is associated with an increase in the strength of the electrical double layer force diminishing the net inter-particle attractive potential.

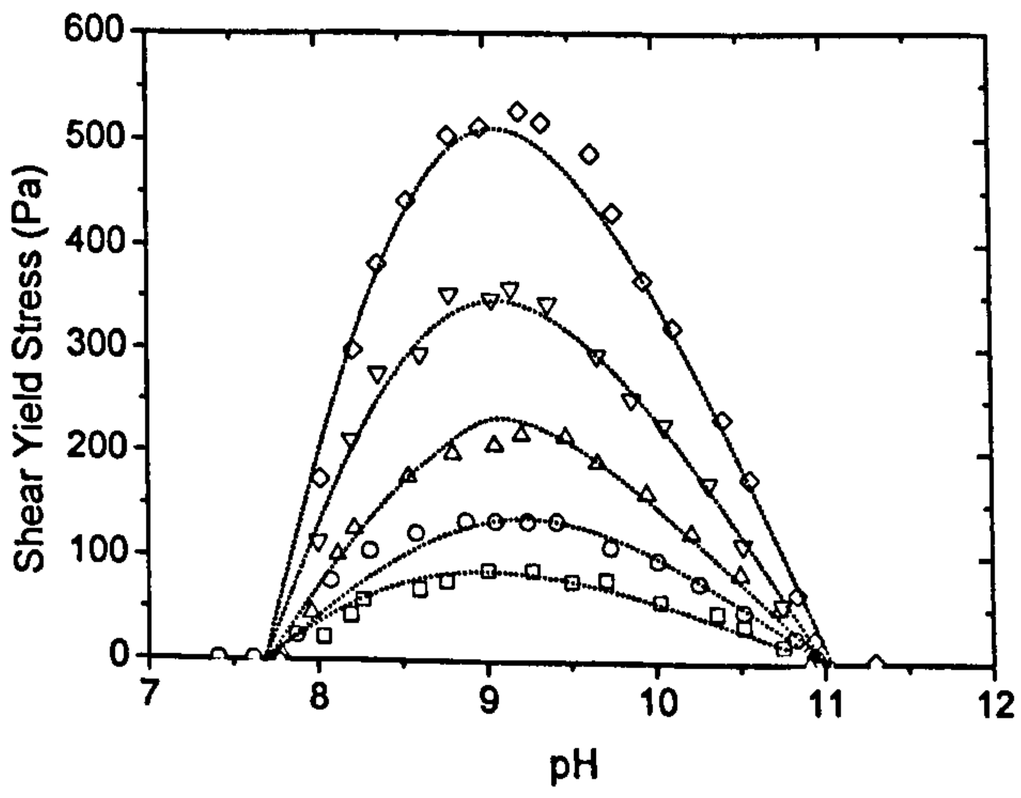

Figure 5.8 The shear yield stress of concentrated α-alumina suspensions as a function of pH and solids volume concentration. Symbols: square 20% volume, circle 22.5% volume, triangle 25% volume, inverted triangle 27.5% volume and diamond 30% volume. Figure taken from reference [32].

In 1998 Scales et al. [33] derived an expression for the shear yield stress of a flocculated suspension of spheres, accounting for the effects of particle size distribution, solids volume fraction and the electrokinetic properties of the suspension. A simplified version of the expression is defined as:

$$\tau_y = K_{stucture}\,[V_A - V_R] \qquad [5.0]$$

where $K_{stucture}$ is dependent upon the particle size, the solids volume fraction and the mean coordination number ($\frac{36}{\pi}\emptyset$ when $\emptyset \leq 0.47$)[33]. The bracketed term defines the electrokinetic properties includes the van der Waals and the electrical double layer forces, which have been previously discussed in chapter 2.

Here using the technique described by Nguyen Quoc and Boger [38], the shear yield stress of the consolidated silica sediments varied as a function of both the electrolyte concentration and type (see figures 5.9a and b). With an increase in the electrolyte concentration from 10^{-4}M to 1M, there is a significant decrease in the shear yield stress of the sediment (200-300Pa). Analysing such behaviour in terms of equation 5.0, both the structural and the DLVO components will be influenced by a change in the ionic concentration. However, assuming that the structural component is independent of the ionic concentration, an increase in the electrolyte concentration would result in a reduction in the magnitude of the repulsive component, and therefore, an increase in the shear yield stress. With a significant reduction in the shear yield stress, structural changes are clearly dominating the behaviour under these conditions. At high electrolyte concentrations the formation of aggregates in the suspension will reduce the solids volume fraction and the number of particle-particle contacts within the sediment. At low electrolyte concentrations the particles remain dispersed and are able to pack more efficiently. As a result, the solids volume fraction and the number of particle-particle contacts within the bed increases, therefore, increasing the shear yield stress of the sediment bed. This behaviour has been shown by several researchers to influence the shear yield stress of a material [17, 41, 42]. Further data which complements these results is provided in the gel-point discussion to follow. Figure 5.9a

shows the yield stress data for high and low electrolyte concentration sediments. At high electrolyte concentrations the shear yield stress is independent of the electrolyte type, with the differences in the shear yield stress considered negligible and within experimental error. At low electrolyte concentrations the sediment shear yield stress appears to be dependent on the type of electrolyte. The sequence of reducing shear yield stress follows:

$KNO_3 > KCl > KBr$

which is in accordance with the electrophoretic mobility data, and the understanding that the ion dissociation energy plays an important role at low electrolyte concentrations. All experiments were repeated 5 times to provide a reasonable assessment of the error of uncertainty.

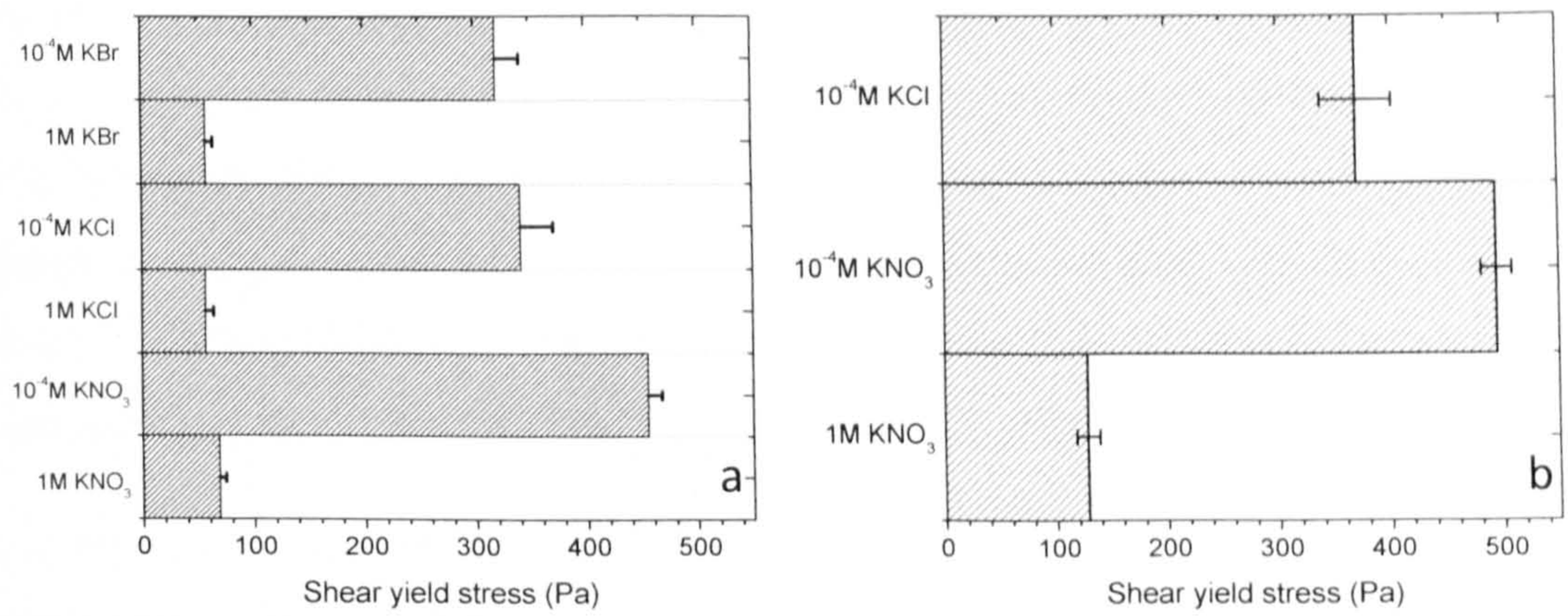

Figure 5.9 Sediment shear yield stress. a) comparison between electrolyte concentration and type. Trend in the data corresponds to the electrophoretic mobility data for silica (see figure 5.7). b) comparison of the three sediments to be further investigated in the slurry pipe loop.

Figure 5.10 below visually shows the change in the structure yield strength when the force acting on the sediment is rotated 90°. The 10^{-4}M KNO_3 which has a high yield strength due to a densely packed sediment holds is structure, while the 1M KNO_3 which is characterised by a lower solids packing fraction, and therefore, a lower yield strength, "slumps" when the beaker is rotated onto its side.

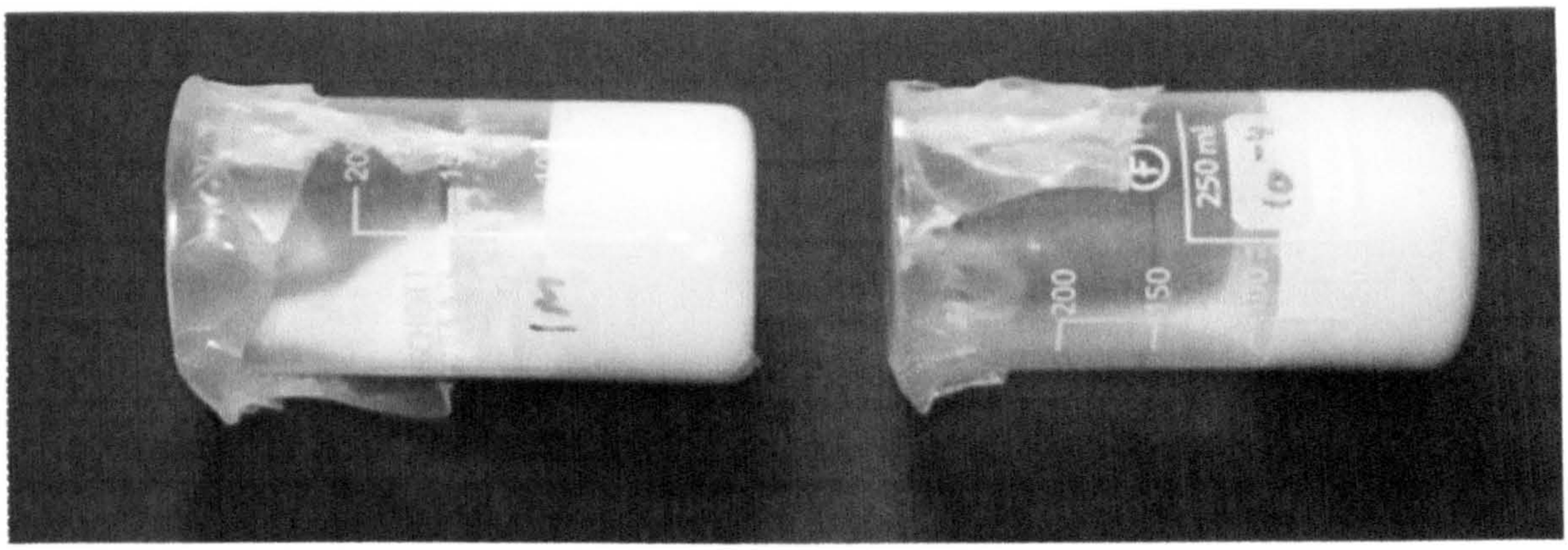

Figure 5.10 Silica sediments prepared in 1M KNO_3 electrolyte (left hand side) and 10^{-4}M KNO_3 electrolyte (right hand side).

5.5 Sedimentation and Gel Point

The rate of sedimentation of a single sphere falling in a Newtonian fluid can be calculated using Stokes' law; relating the settling velocity to the gravitational and the frictional drag force acting upon the particle. Frequently the Stokes' equation is modified by scaling factors to account for particle shape (changes in the drag coefficient) and solids loading (hindered settling effects). Generally, both a deviation from sphericity and an increase in solids loading will act to reduce the settling rate of the particles.

For hard spheres of equal size the settling system can be divided into three zones: a clear supernatant at the top, a free falling zone, and a collapse zone. With particles depositing at the same rate, the settling velocity can easily be determined by tracking the interface between the clear supernatant and the free falling zone. As the free falling zone diminishes, the constant rate of settling reduces to the consolidation rate of the sediment [43].

In a poly-dispersed system the boundaries between the three zones become diffuse. Visual assessment of the clear supernatant-free settling zone boundary is no longer achievable, and techniques such as light monitoring (Turbiscan®, LUMiFuge®) and X-ray adsorption scanning [31] are commonly employed to determine the settling properties. The settling behaviour of a poly-dispersed system is more representative of the settling characteristics observed in an aggregated system, where the particle size can range from the singlet up to large clusters where the effective radii is a hundred times or more that of the primary particle [44, 45]. The formation of aggregates in the suspension complicates the analysis as it is no longer appropriate to treat the system using hard sphere models. Aggregates tend to

form non-ideal shapes which are permeable, resulting in both an increase (shape factor) and a decrease (porosity factor) in the hydrodynamic fluid drag, when compared to impermeable primary particles of the same size.

In his review on techniques to determine the mass fractal dimension of an aggregate, Bushell et al. [46] provides the terminal velocity (U_t) equation for an aggregate in a Newtonian fluid:

$$U_t = \sqrt{\frac{V_a}{A_a C_D} \cdot \frac{2(1-\varepsilon)(\rho_s-\rho_l)g}{\rho_l}} \qquad [5.1]$$

which for spherical, impermeable objects in the Stokes regime ($Re \ll 1$) reduces to:

$$U_t = \frac{4(1-\varepsilon)(\rho_s-\rho_l)gr^2}{18\mu} \qquad [5.2]$$

where V_a is the aggregate volume, A_a is the aggregate projected area in the direction of flow, C_D is the drag coefficient, ε is the aggregate porosity, ρ_s and ρ_l are the densities of the primary particles and the fluid respectively and r is the aggregate radius.

The equation includes three parameters (A_a, C_D, ε) that are dependent upon the overall size of the aggregate, with the reciprocal actions of each parameter influencing the terminal settling velocity. Detailed discussions on each individual parameter and their effects on the settling rate are considered outside the scope of this study. Readers are referred to the following publications for further information [46-48].

In an aggregated suspension the transition from free (un-hindered settling) to zone (segregated settling zones, observed in polydispersed suspensions), and finally compression (sediment consolidation- multi particle contacts) settling is not exclusively determined by the solids concentration, consideration should also be given to the degree of aggregation. Figure 5.11 redrawn from reference [47] illustrates these effects mapping the regions according to both the solids concentration and the degree of aggregation.

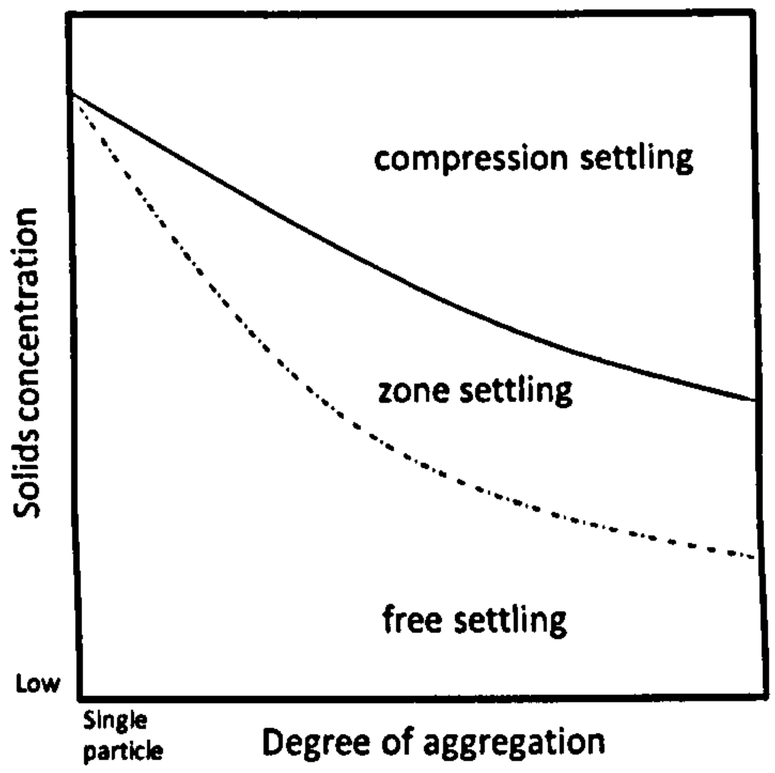

Figure 5.11 Suspension settling regimes depending on the degree of aggregation and suspension concentration. Figure redrawn from reference [47].

In a dispersed suspension where particle-particle interactions are minimal, the free settling regime spans a large concentration range. With an increase in the collision efficiency and the formation of open porous aggregates, the transition to zone and compression settling occurs over a smaller concentration range, due to an increase in the effective volume fraction of the solids.

The consolidation behaviour and the rheological properties of sediment beds are also sensitive to the degree of suspension aggregation [21, 31, 32, 49-52]. The lowest concentration of particles in a suspension that can form a 3-dimensional space filling heterogeneous network is known as the suspension gel point. In many process industries slurries are pumped at concentrations well below the gel point to reduce pumping costs and to avoid particle jamming in the pipeline. However, during process shut down, sediment beds form on the pipe invert with a shear yield stress dependent upon the number of particles per unit volume and the particle-particle interaction strength.

Buscall et al. [49, 53] provides a quantitative approach to modelling the consolidation behaviour of aggregated suspensions. The consolidation behaviours of a strongly and weakly aggregated suspension are compared in terms of the compressive yield strength (P_y) and the vertical component of the static stress (P_s). With the formation of a self-supporting network, the load bearing stress resulting from the weight of each individual particle and aggregate is transmitted directly throughout the network structure. As the static stress

increases with increased loading, a point can be reached where the compressive strength of the network is exceeded, resulting in densification of the network.

In a strongly aggregated suspension where the interaction potential consists of a deep primary minimum and the particles are in contact with one another, the compressive yield strength is likely to exceed the vertical component of the static stress. The sediment concentration throughout the bed will therefore be equal to the gel point concentration. As the aggregation strength is reduced and the interaction potential moves to a secondary minimum, resulting in a weakly attractive network of particles, it is most likely that the vertical component of the static stress at the base of the sediment will exceed the compressive strength of the network. Depending upon the load bearing stress and the strength of aggregation, a density gradient increasing from the gel point concentration can be measured as a function of sediment bed depth.

Figure 5.12 represents the compressional mechanics of aggregated sediments with the governing equations for consolidation given as:

$$P_s = \Delta\rho g \int_0^h \emptyset dz \qquad [5.3]$$

$$P_y = \left[\Delta\rho g + \frac{\gamma}{v\Delta\rho g}\frac{dh}{dt}K(\emptyset_0)\emptyset_0\right](h - z_c) \qquad [5.4]$$

where $\emptyset_0$ is the solids volume fraction in the settling column, $\Delta\rho$ is the solid – liquid density difference, g the acceleration due to gravity, γ the friction coefficient of a particle at infinite dilution, v the volume fraction of a particle (assumed mono-dispersed), $K(\emptyset_0)$ the hindered mobility coefficient, h the suspension height, *dh/dt* the rate of descent of the suspension supernatant interface and z_c the position of the moving boundary between the compression zone and the free settling zone where $\emptyset = \emptyset_0$.

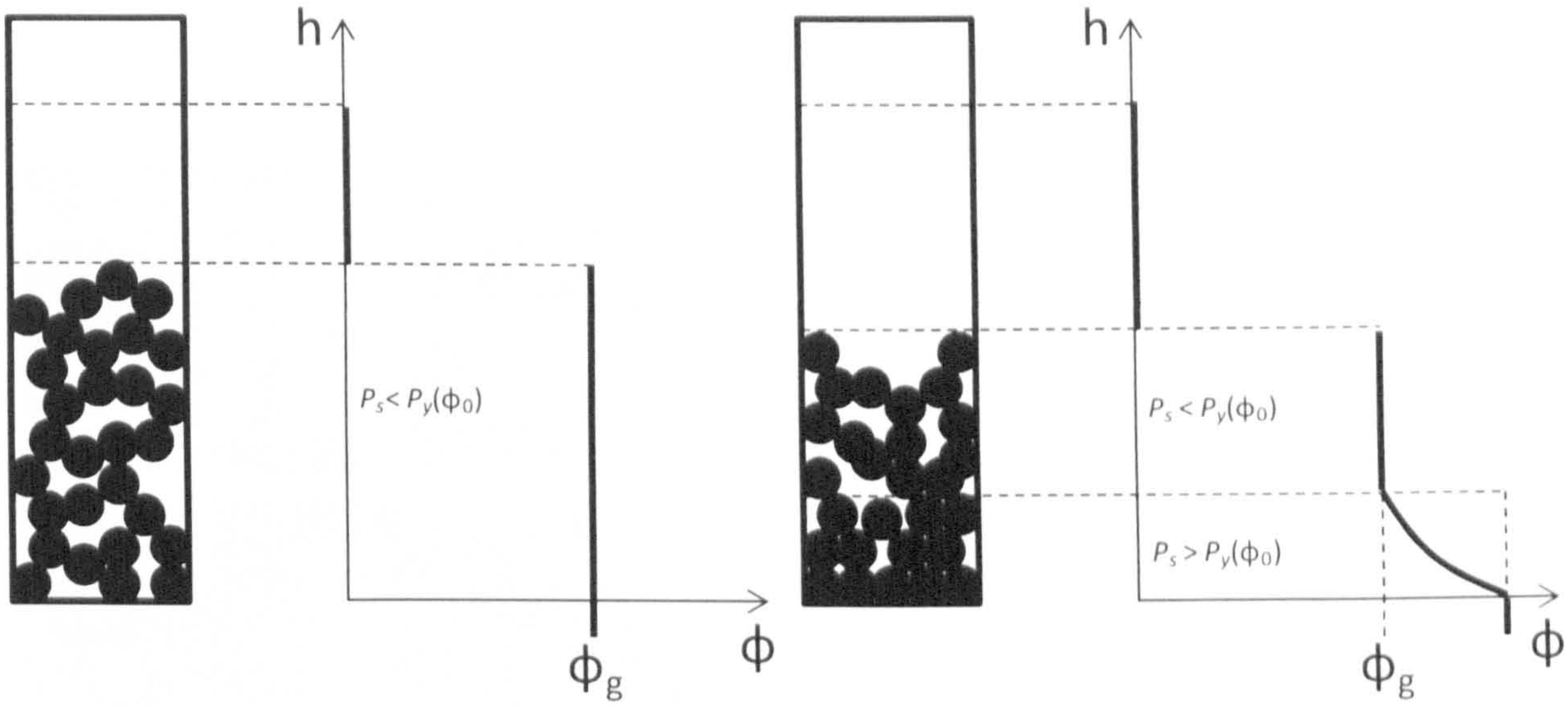

Figure 5.12 Schematic representation of sediment bed consolidation in terms of the vertical component of the static stress (P_s),the compressive yield strength (P_y) and Φ_g the gel point.

In the current study the suspension settling rates and the gel points are compared as a function of the electrolyte type and concentration. Settling columns were used to determine the settling rate as well as the suspension gel point for particles dispersed in 10^{-4}M KNO_3 and KCl and 1M KNO_3 background electrolytes. Images collected at time intervals during the settling process up until the point of no further sediment bed consolidation are shown in figure 5.13a-g (10^{-4} M KNO_3) and figure 5.14a-g (1M KNO_3).

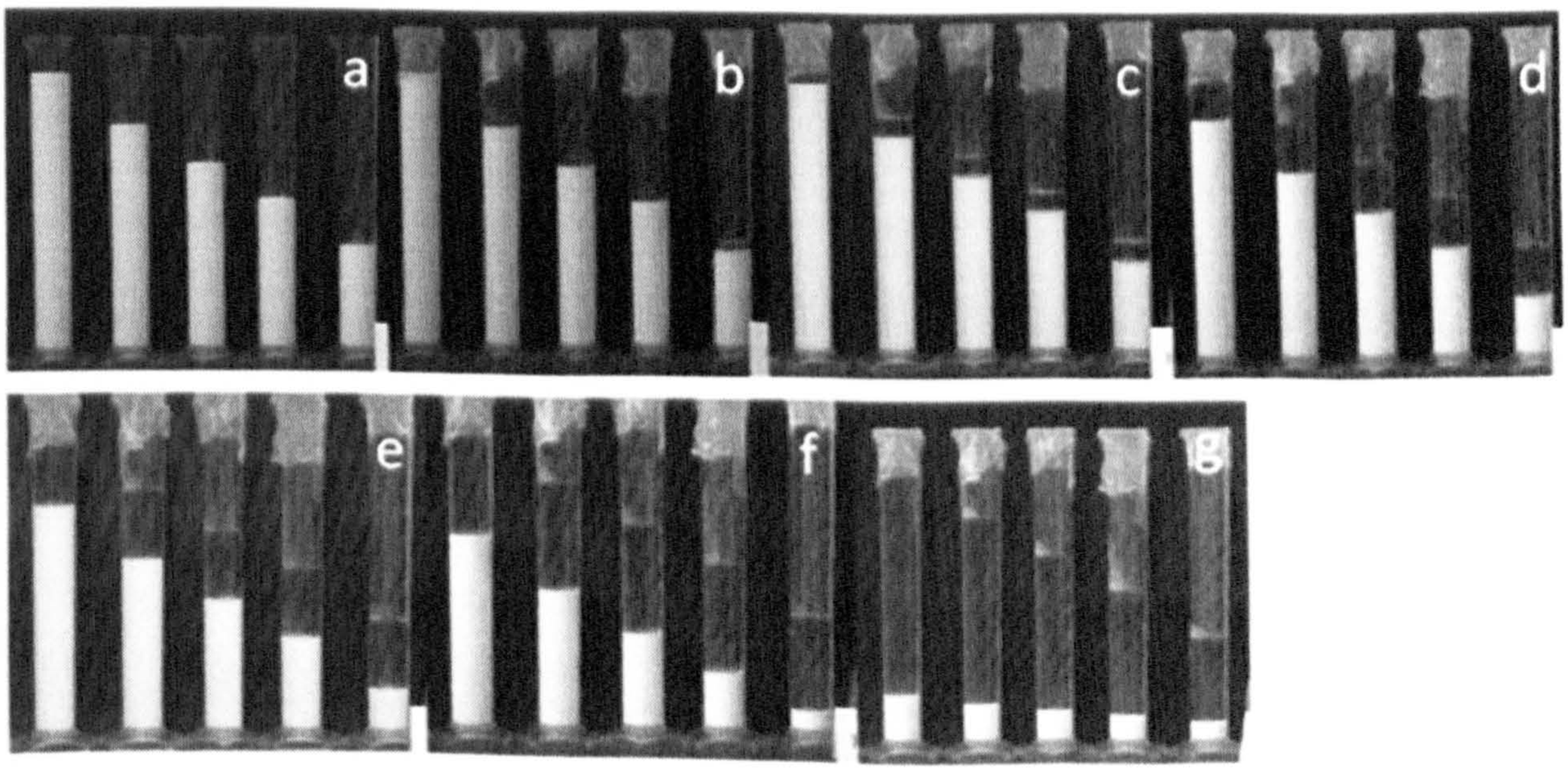

Figure 5.13 Settling column experiments to determine the suspension gel-point. 10^{-4}M KNO_3 silica suspensions prepared to pH 6. Time intervals (hrs): a) 0 b) 3.9 c) 9.7 d) 24 e) 32.4 f) 49.4 g) 94

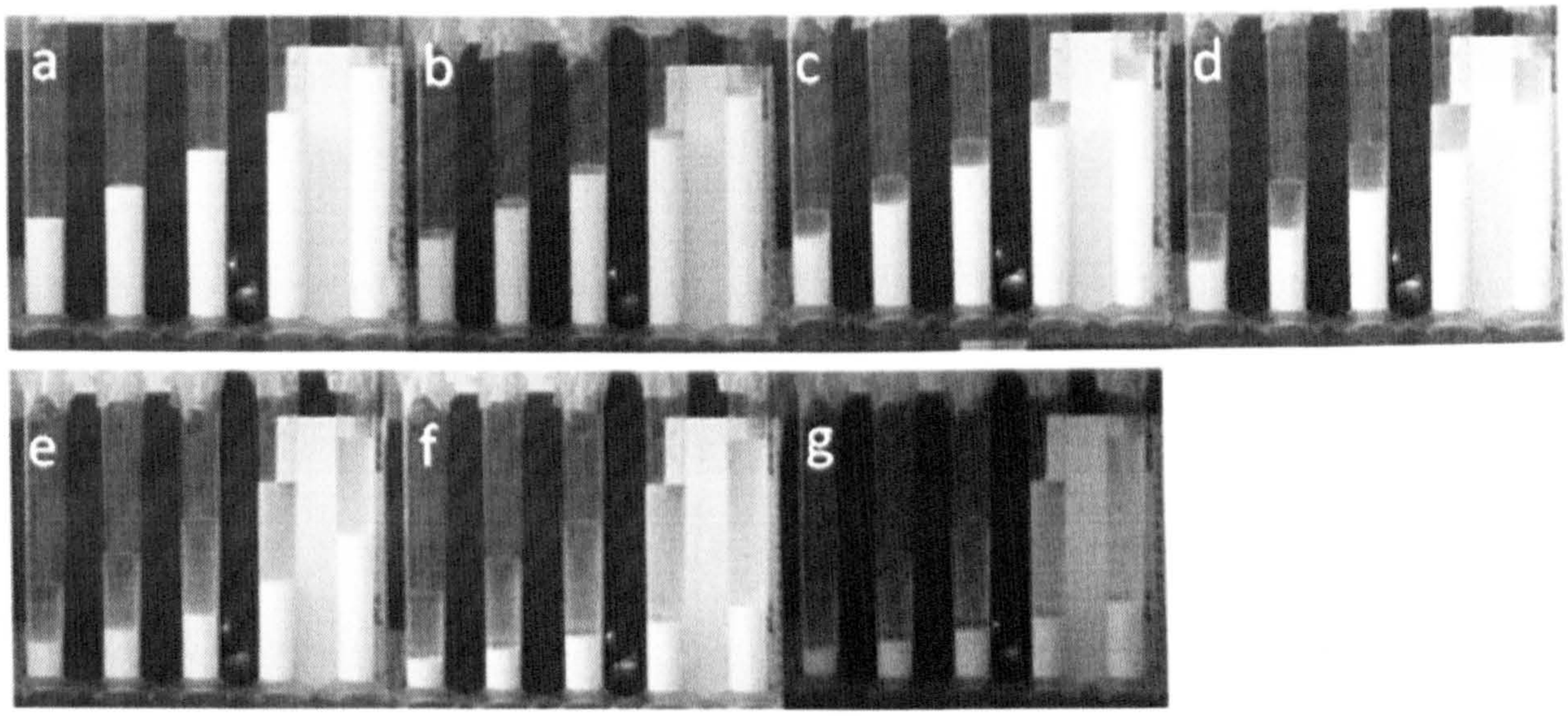

Figure 5.14 Settling column experiments to determine the suspension gel-point. 1M KNO_3 silica suspensions prepared to pH 6. Time intervals (hrs): a) 0 b) 0.1 c) 0.3 d) 0.6 e) 1.5 f) 4.5) g) 7

From the images collected there is a marked difference in the rate at which the solid front descends and the final sediment height when the electrolyte concentration is increased from 10^{-4}M to 1M. Figure 2.3 in chapter 2, shows a demarcation between slow and accelerated settling, related to the critical coagulation concentration (c.c.c.) of the suspension. Below the c.c.c. particles fall as single spheres with the rate controlled by the solids concentration. Above the c.c.c. the formation of aggregates enhances the rate of suspension clearing due to: i) increased particle size (Stokes' equation dependent on the length squared) and ii) slip-streaming effects (larger aggregates drag smaller particles in flow field).

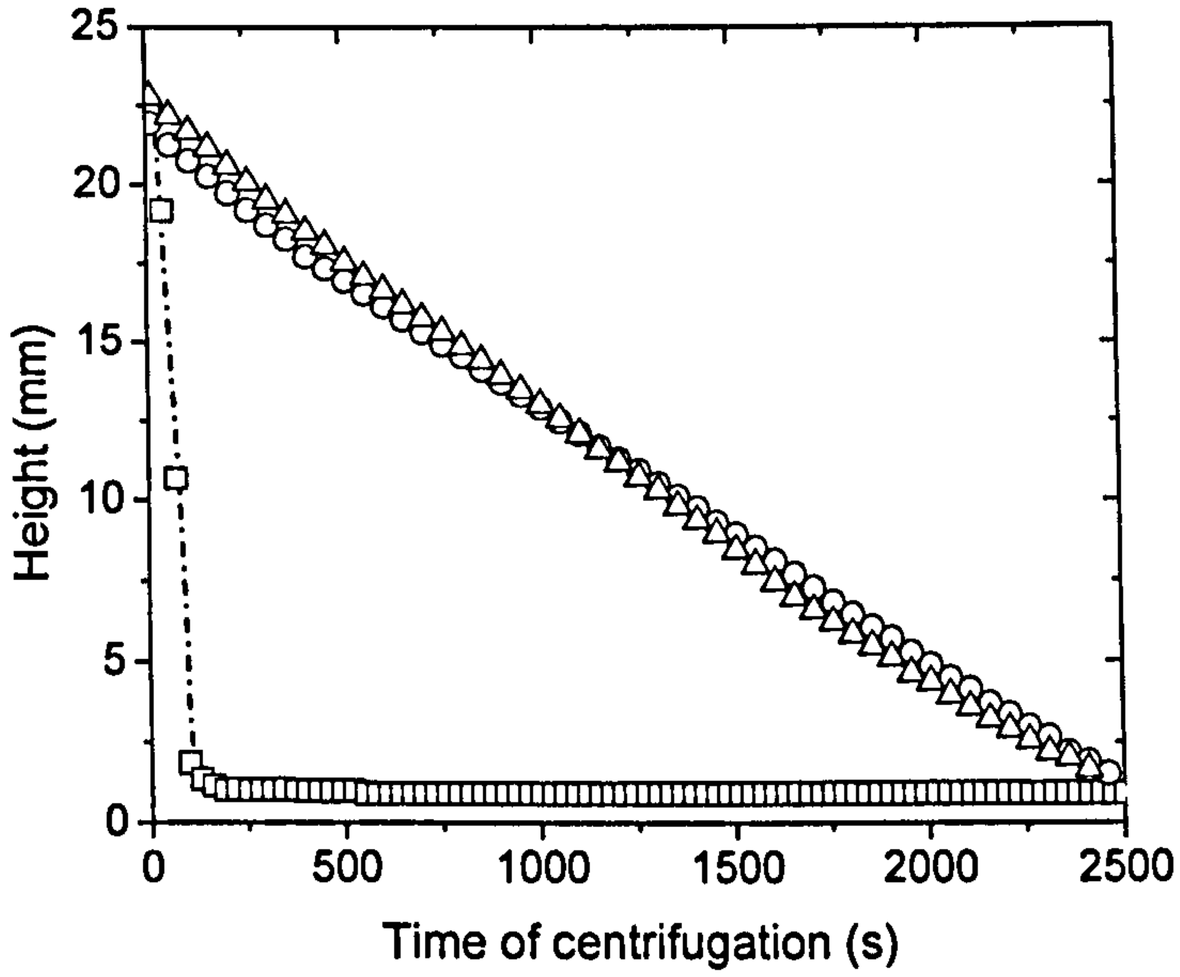

Figure 5.15 Suspension settling profiles determined from centrifugal sedimentation (LUMiFuge®). Symbols: square – 1M KNO_3, circle – 10^{-4}M KNO_3 and triangle 10^{-4}M KCl. Profiles at 11 xg.

Table 5.2 summarises the initial descending rates of the solid-liquid interfaces determined from a linear fit of the profiles which are presented in figure 5.15. The settling profiles are determined from monitoring the light transmission through a sediment cell which is experiencing an increased gravitational force (refer to section 4.5.2 – LUMiFuge®). Figure 5.16 shows the raw data light transmission profiles collected for a 1M KNO_3 silica suspension and a 10^{-4}M KNO_3 silica suspension. There is a clear difference in the settling behaviour of the two suspensions. For a monodispersed particulate suspension the solid-liquid interface height falls at a constant rate (equally spaced profiles). This type of settling behaviour is observed for the Fuso particles dispersed in a 10^{-4}M electrolyte. When the particles are dispersed in a 1M KNO_3 electrolyte, the raw data profiles are visually very different (see figure 5.16a). Instead of having equally spaced settling profiles, the spacing between the light transmission profiles reduces over equivalent time intervals. Initially, there is a clear separation between the transmission profiles but this reduces over time with all profiles collapsing onto one another. Such a trend indicates that all the particles have fallen out of suspension and are within the sediment bed which has formed at the base of the measurement cell. A second difference between the two suspensions is related to the shape of the transmission profiles. In the 1M KNO_3 suspension, it is no longer the case that

the light transmission value decreases sharply over a narrow distance. There is a more gradual reduction in the transmission value at different radial positions. This type of profile is more representative of a polydispersed particle suspension, where different particle settling rates result in zonal sedimentation.

The settling profiles (figure 5.1.5) show that in a low concentration electrolyte solution, the settling rates are independent of the electrolyte type, which is to be expected when one considers the strength of the electrical double layer force acting between the particles (see figure 5.19). As the electrolyte concentration increases, a decrease in the electrical double layer force lowers the energy barrier for interaction, thus enabling aggregates to form. Such behaviour results in a significant enhancement in the sedimentation rate of the suspension, an increase from 2mm/hr to nearly 50mm/hr.

Table 5.2 Suspension sedimentation rates determined using the LUMiFuge®. Primary particle size 0.8 µm.

Electrolyte	Particle / Aggregate d_{50} size (µm)	Settling rate (mm/hr)
1M KNO_3	4.6	47.8
10^{-4}M KNO_3	0.8	1.9
10^{-4}M KCl	0.8	2.0

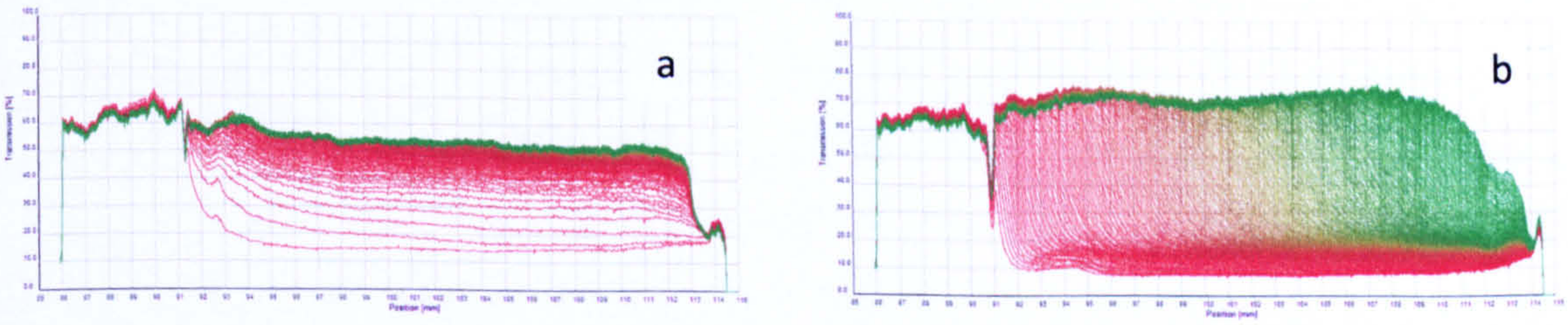

Figure 5.16 Sedimentation profiles collected using LUMiFuge® technique. Axes – Cell position versus % Transmission. Cell base at 114mm, cell top at 92mm. Colour change from red to green with time. a) 1M KNO_3, b) 10^{-4}M KNO_3. Data collected at 300rpm, equivalent to 11*xg*. Solids concentration 0.5% by volume at pH 6.

As will be discussed later in chapter 7, aggregates which are formed due to the "fruitful" collisions between primary particles are shear sensitive. This shear can be generated either from fluid flow, such as in pipe flow or during sedimentation when the aggregates settle relative to the stationary fluid. In a settling column, aggregates will grow to a maximum

size before the aggregate mass exceeds the buoyancy force and the aggregate begins to settle. Depending upon the level of shear during sedimentation, the size of the aggregate can reduce in size during settling. With the Fuso aggregates experiencing enhanced sedimentation at 11xg in the LUMiFuge® the settling rates were compared to settling rates measured at 1xg (collected from settling columns), to provide confidence in the LUMiFuge® data.

The solid-liquid interface as a function of time for a 1M KNO_3 suspension and 10^{-4}M KNO_3 and KCl suspensions are shown in figure 5.17. The settling rates determined from the linear portion of the profiles are given in table 5.3. Comparing the visually determined settling rates to those measured using the LUMiFuge® there is little difference, thus confirming that the aggregates formed in the 1M KNO_3 suspension do not break-up during the centrifuge measurement.

Table 5.3 Visually determined suspension sedimentation rates. Primary particle size 0.8 µm.

Electrolyte	Particle / Aggregate d_{50} size (µm)	Settling rate (mm/hr)
1M KNO_3	4.6	46.6
10^{-4}M KNO_3	0.8	1.87
10^{-4}M KCl	0.8	1.86

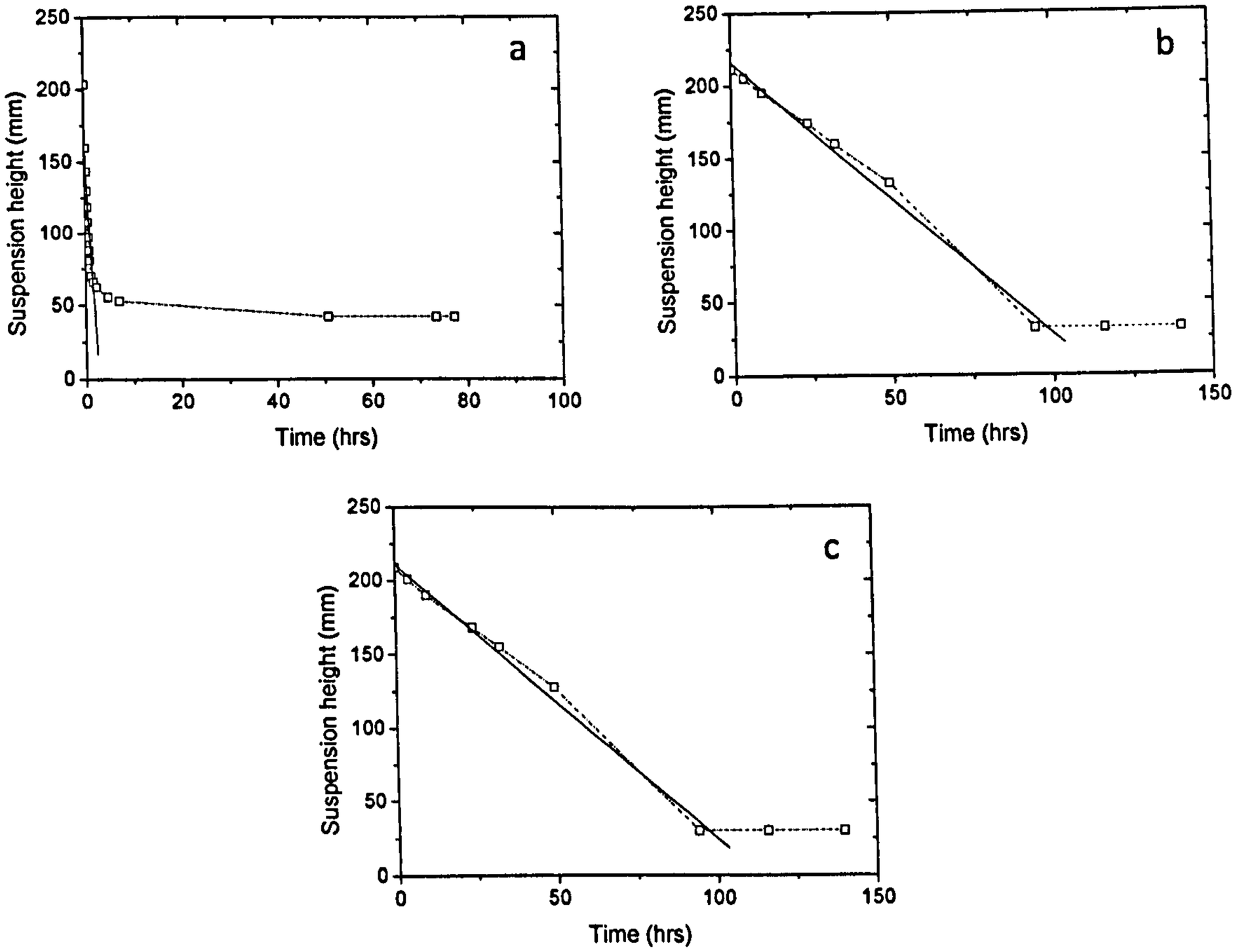

Figure 5.17 Visually determined settling profiles a) 1M KNO_3 suspension b) 10^{-4}M KNO_3 suspension and c) 10^{-4}M KCl suspension.

The settling profiles shown in figure 5.17 also provide information on the consolidation behaviour of the sediment. For the two dispersed suspensions, 10^{-4}M KNO_3 (5.17b) and 10^{-4}M KCl (5.17c) there appears to be no consolidation of the bed. This is expected due to the efficient packing of particles when the repulsive force is significant. Because the particles do not "stick" on contact, they are able to slide past one another forming compacted sediments. As the sediment bed depth increases, the bed loading cannot overcome the compressive yield strength of the sediment, hence no consolidation. In an aggregated suspension the attractive potential dominates the interaction, forming fractal, open porous structures. As the aggregates settle they form an open porous bed due to the porosity of the aggregates, and the inefficient packing. The open porous structure can then be consolidated when the bed load stress exceeds the compressive yield strength of the network. As is shown in figure 5.16a, a rapid decrease in the solid-liquid interface height is followed by a much slower reduction in the solid-liquid interface height. This region is

known as the region of sediment compaction (consolidation) and has a settling rate much lower than hindered settling. For the settling experiments considered here, the consolidation time for a dispersed suspension is negligible, while for an aggregated suspension the consolidation time is in excess of 40hrs. Clearly, as the suspension height or solids concentration varies, the consolidation time will also vary.

The packing structure of a sediment bed is determined by the number of particle-particle contacts and the strength of each contact. In order to determine the effect of the particle-particle contact energy on the sediment structure, the gel point is to be measured. Figure 5.18 and table 5.4 show that the gel point is very sensitive to the electrolyte concentration. At low electrolyte concentrations the primary particles are able to pack more efficiently forming a dense, tightly packed structure with a high solids volume fraction. At high electrolyte concentrations it is typical for aggregates which form under DLCA conditions (refer to section 2.4), to produce an open porous structure with no possibility of further rearrangement to form a more compacted sediment (at this point the reader should be reminded that the gel point is a measure of the bed structure in the absence of any consolidation – refer to chapter 4). As these aggregates settle they form a voluminous three-dimensional structure with a high void ratio, and therefore, a lower gelling point. At low electrolyte concentrations the suspension gel points are within 10% of each other and can be considered equal within experimental error. Although the two gel points in low electrolytes are within error, it should be recognised that the slight difference which is observed corresponds to the differences observed in the zeta potential and shear yield stress measurements. Therefore, the anion effect at low electrolyte concentrations is once again observed.

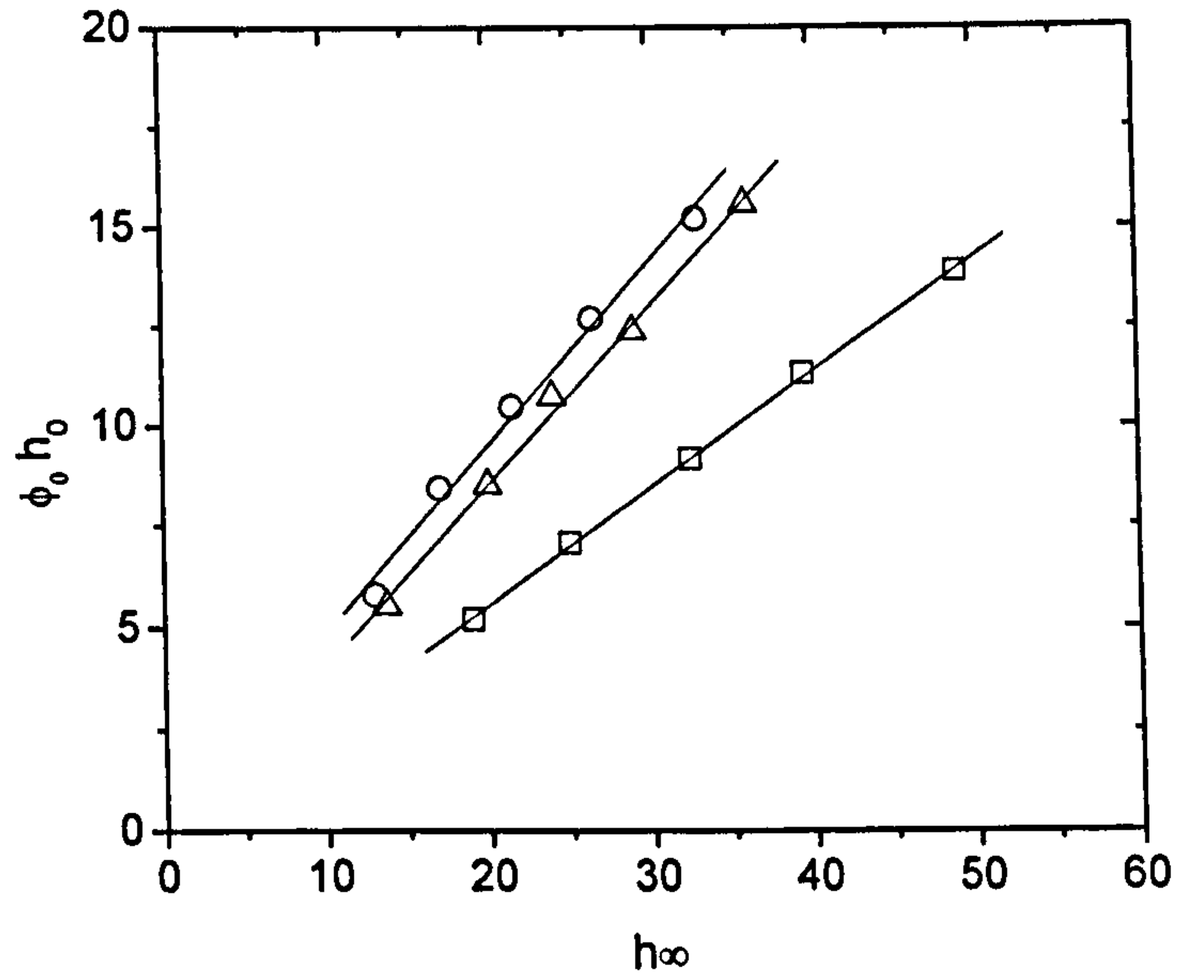

Figure 5.18 Gel point determination given by$\frac{\partial \phi_0 h_0}{\partial h_\infty}$. Symbols:, square – 1M KNO3 (0.29), circle – 10^{-4}M KNO_3 (0.47) and triangle – 10^{-4}M KCl (0.44). Suspension gel points given in brackets. Units of *h* (mm).

Table 5.4 Suspension Gel Points

Electrolyte	Particle / Aggregate d_{50} size (μm)	Gel Point (% solids vol.)
1M KNO_3	4.6	29
10^{-4}M KNO_3	0.8	47
10^{-4}M KCl	0.8	44

5.6 Normal and Lateral Force Interactions

Figure 5.19 shows typical AFM retraction force curve data between two silica surfaces, and figure 5.20b shows frictional forces measured as a function of the applied load. There is no significant difference between the retraction force curves at low electrolyte concentrations, with the interaction staying purely repulsive with no adhesion. At high electrolyte concentrations the long range repulsive force is screened and an adhesion force of 4.6nN is measured during retraction.

A minimum contact force of 29nN is required to bring the two surfaces into intimate contact. All lateral force experiments were completed at higher loadings with the sliding motion of the two partially hydrophobic silica surfaces representing stick-slip type behaviour, as shown in figure 5.20a. At high electrolyte concentrations the linear dependence of the friction force on the applied load obeys Amonton's law [54]. The drift from a linear dependency at low electrolyte concentrations is most likely due to low signal to noise, as the sensitivity limits of the set-up are approached in the low loading regime.

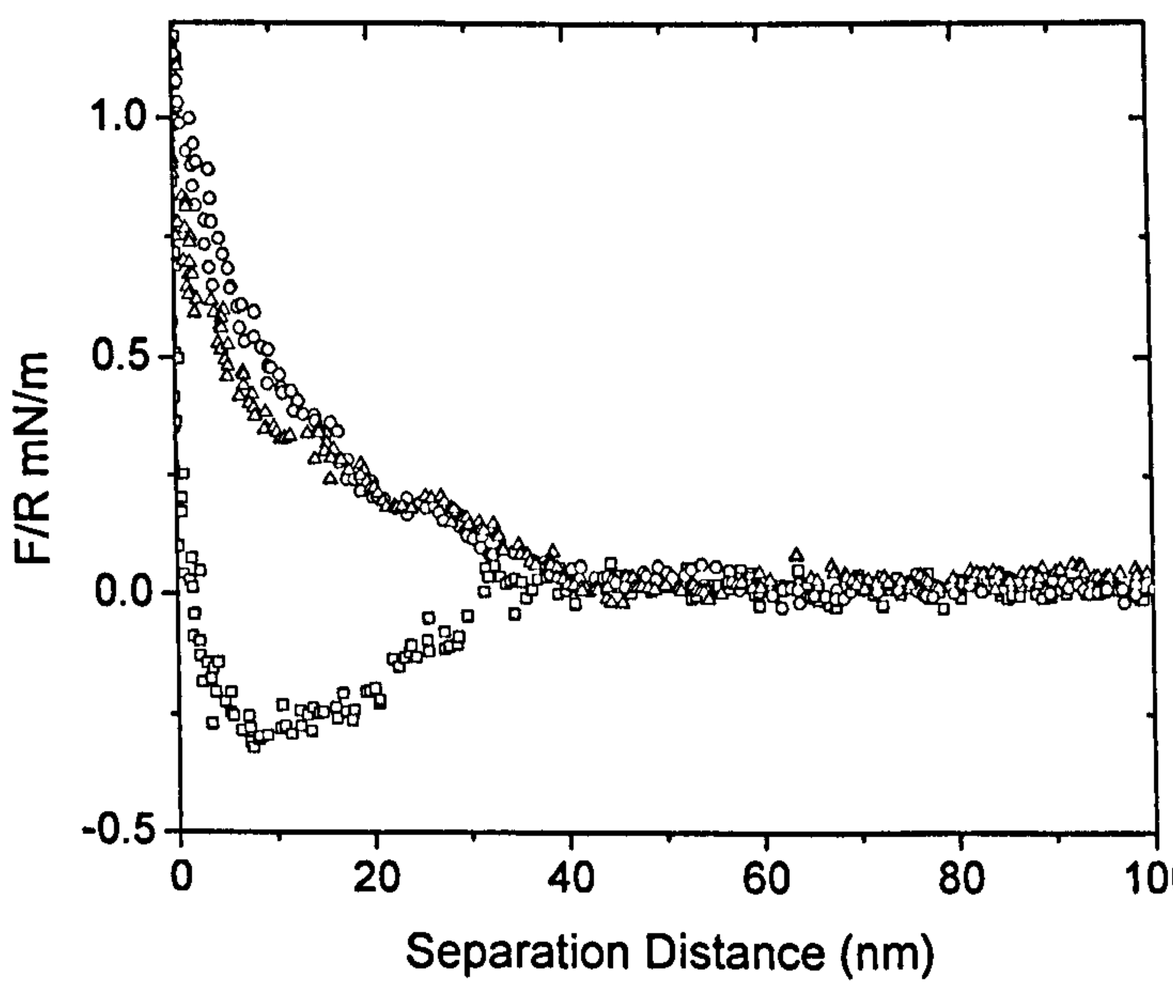

Figure 5.19 Typical retraction force curve data. Symbols: square 1M KNO_3 pH6, circle 10^{-4}M KNO_3 pH6 and triangle 10^{-4}M KCl pH6. Pull-off force in 1M KNO_3 electrolyte solution equal to 4.6nN.

It is not expected that the differences in the frictional forces measured at low electrolyte concentrations are a result of cross contamination or surface smoothing, since the experimental programme was carefully designed to remove any such issues. With limited data at low electrolyte concentrations obeying Amonton's law, it is however difficult to conclusively state that the difference in the frictional forces as a function of electrolyte type are real.

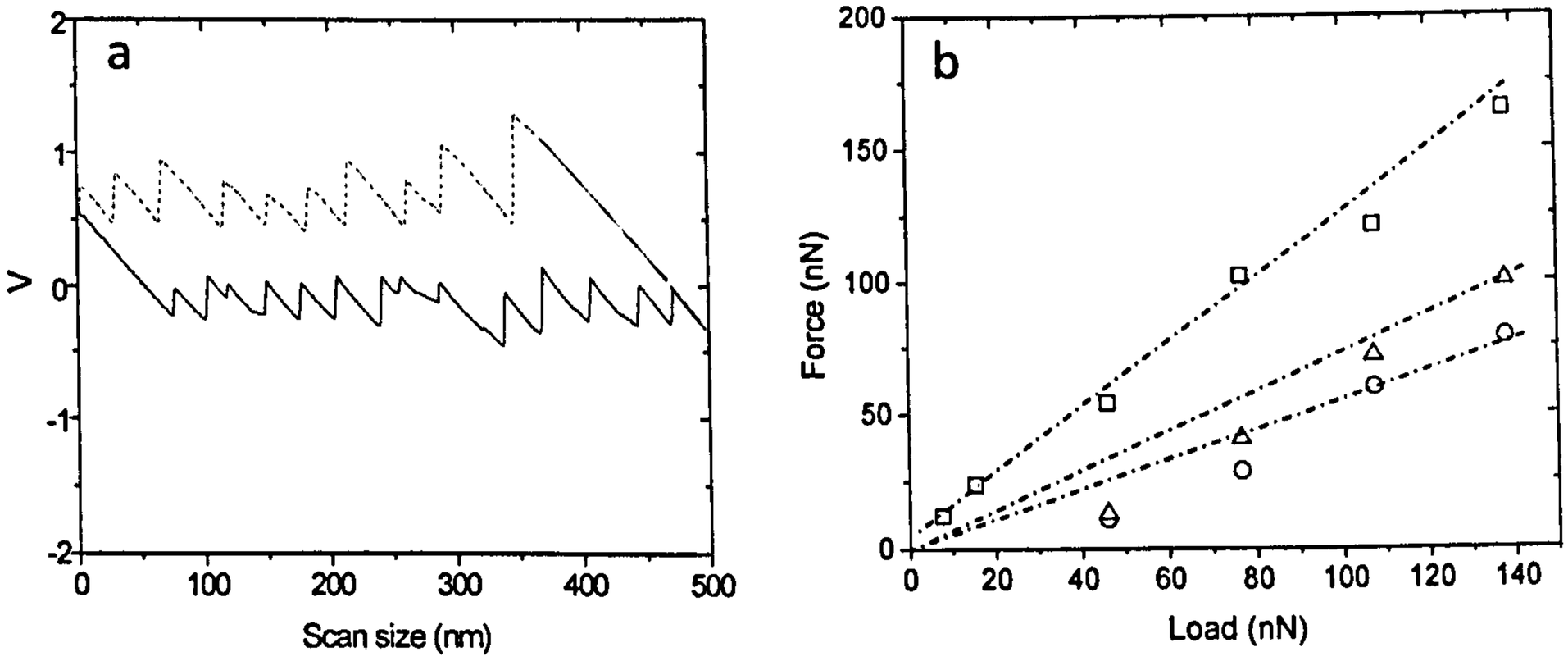

Figure 5.20 a) typical loop data of lateral force measurement exhibiting stick-slip behaviour. Data: 1M KNO_3, 500nm scan, 9V loading. Trace solid line, retrace broken line. b) the relation of the lateral force versus applied loading for a 29μm silica particle and a silica wafer. Pull-off force in 1M KNO_3 electrolyte solution equal to 4.9nN.Symbols: square – 1M KNO_3, circle – 10^{-4}M KNO_3, triangle – 10^{-4}M KCl.

The experimental data is compared with data published by Taran et al.[55]. Taran et al. investigated the lateral force interaction between two silica surfaces in 10^{-3}M NaCl at pH 5.6 and pH 10.6 (see figure 5.21a for published data). For both suspensions the authors observed a linear relationship with applied load. However, for the suspension at pH 10.6 a critical load is reached where the linear relationship no longer holds. The authors explain these observations in relation to the silica gel layer which can be present on the surface of the oxide. In the low loading region the gel layer effectively creates a lubrication layer, with water molecules freely moving between the two surfaces, thus the surfaces slide over one another with little interaction force. Above the critical load in the pH 10.6 suspension, the authors conclude that the loading force is sufficient to push the two gel layers into intimate contact which results in the "hairy" layers interacting, thus increasing the lateral force of interaction. This study was specifically chosen as it shows typical data on the lateral forces acting between silica surfaces when a gel layer or hydration layer is present. As discussed previously the manufacturing processes of the silica used in the current study (Fuso silica and the 29μm sphere used in the AFM study) have resulted in oxide surfaces which are partially hydrophobic and do not appear to be influenced by any of these "complicated" surface chemistries of silica which are so frequently discussed. Figure 5.21b

compares the data in the current study to the data of Taran et al.[55, 56]. For the same applied load it is clear that the silica-silica interaction in the current study produces a significantly greater lateral force interaction. Once again this data supports the belief that the surfaces are partially hydrophobic and not influenced by any hydration layer.

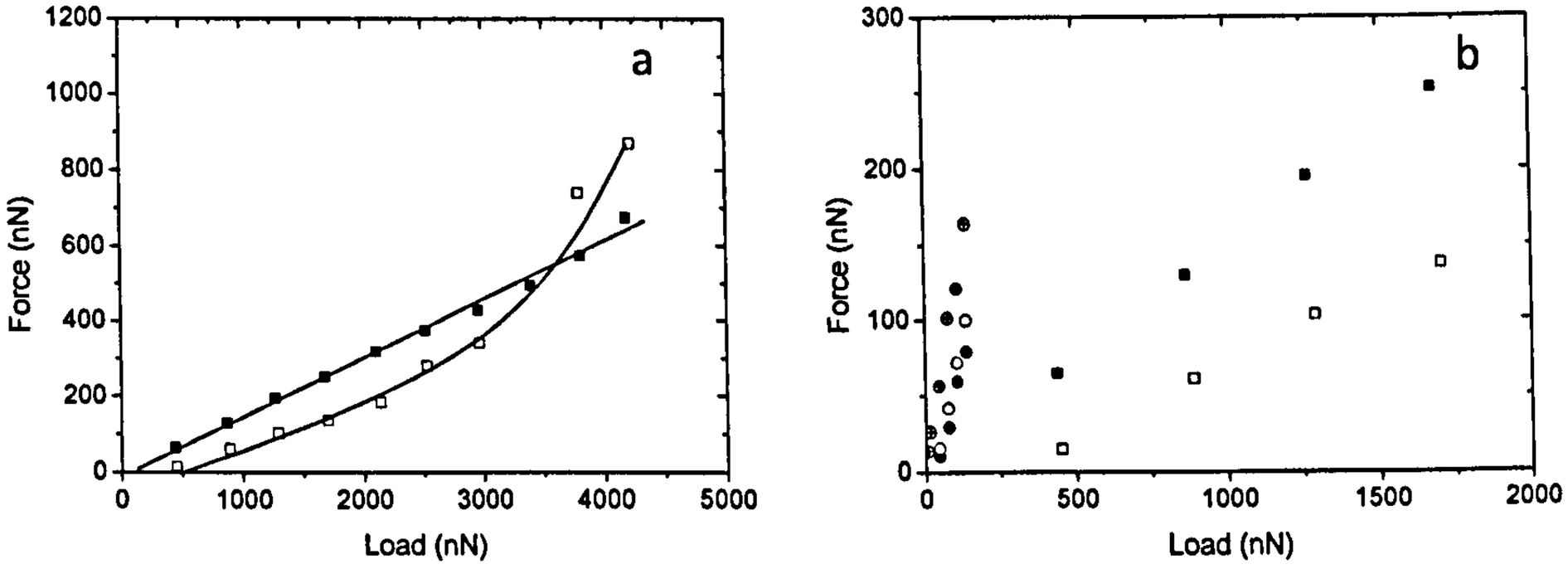

Figure 5.21 a) Lateral force as a function of the applied load at pH 5.6 (solid squares) and pH 10.6 (open squares) between a 20μm silica particle and a silica wafer. Figure taken from reference [56]. b) Comparison of experimental data in the current study with Taran et al. [56]. Symbols: crossed circle – 1M KNO_3 pH 6, open circle 10^{-4}M KCl pH6, solid circle 10^{-4}M KNO_3 pH, closed and open squares refer to symbols used in (a).

The AFM data collected in this study indicates that the primary particles dispersed in a 1M electrolyte will interact with each other (small adhesion force), while a purely repulsive interaction between two silica surfaces in the presence of a 10^{-4}M electrolyte prevents any adhesion, thus the particles in suspension remain dispersed. The data is supported by images of the particles dispersed in a low concentration and a high concentration electrolyte (refer to chapter 4 and 7). In chapter 7 when studying the turbulence properties of the colloidal suspensions, it is observed that the level of turbulence is influenced by aggregate break-up which is initiated at a critical Reynolds number. This critical Reynolds number relates to a fluid shear stress which is sufficient to overcome the interaction force between the primary particles in the aggregate. If the adhesion force is increased (eg. dispersed in di- or tri-valent salts) it would be expected that this critical shear stress will occur at a higher Reynolds number. The direct relationship between a single particle-particle interaction and the break-up of an aggregate is difficult to achieve and to the authors knowledge has not received any attention in the literature.

5.7 Conclusion

This chapter has provided detailed characterisation of the silica used in the current study. Characterisation of the silica and suspensions was necessary to identify chemical environments which would provide contrasting suspension properties when in the pipe loop. Clearly, the change in the electrolyte concentration from 10^{-4}M KNO_3 to 1M KNO_3 would provide such contrasting behaviours, and this has been observed in the shear yield stress, settling, gel point and force interaction studies. Of particular interest and novelty has been the results collected when the electrolyte concentration remains at 10^{-4}M, but the co-ion type is changed from NO_3^- to Cl^-. Changes in the zeta potential would not have been expected as the counter-ion which has a greater affinity of attraction for the silica surface remains constant K^+. As a result, one would expect the surface potential to be equivalent in both cases. However, a difference was observed at low pH's and this has been explained in terms of the ion-dissociation properties of the salt. KBr was briefly used in the study to provide support for this theory, as the ion dissociation constant for KNO_3 could not be located within the published literature. When considering all of the data, the anion effect is observed in the zeta potential, shear yield stress and gel point studies. However, in the sedimentation and force interaction studies the effect does not appear to be as great, considered within error. Such behaviour may be related to the solids concentration and the proximity of neighbouring particles. For example, the shear yield stress and the gel point results are influenced by particles sliding past one another to a more energetically stable position, thus altering the network structure and in doing so changing the yield strength of the sediment. If we use the 10^{-4}M and 1M situation (KNO_3) as an example, the shear yield stress and gel point are significantly lower in the higher electrolyte suspension. This is a result of inefficient packing due to particles not being able to slide past one another upon contact, unlike in the lower electrolyte suspension where the particles are free to slide past one another, a result of the strong electrical double layer force acting between the neighbouring surfaces. When considering the behaviour of the low electrolyte suspensions, this mobility (ie. the ability for one particle to slide past another) of particles upon contact may provide reasoning for the experimental trends. At pH 6 the zeta potential of the 10^{-4} M KNO_3 suspension = -70mV, while the zeta potential of the 10^{-4}M KCl suspension = -47mV. With a reduced surface potential it is feasible that the mobility is lower and therefore the packing efficiency of the bed is reduced. In a dilute system such as

a settling column or a single particle-particle interaction measured using an AFM, it is possible that this mobility effect is not observed as the solids concentration is too low. To the author's knowledge this type of behaviour has never been discussed in the literature. In order to fully validate this theory a more in depth experimental programme is required which may involve considering different oxide surfaces.

Chapter References

1. Bergna, H.E., *Colloid Chemistry of Silica: An Overview.* Colloidal Silica: Fundamentals and Applications, 2006. **Surfactant Science Series Volume 131**: p. 9-36.
2. Chuiko, A.A., V.V. Lobanov, and A.G. Grebenyuk, *Strucutre of Disperse Silica: Surface and Electrostatic Aspects of Adsorption.* Colloidal Silica: Fundamentals and Applications, 2006. **Surfactant Science Series Volume 131**: p. 331-360.
3. Zhuravlev, L.T., *Surface characterization of amorphous silica--a review of work from the former USSR.* Colloids and Surfaces A: Physicochemical and Engineering Aspects, 1993. **74**(1): p. 71-90.
4. Vigil, G., et al., *Interactions of Silica Surfaces.* Journal of Colloid and Interface Science, 1994. **165**(2): p. 367-385.
5. Derjaguin, B.V. and L. Landau, *Theory of the stability of strongly charged lyophobic sols and of the adhesion of strongly charged particles in solutions of electrolytes.* Acta Physicochim. URSS, 1941. **14**: p. 633-662.
6. Verwey, E.J.W. and J.T.G. Overbeek, *Theory of the stability of lyophobic colloids.* 1948, Amsterdam: Elsevier.
7. Healy, T.W., *Stability of Aqueous Silica Sols.* Colloidal Silica: Fundamentals and Applications, 2006. **Surfactant Science Series Volume 131**: p. 247-252.
8. Horn, R.G., D.T. Smith, and W. Haller, *Surface forces and viscosity of water measured between silica sheets.* Chemical Physics Letters, 1989. **162**(4-5): p. 404-408.
9. Depasse, J. and A. Watillon, *The stability of amorphous colloidal silica.* Journal of Colloid and Interface Science, 1970. **33**(3): p. 430-438.
10. Allen, L.H. and E. Matijevic, *Stability of colloidal silica , , : II. Ion exchange.* Journal of Colloid and Interface Science, 1970. **33**(3): p. 420-429.
11. Israelachvili, J.N., *Forces between surfaces in liquids.* Advances in Colloid and Interface Science, 1982. **16**(1): p. 31-47.
12. Colic, M., M.L. Fisher, and G.V. Franks, *Influence of ion size on short-range repulsive forces between silica surfaces.* Langmuir, 1998. **14**(21): p. 6107-6112.
13. Pashley, R.M., *Hydration forces between mica surfaces in electrolyte solutions.* Advances in Colloid and Interface Science, 1982. **16**(1): p. 57-62.

14. Oh, S.G. and D.O. Shah, *Effect of counterions on the interfacial tension and emulsion droplet size in the oil/water dodecyl sulfate system.* Journal of Physical Chemistry, 1993. **97**: p. 284-286.

15. Sahai, N., *Estimating adsorption enthalpies and affinity sequences of monovalent electrolyte ions on oxide surfaces in aqueous solution.* Geochimica et Cosmochimica Acta, 2000. **64**(21): p. 3629-3641.

16. Dumont, F., *Stability of Sols: Do the Silica Hydrosols Obey the DLVO Theory?* Colloidal Silica: Fundamentals and Applications, 2006. **Surfactant Science Series Volume 131**: p. 243-245.

17. Franks, G.V., *Zeta potentials and yield stresses of silica suspensions in concentrated monovalent electrolytes: Isoelectric point shift and additional attraction.* Journal of Colloid and Interface Science, 2002. **249**(1): p. 44-51.

18. Franks, G.V., et al., *Ion-Specific Strength of Attractive Particle Networks.* Langmuir, 1999. **15**(13): p. 4411-4420.

19. Dumont, F., J. Warlus, and A. Watillon, *Influence of the point of zero charge of titanium dioxide hydrosols on the ionic adsorption sequences.* Journal of Colloid and Interface Science, 1990. **138**(2): p. 543-554.

20. Milonjic, S.K., *A relation between the amounts of sorbed alkali cations and the stability of colloidal silica.* Colloids and Surfaces, 1992. **63**(1-2): p. 113-19.

21. Leong, Y.K. and D.V. Boger, *Surface chemistry effects on concentrated suspension rheology.* Journal of Colloid and Interface Science, 1990. **136**(1): p. 249-58.

22. Kosmulski, M. and J.B. Rosenholm, *Electroacoustic Study of Adsorption of Ions on Anatase and Zirconia from Very Concentrated Electrolytes.* Journal of Physical Chemistry, 1996. **100**(28): p. 11681-11687.

23. Kosmulski, M., *pH-dependent surface charging and points of zero charge: III. Update.* Journal of Colloid and Interface Science, 2006. **298**(2): p. 730-741.

24. Kosmulski, M. and J.B. Rosenholm, *High ionic strength electrokinetics.* Advances in Colloid and Interface Science, 2004. **112**(1-3): p. 93-107.

25. Kosmulski, M., *Confirmation of the Differentiating Effect of Small Cations in the Shift of the Isoelectric Point of Oxides at High Ionic Strengths.* Langmuir, 2002. **18**(3): p. 785-787.

26. Kosmulski, M. and J.B. Rosenholm, *The Specific Adsorption of Sodium Cations on Less Common Metal Oxides at High Ionic Strengths.* Journal of Colloid and Interface Science, 2002. **248**(1): p. 30-32.

27. Taghikhani, V., H. Modarress, and J.H. Vera, *Individual anionic activity coefficients in aqueous electrolyte solutions of LiCl and LiBr.* Fluid Phase Equilibria, 1999(166): p. 67-77.

28. Buscall, R., R. Ettelaie, and T.W. Healy, *Yield stress and contact forces in coagulated oxide dispersions Role of electrostatic interactions.* Journal of the Chemical Society, Faraday Transactions, 1997. **93**(22): p. 4009-4015.

29. de Kretser, R.G., P.J. Scales, and D.V. Boger, *Surface chemistry-rheology inter-relationships in clay suspensions.* Colloids and Surfaces, A: Physicochemical and Engineering Aspects, 1998. **137**(1-3): p. 307-318.

30. Franks, G.V., et al., *Effect of interparticle forces on shear thickening of oxide suspensions.* Journal of Rheology (New York), 2000. **44**(4): p. 759-779.

31. Gustafsson, J., E. Nordenswan, and J.B. Rosenholm, *Effect of pH on the sedimentation, z-potential, and rheology of anatase suspensions.* Colloids and Surfaces, A: Physicochemical and Engineering Aspects, 2003. **212**(2-3): p. 235-247.

32. Johnson, S.B., et al., *Surface chemistry-rheology relationships in concentrated mineral suspensions.* International Journal of Mineral Processing, 2000. **58**(1-4): p. 267-304.

33. Scales, P.J., et al., *Shear yield stress of partially flocculated colloidal suspensions.* AIChE Journal, 1998. **44**(3): p. 538-545.

34. Kosmulski, M., *Positive Electrokinetic Charge of Silica in the Presence of Chlorides.* Journal of Colloid and Interface Science, 1998. **208**: p. 543-545.

35. Krane, K., *Modern Physics.* Wiley, 1996.

36. Barnes, H.A., *The yield stress-a review or 'pialphanutaualpha rhoepsiloniota-everything flows?'* Journal of Non-Newtonian Fluid Mechanics, 1999. **81**(1-2): p. 133-178.

37. Hartnett, J.P. and R.Y.Z. Hu, *The yield stress - an engineering reality.* Journal of Rheology (New York, NY, United States), 1989. **33**(4): p. 671-9.

38. Nguyen Quoc, D. and D.V. Boger, *Yield stress measurement for concentrated suspensions.* Journal of Rheology (New York, NY, United States), 1983. **27**(4): p. 321-49.

39. Addai-Mensah, J. and J. Ralston, *Investigation of the role of interfacial chemistry on particle interactions, sedimentation and electroosmotic dewatering of model kaolinite dispersions.* Powder Technology, 2005. **160**(1): p. 35-39.

40. Johnson, S.B., A.S. Russell, and P.J. Scales, *Volume fraction effects in static shear rheology and electroacoustic studies of concentrated alumina and kaolin suspensions.* Colloids and Surfaces, A: Physicochemical and Engineering Aspects, 1998. **141**(1): p. 119-130.

41. Zhou, Z., et al., *The yield stress of concentrated flocculated suspensions of size distributed particles.* Journal of Rheology (New York), 1999. **43**(3): p. 651-671.

42. Franks, G.V., et al., *Effect of aggregate size on sediment bed rheological properties.* Physical Chemistry Chemical Physics, 2004. **6**(18): p. 4490-4498.

43. Franks, G.V., C.V. Sepulveda, and G.J. Jameson, *pH-sensitive flocculation: settling rates and sediment densities.* AIChE Journal, 2006. **52**(8): p. 2774-2782.

44. Glover, S.M., et al., *Bridging flocculation studied by light scattering and settling.* Chemical Engineering Journal (Lausanne), 2000. **80**(1-3): p. 3-12.

45. Martin, J.E., et al., *Fast aggregation of colloidal silica.* Physical Review A: Atomic, Molecular, and Optical Physics, 1990. **41**(8): p. 4379-91.

46. Bushell, G.C., et al., *On techniques for the measurement of the mass fractal dimension of aggregates.* Advances in Colloid and Interface Science, 2002. **95**(1): p. 1-50.

47. Elimelech, M., et al., *Particle Deposition & Aggregation - Measurement, Modelling and Simulation.* Colloid and Surface Science Engineering Series, 1995.

48. Tang, P. and J.A. Raper, *Modelling the settling behaviour of fractal aggregates - a review.* Powder Technology, 2002. **123**(2-3): p. 114-125.

49. Buscall, R. and L.R. White, *The consolidation of concentrated suspensions. Part 1. The theory of sedimentation.* Journal of the Chemical Society, Faraday Transactions 1: Physical Chemistry in Condensed Phases, 1987. **83**(3): p. 873-91.

50. McFarlane, A., K. Bremmell, and J. Addai-Mensah, *Improved dewatering behavior of clay minerals dispersions via interfacial chemistry and particle interactions optimization.* Journal of Colloid and Interface Science, 2006. **293**(1): p. 116-127.

51. Tudor, P.R., et al., *The effect of adsorbed and non-adsorbed additives on the stability of coal-water suspensions.* Fuel, 1996. **75**(4): p. 443-52.

52. Furuuchi, M., S. Mori, and K. Gotoh, *Sediment structure of fine silica spheres in an electrolyte solution.* Powder Technology, 1994. **80**(2): p. 159-63.

53. Buscall, R., *The sedimentation of concentrated colloidal suspensions.* Colloids and Surfaces, 1990. **43**(1): p. 33-53.

54. Cain, R.G., N.W. Page, and S. Biggs, *Microscopic and macroscopic effects of surface lubricant films in granular shear.* Physical Review E: Statistical Physics, Plasmas, Fluids, and Related Interdisciplinary Topics, 2000. **62**(6-B): p. 8369-8379.

55. Taran, E., et al., *Nonlinear friction characteristics between silica surfaces in high pH solution.* Journal of Colloid and Interface Science, 2007. **307**(2): p. 425-432.

56. Taran, E., et al., *pH dependence of friction forces between silica surfaces in solutions.* Journal of Colloid and Interface Science, 2006. **297**(1): p. 199-203.

Chapter 6

TRANSPORTATION PROPERTIES OF DISPERSED AND AGGREGATED COLLOIDAL SUSPENSIONS

NOMENCLATURE

a	Radius of particle
a^+	Dimensionless particle radius
C_D'	Dimensionless drag coefficient
C_L'	Dimensionless lift coefficient
C_r	Mean in-situ slurry concentration
C_{lim}	Solids concentration in incipient deposit
c	Solids concentration
D	Diameter of pipe
D'	Effective pipe diameter
d_p	Diameter of particle
d_{85}	Diameter of particle 85th percentile
E	Erosion rate per unit area
F	Lift force
F_{saff}	Saffman lift force
F_L	Flow parameter
F_D'	Longitudinal drag component
F_L'	Vertical lift component
F_L+	Dimensionless lift force
f_{12}	Friction factor at the surface of deposit
g	Gravitational acceleration
M	Erosion rate coefficient
s	Density ratio of solid to liquid
U_t	Terminal settling velocity
U_c	Undisturbed flow velocity at the centre of the particle
u^+	Dimensionless velocity
u'	Turbulent fluctuating velocity
$(u_w)_{V_c}$	Wall shear velocity calculated for the minimum transport velocity
V	Mean velocity

V_s Relative velocity between particle and fluid
V^* Friction velocity
V_1 Pseudo-homogeneous – homogeneous transition velocity
V_2 Heterogeneous – moving bed transition velocity
V_3 Moving bed – stationary deposit transition velocity
V_4 Stationary deposit – pipe plugging velocity
V_c Critical transport velocity
V_c^* Friction velocity calculated at the minimum transport velocity
ν Kinematic viscosity
γ Thickness of incipient deposit
y^+ Dimensionless distance from the wall

α' Eddy velocity dampening constant
ρ_l Density of fluid
ρ_p Density of particle
ρ_m Density of mixture
μ Dynamic viscosity
μ_m Dynamic viscosity of mixture
ε_s Coefficient of particle wall – friction
η Coefficient of rigidity
τ Applied shear stress
τ_y Yield stress
τ_b Bed shear stress exerted by fluid
τ_c Critical bed shear stress
κ Velocity gradient
Δh Change in bed height under shear

ABREVIATIONS

Re Reynolds number
PIV Particle imaging velocimetry
UDVP Ultrasonic Doppler velocity profiling
ERT Electrical resistance tomography
AFM Atomic force microscopy

Synopsis

The transportation properties of dispersed and aggregated colloidal suspensions are investigated. The chapter discusses the hydraulic transportation of fine particulates. Fine particle transport has received little attention in the literature, as it is generally considered that the suspension properties of Newtonian slurries can be determined from rheological measurements. Very few studies have investigated the minimum transport velocity of

fines, with only a few correlations developed experimentally and theoretically considering such particle sizes. This chapter investigates the minimum transport velocity of 0.8μm silica spheres dispersed in 10^{-4}M KNO_3 and 10^{-4}M KCl electrolytes, and silica aggregates dispersed in a 1M KNO_3 electrolyte. The minimum transport velocity is determined by extrapolating the sediment bed transition velocities (slurry velocity at the onset of bed erosion) to remove the effect of the sediment bed. To the authors knowledge this is a novel approach when determining the minimum transport velocity.

6.1 Hydraulic Transport

The hydraulic transport of solids by pipeline has received considerable attention throughout the last century. With suspensions and slurries ubiquitous within the process industry, the research has mainly been driven by industrial needs. The research papers of Blatch [1] and Durand et al. [2, 3] are commonly cited, with their work generally regarded as being the foremost studies in hydraulic transport research. Their research based on sand and coal water slurries examined the effect of solids loading and particle size on the slurry hydraulic gradient and the critical transport velocity. Both research topics have since received much attention with numerous empirical and theoretical models developed to predict the pressure drop and the onset velocity for particle deposition in horizontal pipe flow. In reviewing the literature it becomes apparent that a universal model to predict the pressure drop and the transport velocity is most improbable; all models showing some specificity to process and particle parameters. In the present study, we are only concerned with the minimum transport velocity of colloidal suspensions. A discussion on pressure drop correlations, which are important when determining the energy requirements of a pumping process, are considered beyond the scope of this work. Readers are referred to the following publications [4-6], and the publications by Wilson et al. [7, 8] who predicted the pressure drop for settling slurries using force balances, refer to two layer and modified two layer theory[8].

Classification of a slurry flow is generally divided into four flow regimes to describe the movement of solids in a pipe, with an additional fifth regime tenuously used to account for pipe plugging. The four commonly referred to flow patterns are pseudo-homogeneous flow, heterogeneous flow, moving bed flow and saltation flow. Pseudo-homogeneous and

heterogeneous flows are common when the buoyancy/lift forces significantly exceed the gravitational/sedimentation forces, thus enabling the solids to be distributed across the pipe cross-section. Unlike pseudo-homogeneous flow, heterogeneous flow, a term still used to describe fully suspended flows is characterised by a concentration gradient perpendicular to the pipe axis. As the flow velocity is reduced, the ratio between the balancing forces adjusts accordingly and a situation is observed where the solid particles begin to accumulate on the pipe invert. With the mechanical friction force between the pipe and the sediment bed exceeded, the sediment bed continues to slide along the pipe invert, with a concentration gradient varying from maximum packing in the lower layer, to a minimum in the heterogeneous suspension flow. With a further reduction in the flow rate, the critical energy required to keep the sediment bed in motion is deceeded and a stationary deposit is formed. At the surface of the stationary deposit, particles are observed to slide and hop past one another, with the flow described as saltating. In saltation flow the solids concentration above the bed is common to the heterogeneous flow regime, though the concentration profile is much steeper than in other flow regimes [9]. Between each flow regime there is an associated transition velocity. As the flow rate is reduced, the first transition velocity V_1, pseudo-homogeneous – heterogeneous, is commonly determined through visual inspection or comparison of two pressure drop curves. V_1 is the measured velocity at which the slurry and the hydraulic curves diverge. V_2 (heterogeneous – moving bed), V_3 (moving bed – stationary deposit) and V_4 (stationary deposit – plugging) are three transition velocities which lie in close proximity of each other, with the demarcation between each velocity by visual inspection is difficult to ascertain. However, V_3 and V_4 tend to be overlooked in the literature with the perceived belief that V_2 is the most significant transition velocity, describing the onset of undesirable operating conditions. V_2 is commonly interchanged with the term critical velocity V_c [10], which identifies the velocity between non-deposit and deposit flow. Researchers have also used the following terms, 'minimum transport velocity' [11, 12], 'deposit velocity' [13-15] and 'limit deposit velocity' [16] when describing V_2.

Table 6.0 summarises several models that are often used to predict the minimum transport velocity of dilute fine particulate suspensions. The number of correlations developed to calculate the minimum transport velocity of a suspension exceeds fifty[17], but only a small proportion are applicable for fine particulate transport. The most relevant correlations for the transportation of fine particles in pipes are shown in table 6.0.

Table 6.0 Minimum transport velocity correlations

	Flow equation	Comments	
Durand et al. [2, 3]	$F_L = \frac{V_c}{\sqrt{2gD\,(s-1)}}$	F_L - constant dependent on particle size and solids concentration. Particle diameter (d_p): 20μm < d_p < 100mm Pipe diameter (D): 40mm < D < 700mm	Eq.[6.0]
Spells [18]	$V_c = \left[0.0251 g d_{85} \left(\frac{D\rho_m}{\mu_m}\right)^{0.775} (s-1)\right]^{0.816}$	Particle diameter (d_p): 50μm < d_p < 500μm	Eq.[6.1]
Thomas [19]	$\frac{U_t}{(u_w)_{V_c}} = 0.0083\left(\frac{d_p\,(u_w)_{V_c}\,\rho_l}{\mu}\right)^{2.61}$	Particle diameter (d_p): 0.74μm < d_p < 66μm Particle density (ρ): 1.35g/cc < ρ < 18.9g/cc Pipe diameter (D): 25mm < D < 100mm Solids concentration (%vol): 0.01 – 0.17	Eq.[6.2]
Thomas [13]	$V_c^* = 1.1\left[\frac{g\mu(\rho_p-\rho_l)}{\rho_l{}^2}\right]^{1/3}$	$d_p \ll 0.3\,\delta$ Un-flocculated particles Applicable up to 20% by volume	Eq.[6.3]
Davies [20]	$V_c = 1.08(1+\alpha' c)^{1.09}(1-c)^{0.55n}\left[\frac{\mu}{\rho}\right]^{-0.09} d_p{}^{0.18}\left[\frac{2g\Delta\rho}{\rho}\right]^{0.54} D^{0.46}$	$n \approx 4$ when $1 < Re_p < 10$ $\alpha \approx 3.64$	Eq.[6.4]
Gillies [21]	$V_c^2 = 1.33\left[\frac{\gamma\varepsilon_s}{f_{12}}\right] g(s-1)\left[\frac{(C_{lim}-C_r)(1-C_{lim})}{(1-C_{lim}-C_r)}(1+C_r(s-1))\right]$		Eq.[6.5]

s, density ratio of solid to liquid

$(u_w)_{V_c}$, wall shear velocity calculated as for the minimum transport velocity

U_t, terminal settling velocity

V_c^*, friction velocity calculated as for the minimum transport velocity

δ, thickness of viscous sub-layer

α', eddy velocity dampening constant

γ, thickness of the incipient deposit

ε_s, coefficient of particle – wall friction

C_r, mean in-situ slurry concentration

C_{lim}, concentration in the incipient deposit

f_{f2}, friction factor at the surface of the deposit

Thomas [19] also provides a transport correlation for 'suspensions in compaction', where the solids concentration exceeds the suspension gel point (refer to chapter 4). The minimum transport velocity for suspensions in compaction is identified as the onset of a radial component of momentum transport, and is generally considered as the turbulence transition velocity. This critical velocity which is related to an effective Reynolds number (N_{Re}) which is defined by:

$$N_{Re} = \frac{DV_c\rho_l}{\eta\left(\frac{1+g\,D\,\tau_y}{6V_c\eta}\right)} \qquad [6.6]$$

where η is the coefficient of rigidity, τ_y the yield stress, D the pipe diameter, V_c is the critical transport velocity and N_{Re} is calculated following the procedure outlined by Thomas [19, 22] which involves the Hedstrom number and the Fanning friction factor. A comparison between theoretical and empirical minimum transport velocities for flocculated thorium oxide and kaolin suspensions showed that the calculated Reynolds number consistently under predicts the minimum transport velocity by 10% to 60%. The author attempts to explain such differences in terms of turbulent/laminar slugs in the transitional flow regime (intermittent turbulence). Equation 6.2 is the corresponding model proposed by Thomas to calculate the minimum transport velocity of dilute suspensions (not sediments in compaction) in the hindered settling region. The correlation by Thomas includes a solids settling velocity: friction velocity ratio, where the friction velocity accounts for turbulent fluctuations in the flow acting to maintain the particles in suspension. Through dimensional analysis, Thomas[19] showed this ratio to be equal to a modified Reynolds number where the coefficient and exponent are experimentally determined.

Durand's correlation [3] is frequently used within the hydrotransport community. Although it only provides a very simple interpretation of the suspension properties, it has been proven to be reasonably accurate when determining the minimum transport velocity for a wide range of solid-liquid systems. The correlation is based on the minimum transport velocity of sand and coal slurries in pipes ranging from 40mm to 700mm in diameter, transporting particles in the size range of 20μm to 100mm, up to a solids concentration of 15% by

volume. Durand's approach for calculating the minimum transport velocity relies on graphically determining a flow constant F_L, which is a function of the particle size and solids concentration (see figure 6.0) , a schematic representation of the F_L versus d_p plot adapted from the original publication [3]). Refer to equation 6.0 for the Durand correlation.

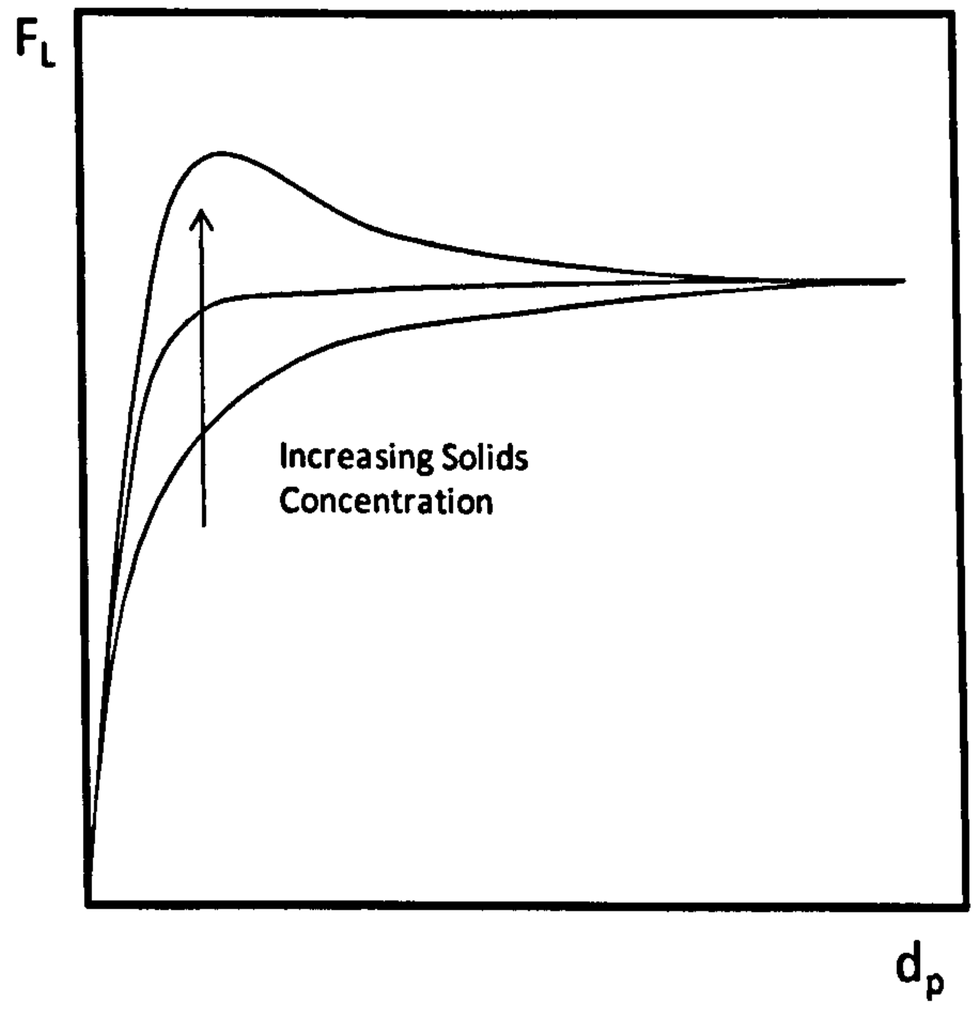

Figure 6.0 Variation of parameter F_L with particle size. Figure redrawn from reference [23].

The theoretical model proposed by Thomas [13] adapted the sliding bed model of Wilson [7, 24], with Thomas accounting for uncertainties in the theoretical predictions when the thickness of the viscous sub-layer exceeds the particle diameter (fine particle transport). Wilson's model does not account for deposition in the viscous sub-layer leading to a lack of agreement between experimental and theoretical data as the particle size is reduced. Particles that reside in the sub-layer are influenced by turbulent eddies and viscous forces which act to keep the particles in motion. Simple substitution to account for the thickness of the viscous sub-layer results in a theoretical expression where $V_c^* = 0.93\left[\frac{g\mu(\rho_p-\rho_l)}{\rho^2_l}\right]^{1/3}$. However, from experimental comparison, relating the theoretical expression to the minimum transport velocity of 17μm and 26μm sand particles, Thomas adjusted the coefficient to 1.1 which led to a better fit (± 10%) with the experimental data up to a solids concentration of 20% by volume (see equation 6.3 for published correlation).

Davies [20] developed a theoretical expression (equation 6.4) based on turbulence theory. He related the sedimentation force $(\left(\frac{\pi}{6}\right) d_p^3 \Delta\rho g(1-c)^n)$ to the eddy fluctuation force $(\rho_L(u')^2(\frac{\pi d_p^2}{4}))$. For the limiting case where all particles are just lifted from the pipe bottom by turbulent eddies, the two opposing forces are balanced. The turbulent fluctuating velocity (u') which is related to the cubed root of the power dissipation per unit mass of fluid [25] and the eddy size, is then used to determine the mean flow velocity of a particle down to $Re_p = 1$.

There is a clear lack of agreement when predicting the minimum transport velocity (see figure 1.0 – Introduction). Such disagreement has been identified and discussed by many authors [15, 26, 27] with criticism aimed at the lack of systematic studies completed, and inconsistencies when defining the boundaries of applicability. Direct and indirect measurement techniques, and techniques of varying sensitivity can provide a source of disagreement (Direct visual observation, observation of the flow regime in transparent tubes is the more commonly used technique to determine the minimum transport velocity). A typical approach to determine the minimum transport velocity through direct visualisation is to start with a high flow velocity so that all solids in the pipeline are suspended. The mean velocity is then reduced until the first sediment is observed to slide along the pipe invert. The velocity is then increased slightly to re-suspend the solids and lowered again to a velocity slightly higher than the sliding bed velocity. The procedure is continually repeated until the system operates for a period of time with no sliding bed, with the suspension transported under saltation flow conditions [19]. Obviously, the outcome is significantly influenced by the judgement of the operator and the thoroughness to which an experimental procedure as described is upheld. Indirect measurement techniques in-part removes the judgement of the operator. The minimum in the pressure drop versus velocity curve is an indirect technique that is sometimes incorrectly applied to determine the minimum transport velocity. In most cases the minimum pressure drop is associated with a velocity that is slightly higher than the minimum transport velocity [28]. However, in their review on the effect of solids concentration and particle size on the minimum transport velocity, Parzonka et al. [14] only considered data obtained by direct visual observation. The author stated that the indirect approach of measuring the slurry pressure drop is too unreliable, referring to data sets that either exhibit a flat minimum, significant scatter

around the minimum due to flow instabilities, or in some cases no minimum when the minimum transport velocity for sand and coal slurries has been deceeded. More recently the introduction of deposition probes, gamma ray gauges and magnetic resonance imaging [29] techniques are helping to reduce these uncertainties associated with indirect measurement of the minimum transport velocity.

With limited agreement between correlations when predicting the minimum transport velocity, there is a need not only to improve upon the measurement protocol, but to also improve upon controlling the slurry properties. The present study aims to highlight the desired control which should be achieved when studying slurry systems. In order to improve upon this continual lack of agreement between data sets, improvements in the experimental approach are required. For example, a considerable number of the minimum transport velocity correlations include a particle size parameter. However, there is generally no accountability in the correlation for the poly-dispersity of the solid. The degree of poly-dispersity can have a significant effect upon the suspension viscosity, the suspension settling rate and therefore, the slurry transportation properties. In this study model particulate slurries where the physical and chemical, and process parameters are sensitively controlled are investigated. The data sets generated should therefore form a small but significant contribution to future hydraulic transport research.

6.2 Influence of solution chemistry on the transportation behaviour of solid-liquid systems.

In reviewing the literature it becomes clear that the hydrotransport community has shown little interest in controlling the chemical properties of the continuous phase to manipulate the flow properties of the dispersed phase. However, with many industries pumping extremely fine material, the hydrotransport community is starting show to awareness for this type of research. The originality of the current study will address some of the requirements for this relatively new area of research.

Although there has been limited research in modifying the solution chemistry to influence the pipe flow properties of slurries, this field of research within the hydrotransport community does date back to the 1970's. Researchers that have been reasonably active in this field are Horsley and co-workers. Horsley and Reizes [30] published a paper titled "Variation in head loss gradient in laminar slurry pipe flow due to changes in zeta

potential". Pumping silica with a mean particle diameter of 17μm, Horsley and Reizes were able to achieve some degree of control on the particle-particle interaction. By adjusting the pH of the sand slurry between pH 6 and pH 11, the author observed a measurable change in the head loss gradient. Above a certain solids concentration (> 30% by volume), the author was able to modify the slurry hydraulic gradient curve to approach the hydraulic gradient line of a sediment free flow by increasing the suspension pH. The author's recognised that the change in the hydraulic curve with pH is associated to a decrease in the silica zeta potential, and therefore a reduction the degree of flocculation. Plotting the head loss gradient as a function of the zeta potential, a decrease in the zeta potential resulted in a gradual reduction in the head loss gradient for velocities between $0.3ms^{-1}$ and $1ms^{-1}$. When in the turbulent flow regime the hydraulic curves collapse onto one another as the particle-particle interactions are overcome by the fluid shear. This study highlights the lack of control achieved on the physical and chemical properties when studying fine particulate slurries in pipelines. The author's chose to use a silica suspension which had a wide polydispersity, containing particles in excess of 100μm (non colloidal). The sand is then dispersed in tap water (varying conductivity and dirt) with no background electrolyte (ionic concentration varies with pH adjustment). As a result there are many important variables which are not controlled which will influence the strength and number of particle-particle interactions in the suspension.

Additional pipe loop studies by Horsley include work on gold slime tailings [31] where the flow properties are influenced by the addition of additives. Additives such as sodium phosphate, sodium hexametaphosphate, sodium oyrophosphate and sodium tripolyphosphate are observed to reduce the suspension viscosity and therefore the hydraulic pumping gradient.

Additives (slurry thinners) have also been studied by MacInnes [32] who investigated their effects on the slurry rheology of a chalk suspension transported down a 92km pipeline from Kensworth Quarry to the Rugby cement plant in the United Kingdom. Current approaches to treating the suspension prior to pumping have frequently resulted in pipeline blocking. Several additives were investigated to obtain the desired behaviour of lowering the suspension viscosity for pumping, while retaining a low enough yield stress to keep the

particles in suspension. Sodium lignosulphonate was chosen to replace the existing dosing additive.

So far the discussion has considered the use of additives as a rheological modifier to reduce the energy requirements of pumping. An insightful paper by Heywood and Alderman [33] considered the use of mechanical agitation to modify the rheological properties of the slurry prior to pumping. Thick pastes tend to exhibit non-Newtonian flow behaviour. That is, slurries can either shear thin (a gradual decrease in the apparent viscosity with increasing shear rate) or shear thicken (a gradual increase in the apparent viscosity with increasing shear rate). Many mineral and oxide suspensions exhibit shear thinning behaviour. By agitating the slurry in a mixing vessel prior to pumping, it is possible to break-up the particulate network, thus reducing the apparent viscosity and therefore the energy requirement for pumping. The paper only provides a review of this topic but does not provide "real" examples where such a technique has been proven.

During pipeline shutdown the interaction potential between fine particles can influence the start-up and operating performance of a pipeline. Plewa et al. [34] investigating fly ash suspensions (69% below 0.06mm) showed that the consolidation time of a sediment bed can significantly influence the pressure gradient upon start-up and the time taken to reach steady state flow velocities. Clearly, the time to reach steady state conditions is a function of the interparticle interaction and the degree of sediment bed consolidation. The results presented in the paper are very confusing and rather limited. The introduction of cement to the fly ash can have varying effects upon the time to reach steady state conditions. The author however does not interpret the data very well thus a conclusive interpretation of the influence of cement on the fly ash sediment cannot be drawn.

When transporting fine particulate suspensions, consideration should not only be given to the particle-particle interaction (agglomeration) but also to the particle-wall interaction. Depending upon the chemical nature of the fluid, the surface charge of the particle and the wall may be different leading to an attraction potential, and thus, a build-up of particles on the pipe surface at a flow rate which exceeds the minimum transport velocity. Williamson et al. [35] studying the deposition of haematite particles (0.2μm) in the vertical section of a stainless steel pipe loop showed that the initial deposition rate of haematite particles at a constant flow velocity (Re = 11000) is a function of the suspension pH. At low pH's (pH

3.7 – pH 5.3) there is no deposition of particles onto the stainless steel surface. At intermediate suspension pH's (pH 5.5 – pH 7.0) the initial deposition rate of the haematite particles passes through a maximum before decreasing once again as the suspension pH is adjusted to more basic conditions. The particle deposition rate was determined using a Gamma ray counting technique which is described in detail by the author in his PhD thesis [36].

Vasak et al. [37] investigated the deposition rate of silica spheres onto the surface of a rectangular channel under laminar (*Re* = 960) and turbulent (*Re* = 16040) flow conditions. The glass surface (channel deposition surface) was positively charged after coating with a cationic polymer (2 – vinylpyridine/styrene). Silica spheres (0.88μm) were dispersed in NaCl and pH adjusted using NaOH to produce one silica sample with a zeta potential of -75mV and a second silica sample with a zeta potential of -46mV. By measuring the initial particle deposition rate on the channel surface (deposition rate determined by counting the number of particles in a 78μm by 101μm field of view collected using a microscope), the author showed that transition from laminar to turbulent flow conditions caused a reduction in the initial deposition rate. When comparing the deposition data for the two silica suspensions, the data suggests that the under laminar flow conditions, the deposition of particles onto the glass surface is independent of the potential difference between the silica and glass slide. However, when the flow velocity is increased in to the turbulent flow regime, the difference in surface potentials influences the level of particle deposition. For the same flow Reynolds number, the more negative silica (-75mV) has a greater affinity of attraction for the positively charged glass surface and as a result more particles are deposited. The data below (figure 6.1) shows that 0.88μm silica spheres are still depositing onto the glass surface when the flow Reynolds number exceeds *Re* = 12000.

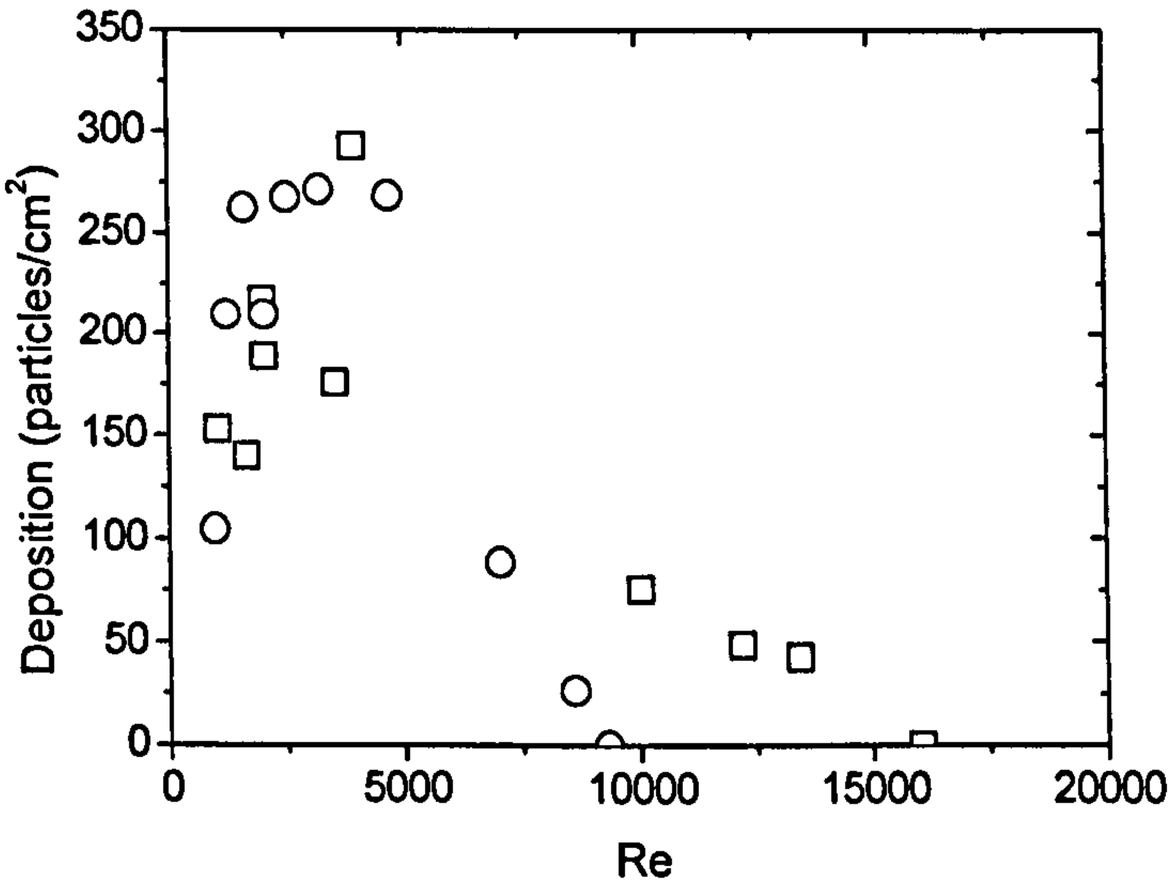

Figure 6.1 Particle deposition rates as a function of the channel Reynolds number. Figure redrawn from reference [37]. Symbols square (-75mV), circle (-46mV).

Another field of research which has received some attention in the literature is the transition point from a laminar to turbulent flow regime for a slurry containing fine particles. Investigating the flow properties of kaolin suspensions, El-Nahhas et al. [38] showed that the laminar/turbulent transition velocity can be significantly increased from 0.9ms^{-1} to greater than 8ms^{-1} when the slurry solids volume concentration is increased from 8.9% by volume to 22.6% by volume. Such a significant increase results from particles structuring within in the suspension. To the author's knowledge there is no published research which has shown how this transition velocity can be "shifted" by sensitively controlling the particle-particle interaction potential.

Further research which is indirectly related to the transportation of fine particulate suspensions, is the study of sediment bed erosion rates. With an increase in the flow velocity a sediment bed can undergo gradual surface erosion where the rate of erosion is typically expressed as[39]:

$$E = M\left(\frac{\tau_b}{\tau_c} - 1\right) \qquad [6.7]$$

where E denotes the erosion rate per unit area, τ_b the bed shear stress exerted by the fluid, and M and τ_c which are dependent upon the physiochemical parameters of the sediment, define the erosion rate coefficient and the critical shear stress of erosion respectively.

Ravisangar et al. [39] looked at the effect of suspension pH on the erosion rate of kaolin sediments. Preparing kaolin suspensions ($d_{50} \approx 2\mu m$) in tap water, the pH was adjusted between pH 3 and pH 9 using H_2SO_4 and NaOH. An increase in the suspension pH resulted in a decrease of the kaolin zeta potential, which corresponded to a reduction in the water content of the sediment bed. Kaolin is an interesting colloid as the behaviour of the suspension is complicated by the heterogeneously charged edges and faces on each particle [40]. In the study of Ravisangar et al.[39] a dramatic reduction in the sediment bed water content was observed at pH 6 when the zeta potential decreased below -30mV, and the edge-face associations that are dominant in low pH conditions, are replaced by predominantly face-face associations resulting in a more densely packed sediment.

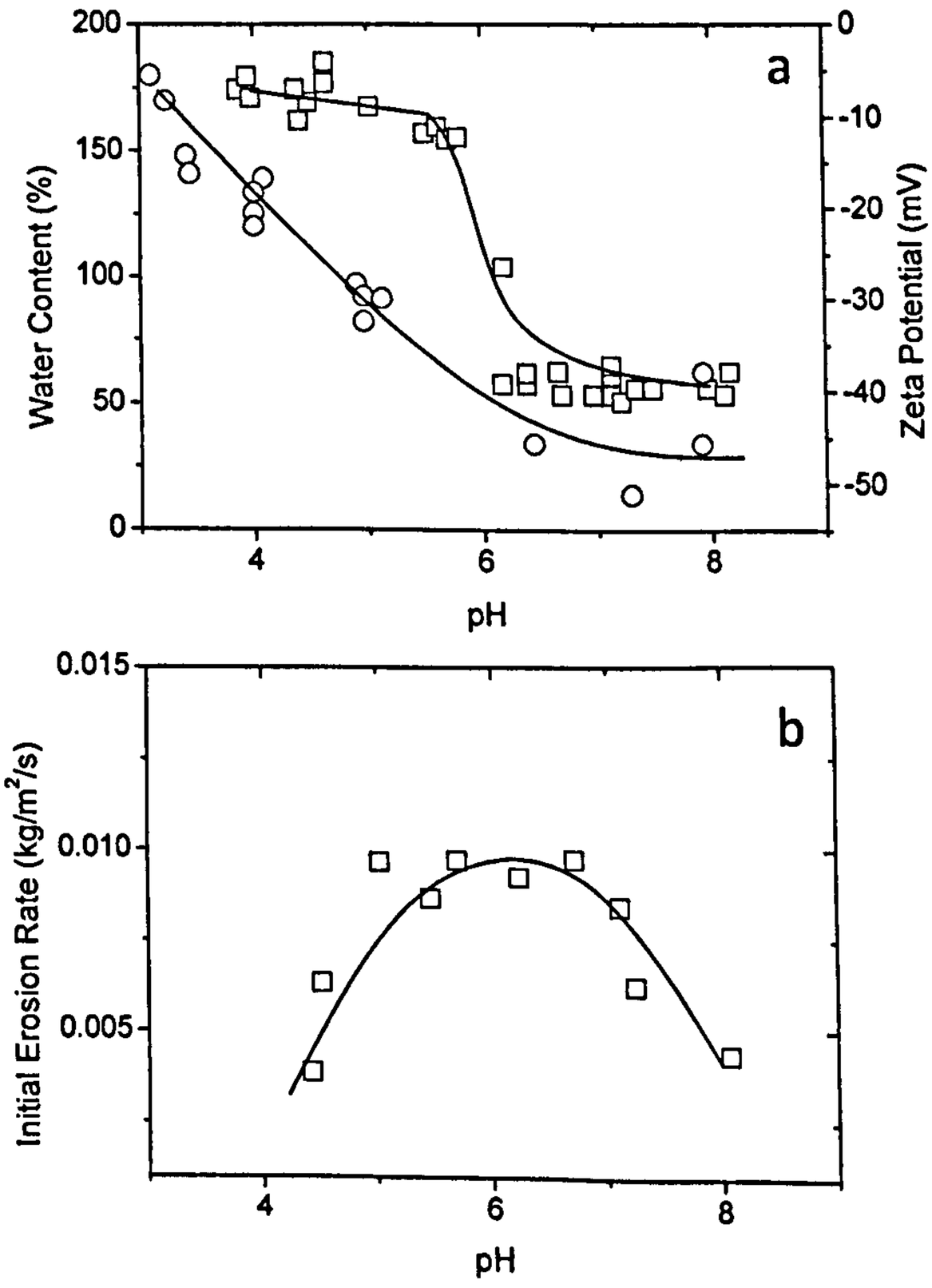

Figure 6.2 a) Kaolin bed water content and particle zeta potential as a function of the suspension pH, b) Initial erosion rate as a function of sediment pH. Figure redrawn from reference [39].

Figure 6.2 b shows the change in the initial sediment bed erosion rate as a function of sediment pH for an equivalent flow velocity. At pH 4 the initial erosion rate is low due to the strong edge-face associations preventing surface erosion. A pH 9 an equivalent erosion rate is measured when face-face associations are dominant leading to a higher sediment density. At the intermediate pH's, the erosion rate passes through a maximum as the total interaction strength reduces during reorientation of particles from an edge-face to an edge-edge association resulting in a weaker sediment bed structure.

In reviewing the hydrotransport literature there are very few studies where the particle-particle interaction energy is controlled. There is a clear desire to optimise pipeline operations by influencing the strength of the interaction, but to date researchers have not introduced the careful control which is needed to ensure that their systems are influenced by only one variable. In the current study we aim to overcome many of these issues by finely controlling the suspension properties.

6.3 Fine Particle Re-Suspension

With a continual reduction in the mean flow velocity below the minimum transport velocity, there is an associated increase in the deposition of solids from suspension. If the flow velocity ceases before the pipeline becomes plugged a sediment bed will form on the pipe invert. The process whereby the negatively buoyant particles are re-entrained back into the bulk fluid in the presence of shear is known as re-suspension. Re-suspension occurs when the lift force exceeds the submerged weight force of the particle, and for fine particles both viscous and turbulent re-suspension effects are to be considered.

Viscous re-suspension occurs at sufficiently low Reynolds numbers that the flow is fully laminar and inertial effects are insignificant [41]. The first study investigating such phenomena was conducted by Gadala-Maria [42] looking at the viscous properties of coal suspensions. Using a parallel plate device the viscosity of the settled suspension was observed to gradually increase and reach equilibrium under gentle shear, signifying the re-suspension of the settled layer of particles. Leighton and Acrivos[41], and Chapman and Leighton [41, 43] explain such behaviour in terms of a shear induced diffusion process. At

equilibrium, the downward flux of the negatively buoyant particles described by a modified Stokes' equation is balanced by a diffusive flux, which is proportional to the local shear rate and the particle radius squared. Through theoretical derivation the authors [41] conclude that once re-suspension of the settled bed has begun, the equilibrium height of the suspension can be defined by:

$$\frac{\Delta h}{a} \approx 2\,\frac{\tau}{ag\Delta\rho} \qquad or \qquad [6.8]$$

$$\frac{g\Delta\rho\Delta h}{\tau} \approx 2 \qquad [6.9]$$

where Δh is the change in height of the re-suspended layer, τ represents the applied shear stress and $\frac{\tau}{ag\Delta\rho}$ is defined as the Shields parameter (ratio of the viscous force to the gravitational force). The theoretical derivation is based on particles that are sufficiently large so diffusion due to Brownian motion can be neglected. Typical particle Reynolds numbers for viscous re-suspension experiments are of the order of 10^{-4}. Experimental observations of the equilibrium bed heights of glass (43μm and 139μm) and polystyrene spheres (46μm) were used to verify the model. Using an annular parallel plate device the constant of proportionality for large Shield values (>5) was observed to equal 2.1.

As highlighted by Chapman and Leighton [43] re-suspension due to shear induced diffusion is not to be confused with shear induced self-diffusion. Viscous re-suspension is due to particle interactions in contact loading where particles are 'pushed' from a region of high concentration to a region of low concentration. Shear induced self-diffusion however, is a term used to describe the random motion of particles as they bounce and roll over one another under shear. Hydrodynamic, thermodynamic and inter-particle interaction forces can all influence the shear induced self-diffusion process of fine particles.

The drag and lift components of the hydrodynamic force acting upon a single stationary particle have been investigated by Feng and Michaelides [44] using the lattice Boltzmann method. The numerical simulation results were restricted to low shear Reynolds number flows (<50), with high shear Reynolds number simulations proving computationally intensive. The two forces were calculated as the dimensionless drag coefficient (C_D'), and the dimensionless lift coefficient (C_L'):

$$C_D' = \frac{F_D'}{\frac{1}{2}\rho d_p U_c^2} \qquad [6.10] \qquad C_L' = \frac{F_L'}{\frac{1}{2}\rho d_p U_c^2} \qquad [6.11]$$

where U_c is the undisturbed flow velocity at the centre of the particle and F_D', F_L', are the longitudinal drag and the vertical lift components respectively. The simulations show that both the lift and drag components of the hydrodynamic force acting on a stationary particle are significantly influenced by free flowing particles, see figure 6.3. The simplest case of a single particle flowing past a stationary particle will be considered here. As the free particle approaches the stationary particle, both the drag and lift components acting on the stationary particle gradually increase. Just before the distance of closest approach is reached, the lift component passes through a minimum which is slightly negative. This negative value indicates that the free particle is acting to 'push' the stationary particle towards the boundary. With an equal and opposite force the free particle is thus lifted to a higher level preventing deposition. At the distance of closest approach the drag component passes through a minimum while the lift component increases rapidly. The maximum in the lift component which is approximately twice the value experienced at the commencement of the interaction occurs at a position almost symmetrical to where the minimum lift was experienced. The lift introduces a suction effect which acts to 'pull' the stationary particle from the boundary. With the separation distance between the stationary and free particle increasing, the force components reduce to their equilibrium values. The author explains the significance of these oscillating forces in the process sediment bed re-suspension. The negative lift component acts to cause a disturbance on the particles at the bed surface, with the incipient motion of the surface particles from a rapid increase in the lift force leading to additional lift components through particle rotation and particle collisions.

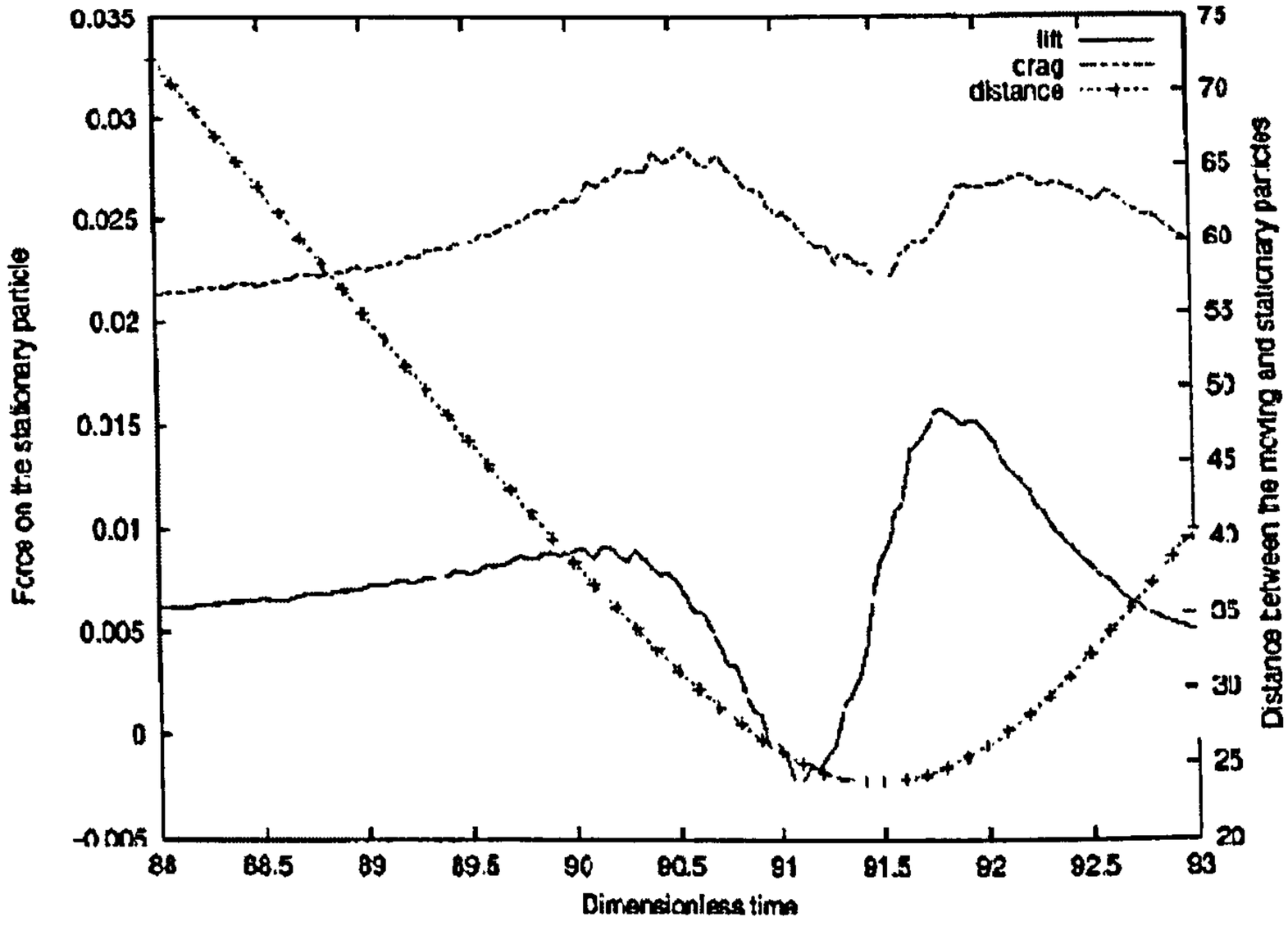

Figure 6.3 Lift and drag forces acting on stationary particle during the passage of a free particle, taken from reference[44].

The lift force acting upon a particle can be separated theoretically in to a 'spin lift' or 'slip-shear lift'. Spin lift, commonly known as 'Magnus lift', results from a pressure distribution across the particle due to the velocity differential between the rotating particle and the free stream flow. The drag pressure acting upon the particle is lower when both the particle rotation and the free stream flow are acting in opposite directions; inducing turbulent separation of the boundary layer. Fluid is transferred from the high drag to the low drag region, pushing the particle in the opposite direction. The force generated by an indifference in the particle and fluid rotation velocities acts perpendicular to the flow streamlines and the axis of rotation [45]. Slip-shear lift, more commonly referred to as the 'Saffman lift'[46], is applicable when the lift force is independent of particle rotation. Saffman derived the lift force for a single sphere moving through a very viscous liquid in an unbounded shear flow, considering small inertial effects to describe the sideways force on a single rigid sphere in creeping flow. The lift is generated by a pressure distribution across the particle in the shear field, with the particle elevated from a region of high pressure (low velocity) to a region of low pressure (high velocity) see figure 6.4.

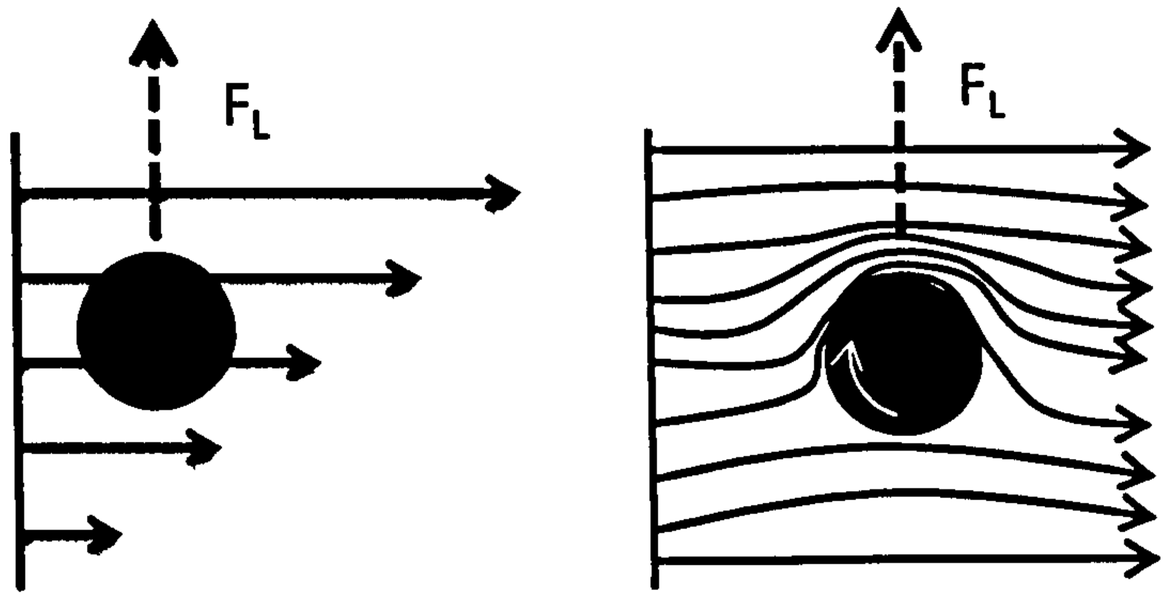

Figure 6.4 L.H.S - Saffman lift force in a velocity flow field. R.H.S. Spin lift – Magnus lift force

The Saffman lift force is determined from:

$$F_{Saff} = \frac{6.46\,\nu\,\rho\,a^2\kappa^{0.5}V_s}{\nu^{0.5}} \qquad [6.12]$$

where a denotes the particle radius, κ the velocity gradient and V_s is the relative velocity of the particle with respect to the fluid.

From an experimental point of view the contributions to lift can be categorised as either i) turbulent diffusion or ii) hydrodynamic lift [45, 47]. Turbulent diffusion is dominant in the turbulent core where the turbulent eddies provide the energy to maintain the suspended load. Hydrodynamic lift at the pipe wall or close to a stationary bed describes the mechanism through which a pressure difference around the particle creates lift. In this respect the Magnus and Saffman lift forces can be considered the same, with the importance of defining a difference between the two only required in computational particle dynamics. Several lift force models modifying the parameter range have been published in the literature to account for single particle wall contact [48], single particle wall induced lift force [49, 50] and the lift force in multi-component flows [51]. However, in-depth discussion on such theoretical equations is believed outside the focus of this study.

One of the few empirical correlations to predict the lift force on a small isolated particle embedded within the viscous sub layer of a turbulent boundary layer was published by Mollinger and Nieuwstadt [52]. Using the principles of surface force apparatus the authors measured the displacement of the cantilever to which a single spherical particle was glued. For $0.3 < a^+ < 2$ the mean lift force is given as:

$$F_L^+ = (56.9 \pm 1.1)(a^+)^{1.87\pm0.04} \quad [6.13]$$

with the dimensionless lift force (F_L^+) and particle radius (a^+) defined as:

$$F_L^+ = \frac{F}{\rho v^2} \quad [6.14]$$

$$a^+ = \frac{a\,V^*}{\nu} \quad [6.15]$$

where F is the lift force, a is the particle diameter, v the kinematic viscosity and V^* is the friction velocity.

This correlation has a tendency to over predict the lift force measured by Hall [53]. Hall measured the lift force acting on a single spherical particle resting on a smooth surface by attaching a particle to a tungsten support wire and measuring the displacement using a commercially available force transducer. For $1.8 < a^+ < 70$ the mean lift force showed good agreement with the relationship:

$$F^+ = (20.90 \pm 1.57)(a^+)^{(2.31\pm0.02)} \quad [6.16]$$

The author comments that the correlation is valid to predict the lift force acting on a colloidal sphere. With the relationship developed from lift forces acting on spheres within the size range of 1-5mm, this is believed to be incorrect when one considers the data published by Mollinger and Nieuwstadt [52]. It is reasonable that the discrepancy between the two correlations relates to the positioning of the sphere within the turbulent boundary layer. The particles used by Hall [53] would penetrate the viscous sub layer and protrude into the buffer layer and in some instances the logarithmic layer. Whereas Mollinger et al. [52] using particles of 120μm could ensure that the lift effect was a result of viscous sub layer forces only. By penetrating into the buffer layer the particle becomes exposed to increased turbulent energy [54] resulting in a lift force correlation that under predicts the force required to lift a particle submerged within the viscous sub layer.

Much of the discussion so far has focused on the re-suspension of particles under viscous flow conditions, assuming that the viscous sub layer is steady and unaffected by turbulent instabilities within the flow. A study into the lift force acting on a sphere within the viscous sub layer showed that the flow characteristic is largely determined by turbulence in the buffer layer. Measuring the instantaneous lift force, Mollinger and Nieuwstadt [52]

showed a fluctuating force where the particle is occasionally subjected to a very large positive lift force. Cleaver and Yates [55] have discussed a mechanism whereby turbulent bursts within the viscous sub layer are capable of generating instantaneous lift forces which detach particles from the surface. Visual observations have shown particles rolling along the surface before suddenly detaching at right angles into the turbulent core. Through dimensional analysis of the hydrodynamic lift force and drag force, and consideration given to the size and frequency of the turbulent bursts, the authors have shown that for a given fluid under turbulent conditions the particles will detach from the surface when $\tau_w \, d_p^{4/3} > \beta$ is satisfied (τ_w, mean wall shear stress); with the constant β dependent on the particle shape, fluid viscosity and the adhesive force between the particle and the surface. With limited experimental data on colloidal re-suspension, verification of the model is difficult and a sceptical approach should be taken when applying this correlation. The model is associated to the work by Kline et al. [54] and Corino and Brodkey [56] who investigated the flow characteristics of the turbulent boundary layer. Visual studies showed that the flow in the viscous sub layer is continually disturbed by velocity fluctuations and the intrusion of fluid bursts from the buffer region.

This short review on the transportation and re-suspension properties of particles has provided a brief introduction to a subject that is extremely complex and challenging. The review has, however, highlighted some of the more interesting studies in multiphase transport including studies that are specifically relevant to colloidal dispersions.

6.4 Experimental

6.4.1 Single Phase – Pipe Loop Validation

A horizontal pipe loop employing re-circulated flow was used to study the re-suspension properties and the minimum transport velocities of colloidal silica slurries. The test section was positioned in the fully developed flow region free of any entry length disturbances. Figure 6.5 shows three mean velocity profiles along the test section (4D = 4 x pipe diameter), with all profiles showing the expected 'flattened' symmetrical behaviour which is representative of turbulent pipe flow. The mean velocity profiles are independent of the pipe length, indicating that the test section is positioned in the fully developed flow region.

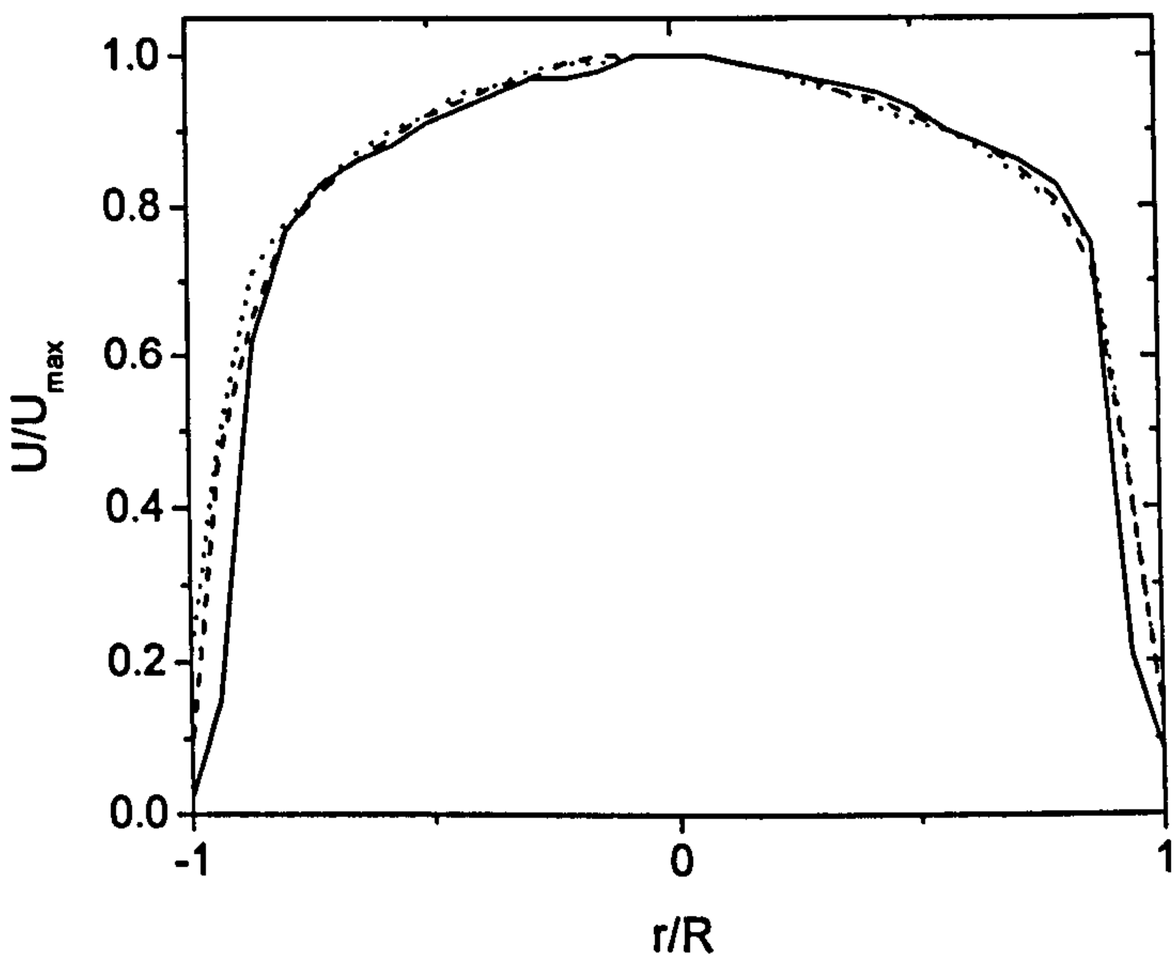

Figure 6.5 Mean velocity profiles as measured with PIV at 3 different locations along the test section. Lines: solid - 0D, dash – 2D, dot – 4D. *Re* = 3780, D = 0.026m

The mean velocity profiles as measured with PIV and UDVP were compared with each other and the universal velocity profile correlation [57]. The universal velocity profile describes the velocity distribution if the pipe wall is hydraulically smooth. The profile is suitably divided into i) the turbulent core, ii) the buffer layer and iii) the viscous sub layer. Within the turbulent core ($y^+ > 30$) where the Reynolds stresses dominate the viscous stresses, the dimensionless velocity (u^+), applying von Karman's constants (A = 2.5, B = 5.5), is given by:

$$u^+ = A \ln(y^+) + B \qquad [6.17]$$

This correlation is modified to describe the buffer layer ($5 < y^+ < 30$) where the two fluid stresses are approximately equivalent. The dimensionless velocity with A' = 5.0, B' = 3.05 is given by:

$$u^+ = A' \ln(y^+) - B' \qquad [6.18]$$

In the viscous sub layer ($y^+ < 5$) where viscous stresses are more important than Reynolds stresses, the dimensionless velocity is equal to the dimensionless distance from the wall (y^+):

$$u^+ = y^+ \qquad [6.19]$$

Both dimensionless terms are related to the friction velocity (V^*), with u^+ and y^+ defined as:

$$u^+ = \frac{u}{V^*} \qquad [6.20]$$

and

$$y^+ = \frac{yV^*\rho_l}{\mu} \qquad [6.21]$$

Figure 6.6 shows typical dimensionless velocity profiles on a semi logarithmic scale comparing both experimental techniques used in this study and the universal velocity profile. Good agreement is observed between the data collected with the UDVP and PIV, while the universal velocity profile tends to under predict the local velocity in the turbulent core. The divergence in the theoretical and empirical data might suggest that the flow is not fully turbulent when *Re* = 3000, but is in a phase of intermittent turbulence. A study completed by Patel and Head [58] showed disagreement between theoretical (universal velocity profile) and empirical pipe flow data for Reynolds numbers below *Re* = 9800. It should be acknowledged that the constants (A and B) used in equation 6.17are based on experimental averages of data showing a considerable degree of scatter. The exact values of these constants are a matter of dispute and are frequently discussed in literature [59, 60]. To provide comparison with another data set, the study of Zalzal et al. [61] was chosen which provides the dimensionless velocity and dimensionless distance from the wall when *Re* = 2800 for a single phase flow measured using a photochromic tracer method (see figure 6.6a).

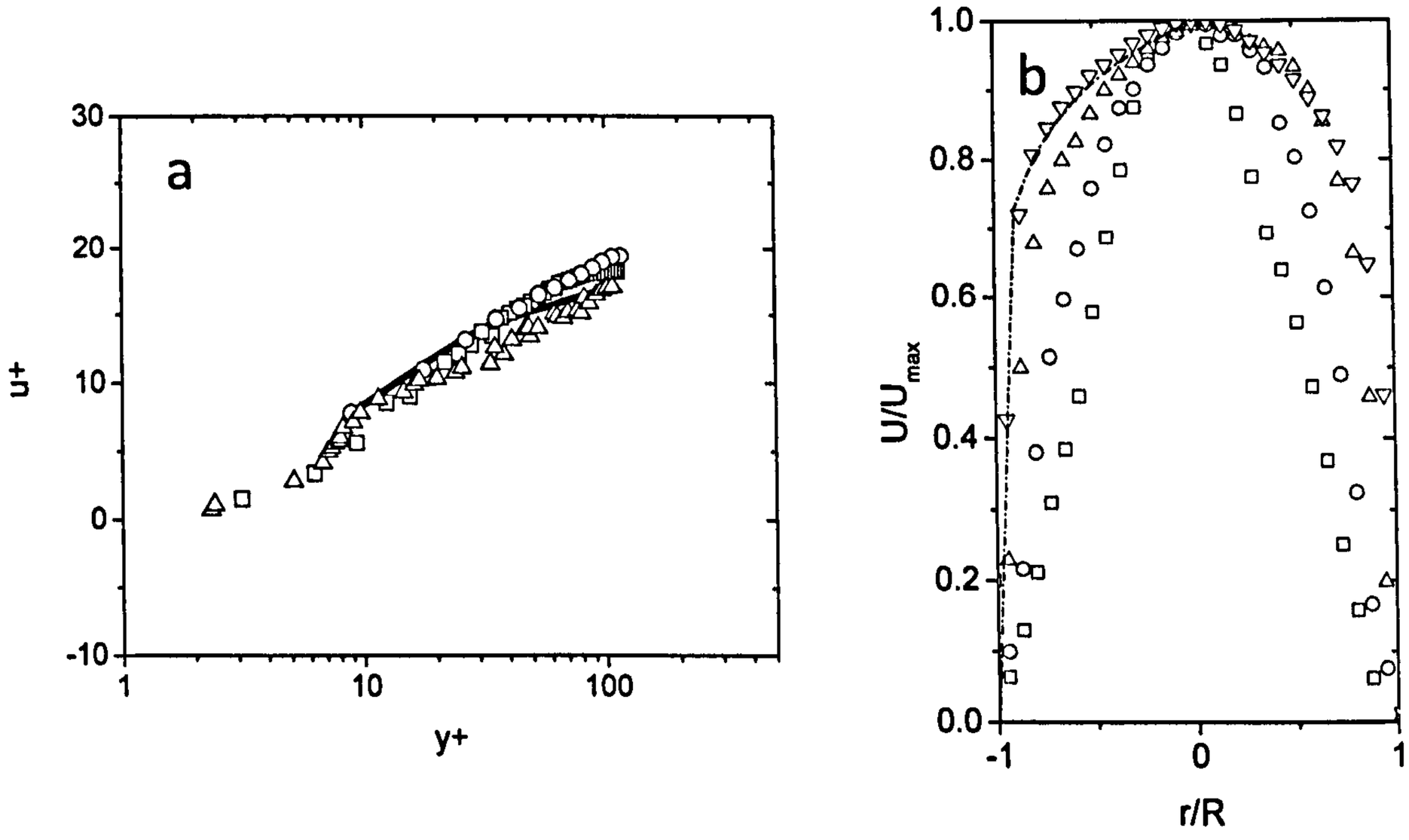

Figure 6.6a) Single phase mean velocity profile - *Re* = 3000. Symbols: line – universal velocity profile, square – particle imaging velocimetry, circle – ultrasonic Doppler velocity profiler, triangle – Zalzal et al. [61] *Re* = 2800. b) Mean velocity profiles as measured with PIV. U_{max} values, square 0.02 m/s *Re* = 250, circle 0.05 m/s *Re* = 650, triangle 0.09 m/s *Re* = 1170 and inverted triangle 0.18 m/s *Re* = 2350. Dashed line - empirical equation for the velocity profile for a smooth pipe at high Reynolds numbers ($U/U_{max} = (y/R)^{1/n}$ n = 7.34 ref.[62].

6.4.2 Minimum Transport Velocity

The minimum transport velocities of the colloidal silica suspensions were determined through extrapolation of the transition velocity (onset velocity for sediment bed erosion) with respect to the initial sediment bed height (eliminate the bed effect). The experimental procedure used in determining the minimum transport velocity differs from many of the conventional studies where direct visualisation is commonly applied. With colloidal particles the error associated with determining the onset of a sliding bed through direct visual assessment is significant. Other approaches such as deposition probes which are commonly used in sand slurry experiments cannot be used, as they require a high conductivity background solution to optimise performance. As discussed in chapter 2, the interaction potential between two colloid particles is significantly influenced by the solution conductivity; as such the use of such probes would therefore preclude the high level of solution chemistry control which is required in the current study. Dilute re-

suspension of colloidal particles in a flow channel with microscope monitoring is another approach[37]. However, the set-up is not representative of a 'practical' application with multi-particle effects at the channel surface and within the suspension not considered.

The experimental procedure to determine the minimum transport velocity has been described in detail in chapters 3 and 4. Briefly, the suspension is circulated in the pipe loop at a velocity where a homogeneous flow regime is maintained. The flow velocity is then suddenly reduced to zero enabling particles to deposit on the pipe invert, forming a sediment bed with a structure dependent on the particle-particle interaction potential. The transition velocity is then determined by monitoring the sediment bed height as a function of time. Images collected using PIV are analysed using a data analysis package to determine the flow velocity when the erosion rate of the sediment bed is equal to zero.

With a sediment bed present in the pipe loop, the mean flow velocity is determined from the volumetric flow rate using circle segment analysis, assuming that the cross-sectional sediment bed height remains level during re-suspension. Images (figure 6.7) collected using Electrical Resistance Tomography (ERT) studying the re-suspension properties of kaolin particles (d_{50} = 6μm) in a 50 mm i.d. horizontal pipe loop, show the sediment bed surface to remain approximately level during re-suspension, with wall effects appearing insignificant (ie. no significant increase in the sediment bed height at the pipe wall). Therefore, such behaviour has been assumed for the colloidal silica spheres used in the current study, thus enabling the flow velocity to be calculated with relative ease. The initial sediment bed heights prior to re-suspension are given in table 6.1.

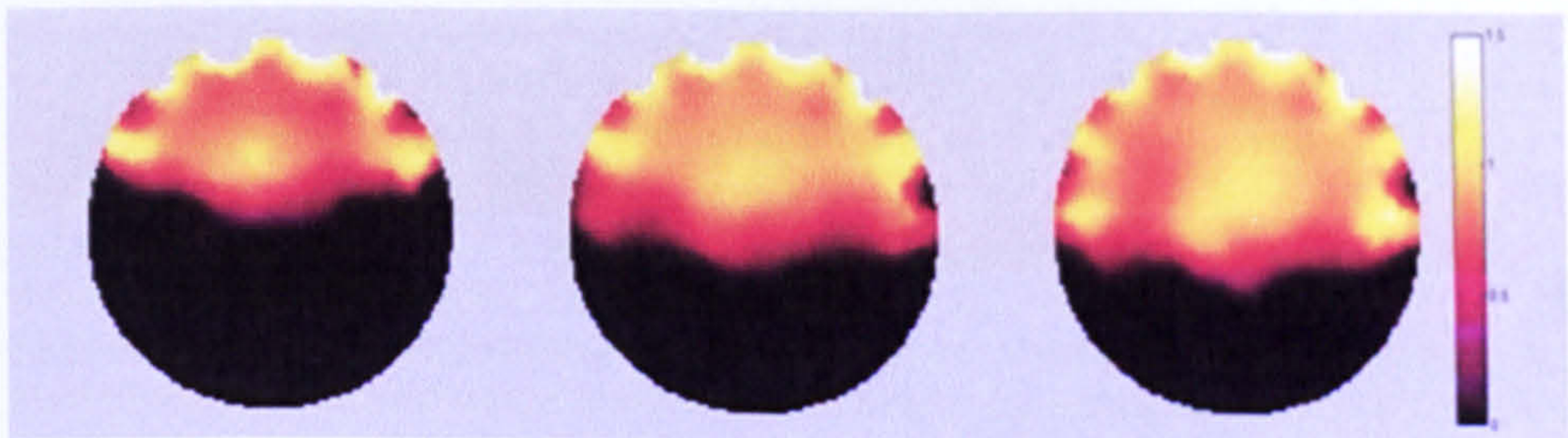

Figure 6.7 ERT images showing the gradual re-suspension of kaolin sediment at a constant mean flow velocity ($0.5ms^{-1}$). Images collected during a secondment to Cape Peninsula University of Technology, South Africa.

To remove any inconsistencies associated with changes in the rate of erosion over time, all flow velocities are presented as an average over the first 30 seconds of pumping. An example of the raw data collected measuring the sediment bed re-suspension behaviour over the first 30 seconds of pumping is shown in figure 6.8, which illustrates the change in the sediment bed height (% bed erosion) as a function of the slurry velocity. The data is representative of a 1M KNO_3 sediment undergoing re-suspension in the presence of a 12.6% by volume slurry. At low flow velocities (below the minimum transport velocity) a negative bed erosion rate (sediment bed depth increases) is observed, resulting from a net flux of particles depositing from the flowing slurry. As the flow velocity is increased the erosion rate becomes positive with a net flux of particles from the sediment bed to the flowing slurry. Further increases in the slurry velocity lead to rapid erosion of the sediment bed with nearly full re-suspension of the bed observed within the first 30 seconds of pumping ($0.441 ms^{-1}$). At such high flow velocities the sediment bed is observed to undergo both surface and bulk erosion as the bed randomly and violently breaks-up during re-suspension.

Figure 6.9 shows experimental data for the initial erosion rate (% bed erosion per minute) versus the initial mean flow velocity for the dispersed and aggregated suspensions of interest. The repeatability of this technique when monitoring sediment bed erosion is shown in figure 6.9a, with repeat experiments conducted at 0.20, 0.30 and 0.38 m/s, resulting in erosion rates within 10% of each other.

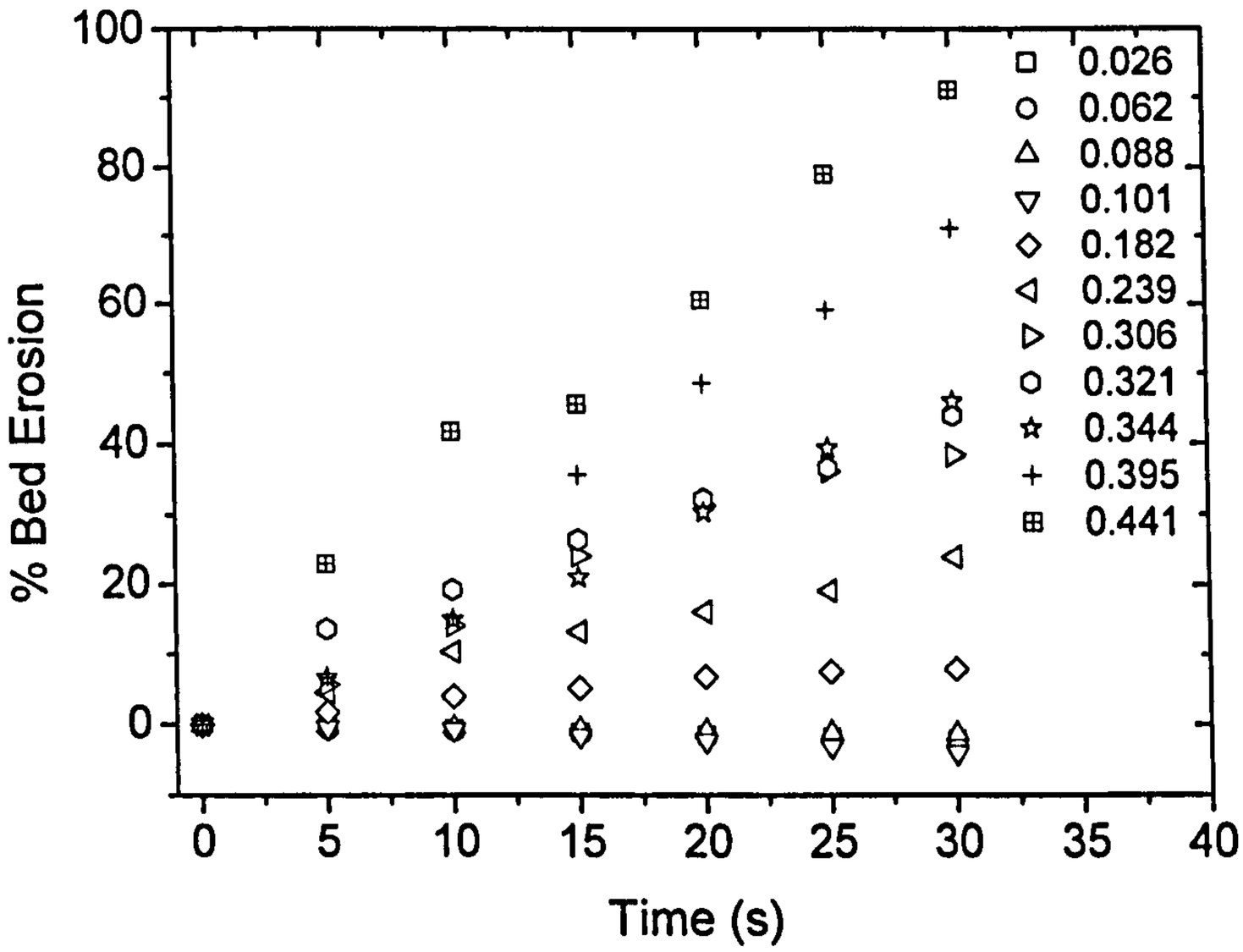

Figure 6.8 % bed erosion with time as a function of the mean slurry velocity. Sediment 1M KNO_3 pH 6, slurry 12.6 %vol. pH 6.

Table 6.1 Initial sediment bed heights

	Solid conc. (%vol)	Bed height (mm)
10^{-4} M KNO_3	12.7	9.0 ± 0.2
	5.5	3.6 ± 0.3
1M KNO_3	12.6	12.8 ± 0.4
	5.7	5.8 ± 0.2
10^{-4}M KCl	6.0	3.4 ± 0.3

The transition velocity is determined at the x-axis intercept of the second order polynomial fit. To account for uncertainties associated with this fit, and the uncertainty between the repeatability of each measurement, a 10% error is included in the analysis. Table 6.2 shows the transition velocity for the five slurries investigated in the current study. For slurries of a similar solid concentration there is a clear effect associated with the electrolyte concentration. For the same electrolyte type (KNO_3) a reduction in the transition velocity is observed as the electrolyte concentration is increased. This behaviour is consistent when the solids concentration is increased, albeit the transition velocities are somewhat lower.

The discussion on the differences in the rheological properties of colloidal silica suspensions at low electrolyte concentrations with different co-ions, has already been discussed in chapter 5 and appears relevant to the pipe flow study also. Within error the two transition velocities could be considered the same. However, the trend in the transition velocities when comparing all 3 electrolytes (1M KNO_3, 10^{-4}M KNO_3 and 10^{-4}M KCl) appears to be consistent with the results presented in chapter 4, where there were consistent trends in the zeta potential, gel point and yield stress measurements when comparing all three electrolytes.

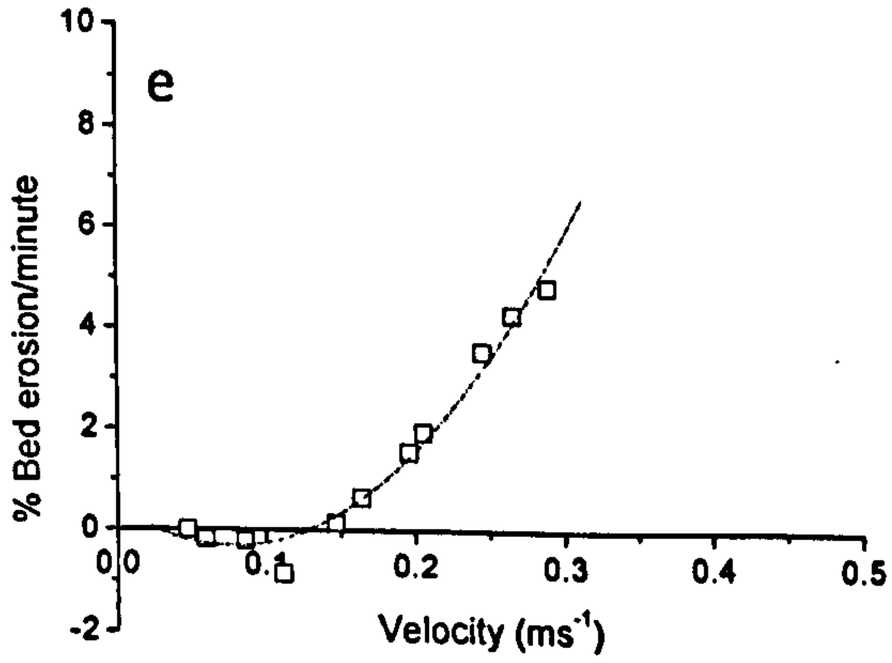

Figure 6.9 Variation in the initial erosion rates as a function of the initial flow velocity. a) 10^{-4}M KNO_3 (5.5 %vol.) b) 10^{-4}M KNO_3 (12.7% vol.), c) 1M KNO_3 (5.7 %vol.), d) 1M KNO_3 (12.6 %vol.) and e) 10^{-4}M KCl (6.0 %vol.). Linear fit (figure 5.5c) shows the region of surface erosion, with bulk erosion effects observed at flow velocities in excess of 0.35ms^{-1} (see discussion on erosion rates below).

Table 6.2 Transition velocities determined at onset of sediment bed erosion.

	Solid conc. (%vol)	Velocity (m/s)
10^{-4} M KNO_3	12.7	0.13
	5.5	0.14
1M KNO_3	12.6	0.08
	5.7	0.11
10^{-4}M KCl	6.0	0.13

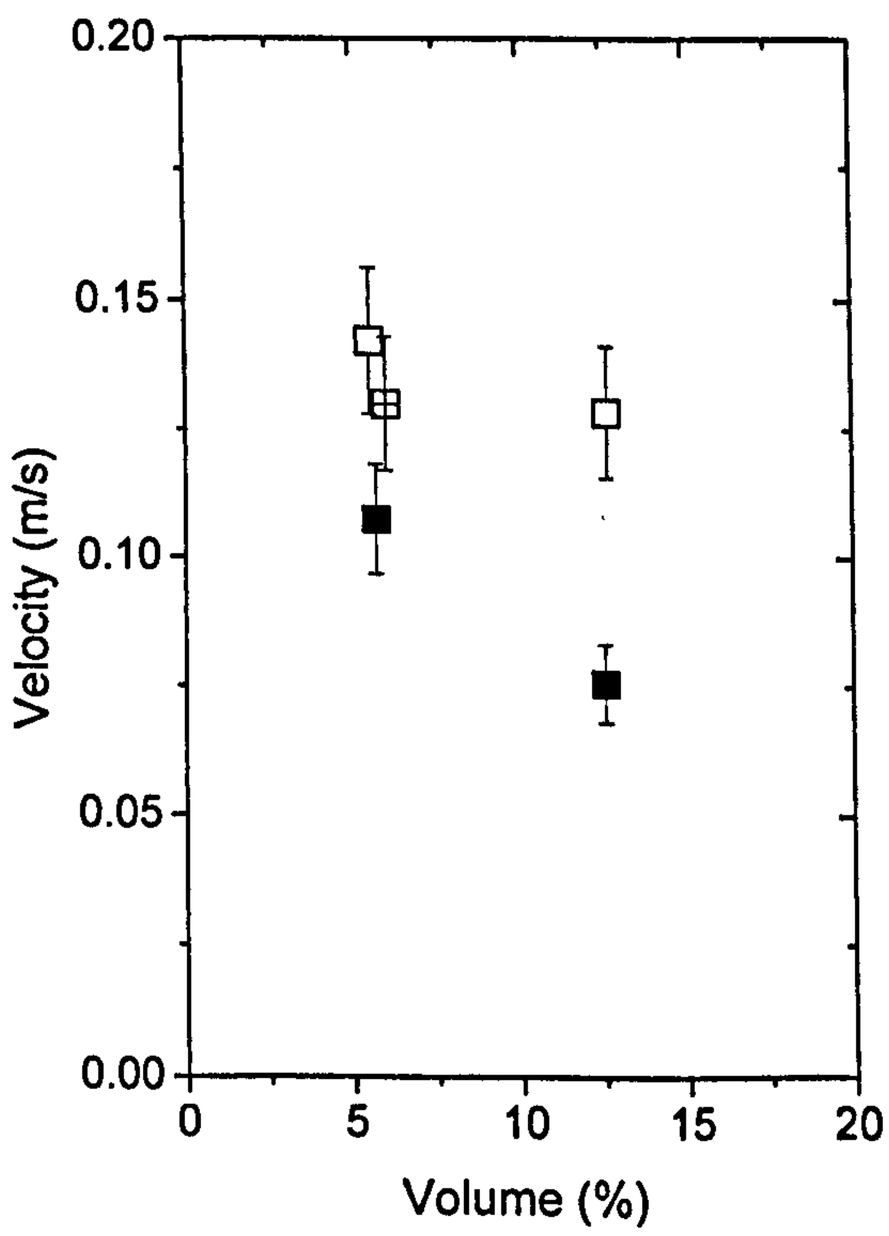

Figure 6.10) Transition velocities at the onset of sediment bed erosion represented graphically, including a 10% degree of uncertainty.

Figures 6.11a and b compare the three transition velocities for the low concentration slurries (≈ 5.5 – 6.0 % vol.) as a function of the zeta potential and the sediment shear yield stress. A decreasing zeta potential and yield stress is associated with a change in the background electrolyte; 10^{-4}M KNO_3 (-70mV), 10^{-4}M KCl (-50mV) and 1M KNO_3 (-

6mV). The relationship between the zeta potential and the sediment shear yield stress has previously been discussed in detail in chapter 5. Changes in the physiochemical properties of the slurry will clearly influence the transportation behaviour of the particles and the sediment rheology, thus influencing the transition velocity. It is observed that an increase in the electrolyte concentration results in a reduction in the transition velocity. Several possible reasons for this behaviour are:

1) At high electrolyte concentration the porosity of the sediment bed is higher, thus fluid is able to penetrate deeper into the sediment bed, leading to both surface and bulk erosion of the sediment. Surface and bulk erosion of a sediment results in a much more rapid rate of bed erosion when compared to a bed which experiences only surface erosion; surface erosion is typical for a bed where the particles are tightly packed (low electrolyte concentration).
2) The formation of aggregates at high electrolyte concentration will result in large, open, fractal structures that will experience enhanced lift in the velocity field when compared to the smaller, denser primary particles. Therefore there is tendency for these aggregates to remain in suspension and not deposit onto the sediment bed.
3) The sediment bed topography is an important parameter when considering bed erosion. At high electrolyte concentrations the formation of aggregates and the inefficient packing of these aggregates in the sediment, leads to an uneven bed surface and an increased solid-liquid contact area. The increased contact area means that more particles in the bed are exposed to the fluid shear; therefore, the sediment bed is more likely to experience particle erosion, than a bed where the particles are tightly packed with little solid-liquid contact area.

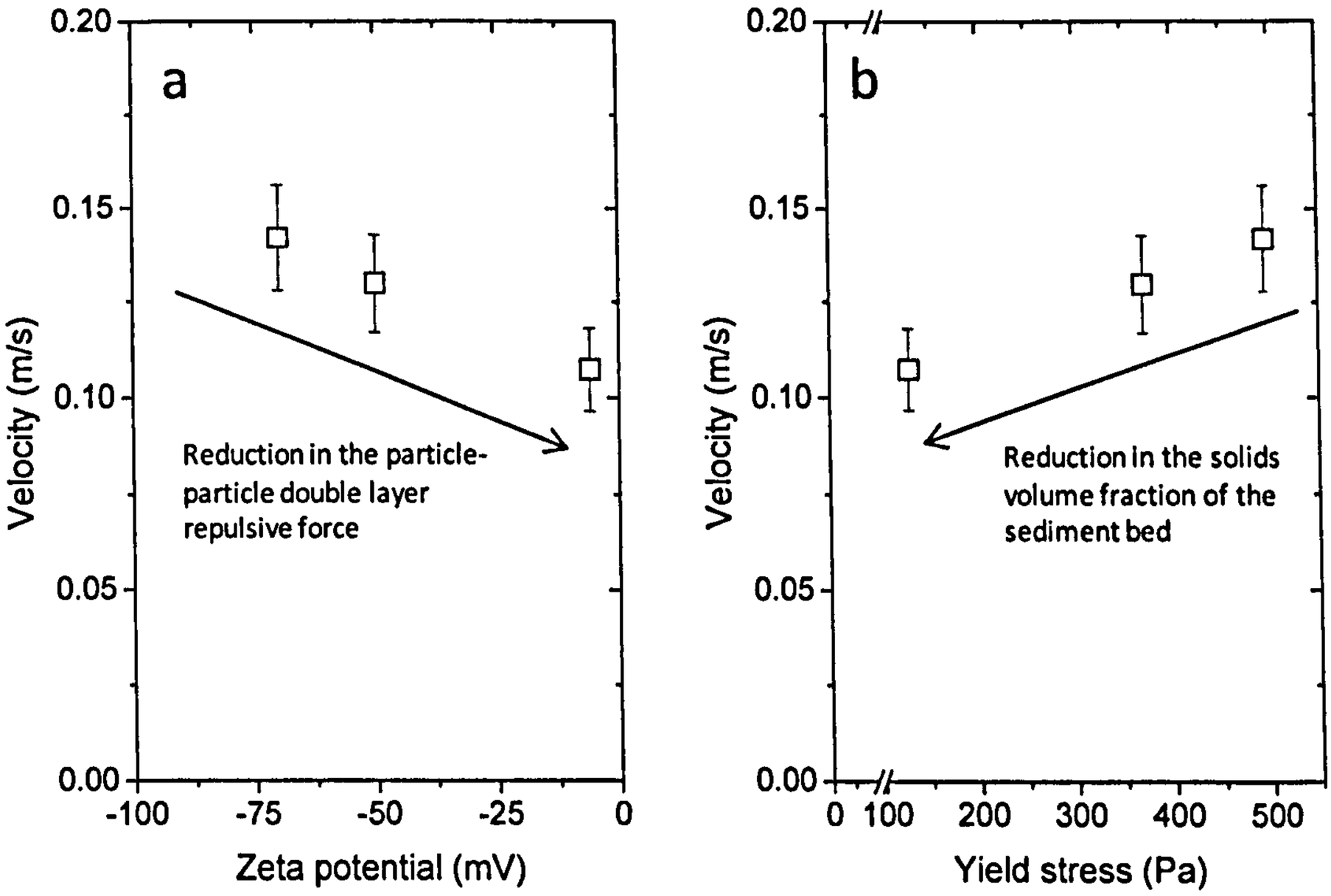

Figure 6.11 Transition velocities as a function of the silica zeta potential (a) and the sediment bed yield stress (b). All data points collected at low solids concentrations.

Sediment bed porosity and its influence on the erosion rate of a sediment bed have been studied in detail by several researchers [39, 63-65], who have shown that the rate of erosion decreases with a corresponding decrease in the bed porosity. A general expression which describes the rate of erosion is given as:

$$E = M\left(\frac{\tau_b}{\tau_c} - 1\right) \qquad [6.22]$$

where E denotes the erosion rate per unit area, τ_b the bed shear stress exerted by the fluid, and M and τ_c which are dependent upon the physiochemical parameters of the sediment, define the erosion rate coefficient and the critical shear stress of erosion respectively.

With τ_c associated to the yield stress of the sediment, a decrease in the bed porosity, which may result from consolidation of the bed as a function time, will lead to a decrease in the erosion rate for an equivalent slurry velocity. The strength of the electrolyte has been shown to have a significant effect on the sediment bed erosion rate. Figure 6.12 shows the erosion rate of a 1M KNO_3 sediment to exceed the erosion rates of sediments formed in 10^-

^{4}M electrolytes (KNO_3 and KCl). As previously discussed, such behaviour is significantly influenced by the packing density of the sediment bed. For example, an open porous structure provides a greater surface area for fluid contact, as well as a pathway for fluid to penetrate deeper into the sediment bed, weakening the structure below the surface. With an open porous structure, it is characteristic for sediments to undergo both surface and bulk erosion, where large clusters of particles are removed from the bed in a random and violent manner. This has been observed several times in the current study when monitoring the erosion behaviour of a 1M KNO_3 sediment bed at high flow velocities. Figure 6.9c shows an example of the transition from surface erosion to both surface and bulk erosion. Below 0.35ms^{-1} a linear relationship between the rate of erosion and flow velocity is observed, which is indicative of a sediment undergoing surface erosion [63]. Above 0.35ms^{-1} the linear relationship is not obeyed and the rate exceeds the rate predicted by the linear relationship, indicating that the bed is undergoing both surface and bulk erosion.

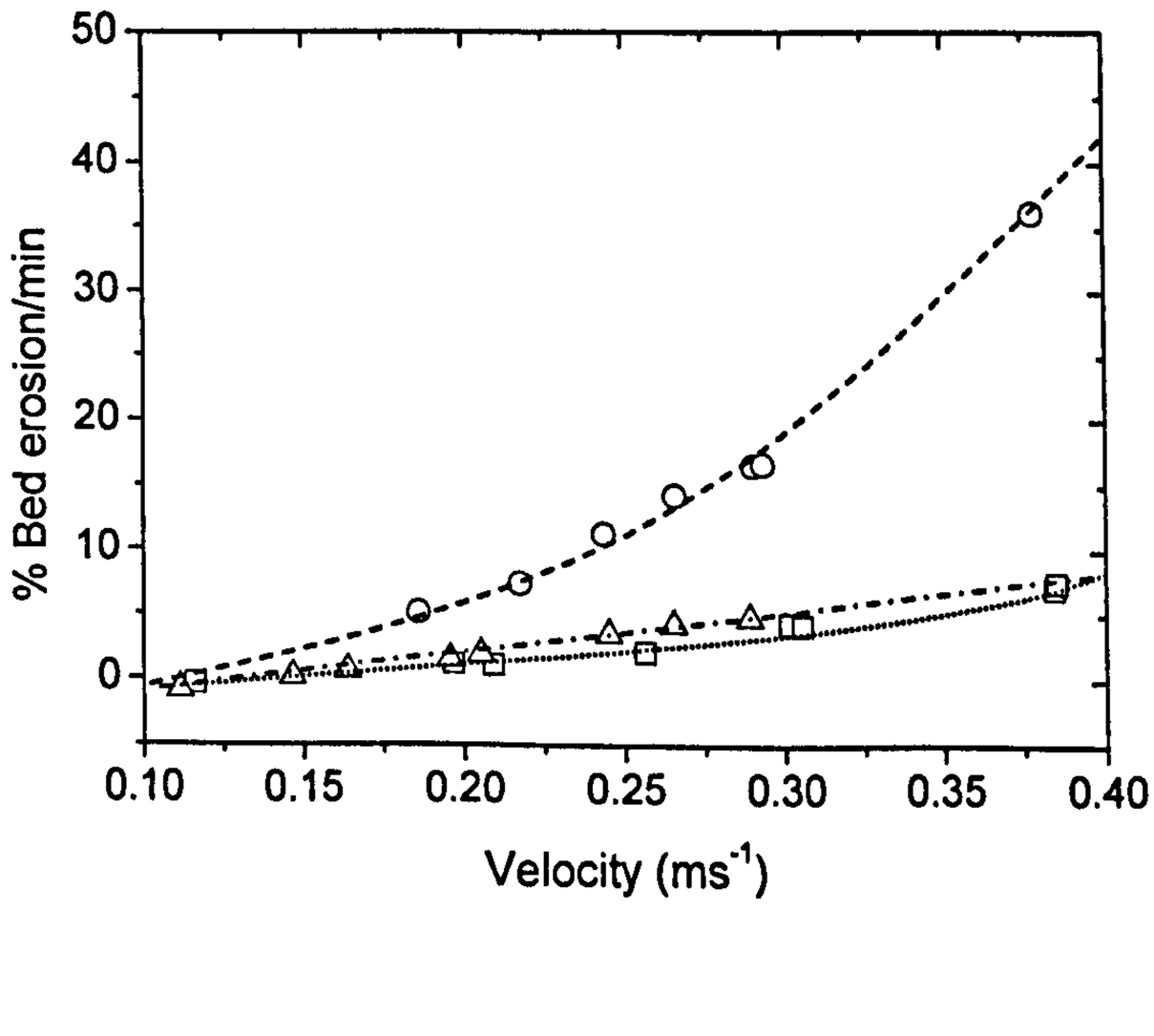

Figure 6.12 Variation in the initial erosion rate at increasing mean flow velocity. Symbols: circle - 1M KNO_3 (5.7 %vol.), triangle – 10^{-4}M KCl (6.0 %vol.) and square - 10^{-4}M KNO_3 (5.5 %vol.).

From the sediment bed transition velocity, the critical bed shear stress of the sediment bed can be calculated to determine the minimum fluid shear stress required for initiating bed erosion. The critical bed shear stress is given by:

$$\tau_c = \mu_m \left(\frac{8V}{D'}\right) \qquad [6.23]$$

where μ_m is the slurry viscosity, V is the mean velocity and D' is the effective pipe diameter. The slurry viscosity in equation 6.23 is the viscosity at 1 reciprocal second, which is equivalent to 0.006Pa.s for the 1M KNO_3 slurry at 5.7 % by volume, and 0.001Pa.s for the two slurries dispersed in 10^{-4}M electrolytes at 5.5 % and 6.0 % by volume for the KNO_3 and the KCl suspension respectively (see figure 6.13).

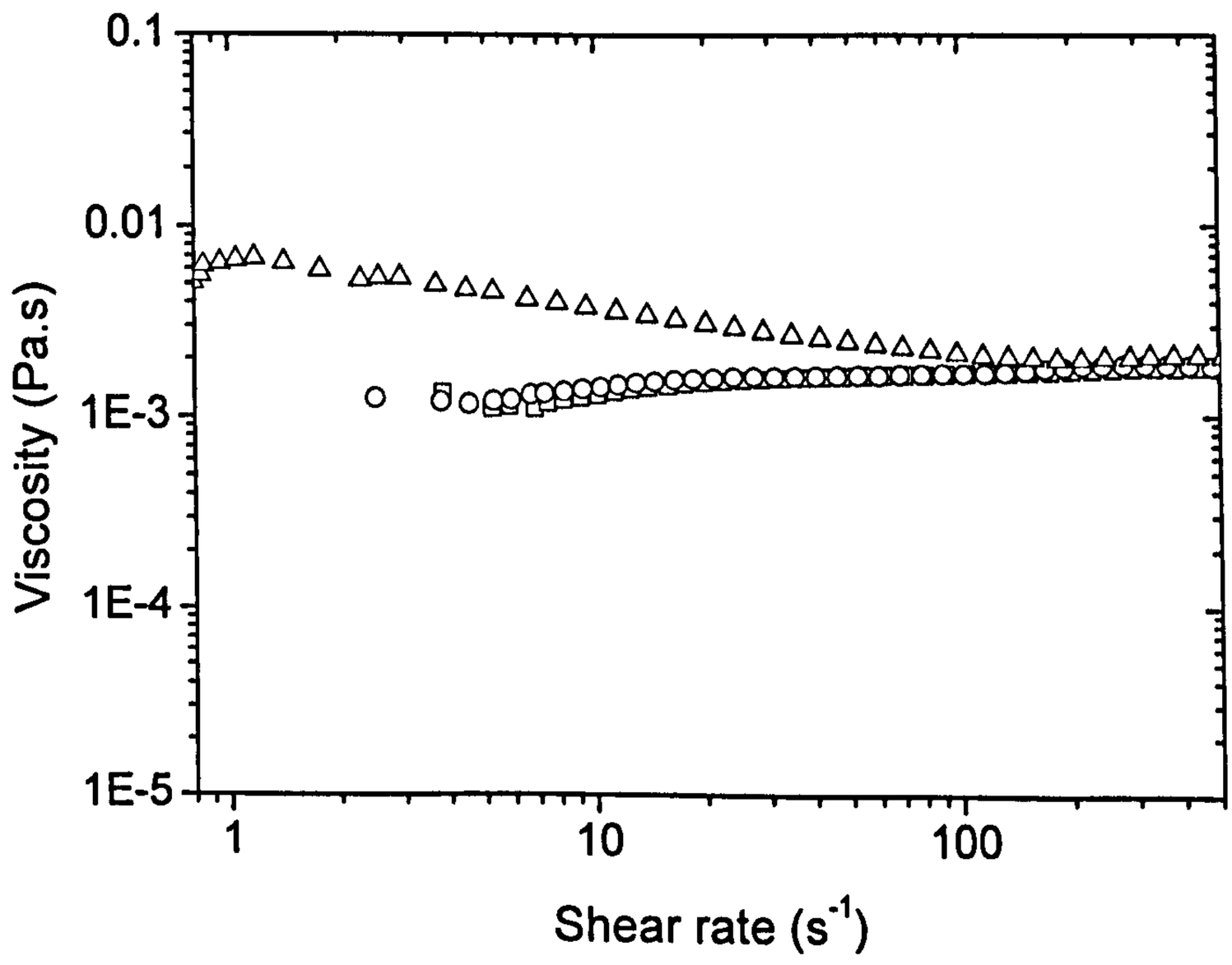

Figure 6.13 Flow curves for colloidal suspensions at pH 6. Symbols: triangle – 1M KNO_3 (5,7%vol), square - 10^{-4}M KNO_3 (5.5%vol.), circle – 10^{-4}M KCl (6.0%vol).

It would be expected that the critical bed shear is only dependent on the concentration and the type of electrolyte; the electrolyte influencing the strength of interaction between neighbouring particles. At low electrolyte concentrations the critical bed shear stress is independent of the solids concentration, but is dependent on the electrolyte type. The higher critical bed shear stress for a 10^{-4}M KCl sediment when compared to a 10^{-4}M KNO_3 sediment is consistent with earlier results which have identified a difference between the rheological properties of sediments formed in a KNO_3 and a KCl electrolyte (refer to chapter 5). The critical bed shear stress at high electrolyte concentration shows a small

variation with solids concentration. This small difference is believed to be error associated with using the same viscosity value for the two slurries (5.7 % and 12.6 % by volume). Table 6.3 shows that an increase in the electrolyte concentration results in an increase in the critical bed shear stress. As shown in chapter 5, an increase in the electrolyte concentration changes the strength of the interaction between two spheres, with the AFM data identifying a small adhesion force between two contacting surfaces when dispersed in a 1M electrolyte. This adhesion force is to be exceeded by the fluid shear to initiate bed erosion; therefore, more energy is required to break particles away from the sediment surface.

Table 6.3 Critical bed shear stress at measured slurry transition velocity

	Solid conc. (%vol)	τ_c (Pa)
10^{-4} M KNO_3	12.7	0.05
	5.5	0.05
1M KNO_3	12.6	0.24
	5.7	0.26
10^{-4}M KCl	6.0	0.06

As will be discussed in chapter 7, the flow properties of the suspensions are independent of the solids concentration and are only influenced by the degree of particle aggregation. With this in mind and a critical bed shear stress that is independent of the solids concentration, an approach was used where by the minimum transport velocity of the slurries could be determined from the sediment bed transition velocities, by extrapolating the transition velocities to remove the "bed effect".

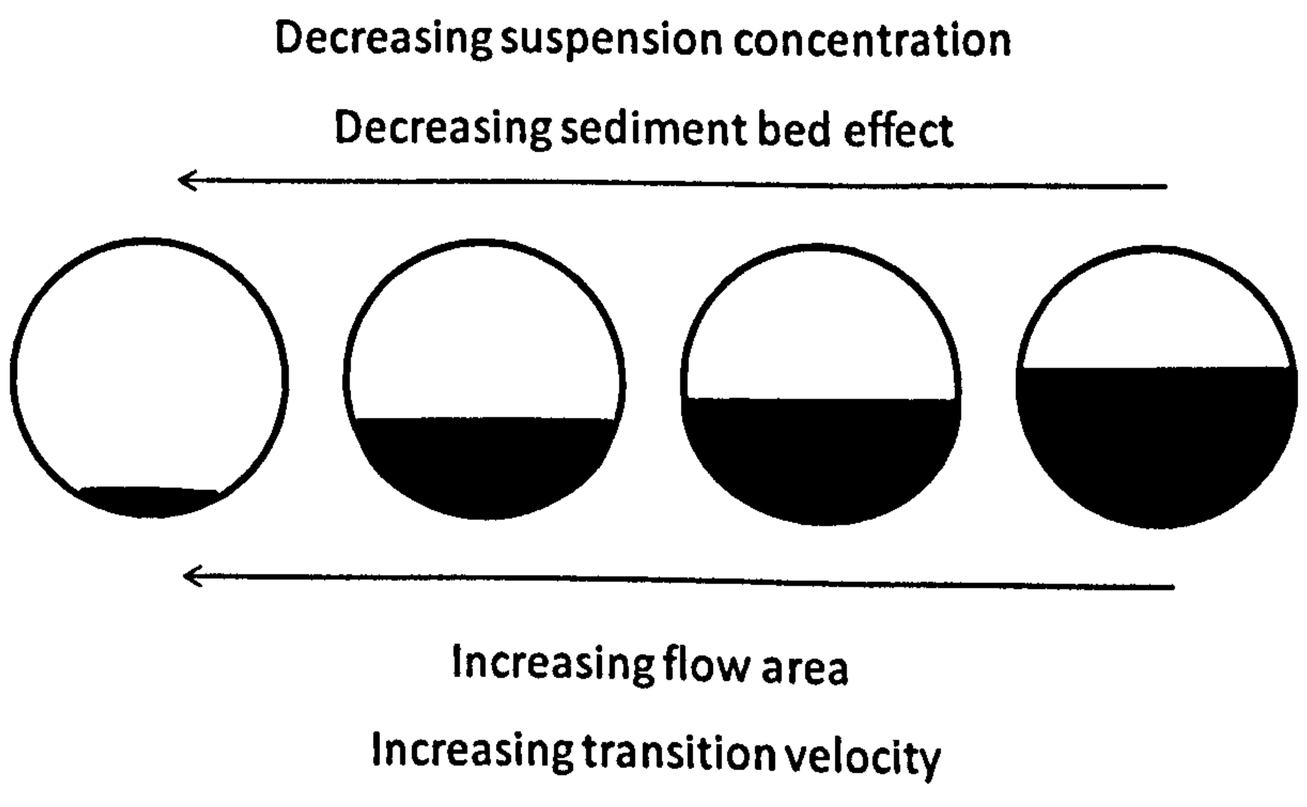

Figure 6.14 Methodology applied to determine the minimum transport velocity. Extrapolation to zero bed height to remove the bed effect on the transition velocity.

It is therefore reasonable that the minimum transport velocity through transition velocity extrapolation for a 1M KNO_3 suspension is equal to $0.13ms^{-1}$, while for a 10^{-4}M KNO_3 suspension the minimum transport velocity is slightly higher at $0.15ms^{-1}$. Due to limitations with the available raw material, the solids loading effect on the transition velocity for a 10-4 M KCl slurry could not be investigated. However, with a similar particle-particle interaction (see AFM data chapter 5) and similar critical bed shear stresses, a reasonable estimate can be made through extrapolating the single data point using the same conditions as for the 10^{-4}M KNO_3 slurry. The minimum transport velocity for a 10^{-4}M KCl slurry is therefore $0.15ms^{-1}$.

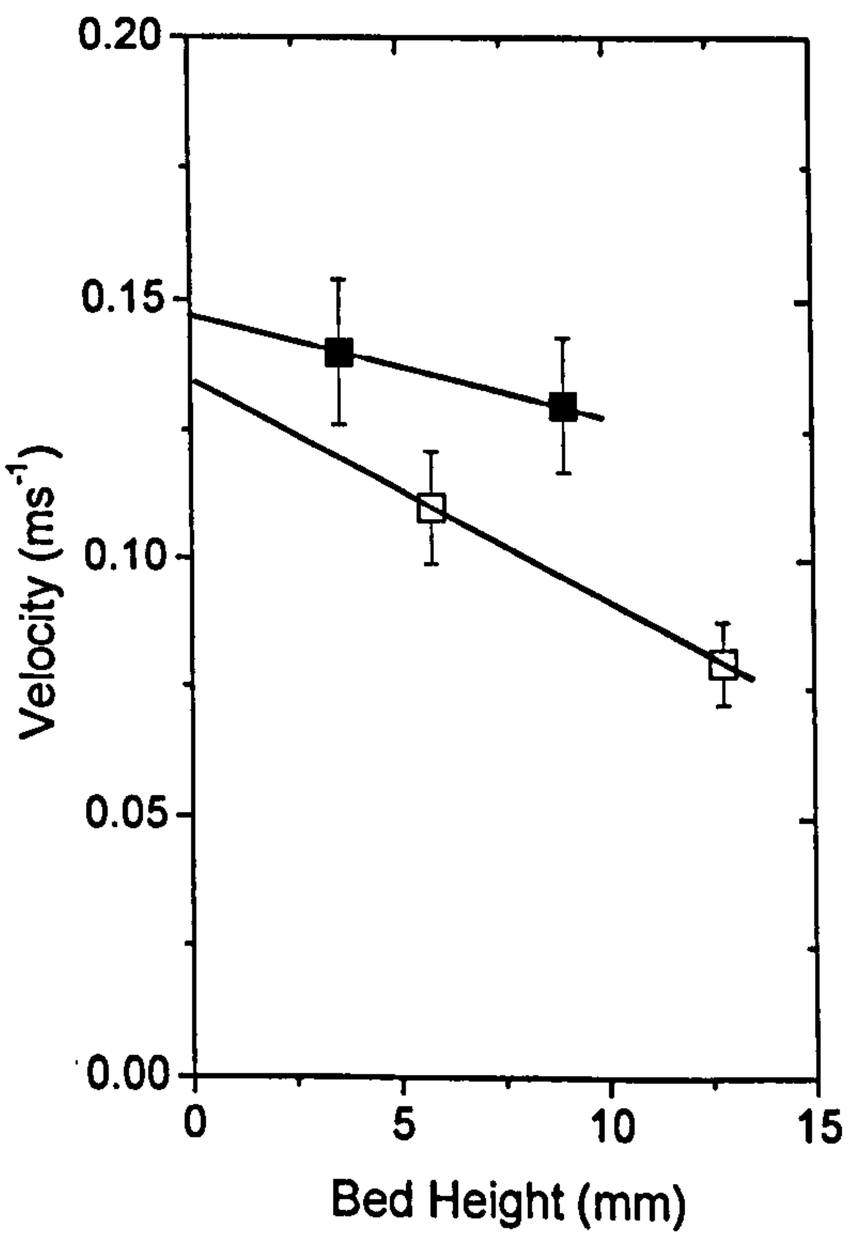

Figure 6.15 Slurry transition velocities as a function of sediment bed height. Extrapolate to 0mm bed height to determine the minimum transport velocity. Symbols: open square 1M KNO_3, closed square 10^{-4}M KNO_3.

An additional attempt to determine the minimum transport velocity of the colloidal suspensions in the absence of a sediment bed was made using ultrasonic Doppler velocity

profiling. The solids effect on the velocity profile of a suspension is determined by comparing the suspension velocity profile to a single phase profile at an equivalent flow velocity. The technique is used to determine the mean flow velocity when the two profiles diverge, and the suspension profile is exceeded (local velocity) by the single phase profile; indicating that the fluid drag is increasing and particles depositing onto the pipe invert. Figure 6.16 shows how the 2 profiles (single phase and suspension) correlate with each other from the pipe centre at r/R = 0 to the pipe wall r/R = 1.0 as a function of the mean flow velocity. Comparing a 10^{-4}M KNO_3 suspension at 5.5 % by volume and a 1M KNO_3 suspension 5.7 % by volume to a single phase profile, the difference in the suspension and single phase profiles at 0.19ms^{-1} can be considered insignificant and within error. For the two suspensions considered in figure 6.16, a reduction in the mean flow velocity to 0.15ms^{-1} identifies a small deviation at the pipe wall which suggests that the particles are depositing out of suspension, thus increasing the drag on the fluid motion. Two further reductions in the mean flow velocity (0.11ms^{-1} and 0.07ms^{-1}) show an ever increasing drag effect at the pipe wall as more and more particles deposit from suspension forming a bed on the pipe invert. The data suggests that the minimum transport velocity for a 10^{-4}M KNO_3 and a 1M KNO_3 suspension is between 0.19ms^{-1} and 0.15ms^{-1} which is in reasonable agreement with the velocities determined by extrapolating the transition velocities which were measured using PIV.

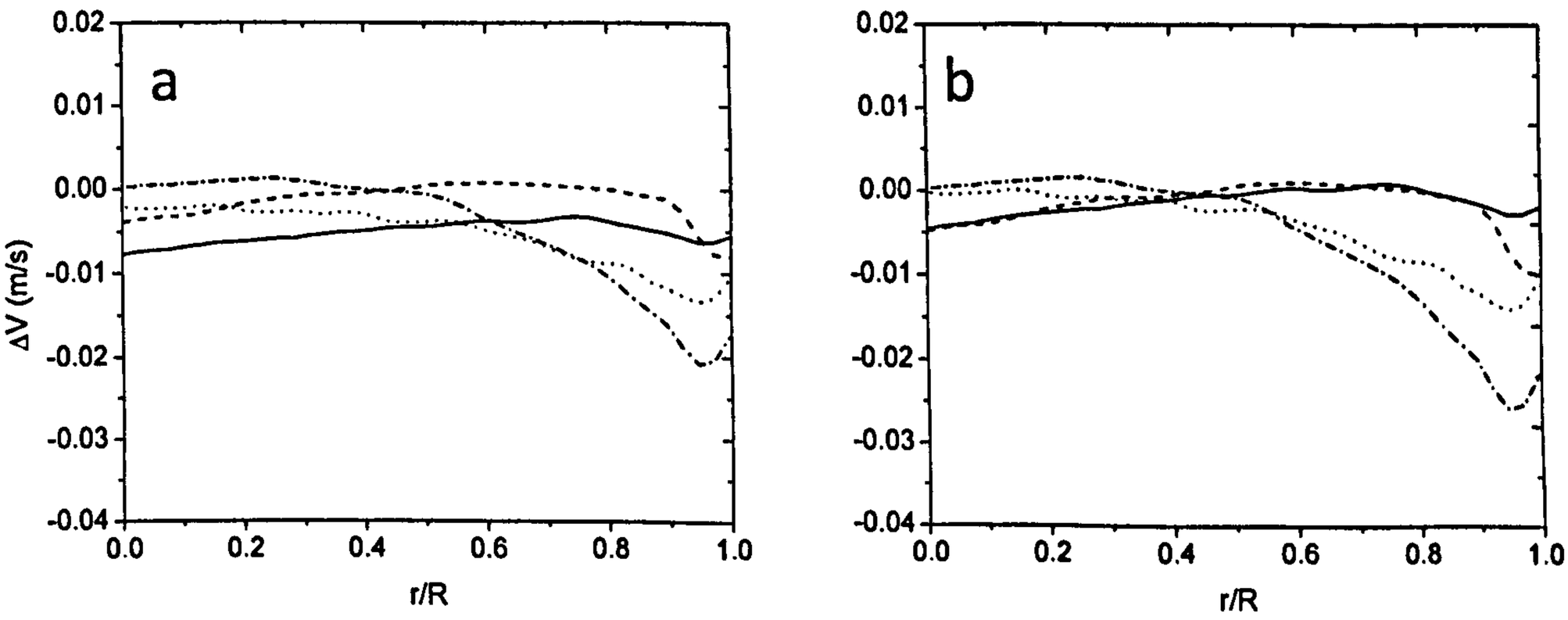

Figure 6.16 Variation in the slurry and single phase velocity profiles at different mean flow velocities. Mean velocity – solid line - 0.19ms^{-1}, dash – 0.15ms^{-1}, dot - 0.11ms^{-1}, dash dot – 0.07ms^{-1}. a) 10^{-4}M KNO_3 (5.5 %vol.) b) 1M KNO_3 (5.7 %vol.).

Having determined the minimum transport velocities experimentally, a comparison has been made with the predicted values using the correlations given in table 5.0. Durand's [2, 3] correlation is within reasonable agreement when F_L = 0.2 (particle size ≈ 0mm), predicting a minimum transport velocity equal to 0.16m/s. The correlation by Spells [18] greatly under predicts the minimum transport velocity predicting 0.00m/s when rounded to two decimal places. The correlations of Thomas [13] and Davies [20] provide similar results to each other with a predicted transport velocity ≈ 0.40m/s. A value of 0.42m/s is determined using Thomas's graphical approach when applying the lower limit parameter (the deposit velocity is equal to the deposit velocity of a 25μm silica sphere). Davies' correlation accounts for changes in the solids concentration, and predicts an increase in the minimum transport velocity from 0.38m/s to 0.40m/s when the solids concentration increases from 5.5 % to 12.5 % by volume. The disagreement between the experimental data and many of the predicted velocities is not unexpected. As previously discussed, colloidal suspensions tend to fall outside the limits to which these correlations have been developed, therefore, resulting in significant error.

6.5 Conclusion

The critical transport velocities of three colloidal suspensions have been studied using two novel experimental approaches. Existing approaches to determine the minimum transport velocity of a solid-liquid suspension were precluded for several reasons which have already been discussed earlier in the thesis. One approach to determine the minimum transport velocity involved plotting the deviation between a single phase velocity profile and a suspension velocity profile across the pipe radius (r/R = 0 to r/R =1) for an equivalent mean flow velocity. When the mean flow velocity exceeds the minimum transport velocity the difference between the two velocity profiles is negligible. As the mean flow velocity is reduced below the minimum transport velocity, the two profiles diverge and the local mean velocity for the suspension flow at the pipe wall is exceeded by the local mean velocity for the single phase flow. The reduction in the local mean velocity for the suspension flow results from an increase in fluid drag as particles deposit and slide along the pipe invert. The data collected using UDVP concluded that for both the dispersed (10^{-4}M) and

aggregated (1M) suspensions, the minimum transport velocity was in the range of 0.19ms^{-1} to 0.15ms^{-1}.

A second technique involved measuring the transition velocity of a sediment bed (onset velocity for bed erosion) to determine the minimum transport velocity of the colloidal suspensions. PIV, with the laser sheet passing through the longitudinal axis of the pipeline provided sufficient illumination for the sediment bed erosion rate to be monitored as a function of the slurry velocity. The transition velocity of the sediment bed is observed to be dependent on the solids loading and the electrolyte concentration. With an increase in the solids concentration the transition velocity for the sediment decreases, while the critical bed shear stress (dependent on the bed yield stress) remains unchanged. With a constant critical bed shear stress, the "bed effect" on the transition velocity is negligible when the transition velocities are extrapolated to zero bed height. The transition velocity at zero bed height is identified as the minimum transport velocity. For the three colloidal suspensions studied the minimum transport velocities are given in table 6.4.

Table 6.4 Colloidal suspension minimum transport velocities.

	Minimum Transport Velocity (ms^{-1})
10^{-4} M KNO_3	0.15
1M KNO_3	0.13
10^{-4}M KCl	0.15

For the same electrolyte concentration (10^{-4}M), the minimum transport velocities are equal and independent of the electrolyte anion. With a purely repulsive particle-particle interaction, the particles will remain dispersed in the flow and should therefore have the same minimum transport velocity. With an increase in the electrolyte concentration, the interaction between the particles in no longer purely repulsive but is influenced by a significant adhesion force. The adhesion force between the particles results in the formation of small aggregates which are nearly an order of magnitude in size greater than the primary silica spheres (refer to chapter 4 for particle size and aggregate structures). The minimum transport velocity of the aggregates is lower than the minimum transport velocity for the smaller, dispersed spheres. With a greater particle diameter and a greater

sedimentation velocity (see chapter 4), it would be expected that the minimum transport velocity would be greater than the velocity measured for the dispersed suspensions. The following chapter provides an answer for this observation with regards to the turbulence intensities in a dispersed and aggregated suspension.

Chapter References

1. Blatch, N.S., Transactions of the American Society of Civil Engineering, 1906. **LVII**: p. 400-408.
2. Durand, R. and E. Condolios, *The hydraulic transport of coal and solid materials in pipes.* Proceedings of a Colloquium on the Hydraulic Transport of Coal, 1952: p. 39-52.
3. Durand, R., *Basic relationships of the transportation of solids in pipes - experimental research.* Proc. Conf. Int. Assoc. Hydraulic Res., 1953: p. 89-103.
4. Molerus, O. and P. Wellmann, *A new concept for the calculation of pressure drop with hydraulic transport of solids in horizontal pipes.* Chemical Engineering Science, 1981. **36**(10): p. 1623-32.
5. Newitt, D.M., et al., *Hydraulic conveying of solids in horizontal pipes.* Transactions of the Institution of Chemical Engineers, 1955. **33**: p. 93-113.
6. Turian, R.M. and T.-F. Yuan, *Flow of slurries in pipelines.* AIChE Journal, 1977. **23**(3): p. 232-43.
7. Wilson, K.C., *A unified physically-based analysis of solid-liquid pipeline flow.* BHRA Fluid Engineering, 1976: p. 1-16.
8. Gillies, R.G., C.A. Shook, and K.C. Wilson, *An improved two layer model for horizontal slurry pipeline flow.* Canadian Journal of Chemical Engineering, 1991. **69**(1): p. 173-8.
9. Doron, P. and D. Barnea, *Flow pattern maps for solid-liquid flow in pipes.* International Journal of Multiphase Flow, 1996. **22**(2): p. 273-83.
10. Turian, R.M., F.L. Hsu, and T.W. Ma, *Estimation of the critical velocity in pipeline flow of slurries.* Powder Technology, 1987. **51**(1): p. 35-47.
11. Thomas, D.G., *Transport characteristics of suspensions. VI. Minimum transport velocity for large particle size suspensions in round horizontal pipes.* AIChE Journal, 1962. **8**: p. 373-8.
12. Lowenstein, J.G., *For horizontal flow of slurries, design so solids cannot settle out.* Chem. Eng., 1959. **66**(No. 1): p. 133-5.
13. Thomas, A.D., *Predicting the deposit velocity for horizontal turbulent pipe flow of slurries.* International Journal of Multiphase Flow, 1979. **5**(2): p. 113-29.

14. Parzonka, W., J.M. Kenchington, and M.E. Charles, *Hydrotransport of solids in horizontal pipes: effects of solids concentration and particle size on the deposit velocity.* Canadian Journal of Chemical Engineering, 1981. **59**(3): p. 291-6.

15. Wasp, E.J. and P.T. Slatter, *Deposition velocities for small particles in large pipes.* 12th International Conference on the Transport and Sedimentation of Solid Particles, 2004: p. 671-680.

16. Gillies, R.G. and C.A. Shook, *A deposition velocity correlation for water slurries.* The Canadian Journal of Chemical Engineering, 1991. **69**: p. 1225-1227.

17. Carleton, A.J. and D.C.H. Cheng, *Design velocities for hydraulic conveying of settling suspensions.* Proc. 3rd Int. Conf. on Hydraulic Transport of Solids in Pipes, 1974: p. 57-74.

18. Spells, K.E., *Correlations for use in transport of aqueous suspensions of fine solids in pipes.* Transactions of the Institution of Chemical Engineers, 1955. **33**: p. 79-82.

19. Thomas, D.G., *Transport characteristics of suspensions: II. Minimum transport velocity for flocculated suspensions in horizontal pipes.* AIChE Journal, 1961. 7(3): p. 423-430.

20. Davies, J.T., *Calculation of critical velocities to maintain solids in suspension in horizontal pipes.* Chemical Engineering Science, 1987. **42**(7): p. 1667-70.

21. Gillies, R.G., et al., *A method for estimating the deposition velocities for psudohomogenous slurries.* ASME Engineering Division 1997.

22. Thomas, D.G., *Heat and momentum transport characteristics of non-Newtonian aqueous thorium oxide suspensions* AIChE Journal, 1960. **6**(4): p. 631-639.

23. Durand, R. and E. Condolios, *The hydraulic transport of coal and solid material in pipes.* Proceedings of a Colloquium on the Hydraulic Transport of Coal, 1953(39-52).

24. Wilson, K.C., *Slip point of beds in solid-liquid pipeline flow.* Proc. Amer. Soc. Civil Eng., 1970. **96**: p. 1-12.

25. Davies, J.T., *Velcoities and Stresses in Turbulent Flows.* Turbulence Phenomena: An Introduction to the Eddy Transfer of Momentum, Mass, and Heat, Particularly at Interfaces, 1972.

26. Shook, C.A., *Developments in Hydrotransport.* The Canadian Journal of Chemical Engineering, 1976. **54**: p. 13-25.

27. Heywood, N.I. and D.C.H. Cheng, *Flow in pipes. Part 2: multiphase flow.* Physics in Technology, 1984. **15**(6): p. 291-300, 314.

28. Doron, P. and D. Barnea, *Pressure drop and limit deposit velocity for solid-liquid flow in pipes.* Chemical Engineering Science, 1995. **50**(10): p. 1595-604.

29. Pullum, L. and L.J.W. Graham, *The use of magnetic resonance imaging (MRI) to probe complex hybrid suspension flows.* Proc. 10th International Conference on Transport and Sedimentation of Solid Particles, 2000: p. 421-433.

30. Horsley, R.R. and J.A. Reizes, *Variation in head loss gradient in laminar slurry pipe flow due to changes in zeta potential.* The South African Mechanical Engineer 1978. **28**: p. 307-311.

31. Horsley, R.R., *Viscometer and pipe loop tests on gold slime slurry at very high concentrations by weight, with and without additives.* Hydrotransport 8 - 8th Internation Conference on the Hydraulic Transport of Solids in Pipes, 1982: p. 367-382.

32. MacInnes, M.A., *Investigation into the effects of slurry thinners on the rheology of chalk slurry.* BHR Group Conference - Hydrotransport 15, 2002: p. 375-384.

33. Heywood, N.I. and N.J. Alderman, *Agitating thixotropic, shear-thinning slurries effectively to reduce pipeline transfer costs.* 12th International Conference on the Transport and Sedimentation of Solid Particles, 2004: p. 403-412.

34. Plewa, F., M. Popczyk, and G. Strozik, *Laboratory measurements of effects accompanying stopping and starting of flow of fine-grained slurries in hydrotransportation systems.* 12th International Conference on the Transport and Sedimentation of Solid Particles, 2004: p. 547-555.

35. Williamson, R., I. Newson, and T.R. Bott, *The deposition of haematite particles from flowing water.* The Canadian Journal of Chemical Engineering, 1988. **66**: p. 51-54.

36. Williamson, R., *Deposition of Iron oxide particles on metallic surfaces from flowing water suspension.* PhD, University of Birmingham, UK., 1988.

37. Vasak, F., et al., *Fine particle deposition in laminar and turbulent flows.* The Canadian Journal of Chemical Engineering, 1995. **73**: p. 785-791.

38. El-Nahhas, K., et al., *The laminar/turbulent transitional condition of non-Newtonian slurries flow in pipes.* BHR Group Conference - Hydrotransport 16, 2004: p. 47-60.

39. Ravisangar, V., et al., *Effect of sediment pH on resuspension of kaolinite sediments.* Journal of Environmental Engineering (Reston, Virginia), 2001. **127**(6): p. 531-538.

40. Johnson, S.B., A.S. Russell, and P.J. Scales, *Volume fraction effects in static shear rheology and electroacoustic studies of concentrated alumina and kaolin suspensions.* Colloids and Surfaces, A: Physicochemical and Engineering Aspects, 1998. **141**(1): p. 119-130.

41. Leighton, D. and A. Acrivos, *Viscous resuspension.* Chemical Engineering Science, 1986. **41**(6): p. 1377-84.

42. Gadala-Maria, F.A., *The rheology of concentrated suspension.* Thesis, 1979.

43. Chapman, B.K. and D.T. Leighton, Jr., *Dynamic viscous resuspension.* International Journal of Multiphase Flow, 1991. **17**(4): p. 469-483.

44. Feng, Z.-G. and E.E. Michaelides, *Interparticle forces and lift on a particle attached to a solid boundary in suspension flow.* Physics of Fluids, 2002. **14**(1): p. 49-60.

45. Crowe, C.T. and E.E. Michaelides, *Basic concepts and definitions* Multiphase Flow Handbook, 2005: p. I - 48.

46. Saffman, P.G., *The lift on a small sphere in a slow shear flow.* Journal of Fluid Mechanics, 1964. **22**(2): p. 385-400.

47. Wilson, K.C. and A. Sellgren, *Near-wall particle lift and deposition in slurry pipelines.* BHR Group Hydrotransport 15, 2002: p. 789-800.

48. Leighton, D.T., Jr. and A. Acrivos, *The lift on a small sphere touching a plane in the presence of a simple shear flow.* Journal of Applied Mathematics and Physics, 1985. **36**: p. 174-178.

49. Cherukat, P. and J.B. McLaughlin, *The inertial lift on a rigid sphere in a linear shear flow field near a flat wall.* Journal of Fluid Mechanics, 1994. **263**: p. 1-18.

50. Cherukat, P. and J.B. McLaughlin, *Wall-induced lift on a sphere.* International Journal of Multiphase Flow, 1990. **16**(5): p. 899-907.

51. Massoudi, M., *On drag and lift forces in two-dimensional flows of a particualate mixture: A theoretical study.* Acta Mechanica, 2006. **185**: p. 131-146.

52. Mollinger, A.M. and F.T.M. Nieuwstadt, *Measurement of the lift force on a particle fixed to the wall in the viscous sublayer of a fully developed turbulent boundary layer.* Journal of Fluid Mechanics, 1996. **316**: p. 285-306.

53. Hall, D., *Measurements of the mean force on a particle near a boundary in turbulent flow.* Journal of Fluid Mechanics, 1988. **187**: p. 451-466.

54. Kline, S.J., et al., *The structure of turbulent boundary layers.* Journal of Fluid Mechanics, 1967. **30**(4): p. 741-773.

55. Cleaver, J.W. and B. Yates, *Mechanism of detachment of colloidal particles from a flat substrate in a turbulent flow.* Journal of Colloid and Interface Science, 1973. **44**(3): p. 464-74.

56. Corino, E.R. and R.S. Brodkey, *A visual investigation of the wall region in turbulent flow.* Journal of Fluid Mechanics, 1969. **37**(1): p. 1-30.

57. Wilson, K.C., et al., *Slurry transport using centrifugal pumps.* Blackie Academic and Professional, 1996.

58. Patel, V.C. and M.R. Head, *Some observations on skin friction and velocity profiles in fully developed pipe and channel flows.* Journal of Fluid Mechanics, 1969. **38**(1): p. 181-201.

59. Den Toonder, J.M.J. and F.T.M. Nieuwstadt, *Reynolds number effects in a turbulent pipe flow for low to moderate Re.* Physics of Fluids, 1997. **9**(11): p. 3398-3409.

60. Eggels, J.G.M., et al., *Fully developed turbulent pipe flow: a comparison between direct numerical simulation and experiment.* Journal of Fluid Mechanics, 1994. **268**: p. 175-209.

61. Zalzal, P., et al., *Visualization of transitional pipe flow using the photochromic tracer method.* Physics of Fluids, 1994. **6**(6): p. 2003-10.

62. Schlichting, H., *Boundary-layer Theory.* McGraw-Hill, New York, 1968.

63. Krone, R.B., *Effects of bed structure on erosion of cohesive sediments.* Journal of Hydraulic Engineering, 1999. **125**(12): p. 1297-1301.

64. Roberts, J., et al., *Effects of particle size and bulk density on erosion of quartz particles.* Journal of Hydraulic Engineering, 1998. **124**(12): p. 1261-1267.

65. Jepsen, R., J. Roberts, and W. Lick, *Effects of bulk density on sediment erosion rates.* Water Air and Soil Pollution, 1997. **99**: p. 21-31.

Chapter 7

TURBULENCE MODULATION STUDY OF A DISPERSED AND AGGREGATED COLLOIDAL SUSPENSION

NOMENCLATURE

D	Diameter of pipe
R	Radius of pipe
U	Mean streamwise velocity
$\bar{U}$	Depth-averaged streamwise velocity
u	Instantaneous velocity
u'	RMS streamwise component of the flow
u''	Turbulence intensity
u_s''	Suspension turbulence intensity
u_f''	Fluid turbulence intensity
η	Small scale eddy length
ν	Kinematic viscosity
ε	Local turbulence energy dissipation rate per unit mass
ρ	Density of fluid
τ	Turbulent shear stress
τ_a	Aggregate shear strength
μ_t	Kinematic eddy viscosity
$\overline{v'_x v'_y}$	Streamwise and vertical fluctuating velocity components
λ *or* l_e	Mixing length parameter
$\frac{\partial U}{\partial y}$	Fluid velocity gradient

ABREVIATIONS

DLVO	Derjaguin, Landau, Verwey and Overbeek Theory
NB	Nominal bore
Re	Reynolds number

RMS Root mean square
UDVP Ultrasonic Doppler velocity profiling

Synopsis

The centre-line and near wall streamwise turbulence intensities of colloidal silica suspensions measured using ultrasonic Doppler velocity profiling in the presence of 10^{-4}M and 1M electrolytes are compared in this chapter. Turbulence which provides the energy to maintain particles in suspension is discussed, prior to a review on turbulence modulation in dilute suspension flows.

7.1 Turbulence and Turbulence Modulation

The transportation mechanisms by which solid particles are carried in pipelines as discussed by Wilson and Sellgren [1] can be considered as either bed load transport, where the submerged weight of the particles is transferred to the pipe wall, or suspended load transport, where the particles are supported by the fluid. Fluid support can be further subdivided into laminar and turbulent flow conditions, with laminar describing viscous transportation (refer to chapter 6) and turbulent describing the contribution in the form of turbulent diffusion[2]. Turbulence is the term given to describe the unsteady chaotic movements of fluid elements in different directions superimposed on the main flow of the liquid. The transition from laminar to turbulent flow is described by the Reynolds number and is typically observed to occur between $Re = 2000$ and $Re = 4000$ depending upon the physical properties of both the pipe and the fluid. The structure of the turbulent boundary layer is defined by the production, transport and dissipation of the turbulence kinetic energy in the flow. Turbulent eddy production is largely concentrated in the near wall region where large velocity gradients provide an environment of high shear which is favourable in the production of fluid eddies. Kline et al. [3], referring to the earlier work of Klebanoff [4], discussed the production rate of turbulence energy in the boundary layer in terms of energy per unit volume. Figure 7.0 which is adapted from Kline et al. [3], shows that nearly half of the total production of turbulence energy is within the near wall region, and that the outer 80% of the boundary layer accounts for as little as 20% of the total energy production.

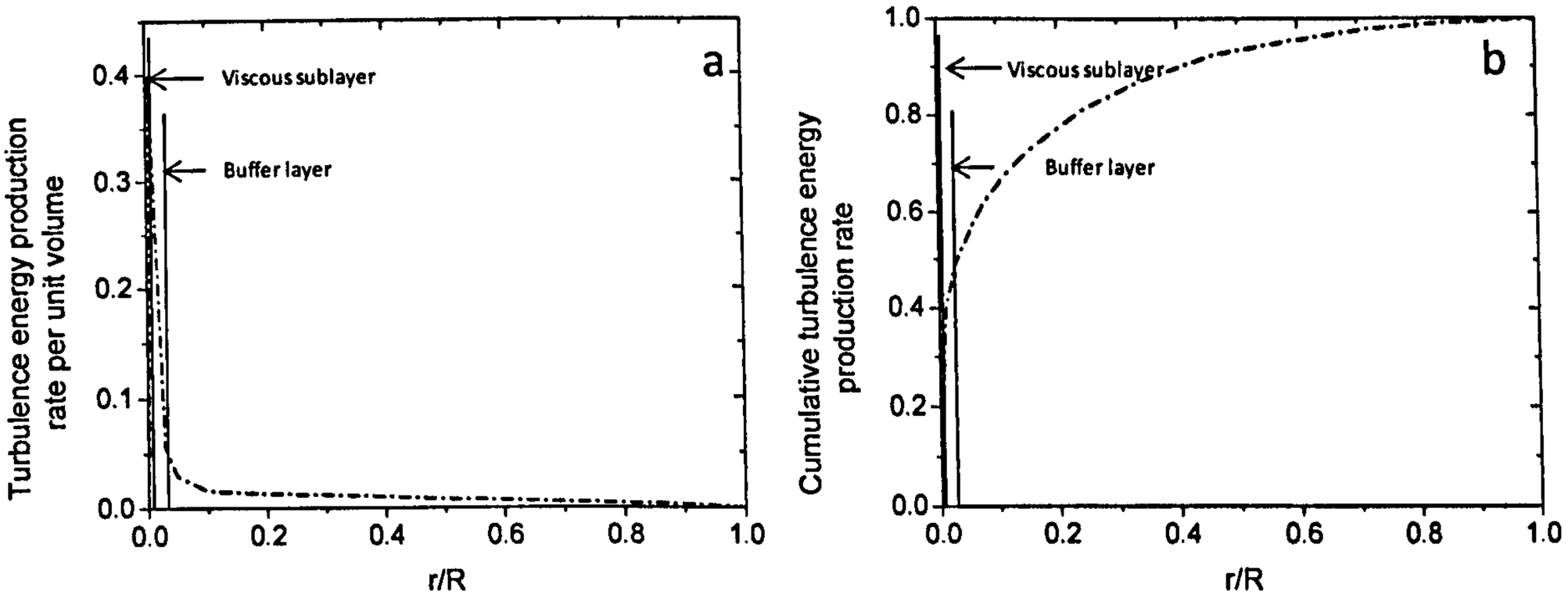

Figure 7.0 a) Normalised turbulence energy production rate per unit volume and b) cumulative turbulence energy production rate in a typical turbulent boundary layer. Figures adapted from reference [3].

Turbulent flows generate a spectrum of eddy lengths from the largest eddy which is dependent on the pipe diameter, down to the smallest eddy which is suitably described by the Kolmogoroff micro-scale equation. The limiting size of the small scale eddy (ŋ) is given as[5]:

$$\eta = \left(\frac{\nu^3}{\varepsilon}\right)^{1/4} \qquad [7.0]$$

where ν is the kinematic viscosity of the fluid and ε is the local turbulence energy dissipation rate per unit mass. Associated with the eddy length spectrum is the turbulence energy spectrum[6]. Large eddies which are relatively long-lived and are independent of the fluid viscosity are considered to be energy producing, transferring energy to the small scale eddies which are considered to be energy dissipating; with significant dissipation of kinetic energy into heat through viscous forces.

Approximate expressions for the eddy length scales in turbulent pipe flow are given in table 6.0[5] which includes the length scales for energy-containing and energy-dissipating. Such eddies relate to the intermediate region of the turbulence energy spectrum.

Table 7.0 Approximate expressions for turbulent eddy lengths.

Eddy	Length scale
Largest	$0.5D$
Energy-containing	$0.05D(Re)^{-0\,13}$
Energy-dissipating	$20D(Re)^{-0\,78}$
Kolmogoroff	$4D(Re)^{-0.78}$

Clearly, the turbulent properties of a fluid are influenced by the scale and intensity of the eddies in the flow. The addition of particles to a fluid has been shown by several researchers to modulate the turbulence intensity [7-13]. This relationship between the fluid and the turbulence properties is shown when one considers the expressions for turbulent shear stress within the boundary layer. The turbulent shear stress (τ) can be expressed by one of the relationships below, depending on the level of representation employed[14]:

$$\tau = -\rho\,\overline{v'_x v'_y} \qquad [7.1]$$

$$\tau = \rho\lambda^2 \left|\frac{\partial U}{\partial y}\right| \left(\frac{\partial U}{\partial y}\right) \qquad [7.2]$$

$$\tau = \rho\mu_t \frac{\partial U}{\partial y} \qquad [7.3]$$

with equation 7.1 including the term ($\overline{v'_x v'_y}$) which accounts for the fluctuating velocity components from the mean in the streamwise and vertical directions ($-\rho\,\overline{v'_x v'_y}$ is commonly referred to as the Reynolds stress). Equation 7.2 includes the mixing length parameter (λ) or the eddy size and equation 7.3 includes the kinematic eddy viscosity (μ_t). ρ and $\frac{\partial U}{\partial y}$ represent the density of the fluid and the velocity gradient respectively.

The addition of particles to a fluid may therefore influence the turbulence intensity through affecting either one or all of the following: i) the velocity gradient [9, 15]; ii) the eddy viscosity; iii) the eddy mixing length[16] and iv) the density of the fluid sediment mixture.

Early studies on turbulence modulation were conducted by measuring the heat transfer rate between the suspension and the pipe wall [17], investigating the effect of both particle concentration and size. An enhancement in the heat transfer rate of a particle laden suspension was related to the increased frequency and intensity of turbulent disturbances

within the viscous sub layer (refer to chapter 6, viscous sub layer turbulent bursts); a result of fluid-particle interactions modifying the strength of both the free stream and near wall turbulence. A 35% enhancement in the heat transfer rate was measured for a suspension containing particles in the size range d_{50} = 25μm at a concentration of 4% by volume. The author also observed a reduction in the heat transfer rate with an increase in the solids concentration, and they implied such behaviour to be linked to turbulence dampening due to an increased importance of particle-particle interactions. To further understand the effects of particle size and concentration on the turbulence properties of fluids, the authors published an additional paper which used laser-Doppler anemometry to measure the flow velocities and the turbulence quantities to within 50μm of the pipe wall [7]. Using methyl benzoate as the carrier fluid and glass particles (d_{50} = 53μm) as the dispersed phase both the free stream and near wall turbulence properties up to a solids concentration of 5.6% by volume were compared. A reduction in the free stream turbulence level to an almost constant value at higher solids loadings was in contradiction with the turbulence modulation behaviour in the near wall region. An enhancement in the streamwise turbulence levels in the near wall region was related to the interaction between the particle and the fluid eddy as both length scales approached within the same order of magnitude. Zisselmar and Molerus [7] confirmed through theoretical derivation using Taylor's micro scale, that the eddy length at the point where the maximum turbulence enhancement was observed was equivalent to $0.25d_p$. This correlation may be coincidental as it corresponds to a distance just outside the viscous sub layer. At the edge of the viscous sub layer the rates of turbulence energy production, dissipation and diffusion pass through a sharp maximum [18]. Therefore, under particle loading any influence of two-way and/ or four-way coupling is most likely to have a greater affect in this region.

A brief communication by Gore and Crowe [8] is one of the most commonly cited turbulence modulation publications. They proposed a simple physical model to explain the modulation characteristics of free stream turbulence caused by the addition of particles. A critical parameter, identified as the ratio between the particle diameter (d_p) and the characteristic length scale of the most energetic eddy ((λ) or l_e in the original publication. Gore and Crowe relate this parameter to $l_e/R \approx 0.2$ which is based on the results of Hutchinson et al. [19], who showed that the turbulence length scale divided by the pipe radius is approximately equal to 0.2 except near the pipe wall. This relationship has been

used by Gore and Crowe [8] to compare all data sets), showed a demarcation between turbulence attenuation and augmentation when $d_p/\lambda \approx 0.1$. Figure 7.1 from the original publication shows the percentage change in turbulence intensity as a function of the length scale ratio. The experimental data used to form the plot included gas-solid, gas-liquid, solid-liquid, and liquid-gas flows, with Reynolds numbers ranging from 8000 to 100,000; solid-fluid density ratio variations from 0.0012 to 2500, and volume concentration variations from 10^{-6} to 0.2. The experimental geometries also differed, with axisymmetric jets and horizontal/vertical (upward and downward) pipe flow data compared. The demarcation is associated with the particle size. The authors comment that when $d_p/\lambda \ll 0.1$, a fraction of the fluid eddy energy is transformed into the kinetic energy of the particle, enabling the particle to maintain its motion within the eddy overcoming any viscous/fluid drag forces, thus reducing the turbulent intensity of the fluid. When $d_p/\lambda \gg 0.1$, vortex shedding from the particle surface creates eddies of the same order of magnitude as the most energetic eddy, thus enhancing the turbulent intensity of the fluid.

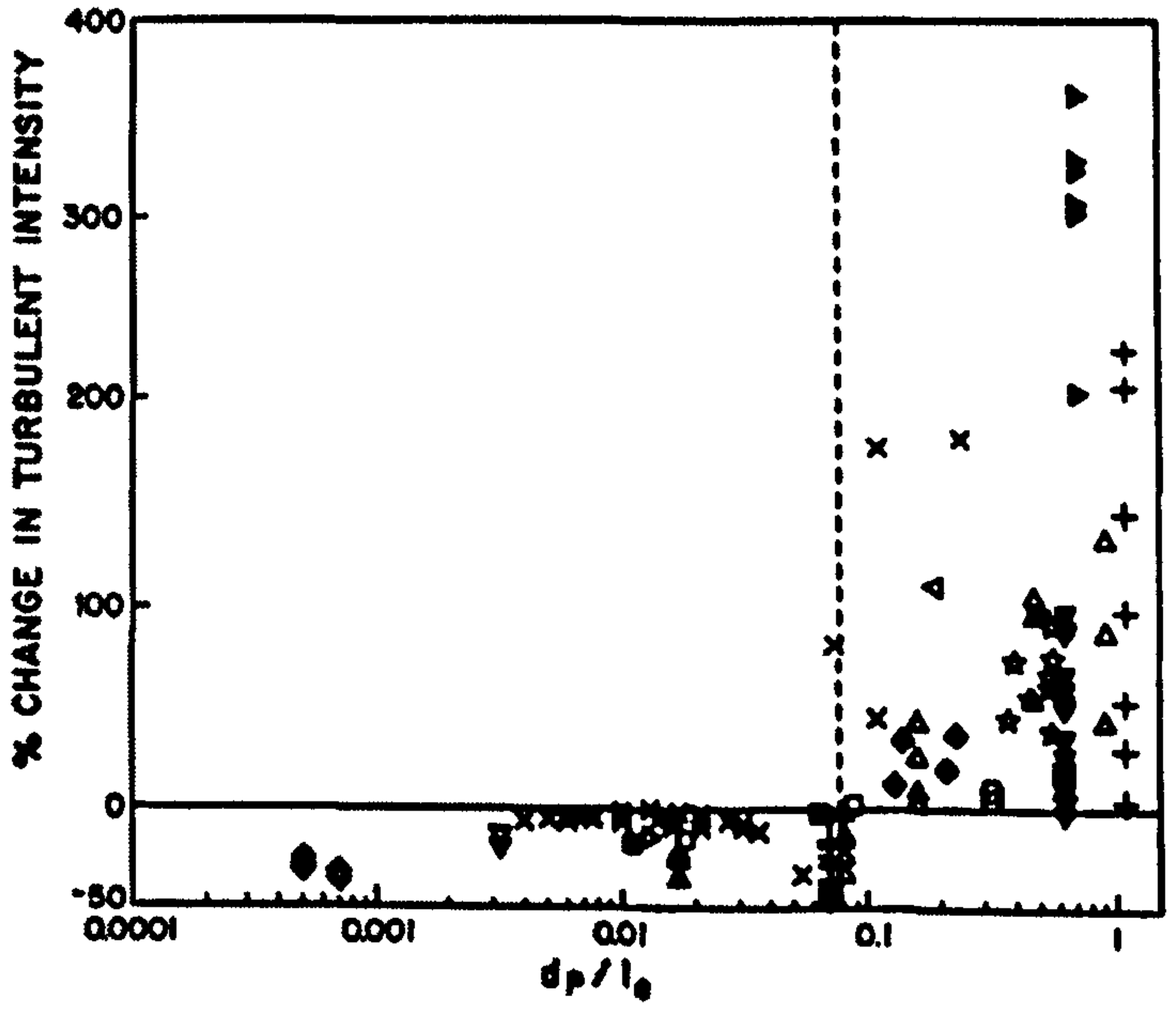

Figure 7.1 Change in turbulence intensity as a function of the critical length scale parameter, taken from reference [8].

Evidently, as the length scale ratio increases and two-way coupling becomes more important the data shows a higher degree of scatter. It should be reiterated that the critical parameter can only provide a means to determine whether the fluid turbulence is augmented or attenuated. In order to reduce the scatter and predict the level of turbulence

modulation, consideration should also be given to the fluid and particle Reynolds numbers[11, 20, 21], the solid-liquid density ratio[22], the fluid viscosity and the solids loading[7]. Gore and Crowe [8] also comment on the selectivity of the data used in the study. A significant exemption from the plot was the data collected by Maeda et al. [23] who investigated the turbulence properties of air flows in the presence of 45μm glass spheres. With $d_p/\lambda < 0.1$, the ratio suggests that the addition of particles would dampen the turbulence intensity of the flow. However, with a mass loading increasing from 0 to 0.49, the centre-line turbulence intensity was observed to increase. The data was not considered in the review[8] as it was thought that the particles had formed aggregates producing secondary flow effects that are not observed when the particles remain dispersed.

7.2 Experimental investigation on the turbulence modulation of dispersed and aggregated colloidal suspensions

The influence of colloidal particles on the turbulence properties of fluids has received very little attention in the literature. The size of such particles and the extremely low solid volume fractions commonly used in turbulence studies means that one-way coupling mechanics dominate the fluid properties, with no modulation of the fluid turbulence through particle-fluid interaction. In the present study suspension concentrations up to 12% by volume are investigated where four-way coupling [24] and possibly two-way coupling become important. The experimental programme has been designed to evaluate the centre-line and near wall turbulence properties of particle un-laden and laden flows. The objective is to understand the influences of i) high solid loadings and ii) aggregates on the turbulence intensities of the flow.

The root-mean square values (u') of the streamwise fluctuating component of the flow are calculated from[14]:

$$u' = \left[\frac{1}{n}\sum_{i=1}^{n}(u-U)^2\right]^{0.5} \qquad [7.4]$$

where u is the instantaneous velocity and U is the mean streamwise velocity. Subsequently the turbulence intensity is then determined by[14]:

$$u'' = \frac{u'}{\bar{U}} \qquad [7.5]$$

where $\bar{U}$ is the depth-averaged streamwise velocity.

To provide a comparison between the particle laden and un-laden flows the percentage change in the turbulence intensity is defined as:

$$\frac{u_s'' - u_f''}{u_f''} \times 100 \qquad [7.6]$$

where subscripts *s* and *f* refer to the suspension and fluid flows respectively.

Experimental results of the streamwise fluctuating component for a particle un-laden fluid at three different mean flow velocities are shown in figure 7.2. The instrument sensitivity of the UDVP probe lowers the data collection resolution at the pipe wall resulting in $u'' > 0$ at r/R = 1. However, the characteristic trend in the turbulence intensity increasing from the pipe centre-line to a maximum in the near wall region and then decreasing at the pipe wall is observed in all three cases, corresponding to the profiles by Laufer [18]. When comparing the turbulence intensity values as a function of the flow Reynolds number there is no difference, within error, at the pipe centre-line. But, at r/R ≈ 1 the three profiles diverge with higher turbulence intensities measured in the near wall region when the flow Reynolds number is reduced. This behaviour has also been observed by Perry and Abell [6] studying the pipe flow longitudinal turbulence component of air at four Reynolds numbers ranging from 78×10^3 to 257×10^3. Perry and Abell suggest [6] that the deviation relates to the increased fluid-wall interaction in the inner region of turbulent flow. Figure 7.2 also presents data from Wang et al. [25] who considered the turbulence properties of water at a Reynolds number of 23×10^3 in a 57mm NB pipe.. The data set provides the closest representation to the experimental parameters used in the present study, thus highlighting the lack of data for water flows in pipes at low Reynolds numbers. The data set however proves to be very useful showing the centre-line turbulence intensity approximating well with the data collected in the current study, whilst following the trend in turbulence intensity divergence in the near wall region.

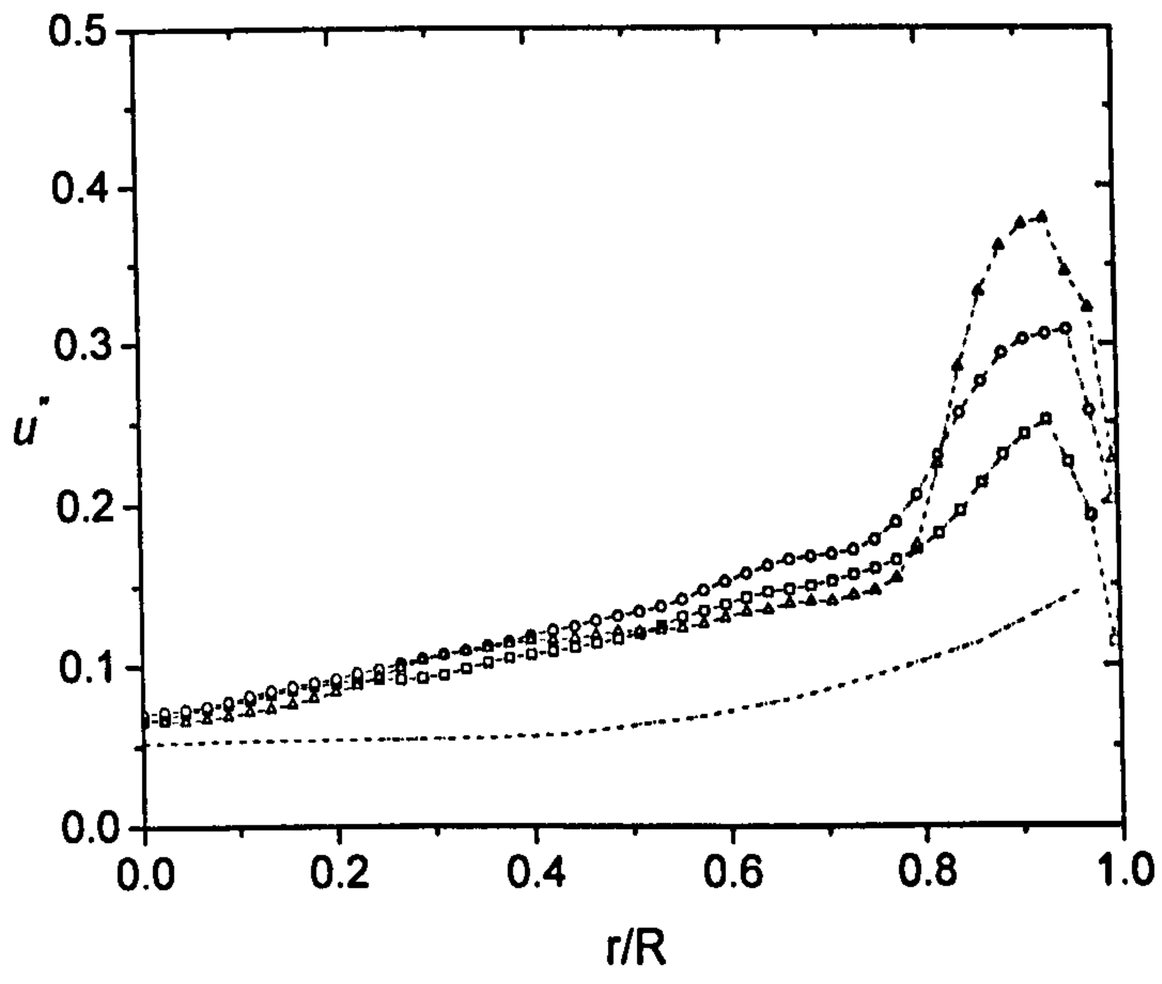

Figure 7.2 Turbulence intensities of the streamwise fluid component: square – *Re* = 10400, circle – *Re* = 7800, triangle – *Re* = 5200. Dashed line published data Wang et al. [25].

Typical data for the streamwise turbulence intensity component for the particle laden flows in this study are shown in figures 7.3 (a-d). The data are separated to illustrate the influence of increased solids loading on the turbulence properties of dispersed and aggregated suspensions. In all cases there is minimal variation in the free stream and near wall turbulence intensities of the flows as the solids concentration is in increased from 6% to 12% by volume. Analysis of the mean velocity profiles (*Re* = 7800 and *Re* = 5200) as a function of solids concentration is also in agreement, showing no variation, thus the turbulence and flow properties of the fluid over the concentration range studied are invariant. Experimental data at low solid concentrations (<1% vol.) [7, 21] illustrates that the degree of turbulence attenuation or augmentation reaches a plateau within 1% solids loading. Clearly, as the suspension becomes sufficiently laden with particles so that structuring within the fluid can occur, the suspension viscosity will significantly increase, therefore, influencing the turbulence properties of the suspension. With the concentrations in the present study intermediate of these two extremes, no considerable change in the turbulence intensities as the solids concentration is increased seems reasonable.

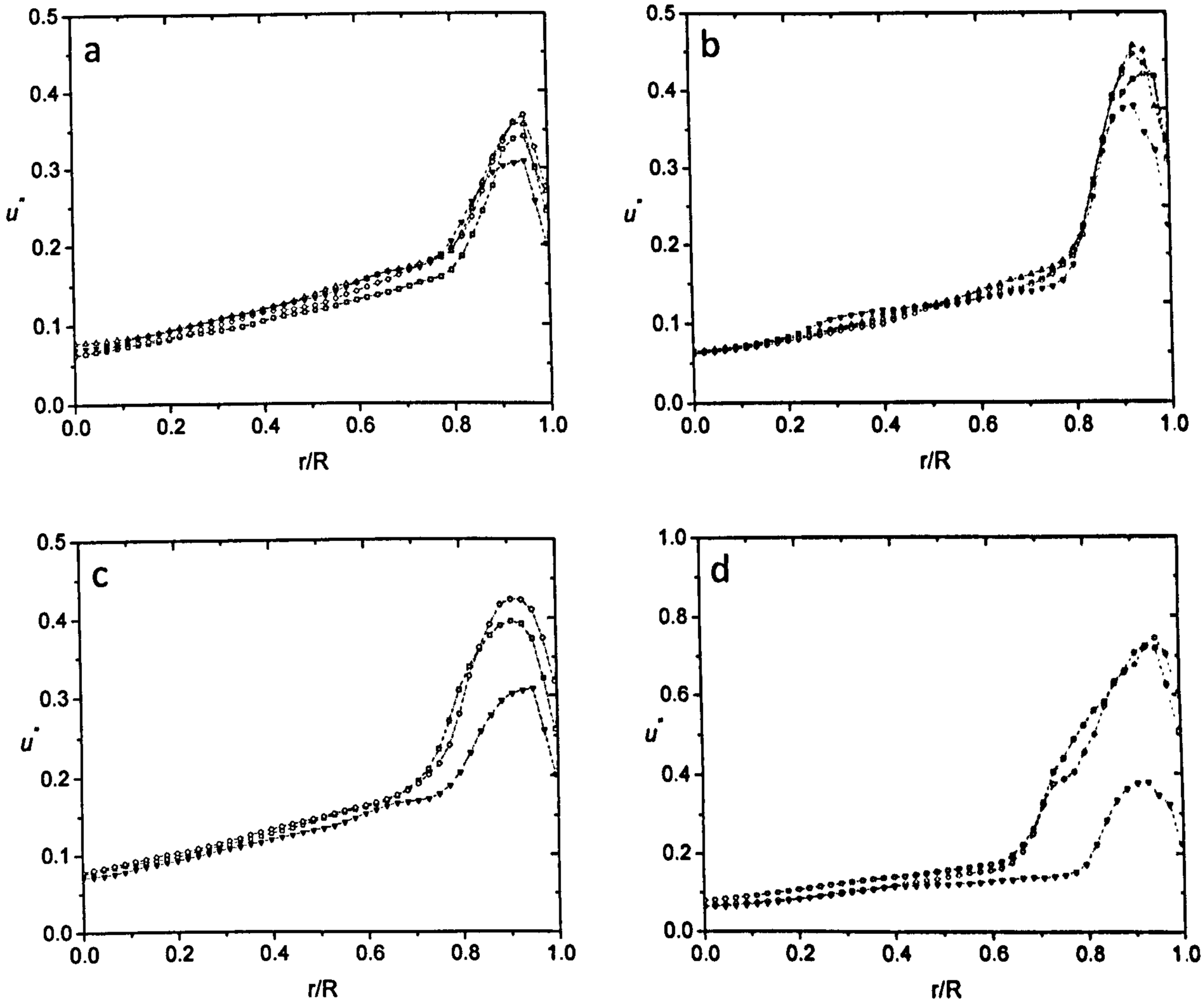

Figure 7.3 Streamwise turbulence results for dispersed and aggregated suspensions: a) Dispersed suspensions *Re* = 7800. Symbols: square – 10^{-4}M KNO_3 (5.5% vol.), circle – 10^{-4}M KNO_3 (12.7% vol.), triangle – 10^{-4}M KCl (6.0% vol.), solid triangle – water. b) symbols as in (a) for *Re* = 5200. c) Aggregated suspensions *Re* = 7800. square – 1M KNO_3 (5.7% vol.), circle – 1M KNO_3 (12.6% vol.), solid triangle – water. d) Symbols as in (c) for *Re* = 5200.

Comparing the turbulence intensities of aggregated and dispersed suspensions at an equivalent solids concentration (see figure 7.4), one can see that there is a clear enhancement in the near wall turbulence when the suspension is aggregated. With the edge of the buffer layer at r/R = 0.82 (*Re* = 5200) and r/R = 0.87 (*Re* = 7500) the turbulence modulation behaviour extends into the mainstream region of the flow. Considering the buffer region first, the turbulence intensity will be a function of the fluid-wall, particle-fluid, particle-wall and particle-particle interactions. Fluid-wall interactions relate to the intermittent low speed fluid ejections from the wall (fluid bursts) and high speed fluid

injections towards the wall (fluid sweeps). With a particle relaxation time ($\tau_p = \rho_p d_p^2/18\mu$; Stokes regime) smaller than the characteristic time of the energy containing eddies ($t_e = \lambda/u^{\cdot}$), the particles will follow the flow, neither dampening or enhancing the intensity of the sweeps or bursts in the fluid boundary layer. The particle Reynolds numbers for the primary particle and aggregate are 3.5×10^{-7} and 6.7×10^{-5} respectively. With such low particle Reynolds numbers the colloidal particles and aggregates in suspension should not influence the fluid-wall or particle-fluid interactions. However, at such a high solids concentration cumulative effects may result where small interferences between the fluid and particle, which are commonly considered to be negligible at extremely low solids concentrations, may in fact become significant and modulate the turbulence intensity. For example, particle collisions at the pipe wall and with each other generate small scale fluctuations within the fluid which in dilute flows can be considered negligible, while in dense flows the effect may become measurable.

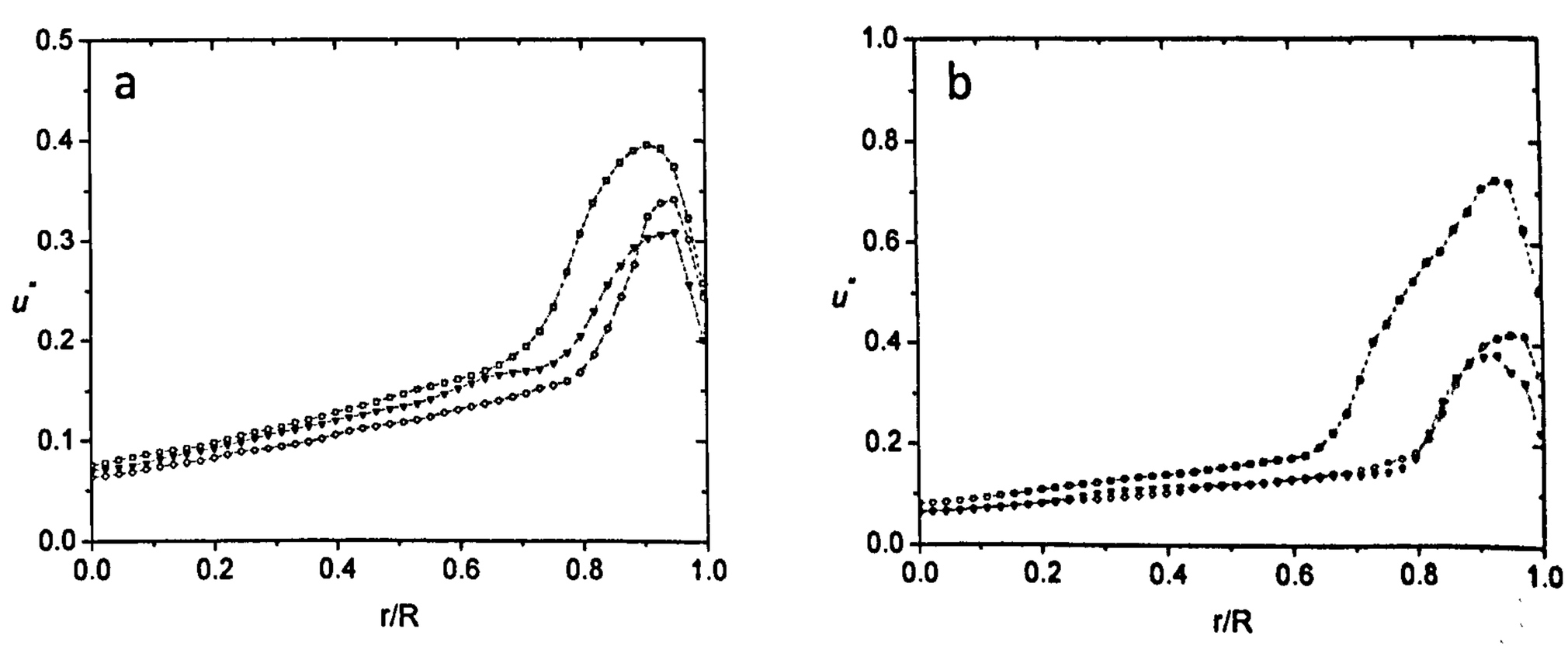

Figure 7.4 Streamwise turbulence intensities. Symbols: square – 1M KNO_3 (5.7% vol.), circle – 10^{-4}M KNO_3 (5.5% vol.), solid triangle – water. a) *Re* = 7800, b) *Re* = 5200.

The differences in the buffer layer turbulence intensities may also result from small differences in the near wall velocity gradients. With the fluid shear stress proportional to the velocity gradient, an increase in the velocity gradient provides a more favourable environment for eddy production and additional turbulence. Comparing the buffer layer velocity gradients; du_x/dy 1M KNO_3 > du_x/dy 10^{-4}M KNO_3 and du_x/dy water.

Table 7.1 Velocity gradients in the near wall region $y^+ < 30$. Units: u_x mm/s, r/R(y) mm. *Re* = 7500

du_x/dy	
1M KNO_3	-75.4
10^{-4}M KNO_3	-61.7
Water	-66.4

Centre-line variations in the turbulence intensities are observed in the raw data profiles, and have been summarised in figure 7.6 illustrating the percentage change in turbulence intensity when compared to a particle un-laden flow. An average of 10 individual measurements at each velocity provides a suitable assessment of the error of uncertainty. The turbulence intensities of a dispersed suspension do not appear to deviate too much from those measured in a particle un-laden flow. The transition from turbulence augmentation to attenuation as the mean flow velocity is increased may not be a real effect, and can be considered within experimental error. However, the data does suggest to a certain degree that the centre-line turbulence intensities are enhanced in the presence of an aggregated suspension. At the wall where the enhanced turbulence can be accounted for by particle-wall interactions, the centre-line turbulence intensity can only be influenced by particle-fluid and particle-particle interactions. Typically, the centre-line turbulence intensities are influenced by vortex shedding from wakes behind particles [8, 21, 26] and changes in the fluid viscosity[7]. Interpretation of the experimental data and critical analysis of the observed behaviour is difficult with no data sets available to validate such work. Commonly, when the particle length scales are significantly smaller than the Kolmogoroff length scale, relatively small changes in the turbulence intensities are observed which are frequently associated with a change in the suspension viscosity. These experiments are controlled such that the particles remain dispersed, thus, not to introduce any variation between large length scale studies due to the formation of aggregates.

The sedimentation study in chapter 5 highlighted the differences between the dispersed particles and aggregates under no flow conditions; the aggregates were observed to settle at a rate twenty five times the settling velocity of the dispersed particles. In addition, a surface area increase in excess of 30 times (aggregate surface area compared to primary particle surface area) makes it difficult to assume that the dispersed particles and aggregates can be treated equally in dynamic flows at such high solid concentrations.

Possible reasons for the observed enhancement in the centre-line turbulence intensities can be related to variations in the micro-hydrodynamic disturbances at the solid-liquid interface, which can result from; inter floc flow fields in an open porous structure[27], changes in the hydrodynamic drag or changes in the angular rotation rates of the particles. Because of the concentrated nature of the suspensions examined, which precluded the use of PIV, information on particle rotation and slip velocities could not be collected. Figure 7.5 shows a clear difference in the particle size and shape in an aggregated suspension which may lead to the development of interesting flow fields and enhanced fluid disturbances.

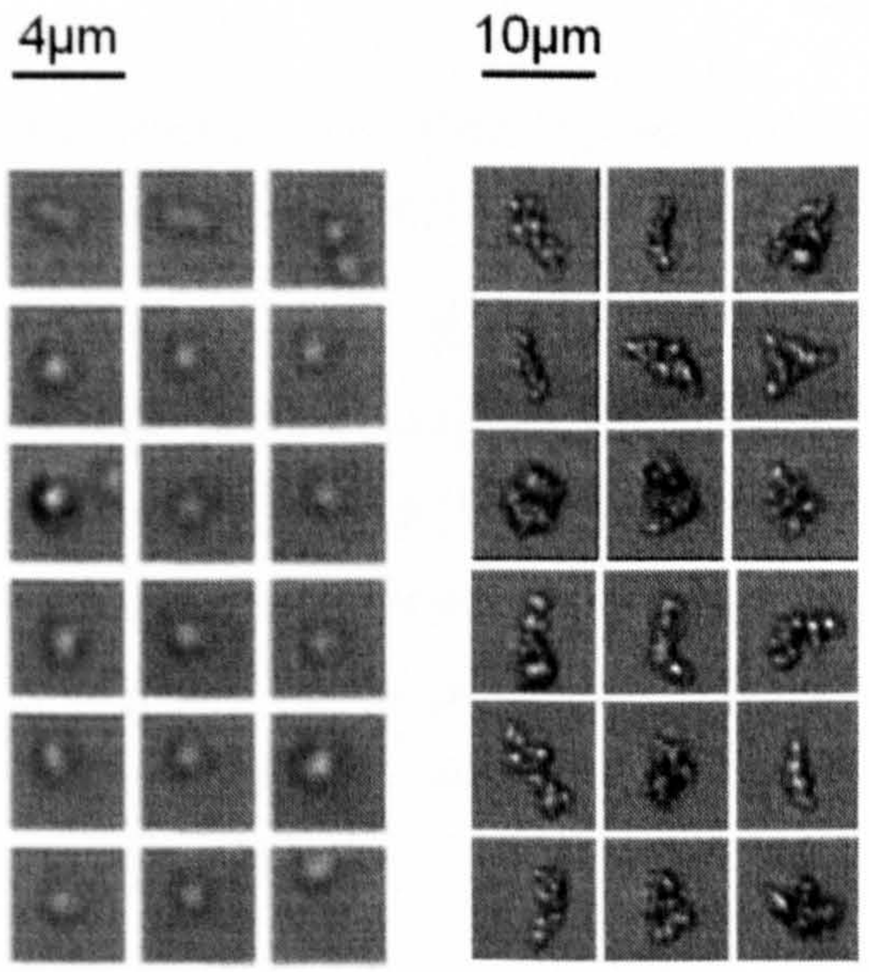

Figure 7.5 Primary particles in the dispersed phase (10^{-4}M KNO_3) and bound together in the aggregated phase (1M KNO_3). Images collected using Sysmex Flow Particle Image Analyser (FPIA-3000). Singlets and doublets imaged at low concentration electrolytes, with multi-particle clusters imaged at high electrolyte concentrations.

Computational modelling by Yang et al. [27] highlighted the complex flow patterns through the tortuous, inter-connected pore networks in an aggregate. Taking activated sludge from a wastewater treatment facility, they employed fluorescence in-situ hybridisation and confocal laser scanning microscopy to build a three-dimensional floc model. They then simulated the flow fields surrounding and passing through the floc which is subjected to an unbound Newtonian fluid. Figure 7.6a below, shows the flow streamlines through a floc

which is subjected to an incoming flow, while figure 7.6b shows the angular distribution of the flow directional velocity at a specific radii of the floc along the middle plane.

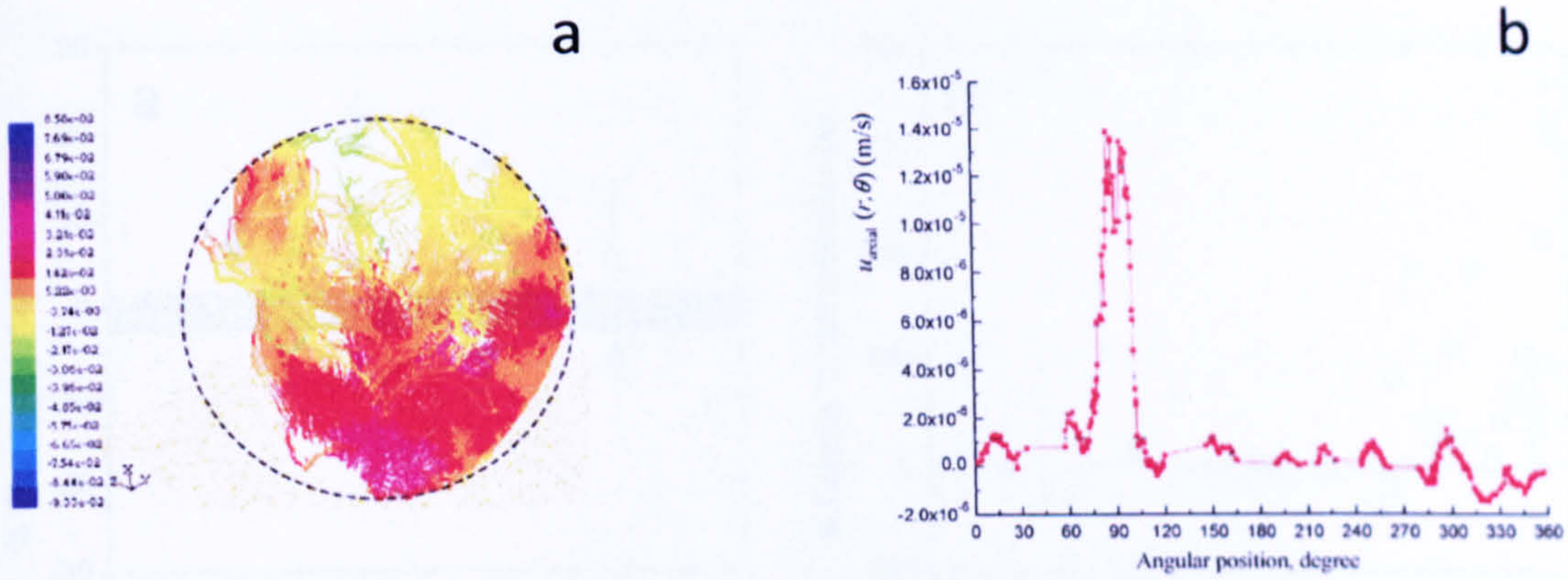

Figure 7.6 a) The streamlines of an interfloc flow (colours represent varying levels of static pressure), b) Angular distribution of flow directional velocity at a specific radial position in the floc[27].

Figure 7.6b shows that the axial velocity at the radial position of interest can vary dramatically and can even reverse in flow direction. Such significant changes in the flow direction and velocity can result in complex flow structures surrounding the aggregate. These complex flow patterns most likely support the turbulence observations in the current study, ie. for a solid sphere the flow passes around the particle with no flow separation, while for an aggregate, flow separation in the pores can lead to an enhancement in the fluid turbulence. It should be noted that in a dilute suspension (<1-2 volume %) such an effect may be regarded as negligible when considering the size of the aggregates in the current study. However, at higher solid concentrations a cumulative effect may result where the small variations in magnitude and direction of the flow produce a measurable difference.

Figure 7.7a summarises the relationship between the centre-line turbulence intensities of the aggregated and dispersed suspensions compared to water as the mean velocity is increased. Initially ($0.1ms^{-1}$, Re = 2600), the two particle laden flows are equivalent showing a small enhancement in turbulence intensity. A maximum deviation occurring at $0.2ms^{-1}$ is observed which results from a significant enhancement in the aggregated suspension turbulence intensity. With a further increase in the mean flow velocity the two turbulence intensities once again begin to approach similar values that are equivalent to the un-laden flow. The trend in the data presented in figure 7.7 suggests that the interparticle

strength of the aggregate is exceeded by the fluid shear force at a critical flow velocity, thus, initiating aggregate break-up [28, 29].

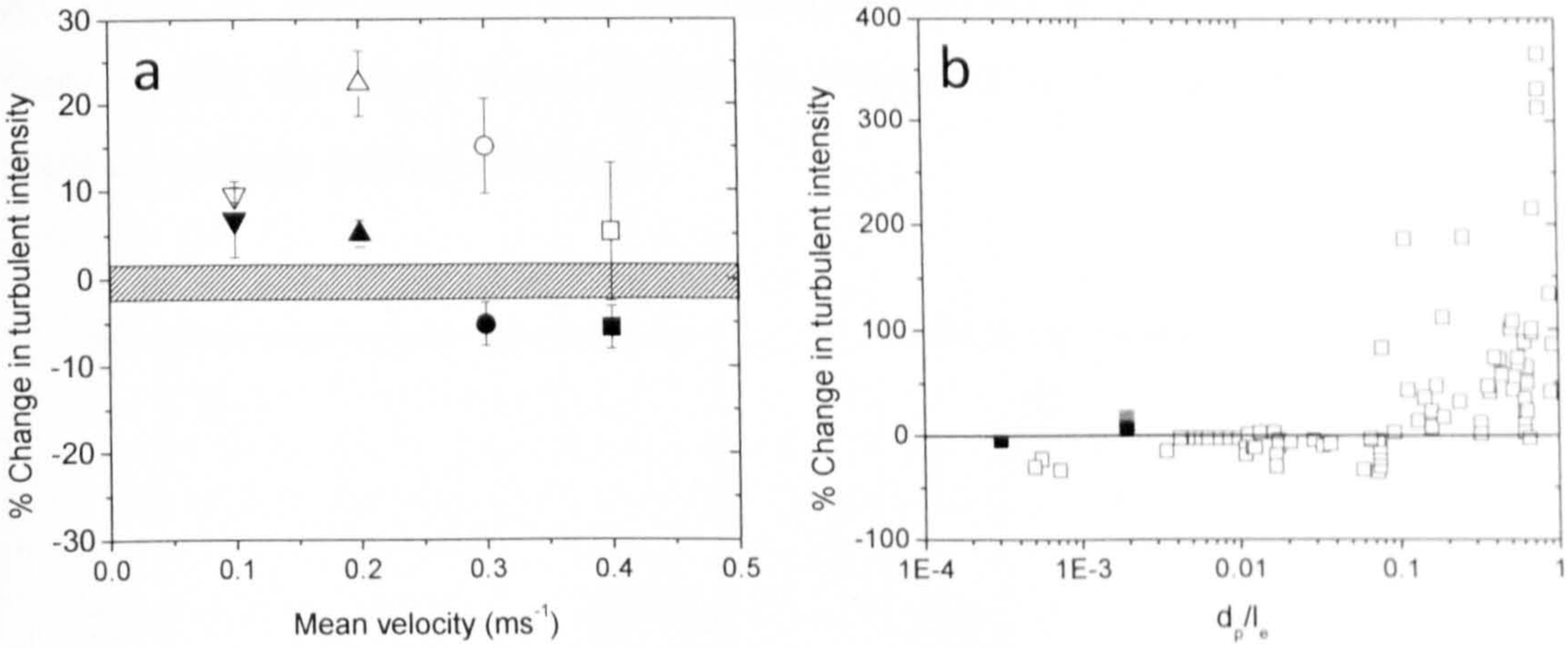

Figure 7.7 a) Percentage change in centre-line turbulence intensity relative to water: open symbols – 1M KNO_3 (5.7% vol.), closed symbols – 10^{-4}M KNO_3 (5.5% vol.), shaded region – water. b) Addition of turbulence modulation data at 0.3ms^{-1} (Grey squares) and 0.4ms^{-1} (Black squares) to the Gore and Crowe plot [8]. Smaller length scale corresponds to 0.8μm spheres (10^{-4}M KNO_3), larger length scale corresponds to an aggregate diameter of 4.6μm (1M KNO_3).

Figures 7.8 a and b compare the RMS values of the streamwise component of the single phase fluid, dispersed (10^{-4}M KNO_3, d_{50} 0.8μm) and aggregated (1M KNO_3, d_{50} 4.6μm) suspensions, and an additional dispersed suspension containing silica spheres with a mean particle diameter equal to 27μm (see Appendix A – Spheriglass 2000). All particle laden suspensions are of equivalent solids loading. Both figures illustrate the changes in the RMS values as the flow progressively develops into fully developed turbulence. The distinguishing sharp peak in the flow fluctuations around the transition region is attributed to intermittent turbulence in the form of turbulence puffs[30, 31], which are observed in both Newtonian and non-Newtonian fluids [15, 32, 33].

Above a critical Reynolds number ($Re \approx 5500$) the RMS streamwise component for an aggregated suspension exceeds the RMS values measured in an un-laden and dispersed suspension flow, with the increase corresponding to the enhancement in turbulence intensity (figure 7.7). The enhancement in the RMS values of the aggregated suspension correlate with the enhancement in the RMS values for the dispersed suspension which contains 27μm silica spheres. The larger silica spheres interact with the fluid (vortex

shedding) which appears to modulate the turbulence to the same extent as the smaller aggregates. As the Reynolds number exceeds $Re \approx 8000$ the two profiles diverge as the RMS values for the aggregated suspension start to decrease and once again approach the RMS values of the un-laden and dispersed suspension flows. Such behaviour is in agreement with the theory that a critical fluid shear stress is reached beyond which the aggregates undergo gradual breakage.

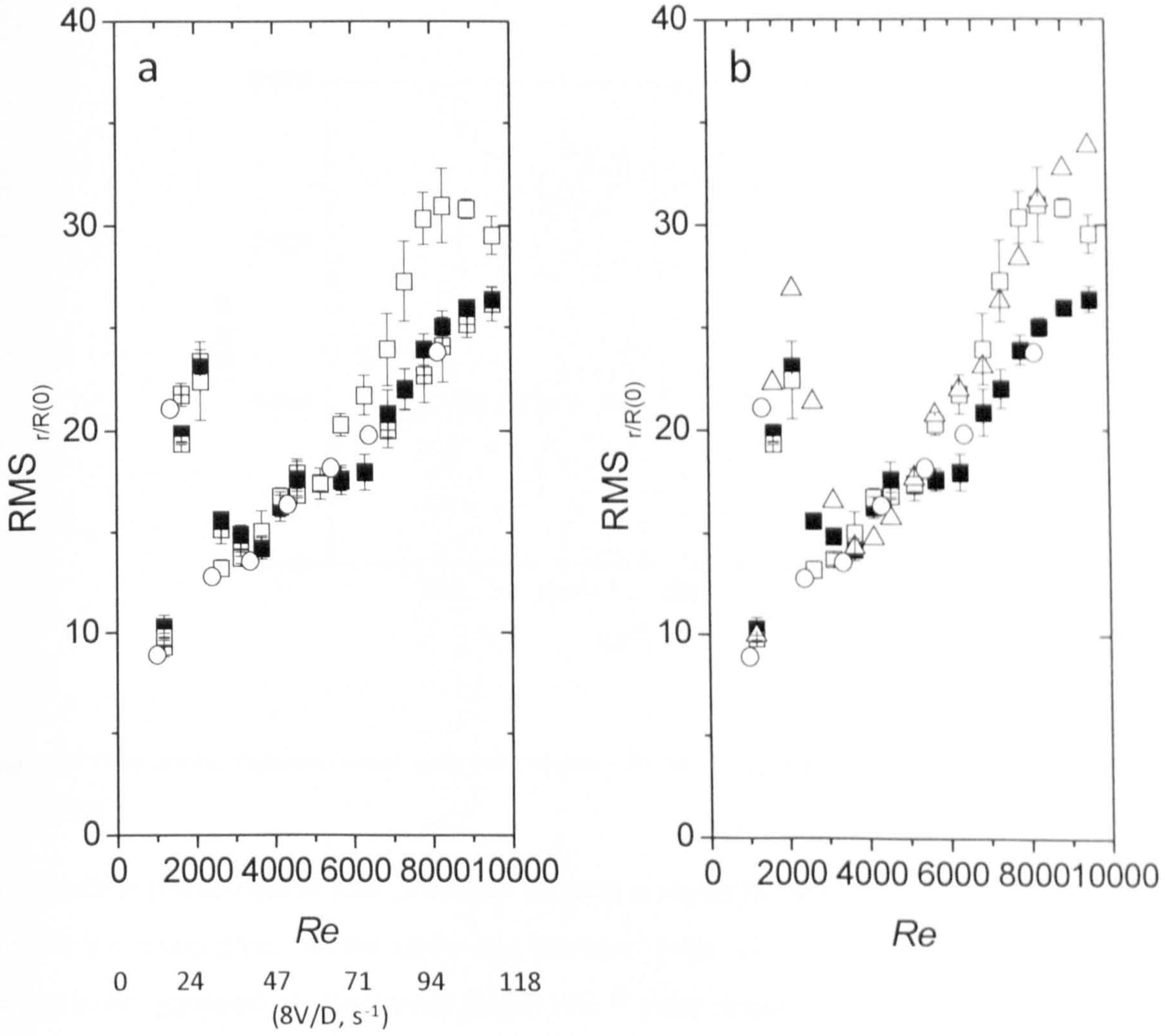

Figure 7.8 Root Mean Square values: a) solid square – 10^{-4}M KNO3 (5.5% vol.), crossed square – 10^{-4}M KNO_3 (12.7% vol.), open square – 1M KNO_3 (5.7%vol), circle – water. b) symbols as in (a), triangle - 27μm silica spheres (5.5% vol.).

A further validation for aggregate break-up is provided in the analysis of a flow curve obtained using a Bohlin CVO-R rheometer, shown in figure 7.9. With an increase in shear rate ($\dot{\gamma}$) the suspension viscosity (η) in the aggregated suspension gradually decreases

(shear thinning) until both the aggregated and dispersed flow curves overlap. A reduction in the suspension viscosity represents a lowering in the resistance to flow, which is common when particles align themselves within the flow field or undergo structure break-down. Comparing the shear rate versus viscosity profile and the pipeline pseudo-shear rate (8V/D) versus RMS profile, the critical shear rate when the aggregated and dispersed suspensions have similar properties (viscosity and RMS values) corresponds within reasonable agreement.

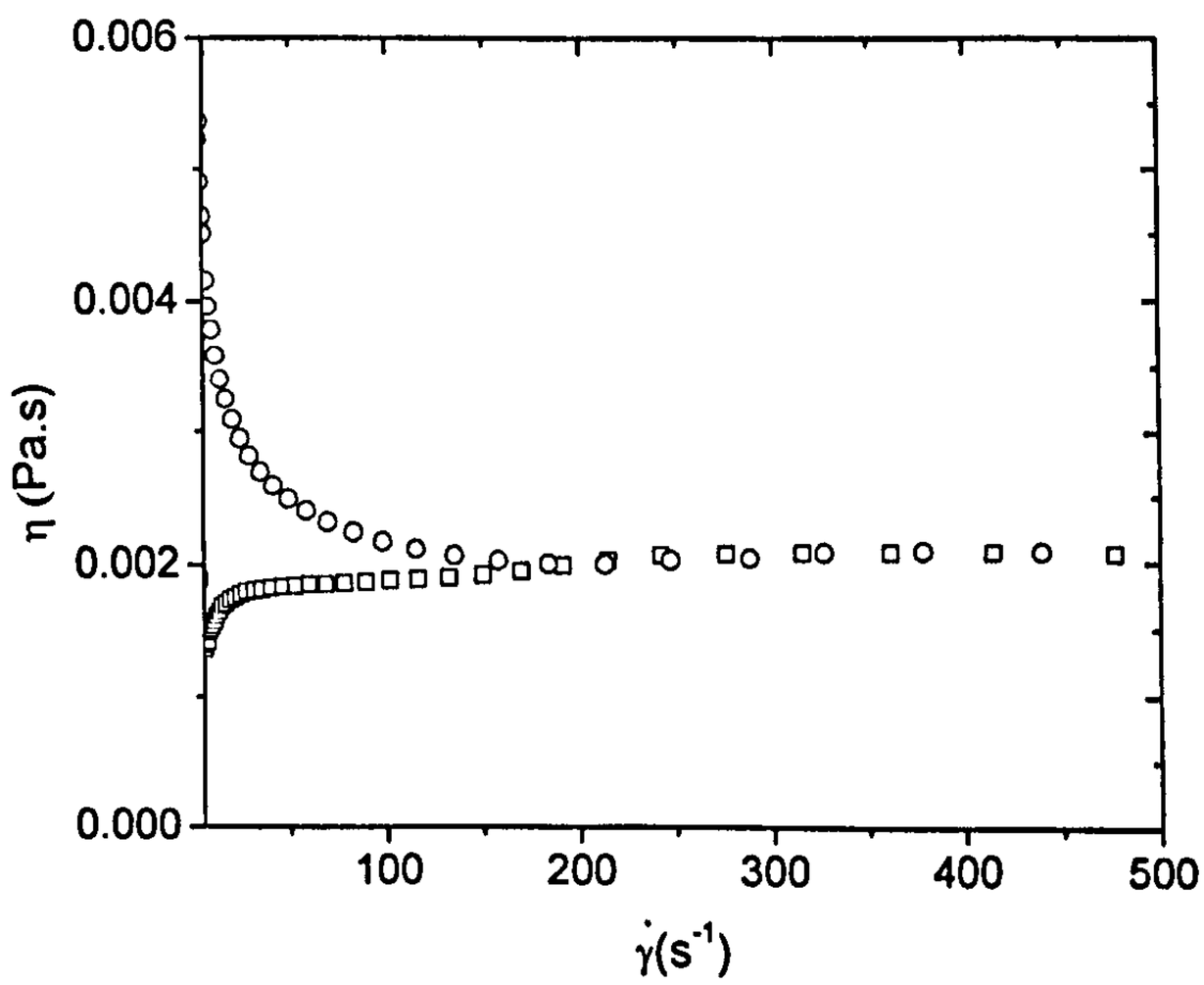

Figure 7.9 Flow curve, viscosity versus shear rate: square – 10^{-4}M KNO_3 (5.5% vol.), circle – 1M KNO_3 (5.7% vol.).

The pipeline pseudo-shear rate (8V/D) is used as a standard representation for the level of shear in a circular pipe. As the shear rate increases with velocity, the shear stress acting on a particle or aggregate also increases (shear rate = shear stress / viscosity (see figure 7.10)). As previously mentioned, a critical shear rate ($\approx 94\ s^{-1}$) is reached after which any further increase results in break-up of the aggregate structure. The strength of the aggregate structure is proportional to the total interaction energy between the particles. To the author's knowledge there is no theoretical relationship between the normal force interaction and the aggregate strength under shear. However, when referring back to the work of Scales et al. [34, 35] who related the bulk yield stress of a particle network to the DLVO force and a structural factor (k) (refer to chapter 5), a similar approach can be adopted to

represent aggregates in suspension, where the aggregate strength is proportional to the DLVO and structural components (fractal dimension). The structural component is essential to account for the free surface exposed to the fluid shear. For example, in laminar flow a spherical aggregate will have many particle-particle contacts exposed to the flow shear, while a long chain aggregate which aligns itself with the flow field, can have no particle-particle contacts exposed to the fluid shear. Thus, for the same interaction energy a spherical aggregate is more likely to undergo break-up than a long chain aggregate. The other difficulty in relating the normal force interaction to the observations in the pipe flow is in quantifying the effect of turbulence on the aggregate structure. In turbulent flow the stresses acting on an aggregate are random. One side of the aggregate can be exposed to a drag force (aggregate extension) while the other side a compressional force. Such instantaneous flow properties can act to either erode the aggregate and / or densify the aggregate (particle re-arrangement towards the aggregate centre). A potential representation for the aggregate strength in fluid shear may be written as:

$$\tau_a \propto k_{structure}[DLVO].F \qquad [7.7]$$

where $k_{structure}$ accounts for the number of particle-particle contacts in the aggregate, DLVO accounts for the strength of a particle-particle contact and F is a parameter related to the Reynolds number of the flow and the mean shear stress applied to the aggregate surface.

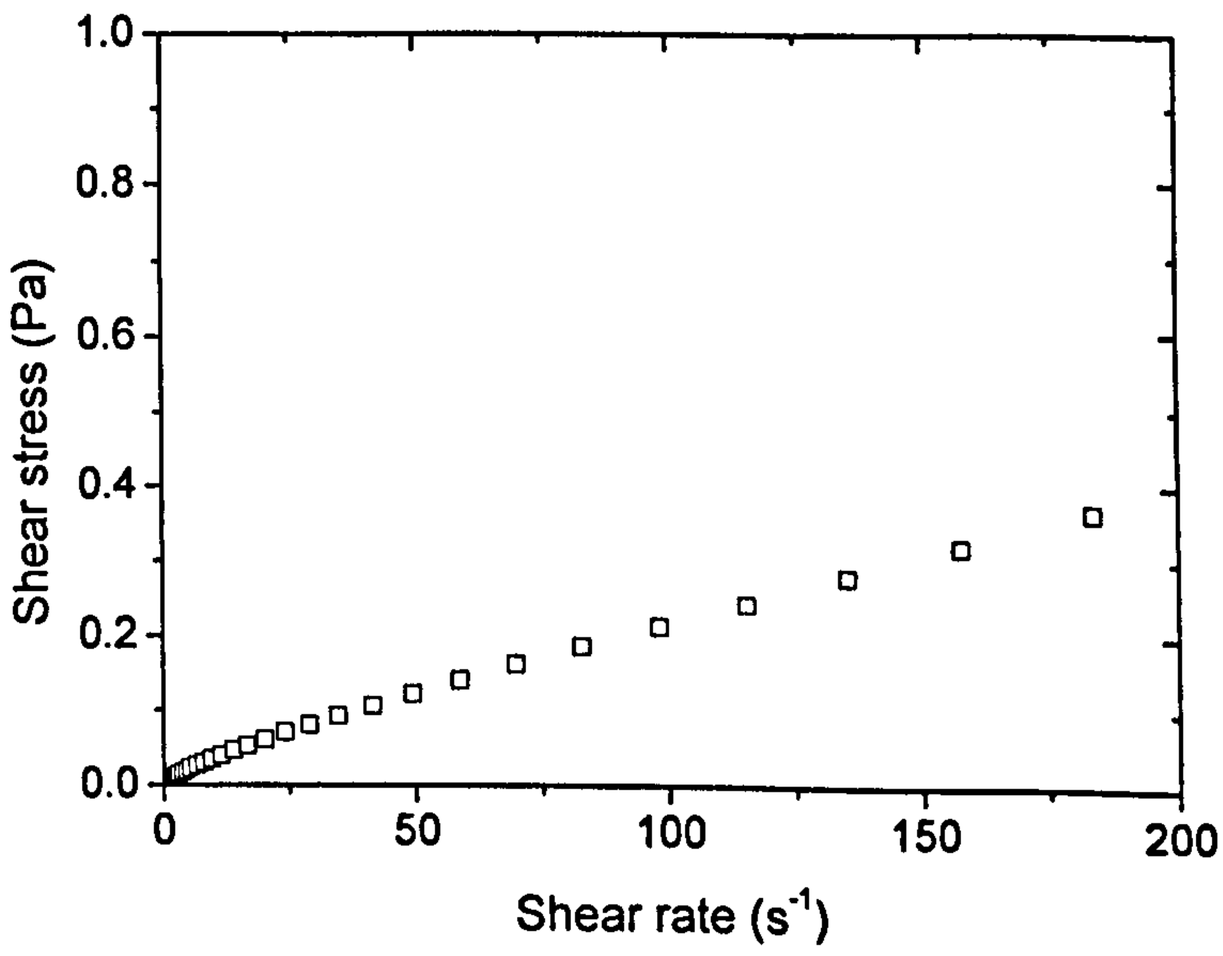

Figure 7.10 Shear rate versus shear stress profile – 1M KNO_3, 5.7%vol, pH6

Figure 7.10 shows the shear rate versus shear stress profile for a 1M KNO_3 slurry at 5.7% by volume. Taking the critical shear rate for aggregate break-up to be between $90s^{-1}$ and $100s^{-1}$, then the critical shear stress at aggregate break-up is equivalent to 0.2Pa and 0.22Pa respectively. Comparing the shear stress for aggregate break-up to the critical bed shear stress for a 1M KNO_3 sediment (0.13-0.14Pa), the values are slightly higher. The difference in the two values may be accounted for by the fluid turbulence densifying the aggregate structure, and therefore increasing the energy required to break-up the aggregate, or due to inefficiencies in the energy transfer to the aggregate when suspended in the flow, ie. the velocity difference between the free aggregate and the fluid is lower than the velocity difference when the aggregate is secured in the sediment bed. Therefore, more energy is required to initiate break-up when the aggregate is freely suspended in the flow.

7.3 Conclusion

The data shows that the turbulence properties of concentrated colloidal suspensions can be modulated through inducing particle aggregation in the suspension. It should be acknowledged that the percentage change in the turbulence intensities are relatively small in comparison with published data (see figure 6.1 - Gore and Crowe [8]); these changes most likely relate to the colloidal particles used in the current study. To the author's knowledge this is the first study where the turbulence properties of a colloidal suspension have been investigated. Both the near wall region and centre-line turbulence intensities are increased in the presence of aggregates, while the dispersed particles have minimal affect on the level of fluid turbulence. A comparison of the streamwise velocity fluctuations for un-laden and laden flows (dispersed and aggregated) identified an initial critical Reynolds number where the presence of aggregates enhances the turbulence intensity when compared with a dispersed suspension and a sediment free flow. A second critical Reynolds number (higher flow velocity) is identified when the aggregates begin to break-up as the particle-particle contact strength is exceeded by the fluid shear, and the RMS profile of the aggregated suspension begins to converge with the RMS profiles of the dispersed colloidal suspension and sediment free flow.

The enhancement in the near wall and centre-line turbulence intensities for an aggregated suspension relative to a dispersed suspension supports the experimental observations in chapter 6. In chapter 6 it was concluded that the minimum transport velocity for an

aggregated suspension is lower than the minimum transport velocity for a dispersed suspension. With the sedimentation rate of the aggregates greater than the sedimentation rate of the primary particle, it would be reasonable to expect the minimum transport velocity for the aggregated suspension to be higher than the minimum transport velocity for the dispersed suspension. However, the enhancement in fluid turbulence can provide an additional energy to keep the aggregates in suspension; while the lower turbulence intensities at an equivalent flow velocity (dispersed suspension) does not provide sufficient turbulent energy to keep the primary particles in suspension. Therefore, a higher minimum transport velocity for the dispersed suspension is measured.

Chapter References

1. Wilson, K.C. and A. Sellgren, *Near-wall particle lift and deposition in slurry pipelines.* BHR Group Hydrotransport 15, 2002: p. 789-800.
2. Rouse, H., *Modern conceptions of the mechanics of fluid turbulence.* Transactions of the American Society of Civil Engineering, 1937. **102**: p. 463-554.
3. Kline, S.J., et al., *The structure of turbulent boundary layers.* Journal of Fluid Mechanics, 1967. **30**(4): p. 741-773.
4. Klebanoff, P.S., *Characteristics of turbulence in a boundary layer with zero pressure gradient.* National Advisory Committee for Aeronautics, 1955.
5. Davies, J.T., *Turbulence Phenomena: An introduction to the eddy transfer of momentum, mass, and heat, particularly at interfaces.* Academic Press, 1972.
6. Perry, A.E. and C.J. Abell, *Scaling laws for pipe-flow turbulence.* Journal of Fluid Mechanics, 1975. **67**(2): p. 257-271.
7. Zisselmar, R. and O. Molerus, *Investigation of solid-liquid pipe flow with regard to turbulence modification.* Chemical Engineering Journal (Amsterdam, Netherlands), 1979. **18**(3): p. 233-9.
8. Gore, R.A. and C.T. Crowe, *Effect of particle size on modulating turbulent intensity.* International Journal of Multiphase Flow, 1989. **15**(2): p. 279-85.
9. Ljus, C., B. Johansson, and A.-E. Almstedt, *Turbulence modification by particles in a horizontal pipe flow.* International Journal of Multiphase Flow, 2002. **28**(7): p. 1075-1090.
10. Parthasarathy, R.N. and G.M. Faeth, *Turbulence modulation in homogeneous dilute particle-laden flows.* Journal of Fluid Mechanics, 1990. **220**: p. 485-514.
11. Tsuji, Y. and Y. Morikawa, *LDV measurements of an air-solid two phase flow in a horizontal pipe.* Journal of Fluid Mechanics, 1982. **120**(385-409).
12. Rogers, C.B. and J.K. Eaton, *The effect of small particles on fluid turbulence in a flat-plate, turbulent boundary layer in air.* Physics of Fluids, 1991. **5**: p. 928-937.
13. Tanaka, M., Y. Maeda, and Y. Hagiwara, *Turbulence modification in a homogeneous turbulent shear flow laden with small heavy particles.* International Journal of Heat and Fluid Flow, 2002. **23**: p. 615-626.

14. Best, J.L., et al., *Turbulence modulation and particle velocities over flat sands at low transport rates.* Journal of Hydraulic Engineering, 1997. **123**(12): p. 1118-1129.

15. Abbas, M.A. and C.T. Crowe, *Experimental study of the flow properties of a homogeneous slurry near transitional Reynolds numbers.* International Journal of Multiphase Flow, 1987. **13**(3): p. 357-64.

16. Eskin, D., Y. Leonenko, and O. Vinogradov, *On a turbulence model for slurry flow in pipelines.* Chemical Engineering Science, 2004. **59**(3): p. 557-565.

17. Plass, L. and O. Molerus, *Heat transfer in solid-liquid suspensions in total pumpable concentration range.* Chemie Ingenieur Technik, 1974. **46**(1): p. 355.

18. Laufer, J., *The structure of turbulence in fully developed pipe flow.* National Advisory Committee for Aeronautics, 1953. **Technical note 2954.**

19. Hutchinson, P., G. Hewitt, and A.E. Dukler, *Deposition of liquid or solid dispersion from turbulent gas streams; a stochastic model.* Chemical Engineering Science, 1971. **26**: p. 419-439.

20. Hetsroni, G., *Particles-turbulence interaction.* International Journal of Multiphase Flow, 1989. **15**(2): p. 735-746.

21. Kim, S., K.B. Lee, and C.G. Lee, *Theoretical approach on the turbulence intensity of the carrier fluid in dilute two-phase flows.* International Journal of Heat and Fluid Flow, 2005. **32**: p. 435-444.

22. Liu, Q.Q. and V.P. Singh, *Fluid-solid interaction in particle laden flows.* Journal of Engineering Mechanics, 2004: p. 1476-1485.

23. Maeda, M., K. Hishida, and T. Furtani, *Velocity distributions of air-solid suspensions in upward pipe flow (effect of particle on air velocity distribution).* Transactions of the Japan Society of Mechanical Engineers, 1980. **46**: p. 2313-2320.

24. Elgobashi, S., *On predicting particle-laden turbulent flows.* Applied Scientific Research, 1994. **52**(4): p. 309-329.

25. Wang, S.K., et al., *3-D turbulence structure and phase distribution measurements in bubbly two-phase flows.* International Journal of Multiphase Flow, 1987. **13**(3): p. 327-343.

26. Achenbach, E., *Vortex shedding from spheres.* Journal of Fluid Mechanics, 1974. **62**(2): p. 209-221.

27. Yang, Z., et al., *Advective flow in spherical floc.* Journal of Colloid and Interface Science, 2007. **308**: p. 451-459.

28. Higashitani, K., N. Inada, and T. Ochi, *Floc breakup along centerline of contractile flow to orifice.* Colloids and Surfaces, 1991. **56**: p. 13-23.

29. Zumaeta, N., E.P. Byrne, and J.J. Fitzpatrick, *Predicting precipitate particle breakage in a pipeline: Effect of agitation intensity during precipitate formation.* Chemical Engineering Science, 2006. **61**(24): p. 7991-8003.

30. Wygnanski, I.J. and F.H. Champagne, *On transition in a pipe. Part 1. The origin of puffs and slugs and the flow in a turbulent slug.* Journal of Fluid Mechanics, 1973. **59**(2): p. 281-335.

31. Wygnanski, I., M. Sokolov, and D. Freidman, *On transition in a pipe. Part 2. The equilibrium puff.* Journal of Fluid Mechanics, 1974. **69**: p. 283-308.

32. Graham, L., et al., *Transition to turbulence in non-Newtonian pipe flow.* 6th World Congress of Chemical Engineering 2001.

33. Banfi, G.P., R. De Micheli, and A. Henin, *Velocity fluctuation enhancement in the transition to turbulence in a pipe.* Journal of Physics D: Applied Physics, 1981. **14**(4): p. 625-32.

34. Johnson, S.B., et al., *Surface chemistry-rheology relationships in concentrated mineral suspensions.* International Journal of Mineral Processing, 2000. **58**(1-4): p. 267-304.

35. Scales, P.J., et al., *Shear yield stress of partially flocculated colloidal suspensions.* AIChE Journal, 1998. **44**(3): p. 538-545.

Chapter 8

CONCLUSIONS

The physical and chemical properties of nuclear sludges and slurries are extremely complex, which makes predicting their rheological and flow properties very challenging. One of the main concerns with transporting nuclear slurries is correctly accounting for the affect of fine particles on the slurry rheology. Fine particles are unique, in such that the interaction energy between particles in close proximity can be manipulated by the solution chemistry. The transportation and turbulence properties of fine particulate (colloidal) suspensions have been investigated. Slurries with a solids concentration between 5.5% and 12.6% by volume (concentration representative of typical solids loading in pumped nuclear slurries) were prepared in different electrolyte solutions (concentration and type).

Chapter 6 considered the minimum transport velocity of colloidal suspensions dispersed in 1M KNO_3 (colloidally un-stable), 10^{-4}M KNO_3 (colloidally stable) and 10^{-4}M KCl (colloidally stable) at pH 6. The minimum transport velocity of a pipeline is important as it identifies the flow velocity required to keep the dispersed particles entrained in the flow. Operating below the minimum transport velocity will result in particle deposition and the formation of sediment beds, with a potential for pipeline blockage. The transportation of fine particles has received little attention to date, a direct result of industrial pipelines pumping at velocities which greatly exceed the low minimum transport velocities observed for fine particulate suspensions (see chapter 6). However, by experimentally determining the minimum transport velocity of fine particulate suspensions, the pipeline operating conditions can be adjusted to make the process more energy efficient (ie. pumping velocities can be reduced to within 10-20% of the minimum transport velocity).

A 26mm NB pipe loop was constructed, and the minimum transport velocities for an aggregated and dispersed colloidal suspension were measured to be $0.13ms^{-1}$ (1M KNO_3) and $0.15ms^{-1}$ (10^{-4}M KNO_3, KCl) respectively. By measuring the onset velocity for sediment bed erosion (transition velocity), the minimum transport velocity was determined

by extrapolating the transition velocities, to remove the sediment bed effect - see chapter 6 (Extrapolation of the sediment bed erosion velocities as a function of the sediment bed height back to zero is a novel approach which has been adopted in the current study to determine the minimum transport velocity. Techniques such as, visual assessment, electrical resistance tomography and deposition probes could not be used for a variety of reasons which have already been discussed in chapters 3 and 6. The current approach is validated because the velocity profiles, turbulence intensities and critical bed shear stresses for given slurries are independent of the solids loading). The minimum transport velocity result seems counterintuitive when the particle size and the sedimentation velocities for the dispersed and aggregated suspensions are considered. With a mean aggregate diameter of 4.6μm compared to 0.8μm (primary particle diameter), and a settling rate which is nearly 25 times greater than the settling rate for a dispersed suspension, it would be reasonable to expect that the minimum transport velocity for an aggregated suspension would exceed the minimum transport velocity for a dispersed suspension.

This trend in the minimum transport velocity is most likely associated to the slurry turbulence intensity. Chapter 7 considered the turbulence properties of an aggregated suspension (1M KNO_3) and a dispersed suspension (10^{-4}M KNO_3). Ultrasonic Doppler velocity profiling was used to measure the streamwise component of turbulence from r/R = 0 (centre line) to r/R = 1 (pipe wall). The turbulence for an aggregated suspension was augmented, while the level of turbulence remained unchanged (considered within error) for a dispersed suspension when compared to a single phase flow. The enhancement in turbulence is most likely due to the "complex" and "tortuous" flow profiles generated as a fluid passes through an aggregate. The inter floc flow can dramatically affect the flow velocity and direction, which results in complex flow structures surrounding the aggregate – see chapter 7. With turbulence providing an energy for re-suspension, the enhancement in the slurry turbulence intensity for an aggregated suspension provides support for minimum transport velocity data in chapter 6.

The centre-line turbulence properties were investigated over a range of flow velocities up to $0.4ms^{-1}$. In the laminar and transitional flow regimes there were no observed differences in the turbulence levels for an aggregated, dispersed and single phase flow. However, in the turbulent flow regime two critical Reynolds numbers were identified. The first critical

Reynolds number is associated with turbulence enhancement in the presence of aggregates. At $Re \approx 5500$, the RMS values for the aggregated suspension exceed the RMS values measured for a dispersed suspension and a single phase flow. The enhancement is believed to be associated to the inter floc flow effect. As the flow velocity is increased a second critical Reynolds number is observed. At $Re \approx 8000$, the RMS values for the aggregated suspension begin to diverge towards the RMS profiles for a dispersed silica suspension and a single phase flow. The reduction in the fluid turbulence above the critical Reynolds number is associated to the break-up of aggregates in the flow. Such behaviour has been verified by comparing the data to the RMS profile of a silica suspension prepared using 27μm silica spheres (increased fluid interaction - vortex shedding), and a flow curve collected using a Bohlin CVO-R rheometer (aggregated and dispersed suspensions at equivalent solids loadings to those suspensions studied in the pipe loop). In the pipe loop the suspension prepared using 27μm silica spheres did not exhibit a second critical Reynolds number, with the RMS profile continuing to diverge from the dispersed suspension and single phase profiles. Using a rheometer the viscosity shear rate data for a dispersed (10^{-4}M KNO_3 5.5% vol.) and an aggregated suspension (1M KNO_3 5.7% vol.) were compared up to $500s^{-1}$. A critical shear rate is reached ($\approx 150s^{-1}$) when the viscosity of the two suspensions are equivalent. An equivalent viscosity indicates that the aggregates in suspension have been broken-up by the applied shear, and the suspension is representative of a dispersed particle suspension. This critical shear rate is compared with pipeline pseudo shear rate for aggregate break-up. In the pipeline, the pseudo shear rate at the perceived on-set of aggregate break-up is $94s^{-1}$, which is in reasonable agreement with the measured critical shear rate ($150s^{-1}$) when all aggregate structures have been broken.

Characterisation of the Fuso silica suspensions and sediments has been discussed in chapter 5. The stability of a colloidal suspension as a function of pH, electrolyte concentration and type was determined through measurement of the silica zeta potential. Determination of the silica zeta potential was important to identify solution chemistries which would provide contrasting suspension and sediment rheologies. At pH6 (approximate suspension pH prior to the addition of any acid or base) the silica zeta potential in the presence of a 1M KNO_3, 10^{-4}M KNO_3 and 10^{-4}M KCl electrolyte is -6mV, -70mV and -50mV respectively. The broad range of zeta potentials provides one un-stable colloidal suspension and two stable colloidal suspensions. Further rheological experiments showed that the change in zeta

potential influenced the sediment shear yield stress, the suspension settling rate and the suspension gel point. Atomic force microscopy data supported the zeta potential results with a purely repulsive interaction measured for the two stable suspensions and an adhesion (pull-off) force measured between two silica surfaces interacting in the presence of a 1M KNO_3 electrolyte.

Typically, when ion-ion, ion-solvent, ion-surface effects on the stability of a colloidal suspension are considered (suspension with a low iso-electric point), it is frequently the effect of different counter-ions which are studied. To the author's knowledge there is very little work where the counter-ion remains unchanged and the co-ion effect on the suspension stability is considered. In the current study, at low electrolyte concentrations (10^{-4}M), and at pH's away from the iso-electric point, the silica zeta potential is observed to be a function of the electrolyte type. With the same cation, the result is somewhat unexpected, but the zeta potential data is also supported by the sediment shear yield stress and suspension gel point data. The results suggest that at a low electrolyte concentration the rheological properties can be influenced by a change in the anion. The observed trends in the data (see chapter 5) indicate that the stability of a suspension at low electrolyte concentrations can be influenced by the degree of electrolyte dissociation. For example, an electrolyte with a high dissociation energy (KCl) will generate a lower concentration of K^+ ions in solution when compared to an electrolyte with a low dissociation energy such as KBr. As the concentration of K^+ ions in solution varies, the level of surface charge screening also varies, thus the suspension stability and rheology changes.

For the two stable suspensions, the change in the zeta potential which is a result of the electrolyte dissociation energy has been shown to influence the sediment shear yield stress and suspension gel point, while having no effect on the suspension settling rate or the single particle-particle interaction force. Such behaviour has been discussed in terms of particle mobilities. In dilute systems such as homogeneous suspensions, the change in the zeta potential (-70mV, 10^{-4}M KNO_3 and -50mV, 10^{-4}M KCl) is not sufficient to bring about a measurable change in the settling rate or level of particle-particle interaction. However, when the solids concentration is extremely high, for example within sediment beds, the change in the zeta potential appears to influence the mobility of particles past one another. With a slightly lower zeta potential, particles dispersed in 10^{-4}M KCl have a reduced

mobility when in close proximity to neighbouring particles. As a result these particles are further restricted in diffusing past one another, leading to a sediment which is more porous (lower gel point) with a lower sediment shear yield stress. To the author's knowledge the mobility of stable colloidal systems (greater than -30mV) has not been studied before. To understand the data further a more detailed experimental programme is to be completed which looks at a wider range of salts and oxide surfaces.

The current study was carried out for two reasons; i) the nuclear industry has large volumes of legacy waste which contains fine particulates, and a better understanding of the flow properties during pipeline transport is required, and ii) fine particulate transport in pipelines has received little attention to date. When considering nuclear slurries, the range of variables considered in the current study is only the "tip of the iceberg". Consideration for more complicated ionic solutions is required, along with more complex particle systems to include a polydispersity and a range of particle shapes. However, the fundamental science that aggregates in suspension can modify the turbulence and minimum transport velocity of slurries should still be applicable.

FUTURE WORK

With several different research topics considered during this study, there are several interesting conclusions which provide a basis for much larger research programmes. Areas of interest that would improve the depth of knowledge in fine particulate transport would include:

Flow through aggregates – The current study has highlighted the importance of aggregates in modifying the turbulence properties of slurries, and the slurry minimum transport velocity. Aggregates are frequently studied in suspension rheology and break-up experiments, but there has been very little interest studying the aggregate-fluid interaction in a dynamic system. A change in the level of slurry turbulence and the minimum transport velocity of a fine particulate suspension has been related to inter floc flows. The complex fluid flow through an aggregate is not well understood. Experimentally, imaging the flow through an aggregate would be extremely difficult. However, computational fluid dynamics can offer a tool to study such flows, assuming a mean aggregate shape from fractal dimensions.

Turbulence modulation – All turbulence modulation studies investigate the particle-fluid interaction and particle-wall interaction, with a few studies considering the particle-particle interaction at higher solid loadings. For fine particulate transport (low particle Reynolds numbers) it has been shown and is frequently assumed that the particles dispersed in the flow do not affect the fluid turbulence properties. However, the current study has shown that for fine particulate transport, turbulence modulation is achievable when the particles are aggregated. These aggregates can still be considered as fine particles, but due to inter floc flows through the aggregate, the turbulence intensity is increased. There is a need to study the turbulence properties of slurries at higher solid loadings. This study has shown that small insignificant changes in the particle-fluid interaction at low concentrations can actually result in measurable differences at a high solids loading.

Minimum transport velocity – The minimum transport velocity of a suspension has been considered in detail over several decades. However, many of the published correlations refer to the transport velocity of coarse, granular material. Colloidal, fine particulate transport has received very little attention, as it is frequently assumed that the fine particles will remain suspended under typical pipeline operating velocities. For the mineral and mining or petroleum industries this is very much the case, however, improvements in the pipeline efficiency can be made if the system is properly characterised. An extension to the pipe loop study is to investigate the minimum transport velocity of coarse material suspended in a fine particulate suspension. The interaction energy between fine particles can be manipulated through changes in the solution chemistry; varying the viscosity and yield strength of the suspension. Changes in the rheology of the carrier fluid will influence the minimum transport velocity of the coarse material. Such a study is building towards a more industrially representative slurry sample. The minimum transport velocity for fine particulates also has relevance to micro-channel flows.

Other techniques to determine the minimum transport velocity of colloidal particles need to be explored. The current approach in-directly determined the minimum transport velocity from the transition velocity at the onset of sediment bed erosion. Techniques such as electrical resistance tomography may well be applied if the resolution of the measurement is sufficient to detect colloidal deposition on to the pipe invert.

Sediment bed consolidation – With the same potential determining ion (K^+) a change in the electrolyte anion at low electrolyte concentrations has been shown to adjust the zeta potential at high pH's, which influences the gel point and the sediment shear yield stress. Such behaviour has not previously been observed because, i) the counter-ion effect in the presence of different co-ions has received very little attention for low iso-electric point surfaces, and ii) the surface chemistry effects on the shear yield stress are always conducted at concentrations exceeding the suspension gel point where sedimentation and consolidation are considered negligible (see chapter 5, "bell curve"). The variation in the zeta potential at low electrolyte concentrations where the single particle-particle interactions remain purely repulsive has been shown to influence the sediment shear yield stress. With the yield stress dependent on the bulk properties of the sediment, a study looking at the degree of sediment consolidation at low electrolyte concentrations in the

presence of different ions (counter-ion and co-ion) may provide support for these initial observations.

APPENDIX A

PARTICLE CHARACTERISATION

Several solid samples were characterised at the start of the project to identify a material most suitable for the desired pipe loop studies. The criteria for selection included; i) raw material cost, ii) particle size and iii) pH stability. The five samples studied were:

1. Monospher 1000 – silica
2. Angstromsphere – silica
3. Calcium carbonate
4. Spheriglass – glass
5. Fuso silica – silica (see chapters 4, 5 and Appendix B and C)

MONOSPHER 1000 – Aldrich, USA

Cost: ≈ £350/KG

Scanning Electron Micrographs

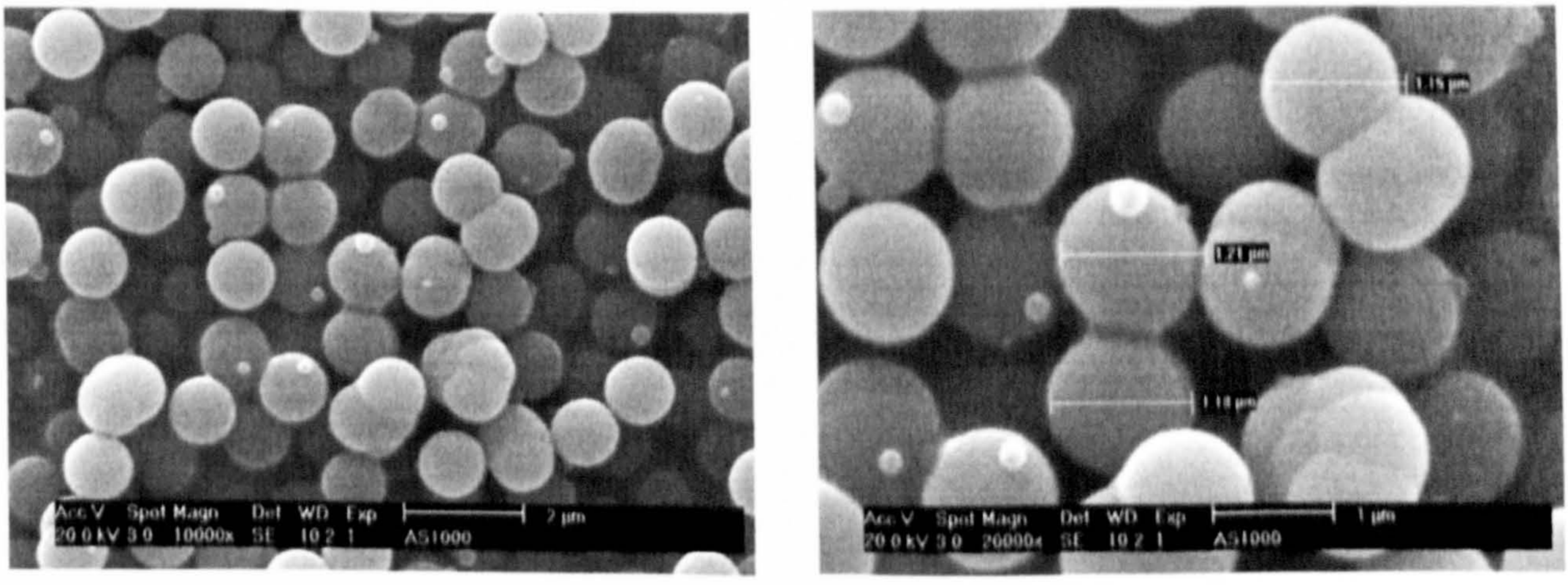

Figure A1 Scanning electron micrographs of the Monospher 1000 silica at 10000 × magnification and 20000 × magnification. Images show small spheres adhered to the larger spheres, along with fusion of several large spheres forming objects in excess of 2 - 3µm.

Zeta Potential

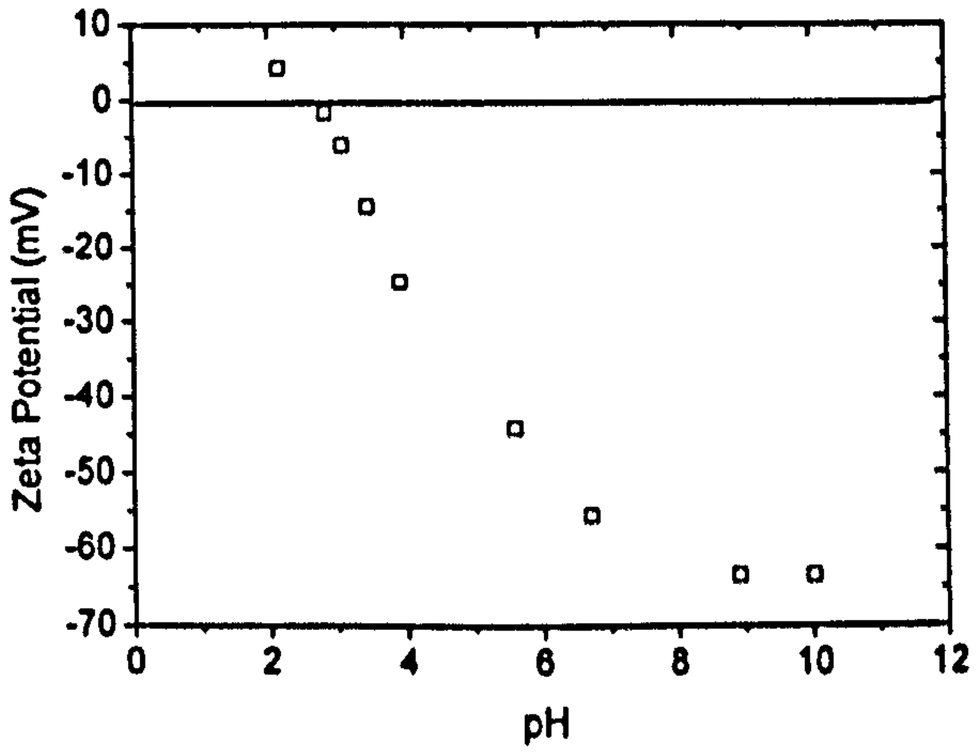

Figure A2 Zeta potential curve determined using the Malvern zeta nanosizer. Suspension prepared to 10000ppm dispersed in 10^{-4}M KNO_3. pH adjusted using KOH and HNO_3. Iso-electric point = pH 2.7

pH Stability

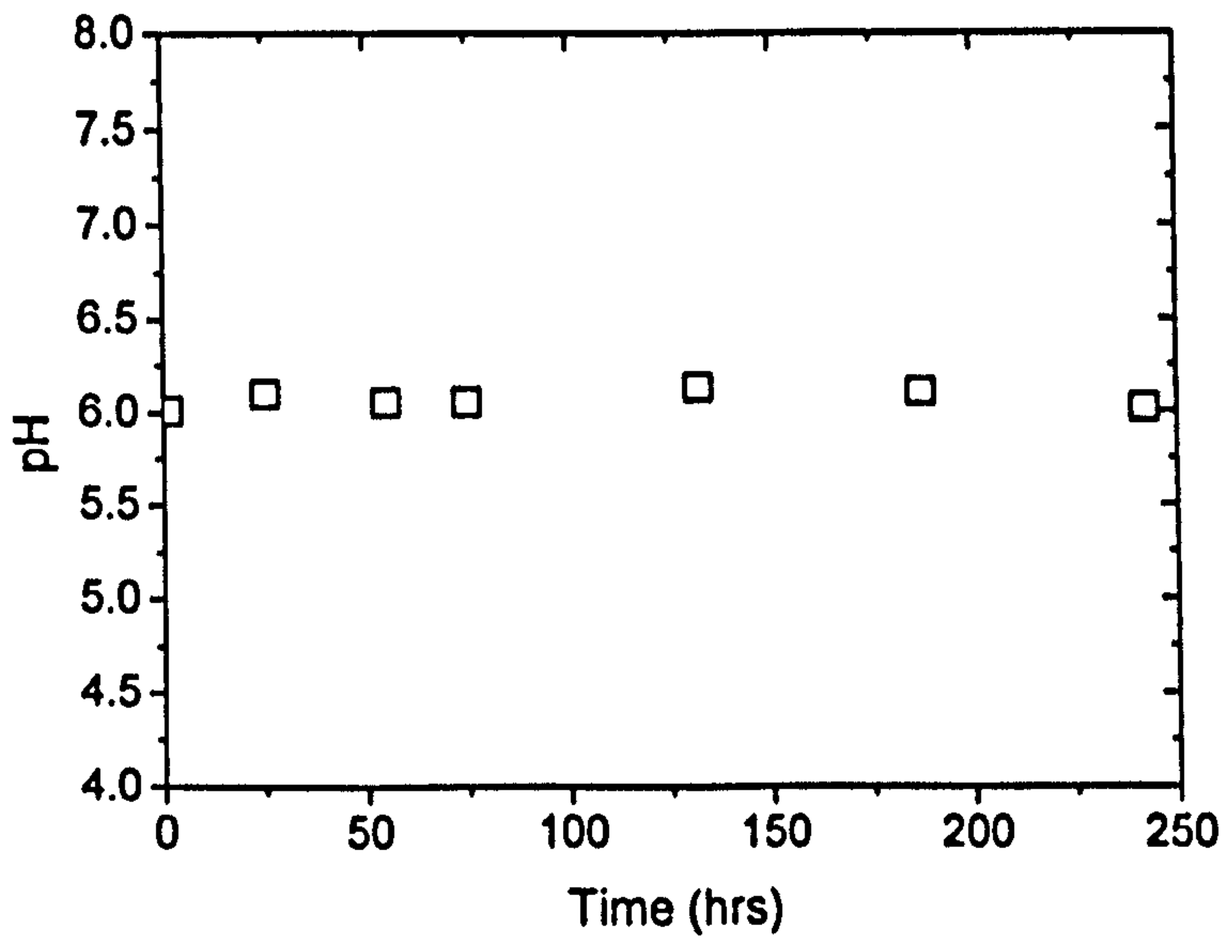

Figure A3 5%vol suspension prepared in 10^{-4}M KNO_3 background electrolyte. Negligible drift in suspension pH; small shifts most likely associated to pH meter calibration.

ANGSTROMSPHERE – Fiber Optic Centre Inc., USA

Cost ≈ £300/KG

Scanning Electron Micrographs

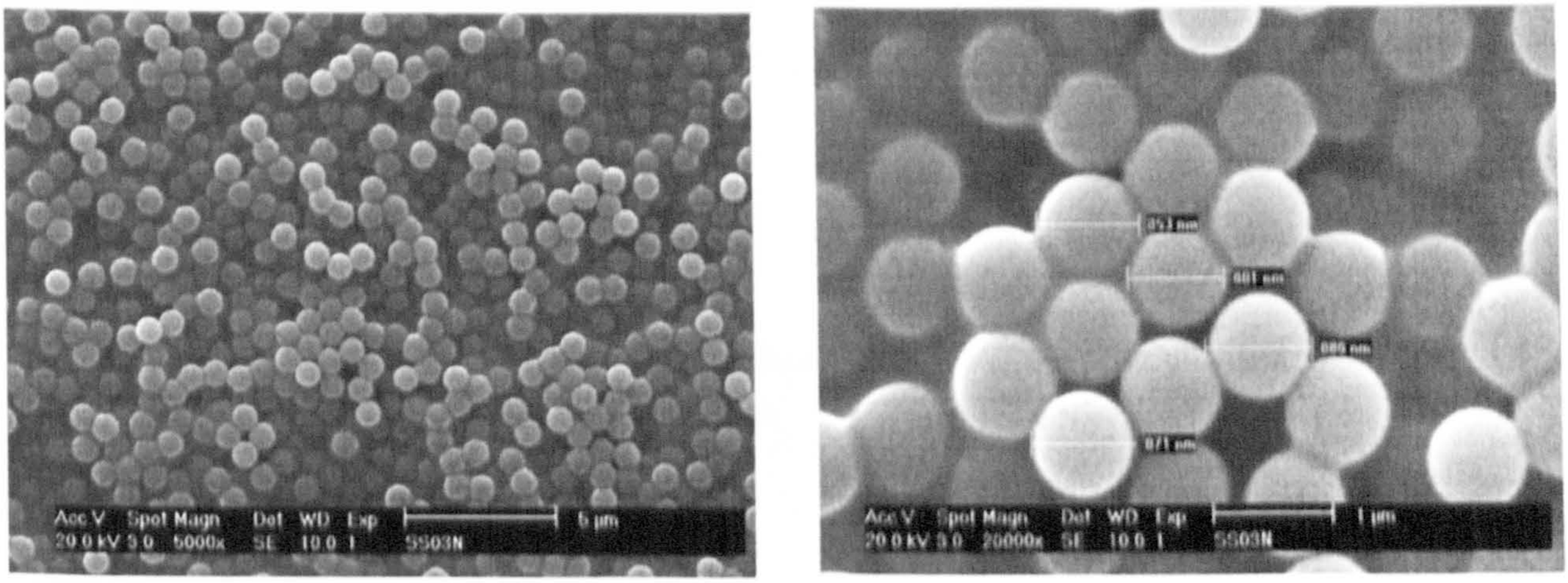

Figure A4 Scanning electron micrographs – Angstromsphere 1000. 5000 × magnification and 20000 × magnification. Manufacturer quoted particle size 1µm.

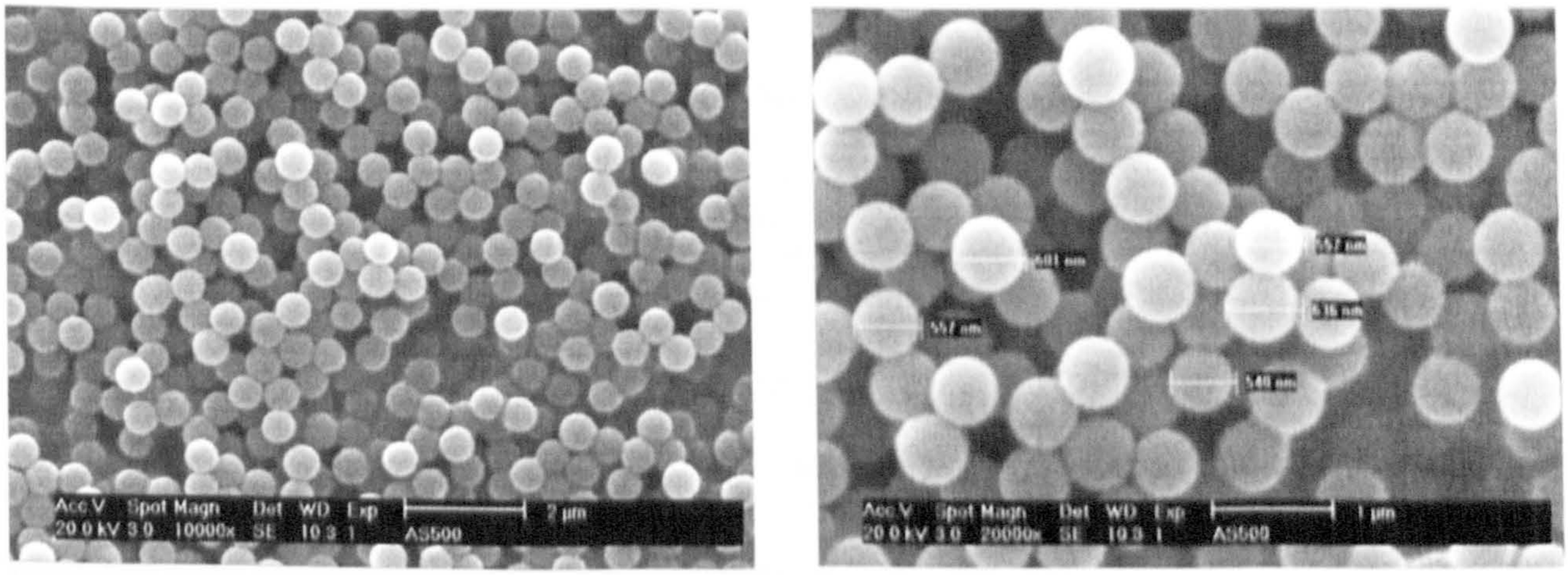

Figure A5 Scanning electron micrographs – Angstromsphere 500. 10000 × magnification and 20000 × magnification. Manufacturer quoted particle size 0.5µm.

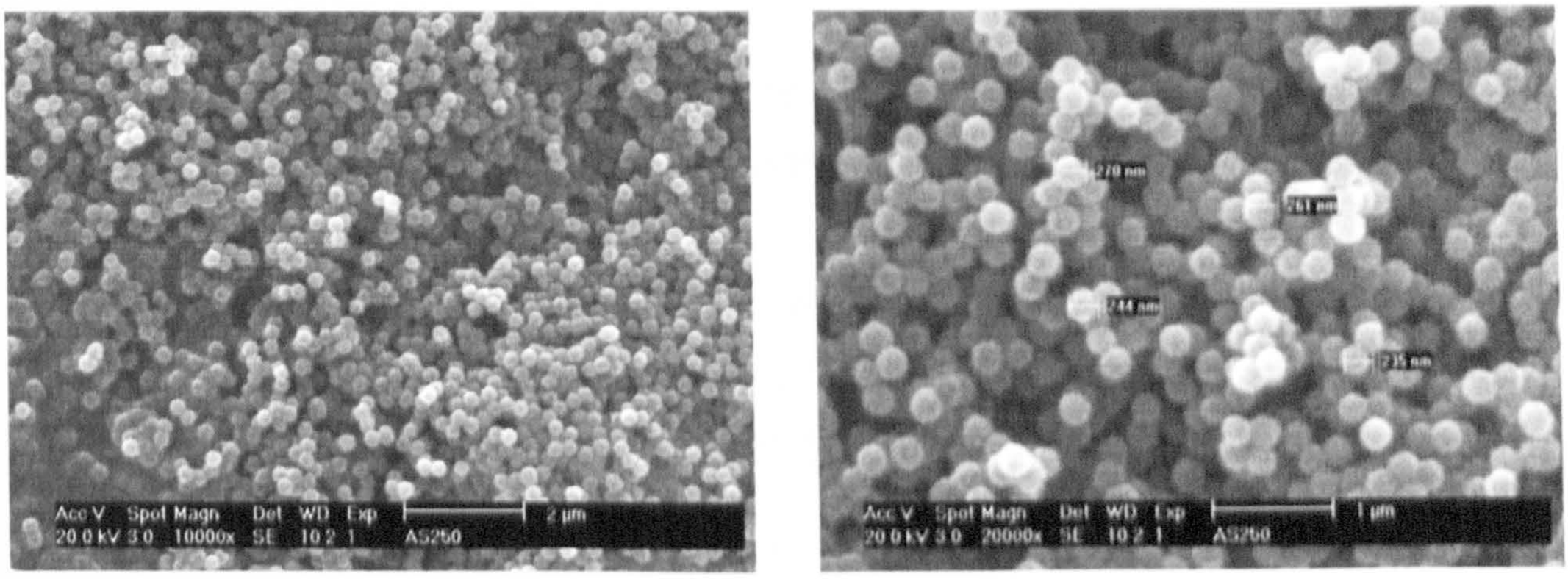

Figure A6 Scanning electron micrographs – Angstromsphere 500. 10000 × magnification and 20000 × magnification. Manufacturer quoted particle size 0.25µm.

Zeta Potential

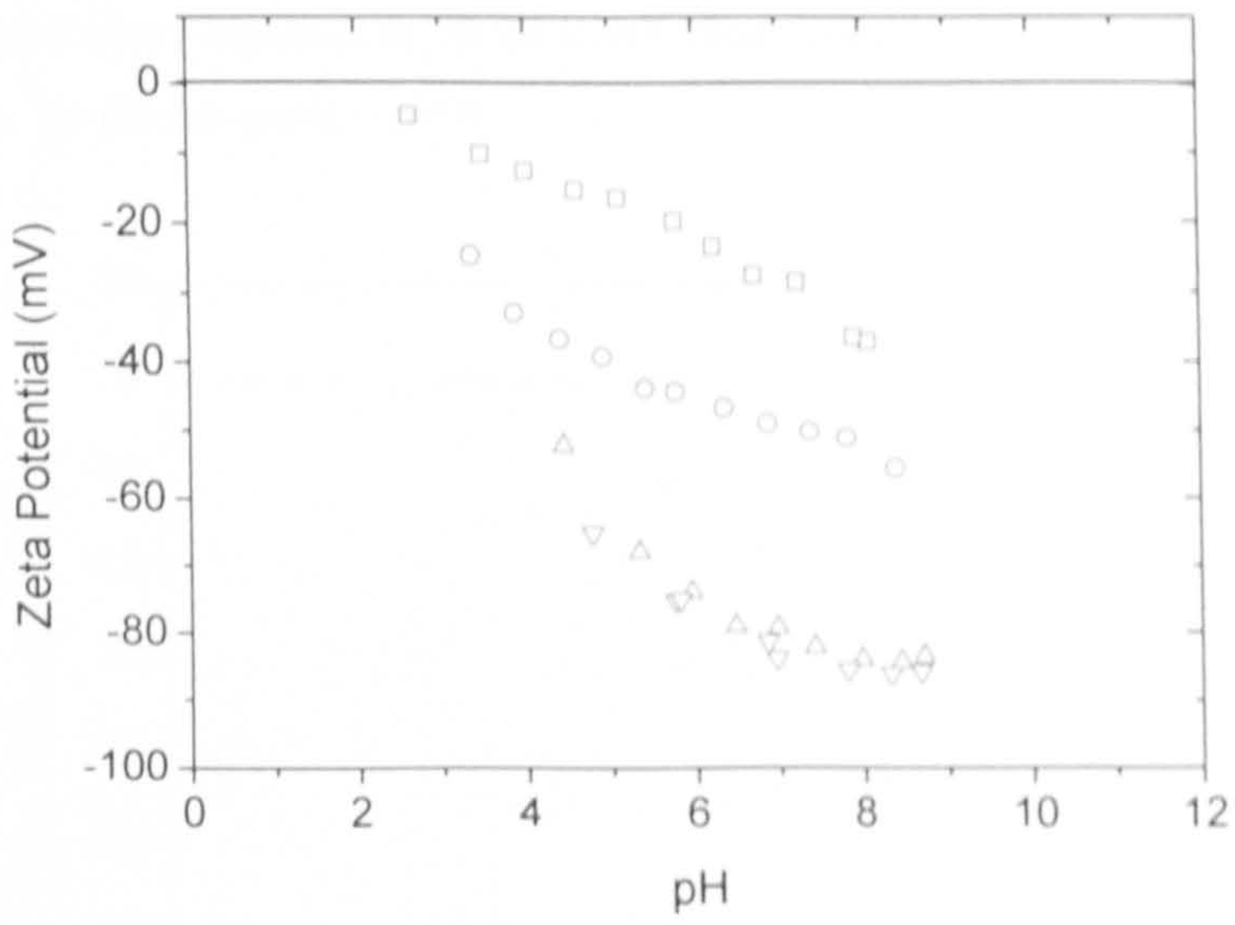

Figure A7 Zeta potential curves determined using the Malvern zeta nanosizer. 1µm Angstromsphere suspensions prepared to 10000ppm dispersed in 10^{-1}M KNO_3 (squares), 10^{-2}M KNO_3 (circles), 10^{-3}M KNO_3 (triangles) and 10^{-4}M KNO_3 (inverted triangles). pH adjusted using KOH and HNO_3. Iso-electric point ≈ pH 2.

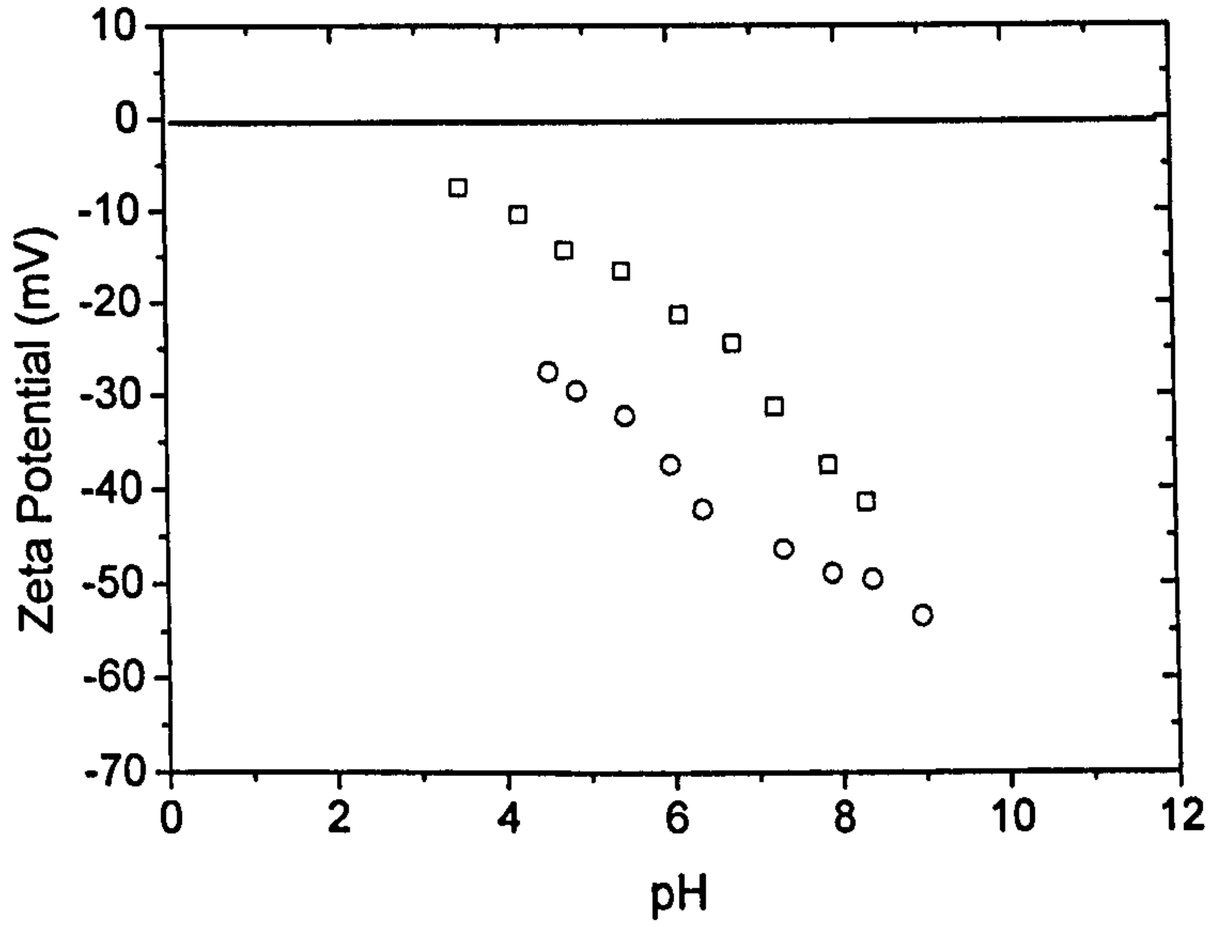

Figure A8 Zeta potential curves determined using the Malvern zeta nanosizer. 0.5μm Angstromsphere silica spheres prepared to 10000ppm, dispersed in 10^{-1}M KNO_3 (squares) and 10^{-2}M KNO_3 (circles). pH adjusted using KOH and HNO_3. Iso-electric point ≈ pH 2

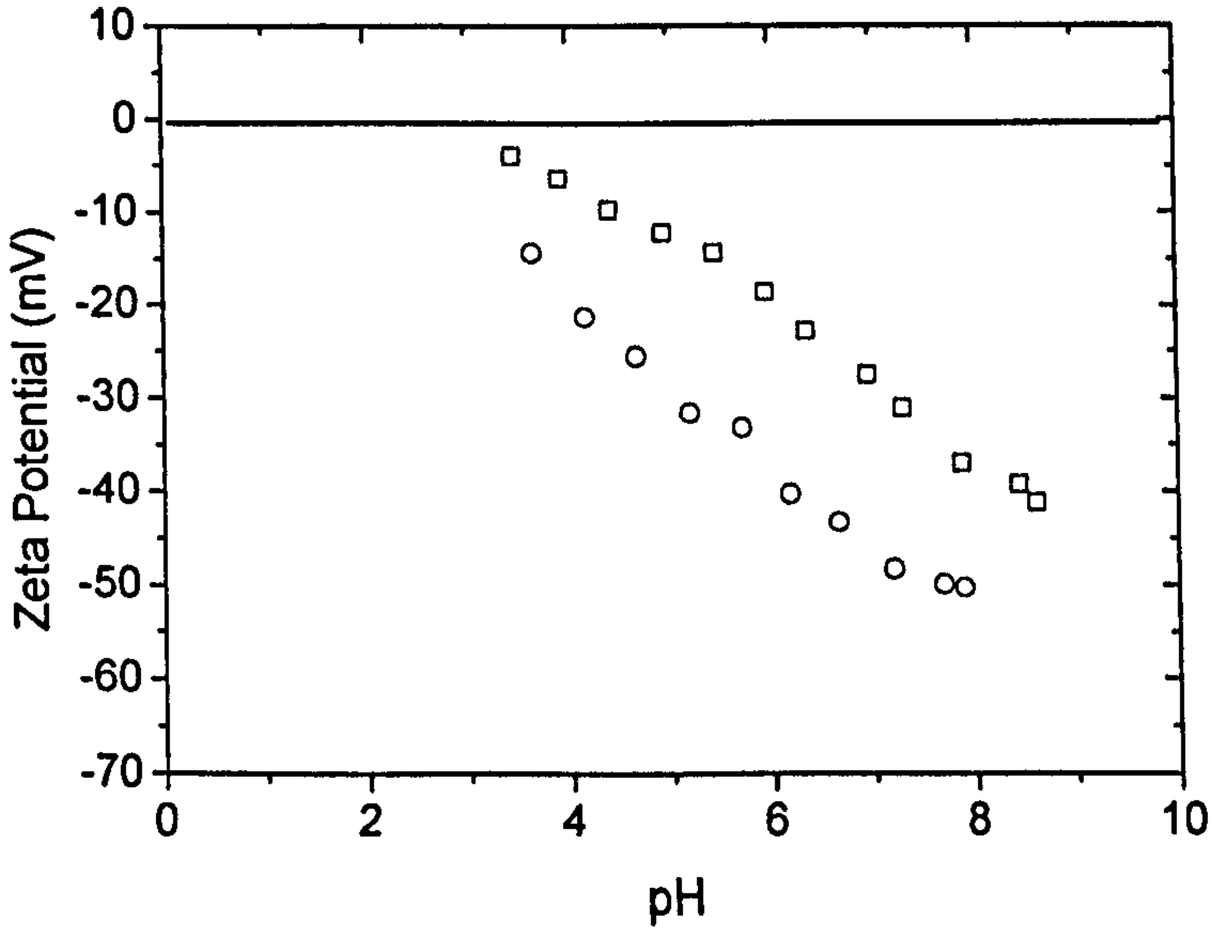

Figure A9 Zeta potential curve determined using the Malvern zeta nanosizer. 0.25μm Angstromsphere silica spheres prepared to 10000ppm, dispersed in 10^{-1}M KNO_3 (squares) and 10^{-2}M KNO_3 (circles). pH adjusted using KOH and HNO_3. Iso-electric point ≈ pH 2.5

pH Stability

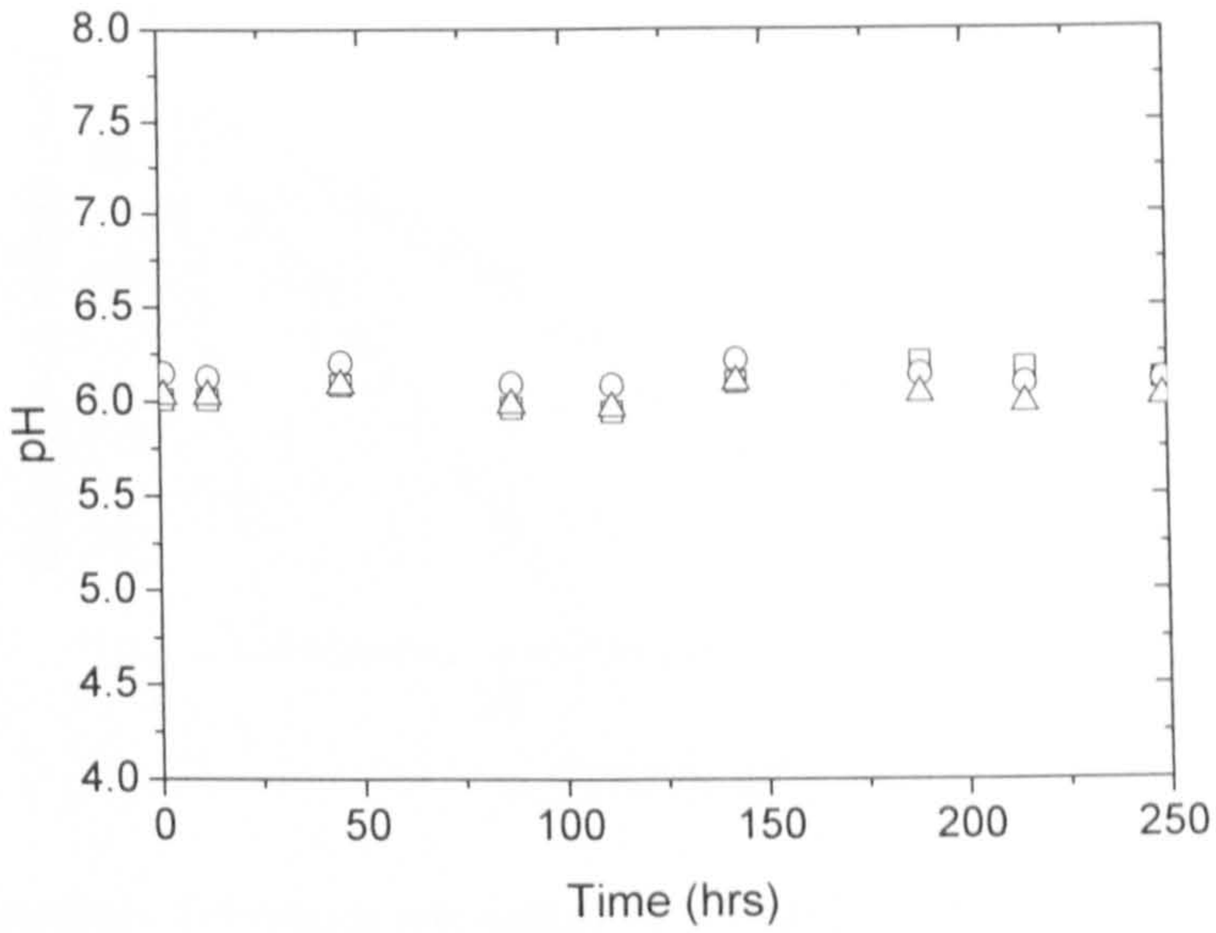

Figure A10 5%vol suspension prepared in 10^{-4}M KNO_3 background electrolyte. Negligible drift in suspension pH; small shifts most likely associated to pH meter calibration. Symbols: 1μm silica (squares), 0.5μm silica (circles), 0.25μm (triangles).

Settling

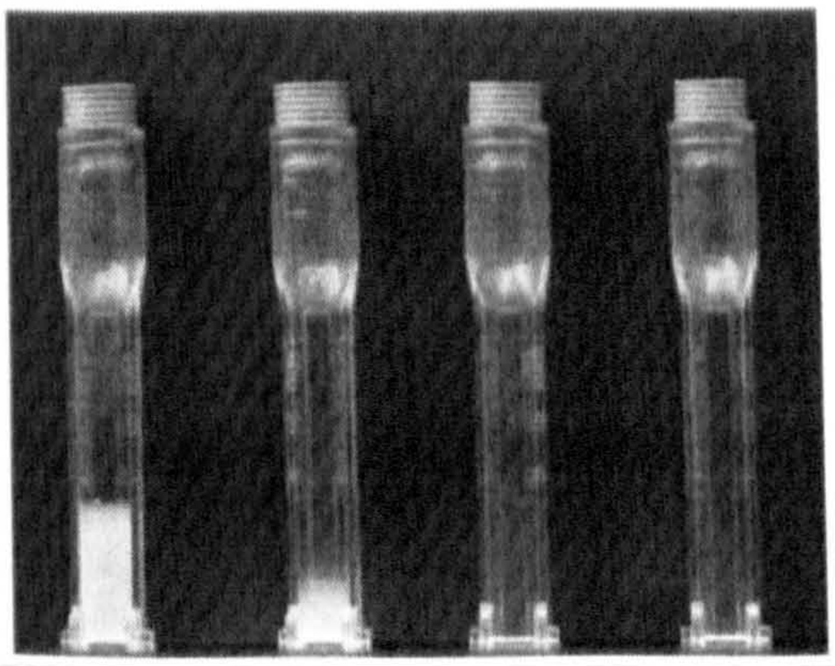

Figure A11 Suspension height after 30 minutes of centrifugal settling at 300rpm. Order left to right: 250nm, 500nm, 1000nm and 1000nm Monospher. Suspension prepared to 10000ppm in 10^{-4}M KNO_3 at pH6. Centrifugal force = 11×g.

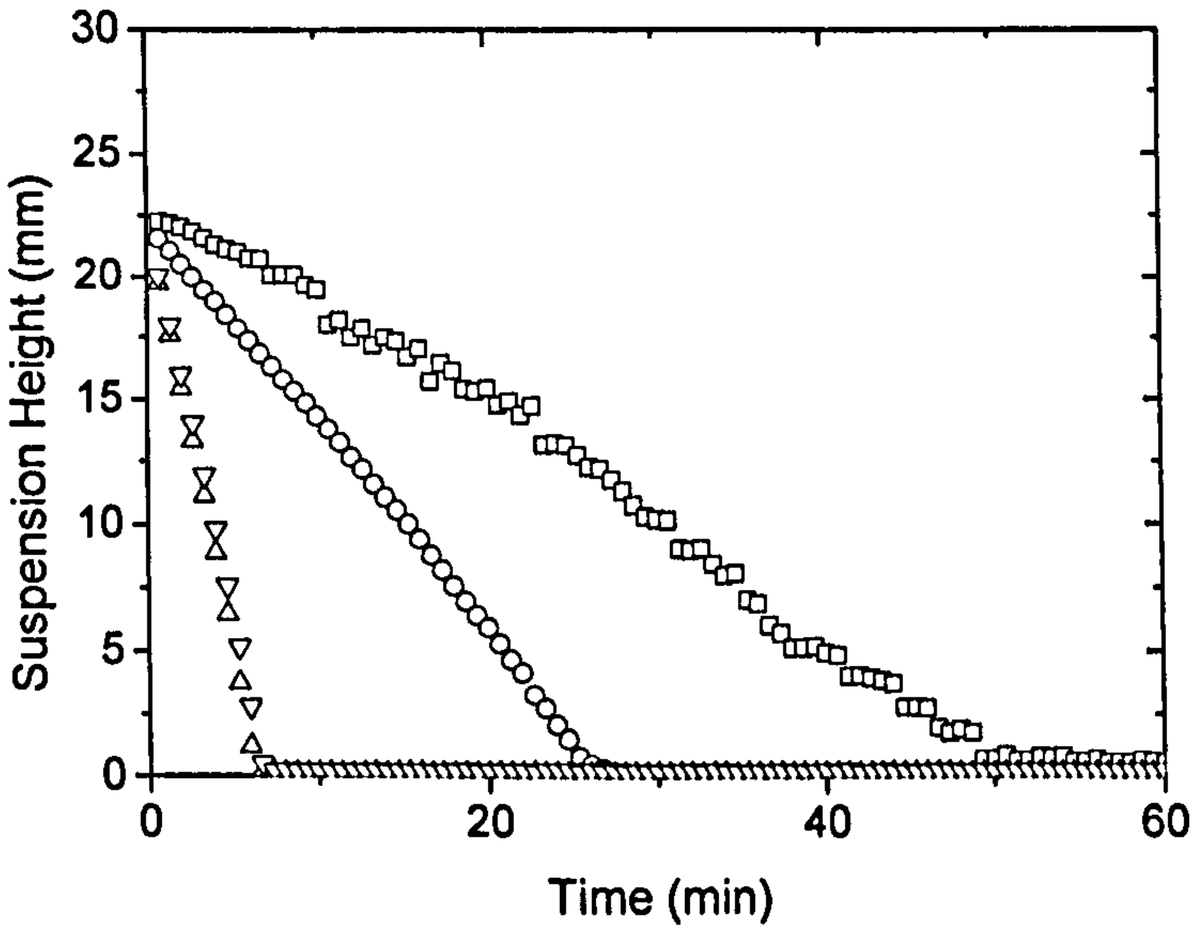

Figure A12 Settling profiles. Suspension prepared to 10000ppm in 10^{-4}M KNO_3 at pH 6. Symbols: 250nm (squares), 500nm (circles), 1000nm (triangles) and 1000nm Monospher (inverted triangles). Centrifugal force = 940rpm (≈ 90×g)

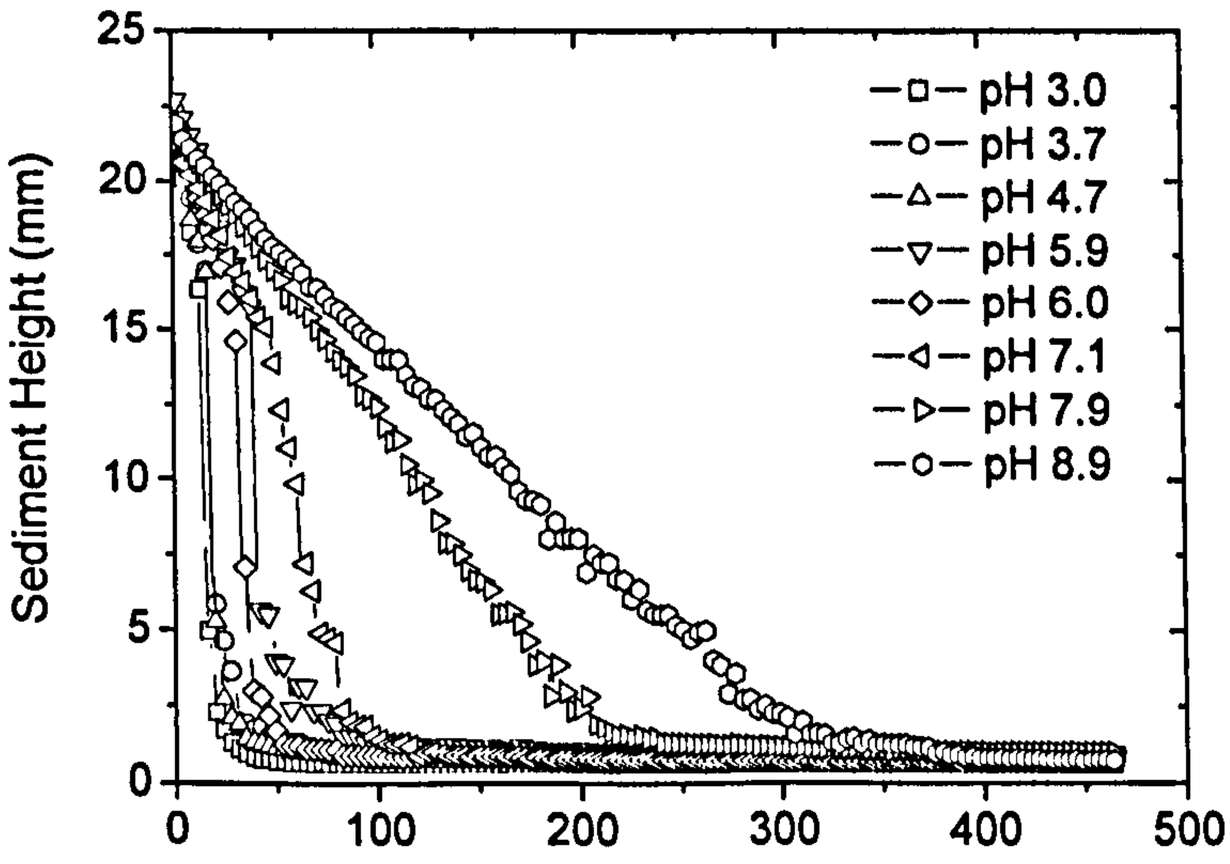

Figure A13 Settling profiles as a function of the suspension pH determined using the LUMiFuge®. 1μm Angstromsphere dispersed in 10^{-1}M KNO_3 electrolyte. Solids concentration = 10000ppm. Profiles equivalent to 1×g.

CALCIUM CARBONATE – Aldrich, USA

Cost: ≈ £50/kg

Scanning Electron Micrograph

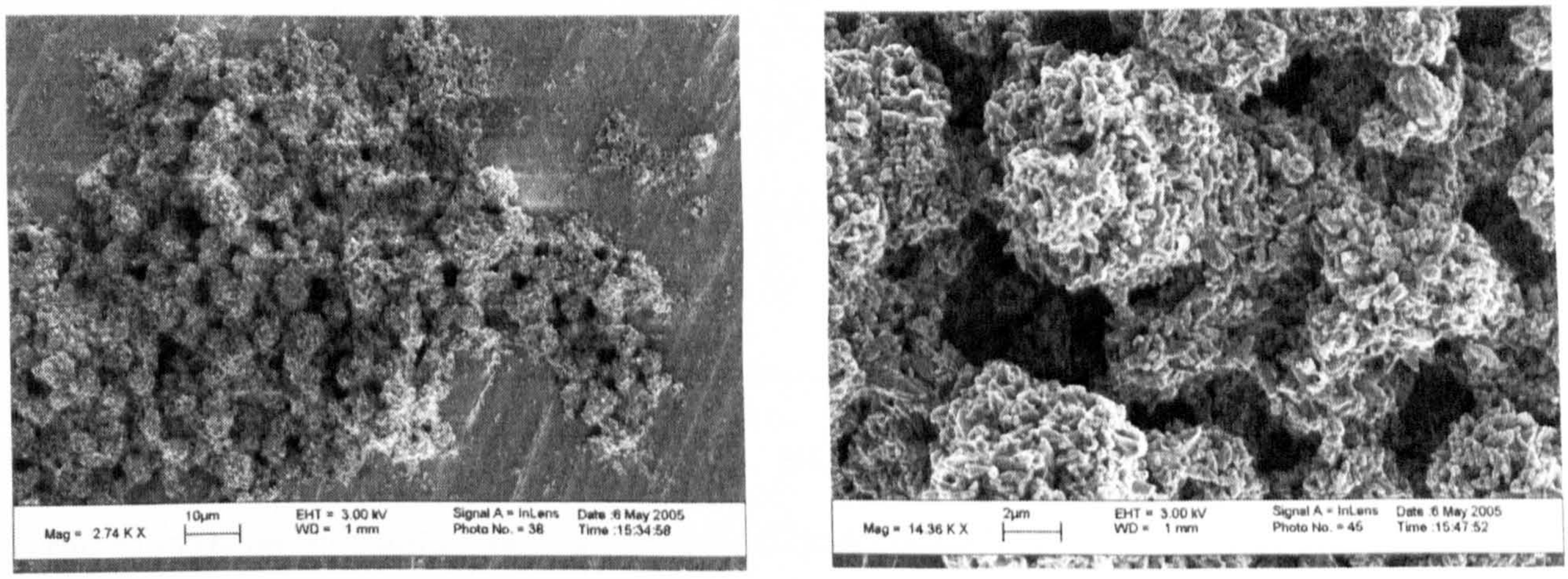

Figure A14 Scanning electron micrographs – Calcium carbonate. 2740 × magnification and 14360 × magnification. Calcium carbonate particles formed due to the agglomeration of smaller nano particles.

Particle Size Distribution

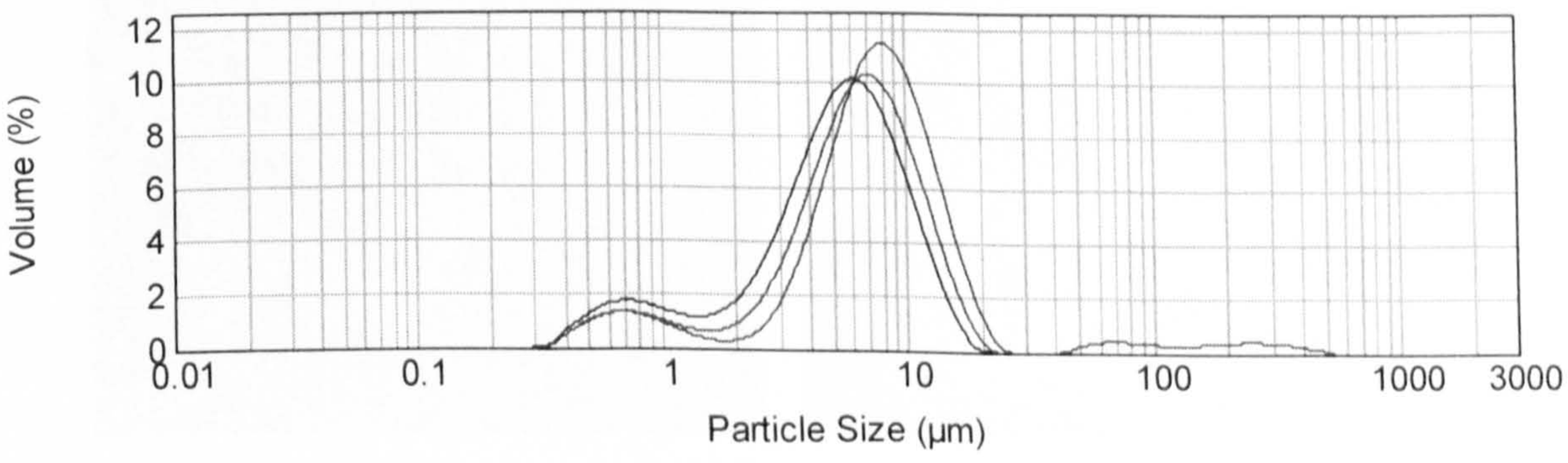

Figure A15 Particle size distribution determined using the Malvern Mastersizer 2000.

Zeta Potential

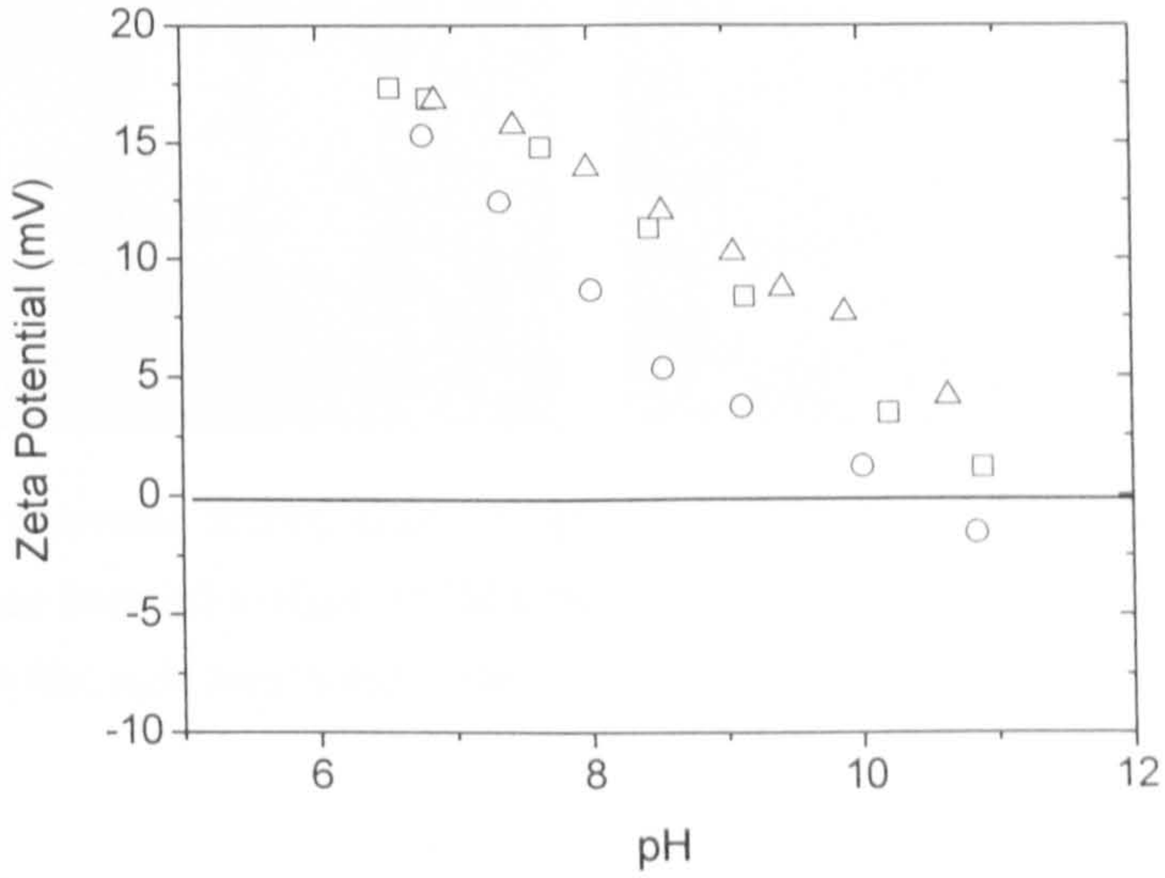

Figure A16 Zeta potential curve determined using the Colloidal Dynamics ZetaProbe. Solids concentration 1%vol. Background electrolyte 10^{-1}M KNO_3 (squares), 10^{-2}M KNO_3 (triangles) and 10^{-3}M KNO_3 (circles). pH adjusted using KOH. Iso-electric point ≈ 10.5

Settling

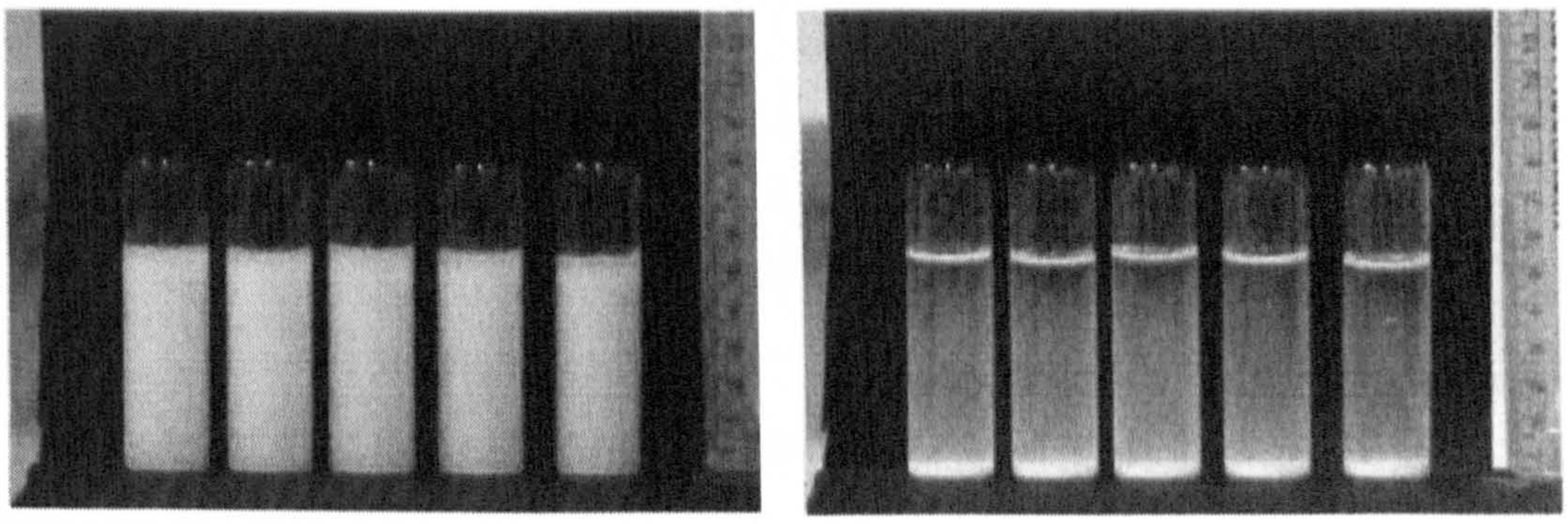

Figure A17 Calcium carbonate settling tests. Background electrolyte - 10^{-3}M KNO_3, pH from left to right: pH6.5, 8.0, 9.5, 11.5 and 12.5. Suspension concentration 5%vol. Settling time - left hand side t = 0hr, right hand side t = 1hr.

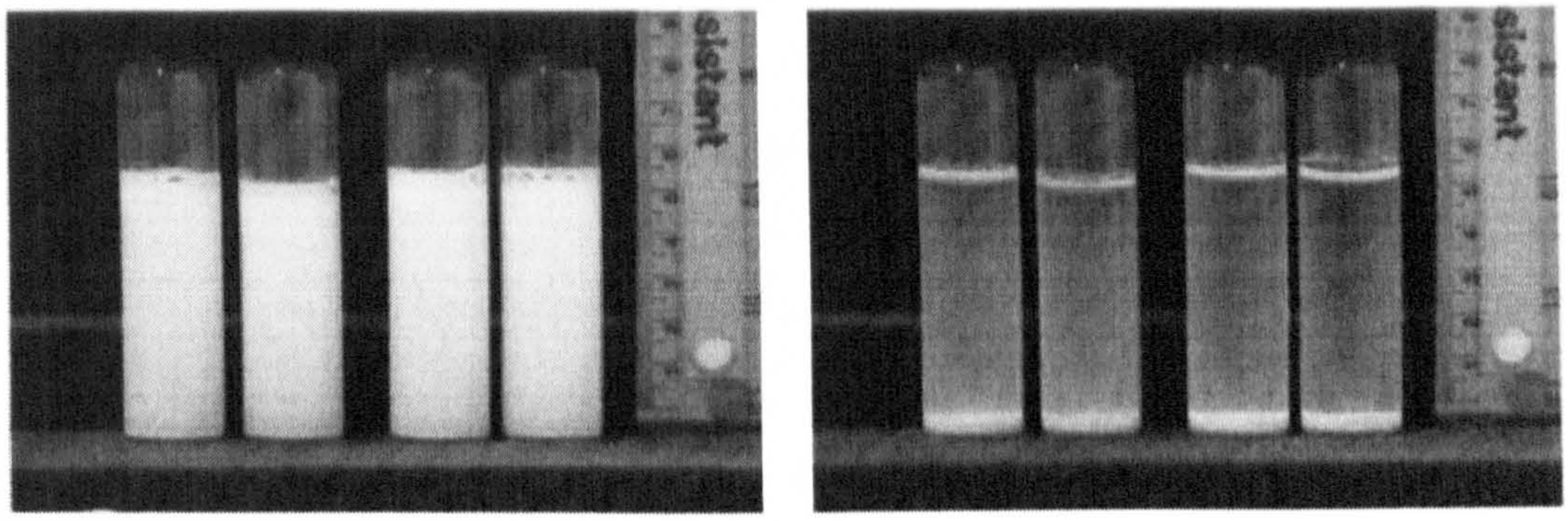

Figure A18 Calcium carbonate settling tests. Suspension concentration 5%vol at pH 6.5. Background electrolyte concentration from left to right: 10^{-3}M KNO_3, 10^{-2}M KNO_3, 10^{-1}M KNO_3 and 1M KNO_3. Settling time - left hand side t = 0hr, right hand side t = 1hr.

SPHERIGLASS SILICA 2000 – Potters Industries Inc., USA

Cost ≈ £50/KG

Particle Size Distribution

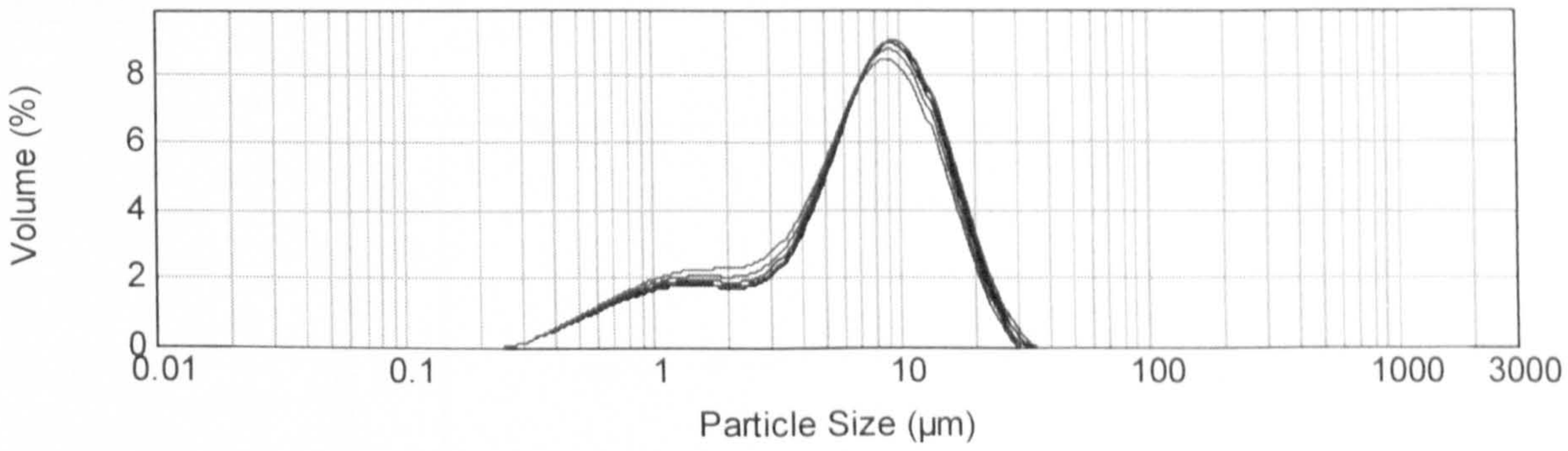

Figure A19 Particle size distribution determined using the Malvern Mastersizer 2000.

Zeta Potential

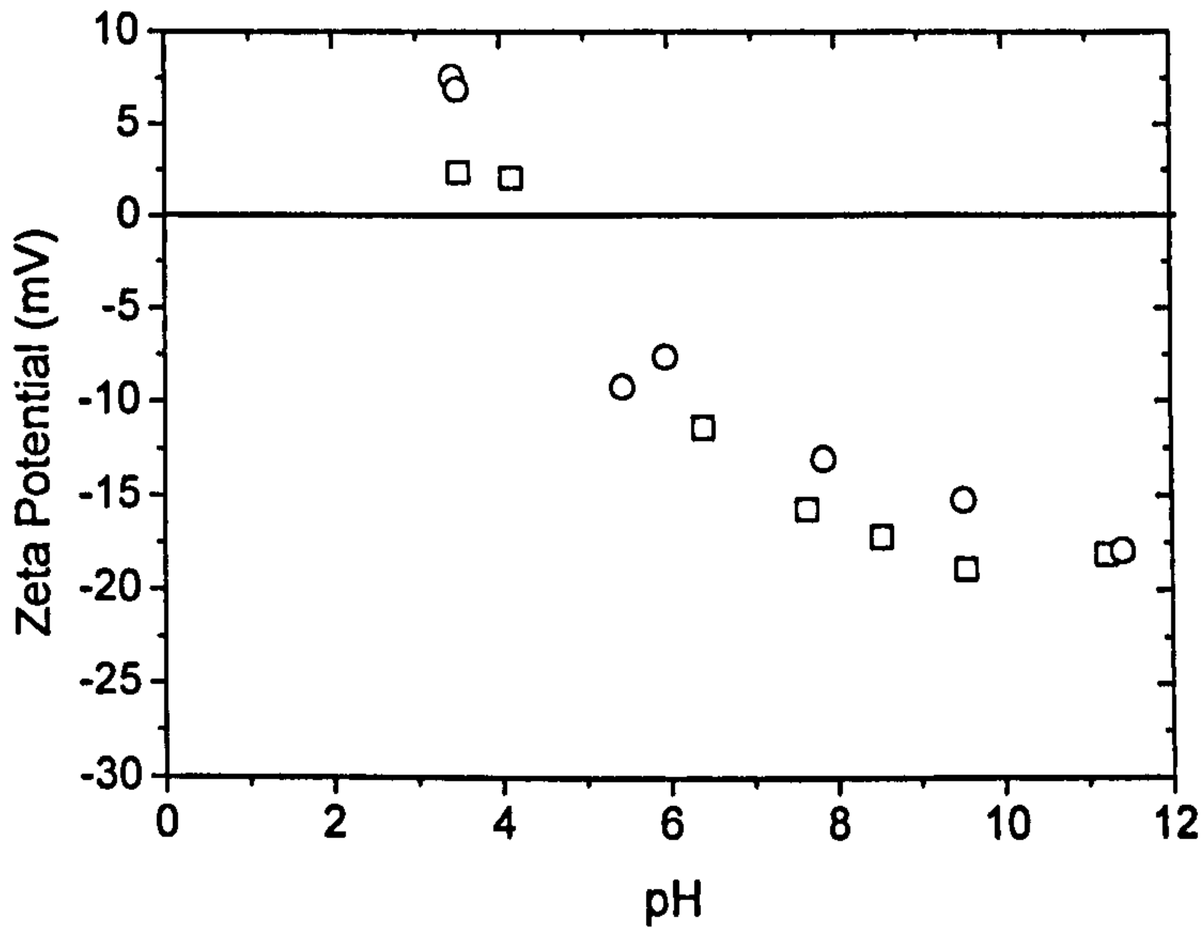

Figure A20 Zeta potential curve determined using the Colloidal Dynamics ZetaProbe. Solids concentration 1% by volume. Background electrolyte 1M KNO_3 (circles) and 10^{-4}M KNO_3 (squares). pH adjusted using KOH and HNO_3. Iso-electric point ≈ pH 4

Gel Point

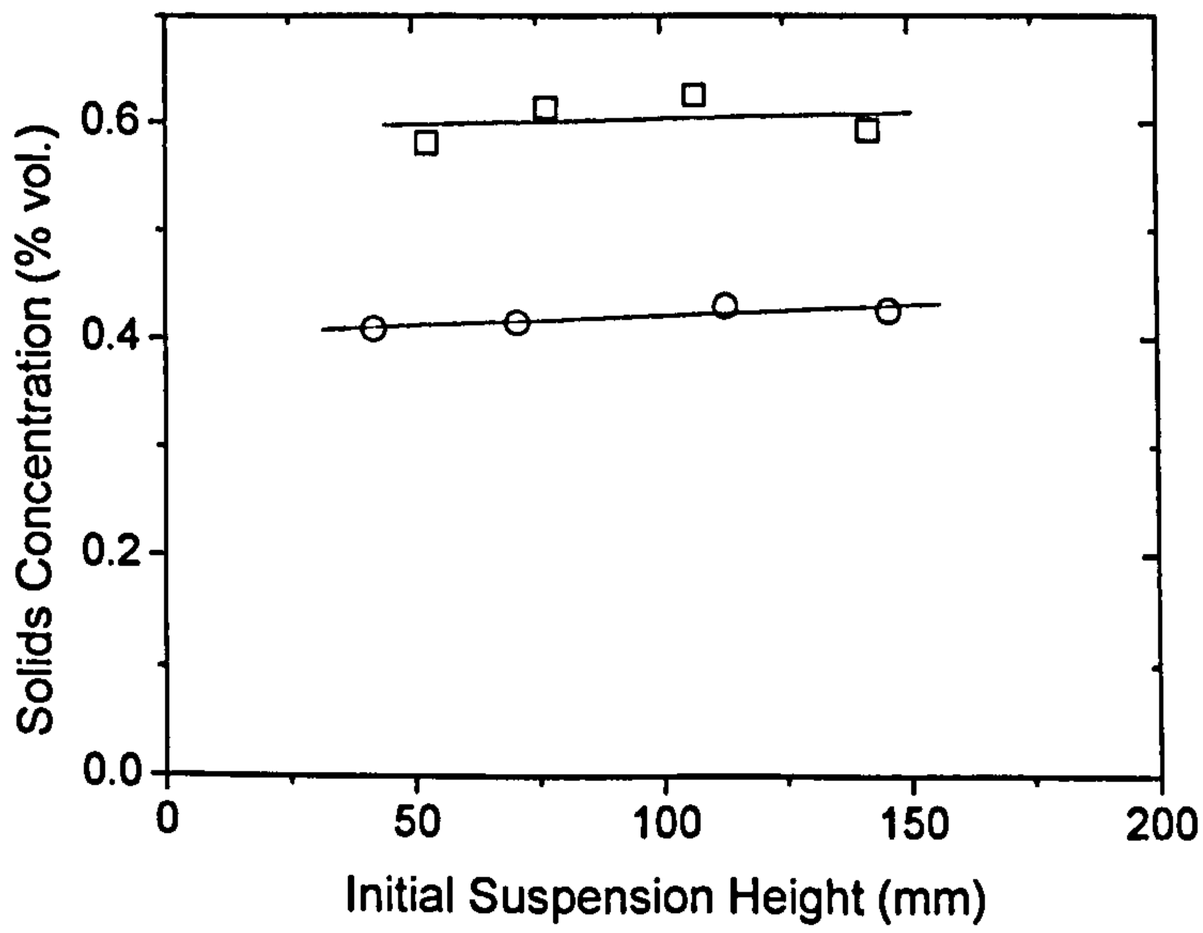

Figure A21 Suspension gel points. Initial suspension concentration 12% by volume at pH 10. Background electrolyte 1M KNO_3 (circles) and 10^{-4}M KNO_3 (squares).

pH Stability

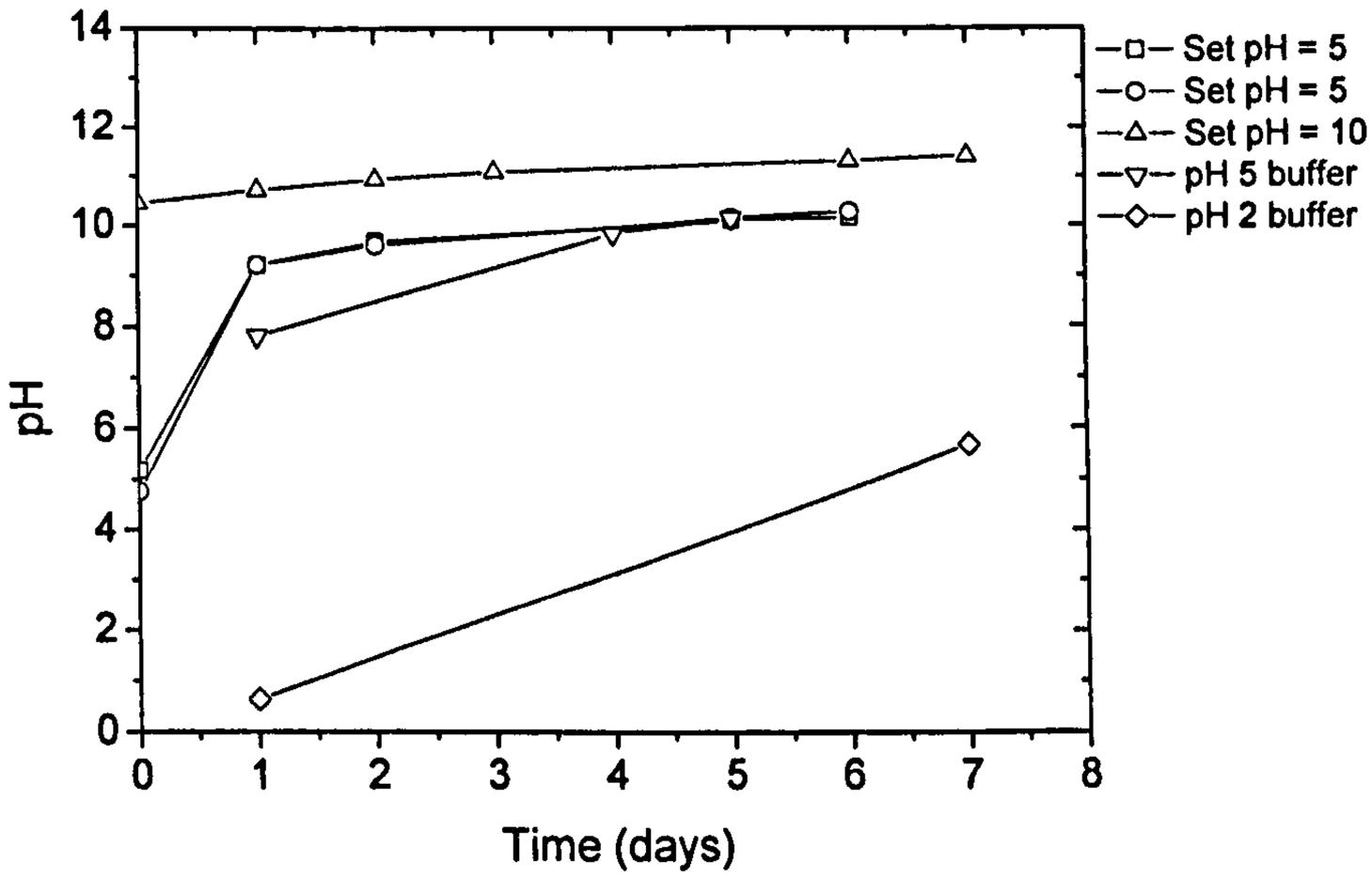

Figure A22 5%vol suspensions prepared in 10^{-4}M KNO_3 background electrolyte. Adjusted pH = 5 – squares and circles. Adjusted pH = 10 – triangles. Adjusted pH = 5 (pH5 buffer) – inverted triangles. Adjusted pH = 2 (pH2 buffer) – diamonds.

Yield Stress

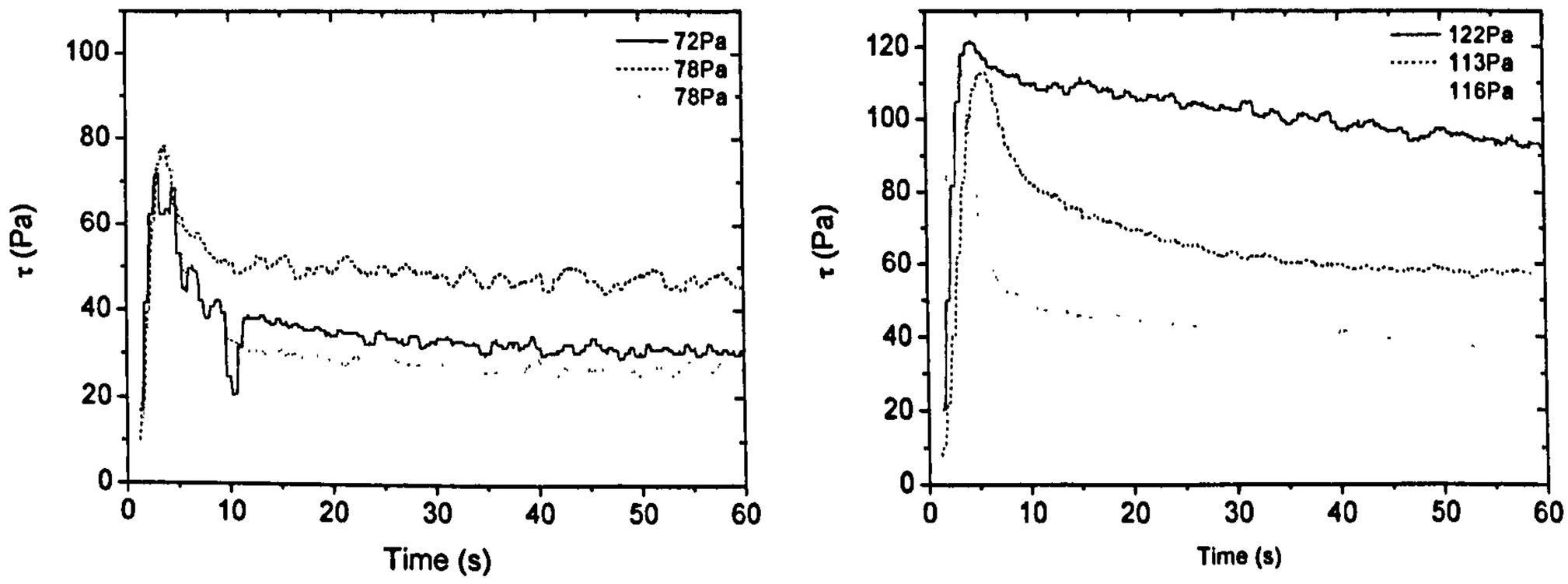

Figure A23 Sediment shear yield stress. Solids concentration ≈ 60%vol at pH 10. 10^{-4}M KNO_3 (left hand side), 1M KNO_3 (right hand side)

SPHERIGLASS SILICA 5000

Particle Size Distribution

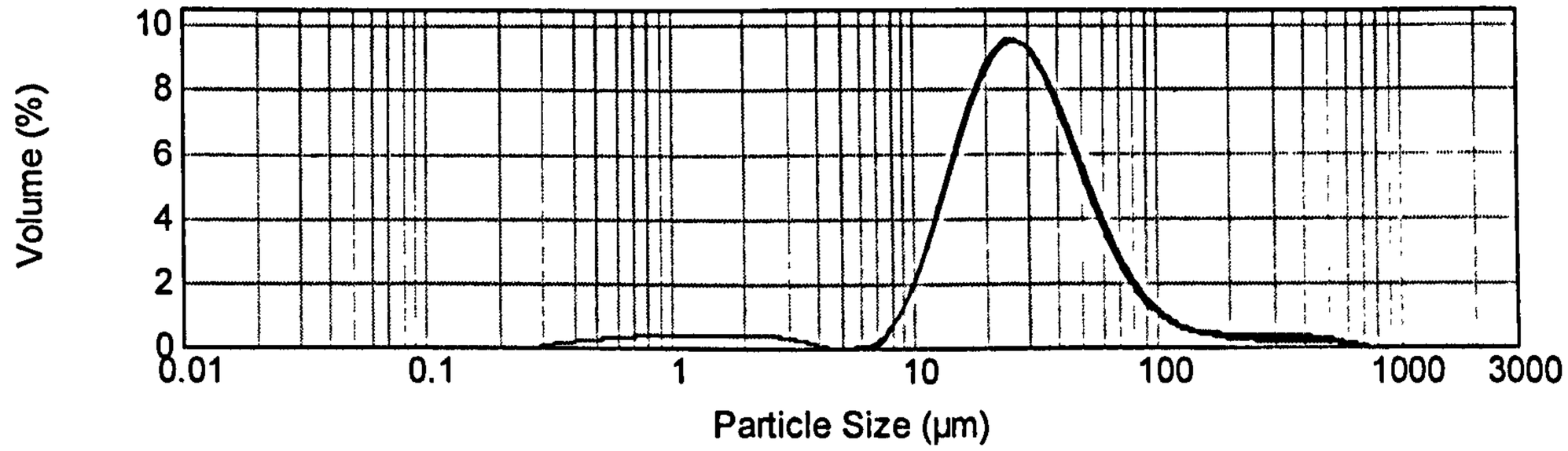

Figure A24 Particle size distribution determined using the Malvern Mastersizer 2000.

Conclusion

From the characterisation experiments Fuso silica was chosen as the most suitable material for the pipe loop study. Fuso silica dispersed in solution provided a stable suspension pH over a long time period (see figure B3), showed a narrow distribution in polydispersity (see figure 4.0) and an iso-electric point which is representative of a clean silica sample (see figure 5.6 – iso-electric point pH ≈ 2.5 – 3). Such characteristics were also observed for the Angstromsphere and Monospher silica. 250nm and 500nm Angstromsphere silica was rejected due to the long settling times required to form consolidated sediments. The 1µm silica's (Angstromsphere and Monospher samples) were also rejected due to the high raw material costs when compared to Fuso silica (approximately £50/KG). The Spheriglass samples were rejected for a variety of reasons which included; i) limited pH control, ii) non-colloidal particle sizes (limited control over the particle-particle interaction strength) and iii) large polydispersity. Calcium carbonate, although having a low raw material cost was rejected on the basis of limited control on the particle-particle interaction strength with electrolyte concentration. It was also rejected as the sample would not provide a "model" solid phase for suspension, with irregular particle shapes formed from smaller nano aggregates.

APPENDIX B

FURTHER FUSO SILICA CHARACTERISATION

Scanning Electron Micrographs

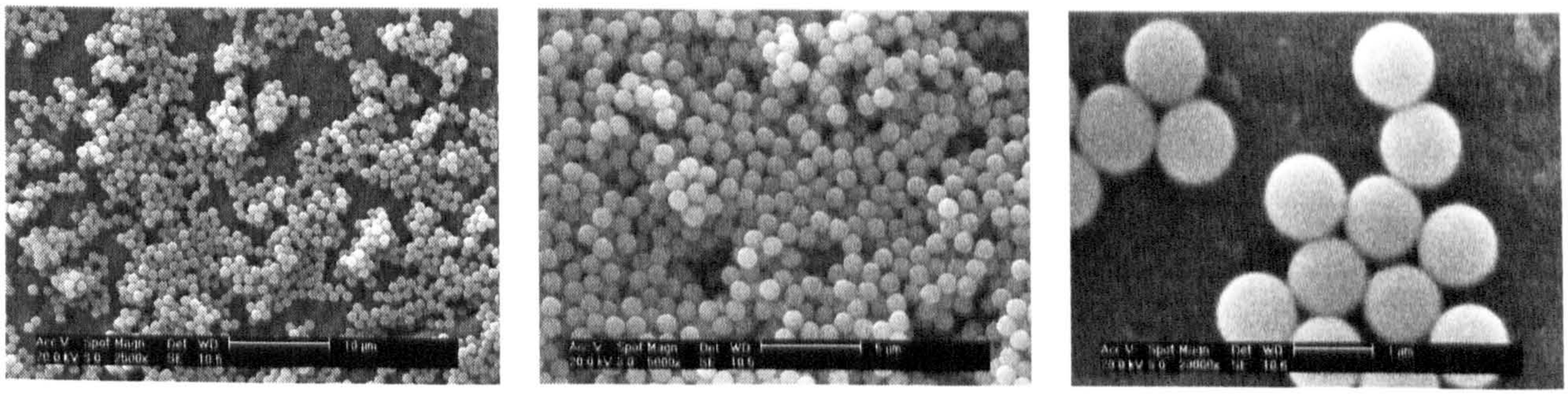

Figure B1. Scanning electron micrographs – Fuso silica. 2500 × magnification, 5000 × magnification and 20000 × magnification.

Particle Size Distribution

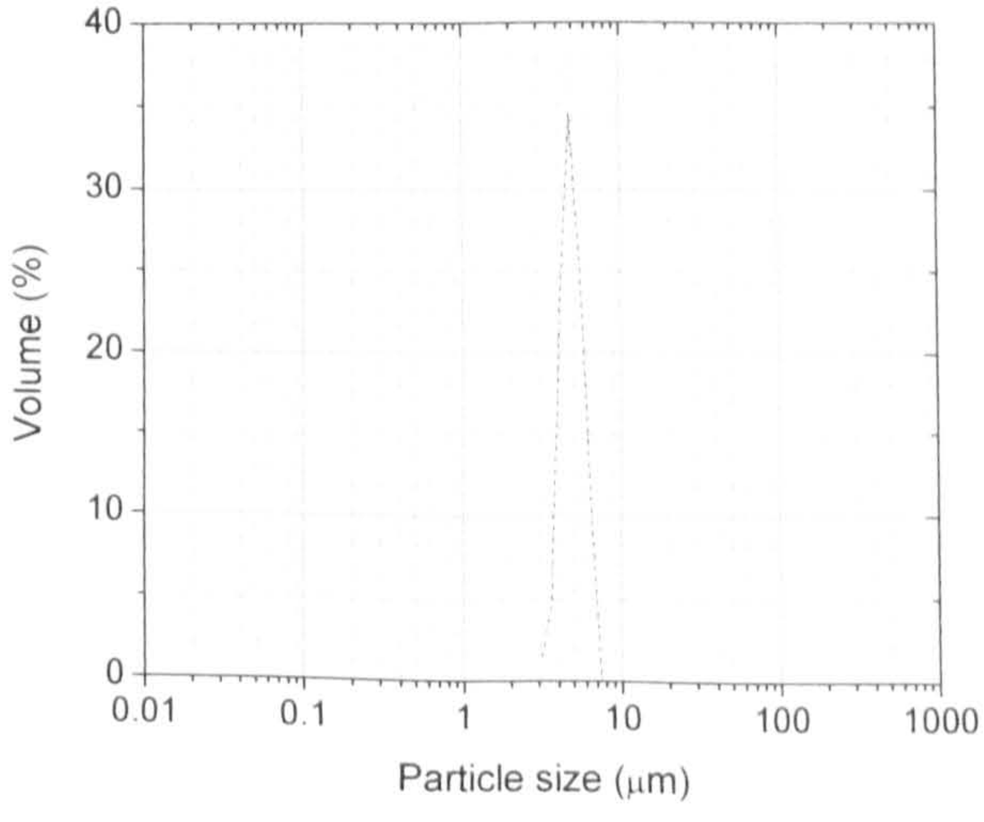

Figure B2. Particle size distribution determined using Malvern Zetasizer Nano. – Fuso silica dispersed in 1M KNO_3 electrolyte (Particle size d_{50} = 4.6nm).

pH Stability

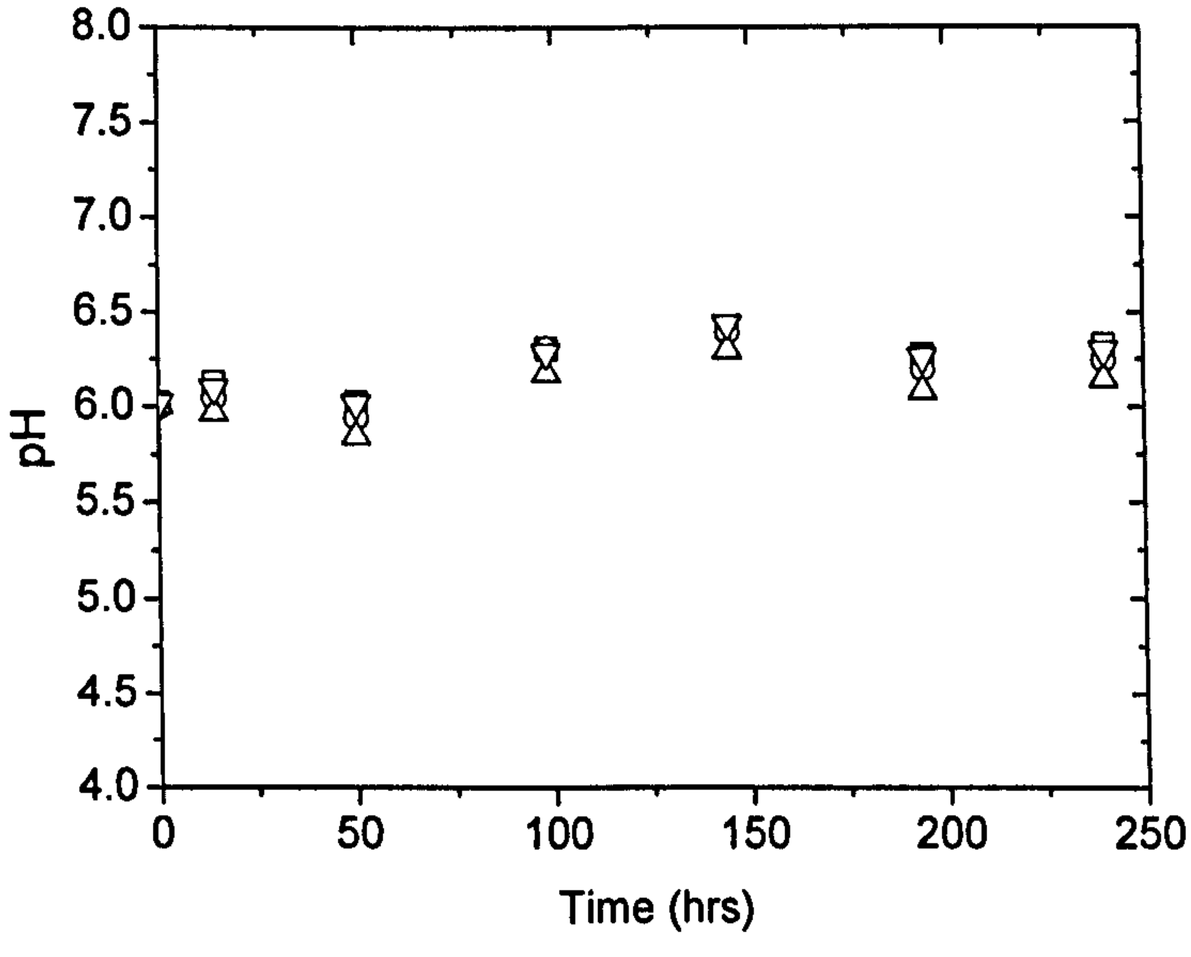

Figure B3. pH stability Fuso silica. Symbols: square – 1M KNO_3, circle – 10^{-1}M KNO_3, triangle – 10^{-2}M KNO_3, inverted triangle – 10^{-4}M KNO_3. Solids concentration 7.5 wt%.

Settling Profiles

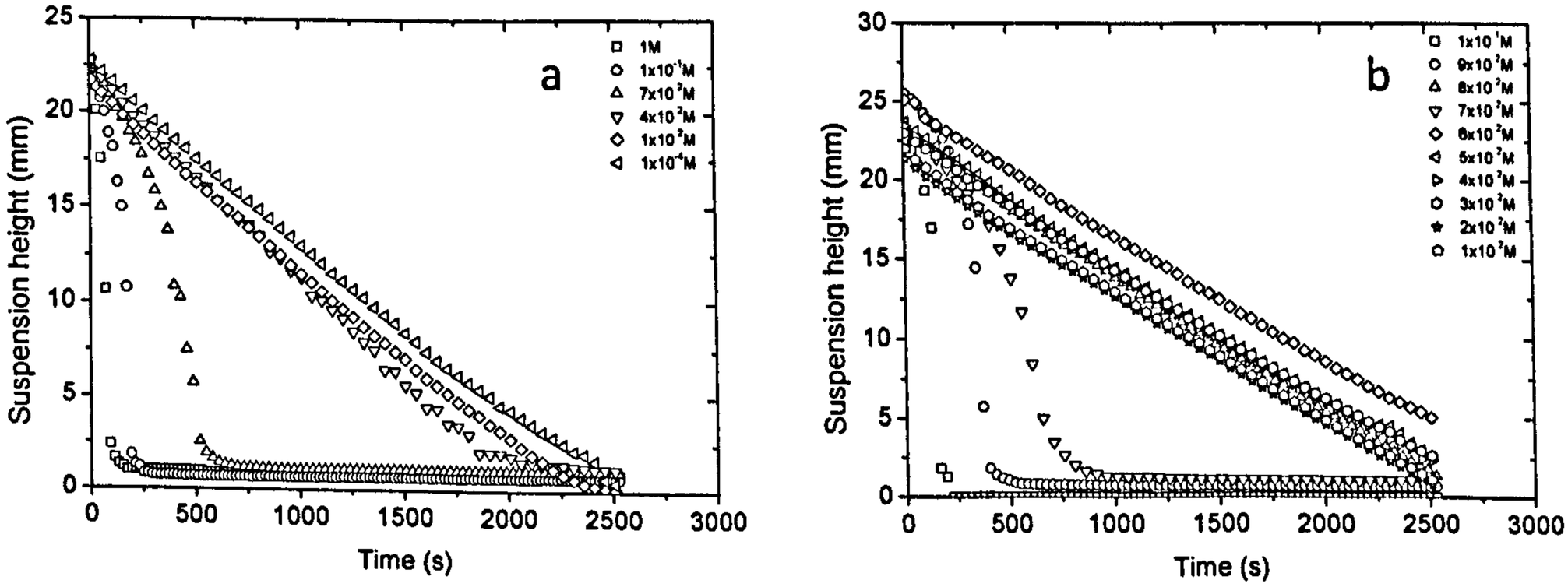

Figure B4. Settling profiles determined from LUMiFuge® transmission profiles. a) KNO_3, b) KCl. Settling at 11g.

Critical Coagulation Concentration

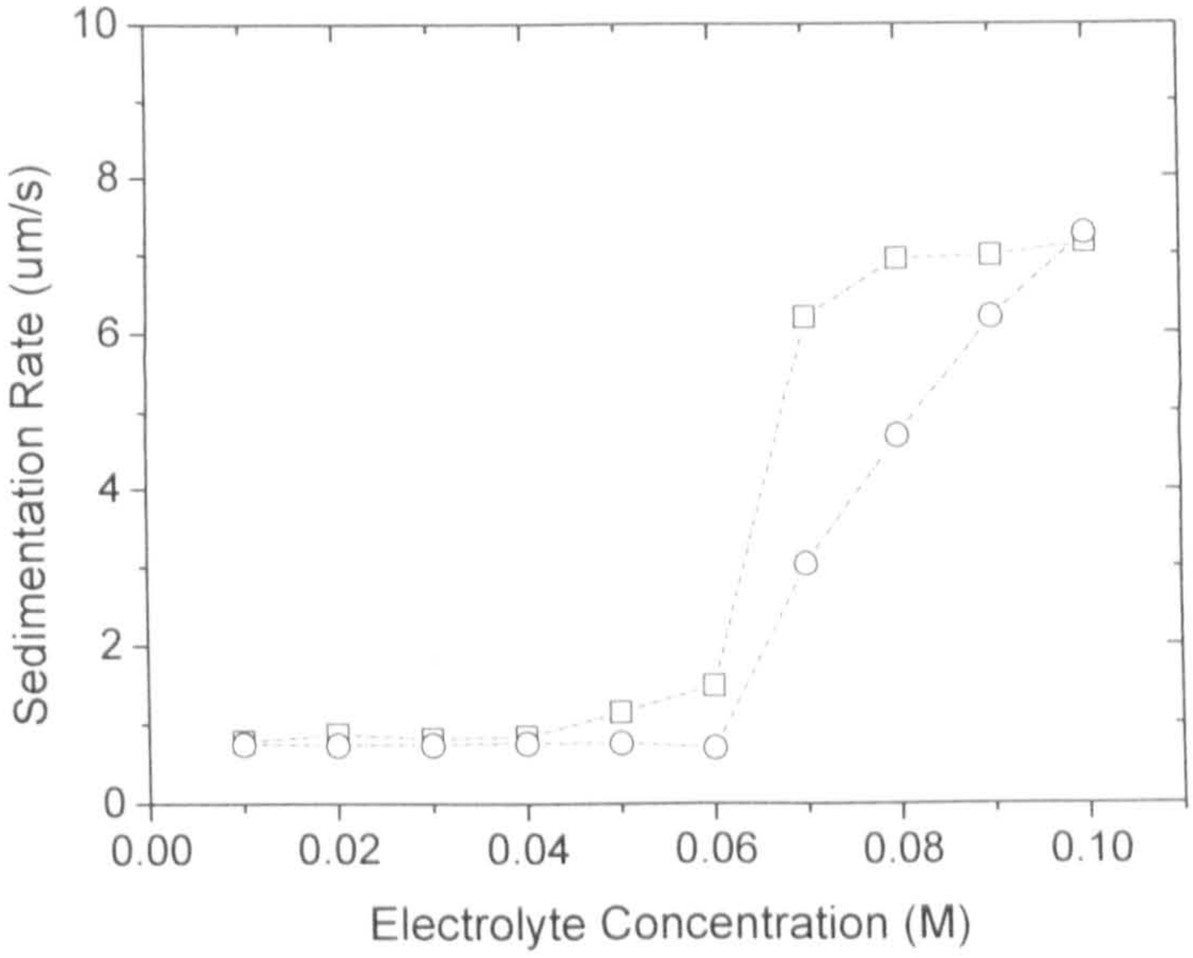

Figure B5. Sedimentation rates as a function of the electrolyte concentration. An observed jump in the sedimentation rates as the c.c.c. is surpassed. Symbols: square – KNO_3, circle – KCl.

Sediment Packing Heights

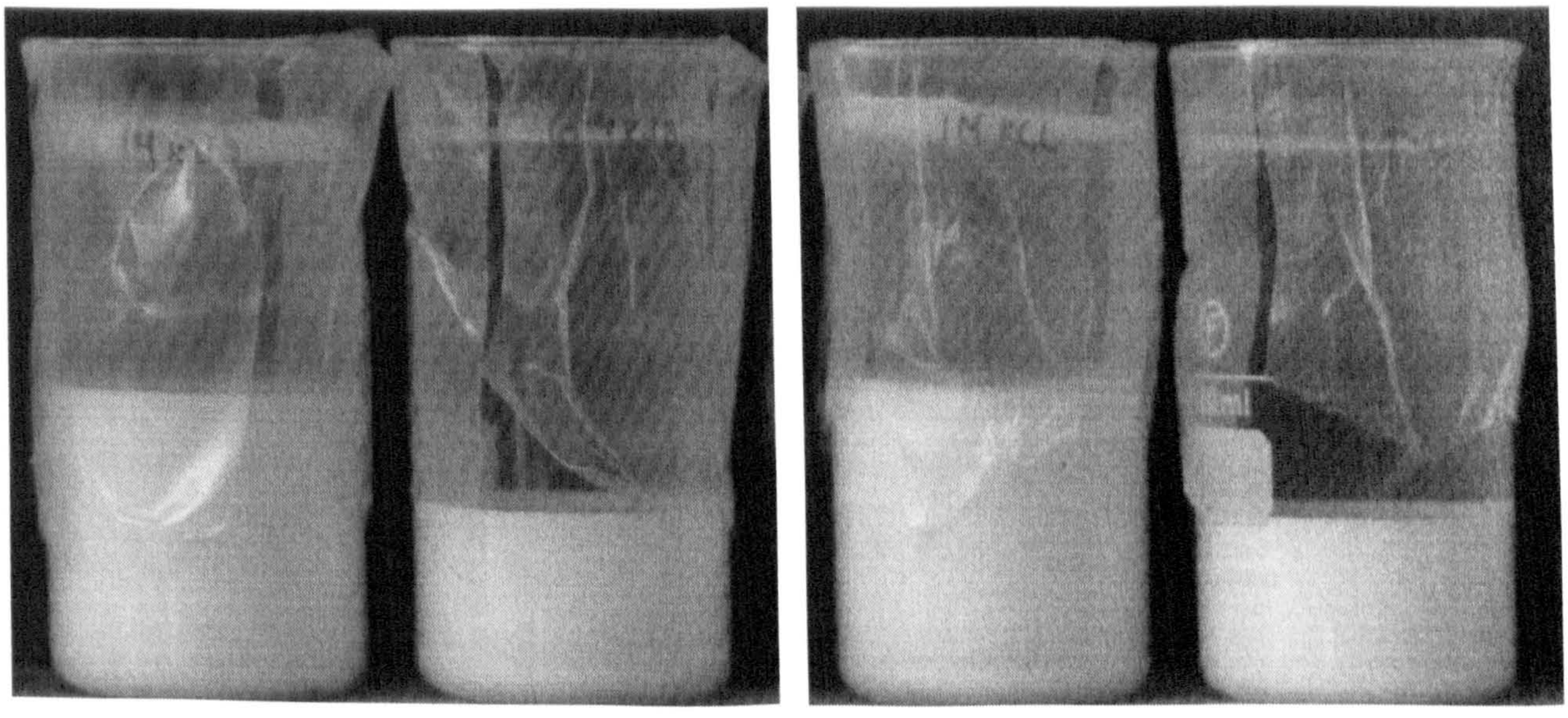

Figure B6. Sediment bed heights as a function of electrolyte type and concentration. Background electrolyte - KNO_3 (left hand side), 1M and 10^{-4}M. Background electrolyte - KCl (right hand side), 1M and 10^{-4}M.

Gel Points

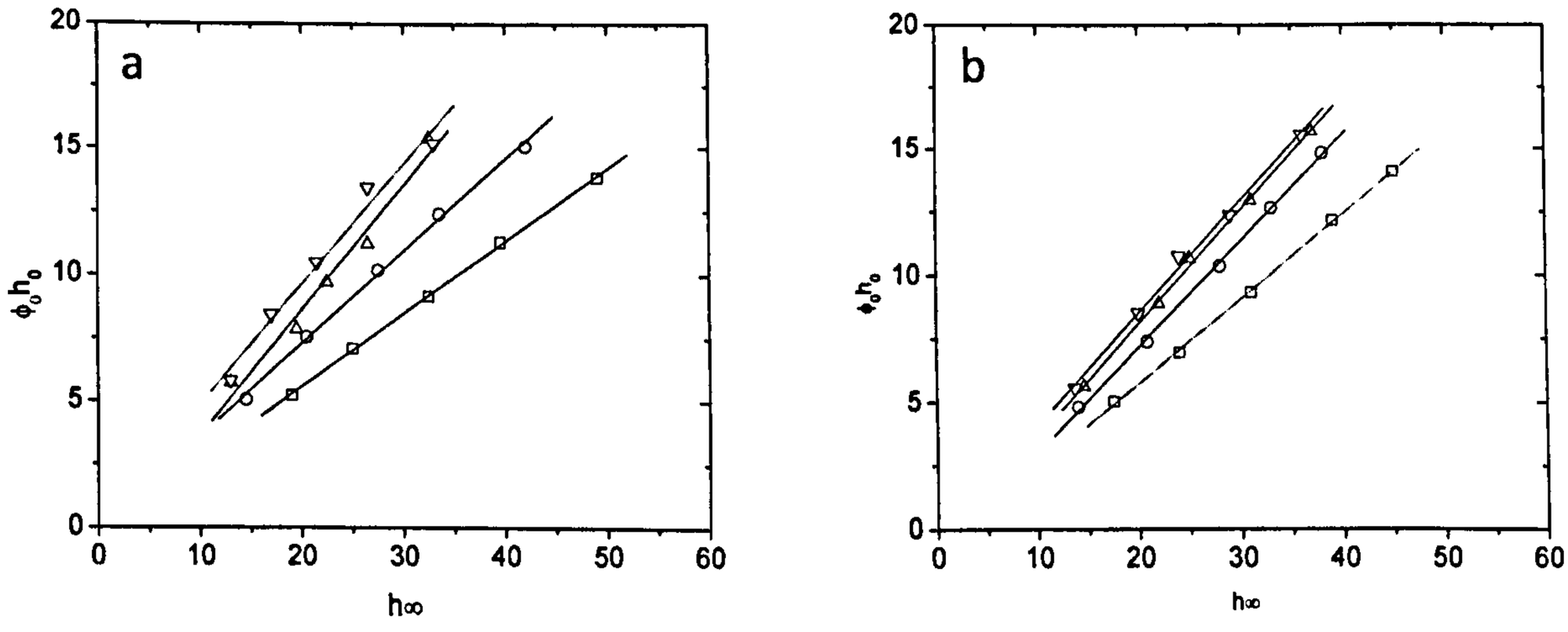

Figure B7. Suspension Gel Points a) KNO_3, b) KCl. Symbols: square – 1M, circle 10^{-1}M, triangle 10^{-2}M, inverted triangle 10^{-4}M. In order of decreasing electrolyte concentration KNO_3 = 0.29, 0.36, 0.49, 0.47. and KCl = 0.33, 0.42, 0.45, 0.44. Units - volume %.

Shear Yield Stress – Function Rotational Speed

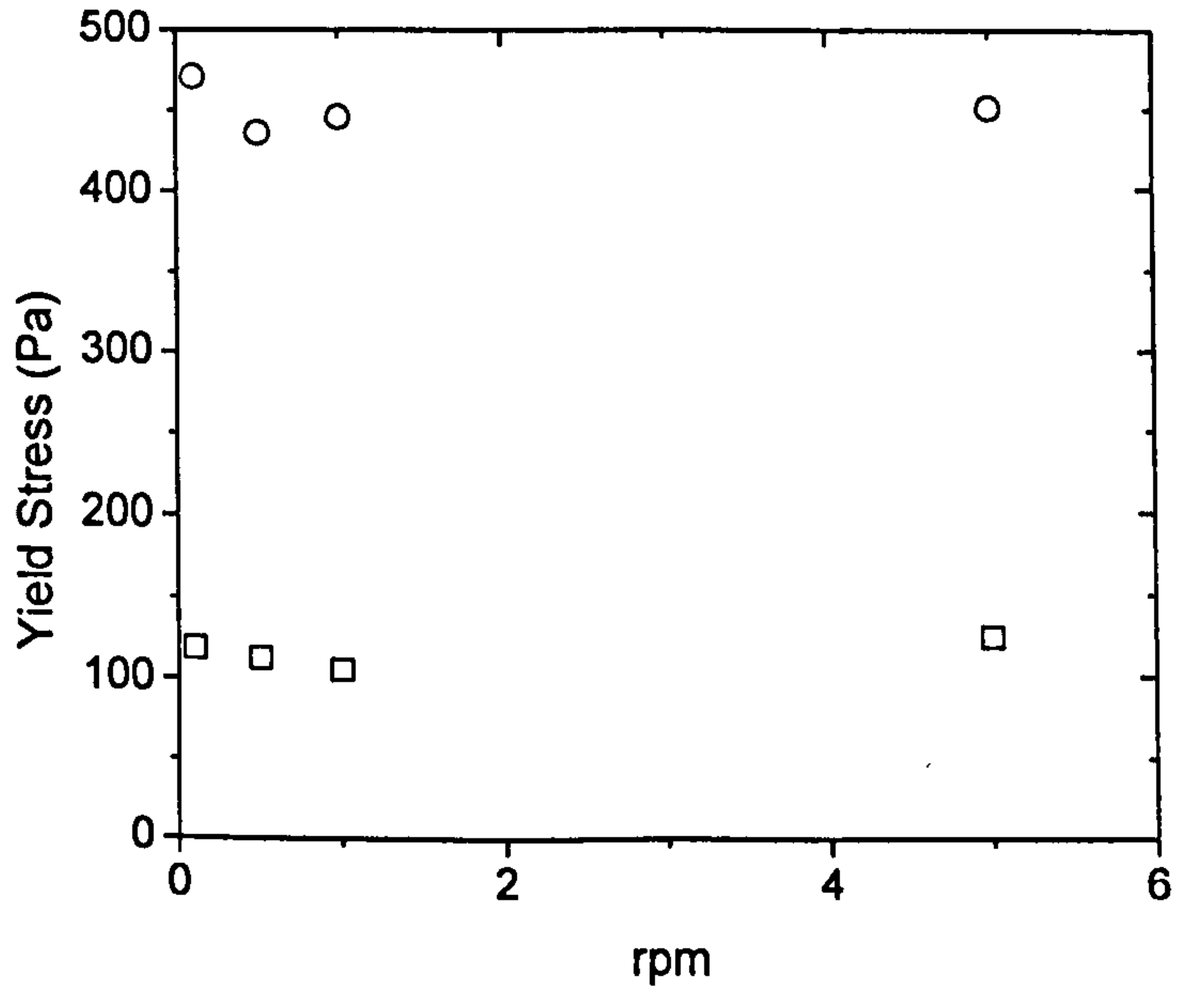

Figure B8. Shear yield stress as a function of constant spindle rotation speed. Symbols: square 1M KNO_3 (vane tool geometry V72), circle 10^{-4}M KNO_3 (vane tool geometry V73). Solids concentration 12% by volume pH 6.

APPENDIX C

LATERAL FORCE MEASUREMENTS – RAW DATA

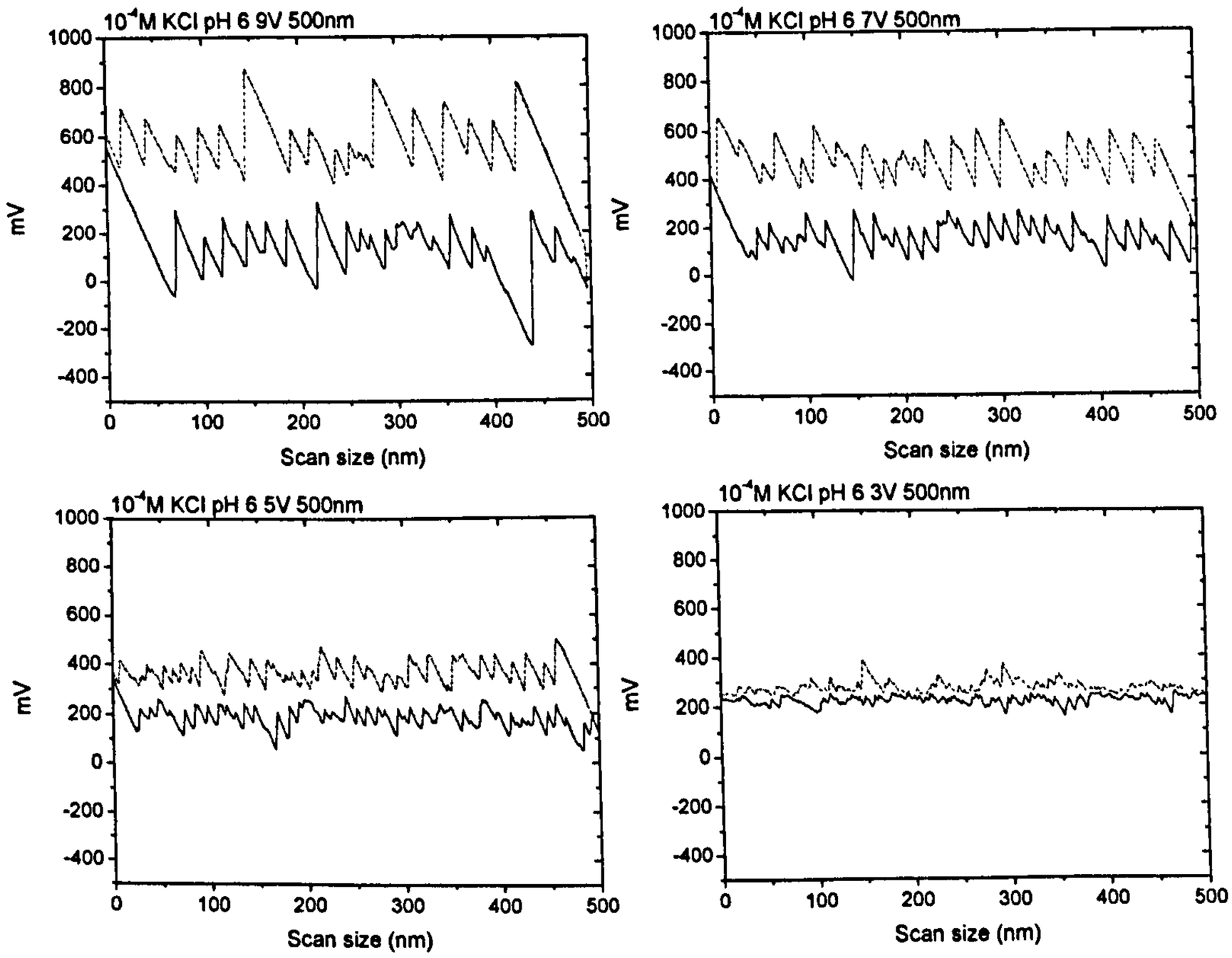

Figure C1. Typical friction force profiles obtained from a friction image. Solid line - trace, broken line - retrace. Electrolyte 10^{-4}M KCl.

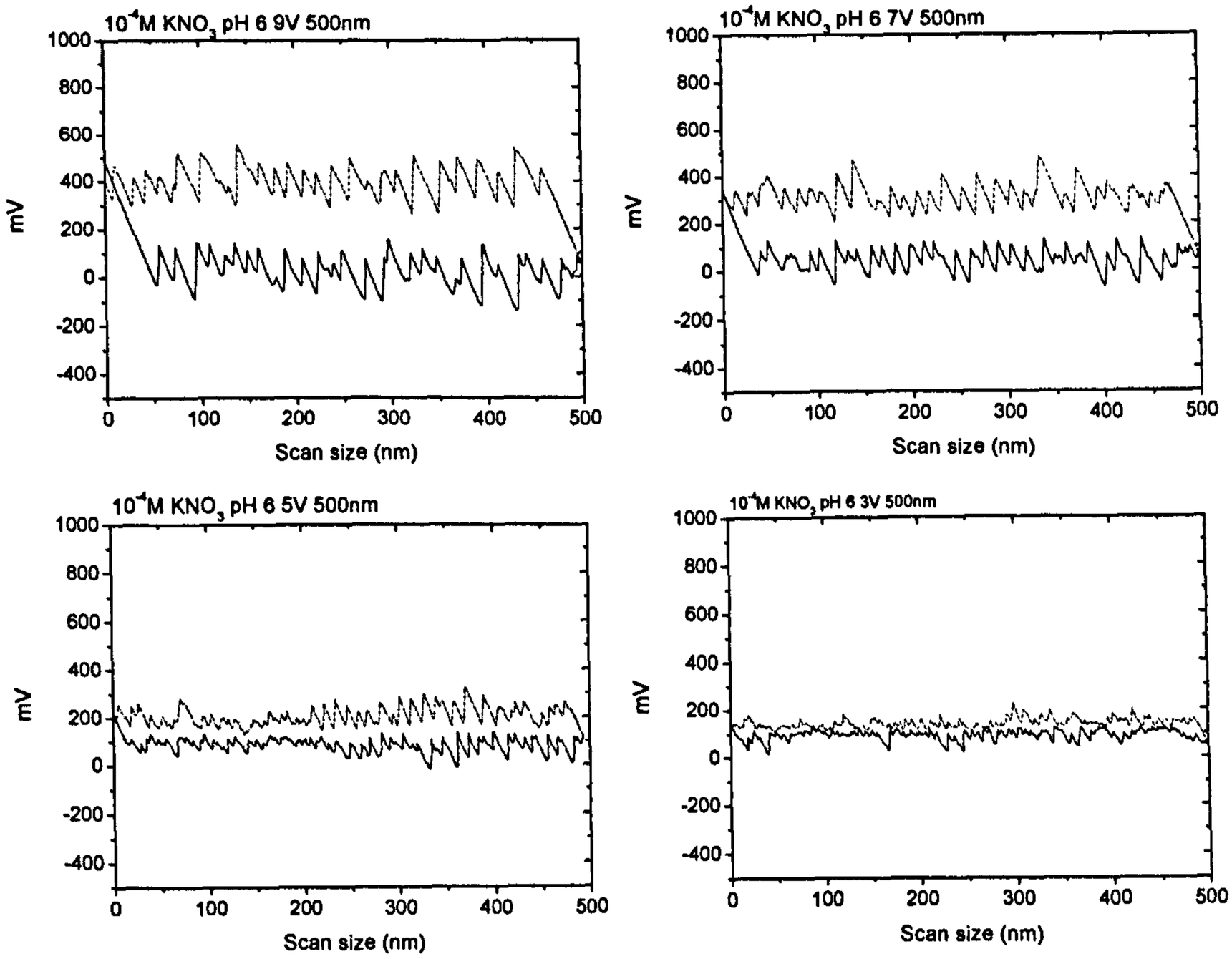

Figure C2. Typical friction force profiles obtained from a friction image. Solid line - trace, broken line - retrace. Electrolyte 10^{-4}M KNO_3.

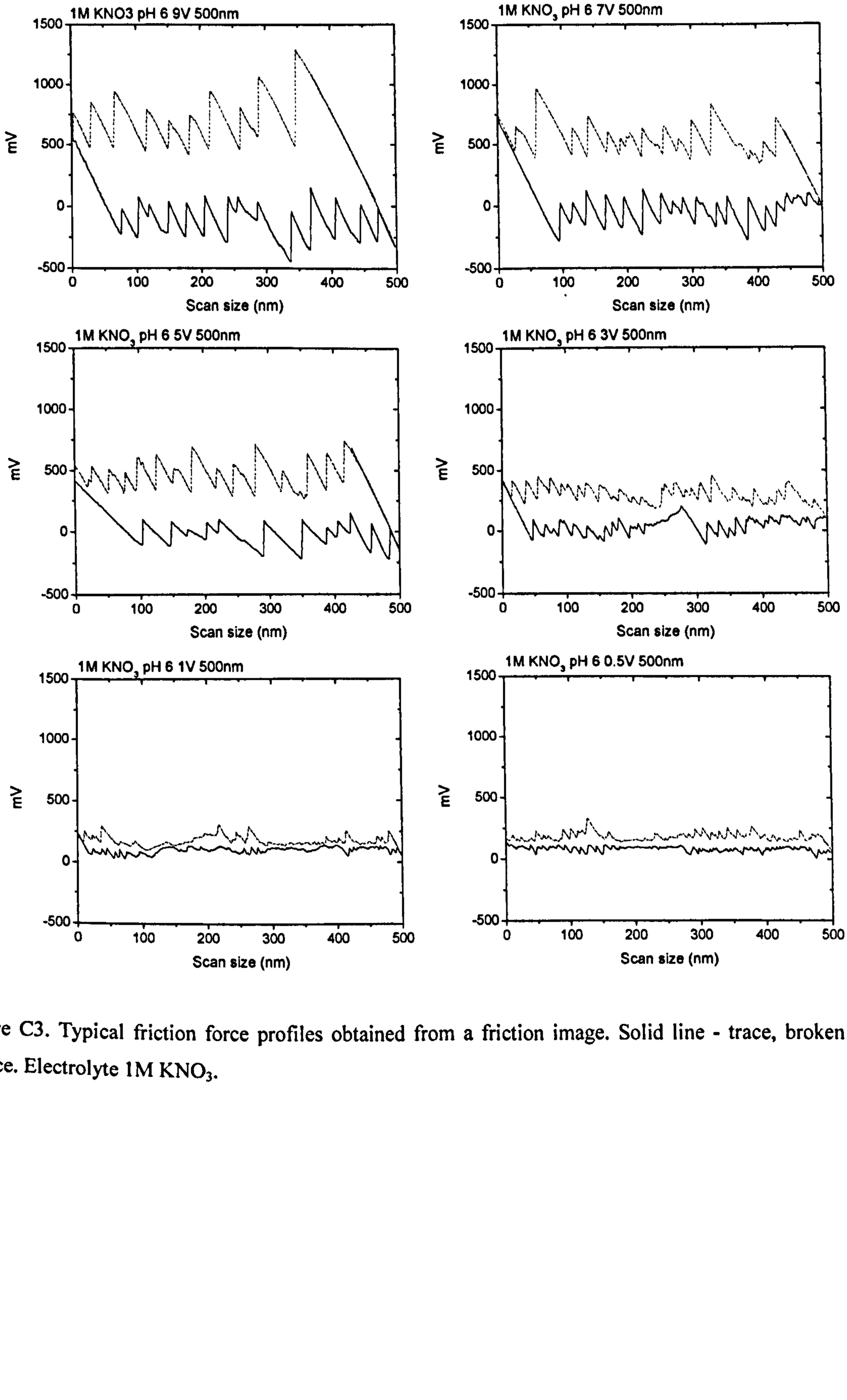

Figure C3. Typical friction force profiles obtained from a friction image. Solid line - trace, broken line - retrace. Electrolyte 1M KNO_3.

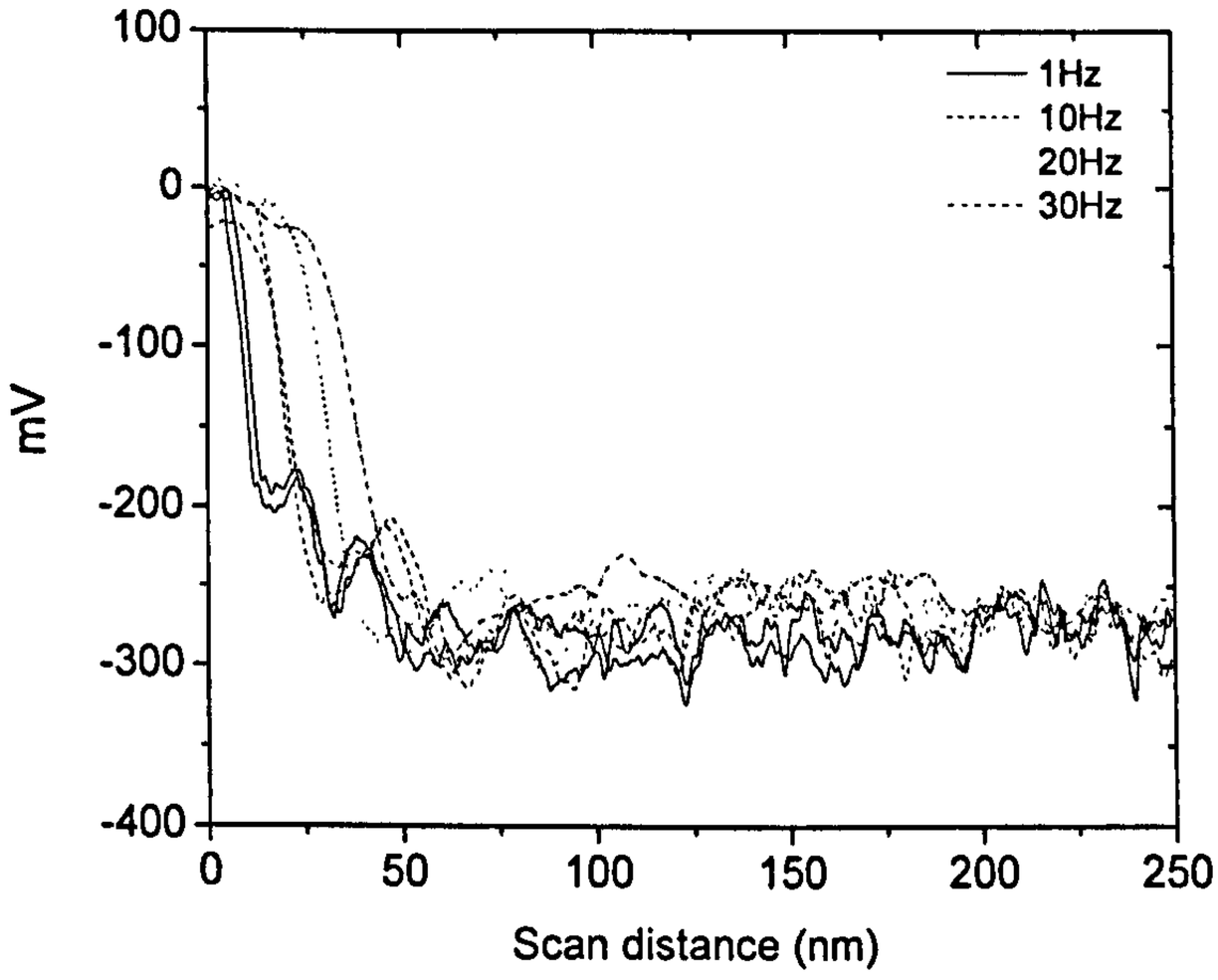

Figure C4. Scan rate dependency on friction trace curve. Silica – silica interaction 10^{-4}M KNO_3 pH 6. Applied load 7V.

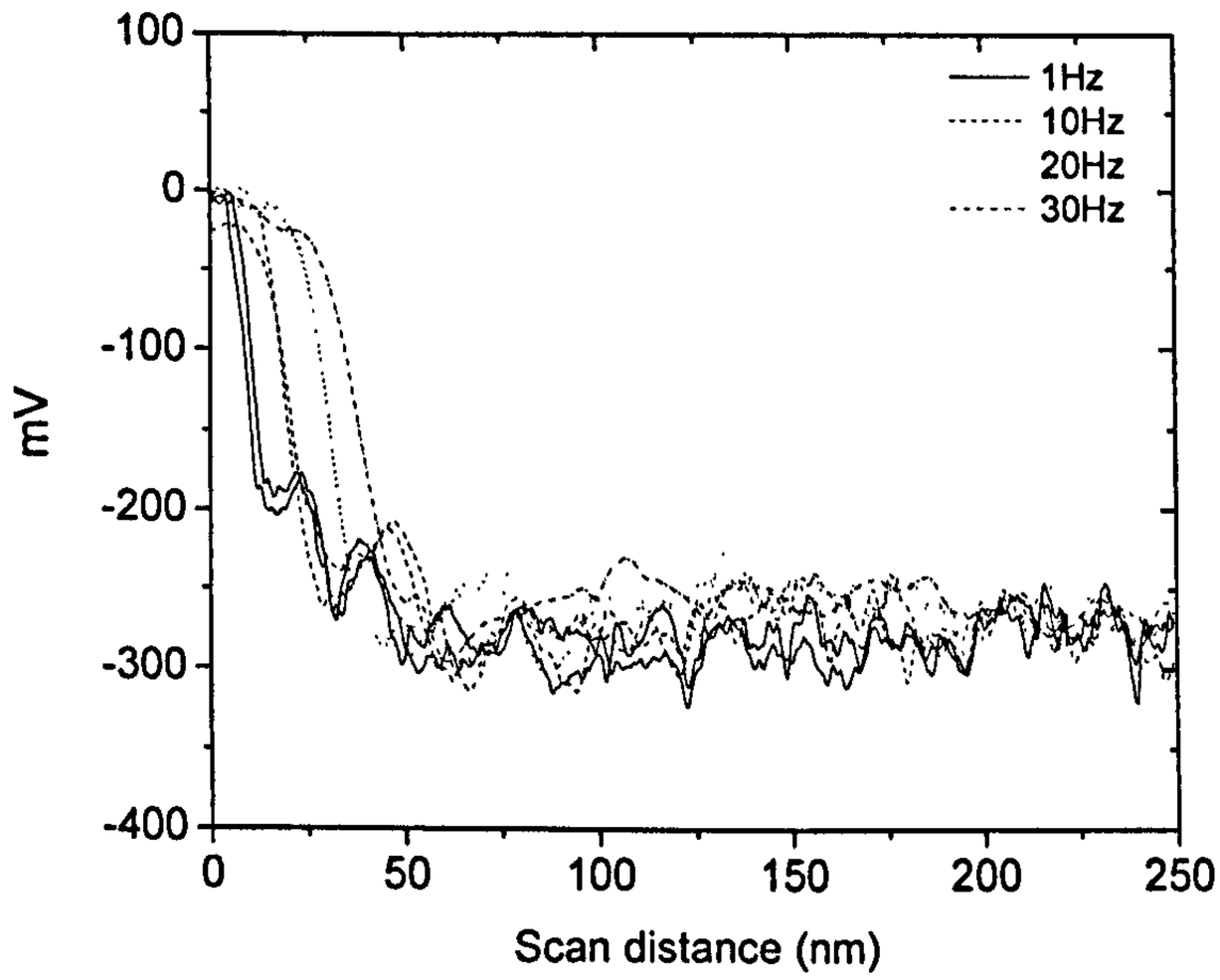

Figure C4. Scan rate dependency on friction trace curve. Silica – silica interaction 10^{-4}M KNO_3 pH 6. Applied load 7V.

APPENDIX D

SLURRY PIPE LOOP

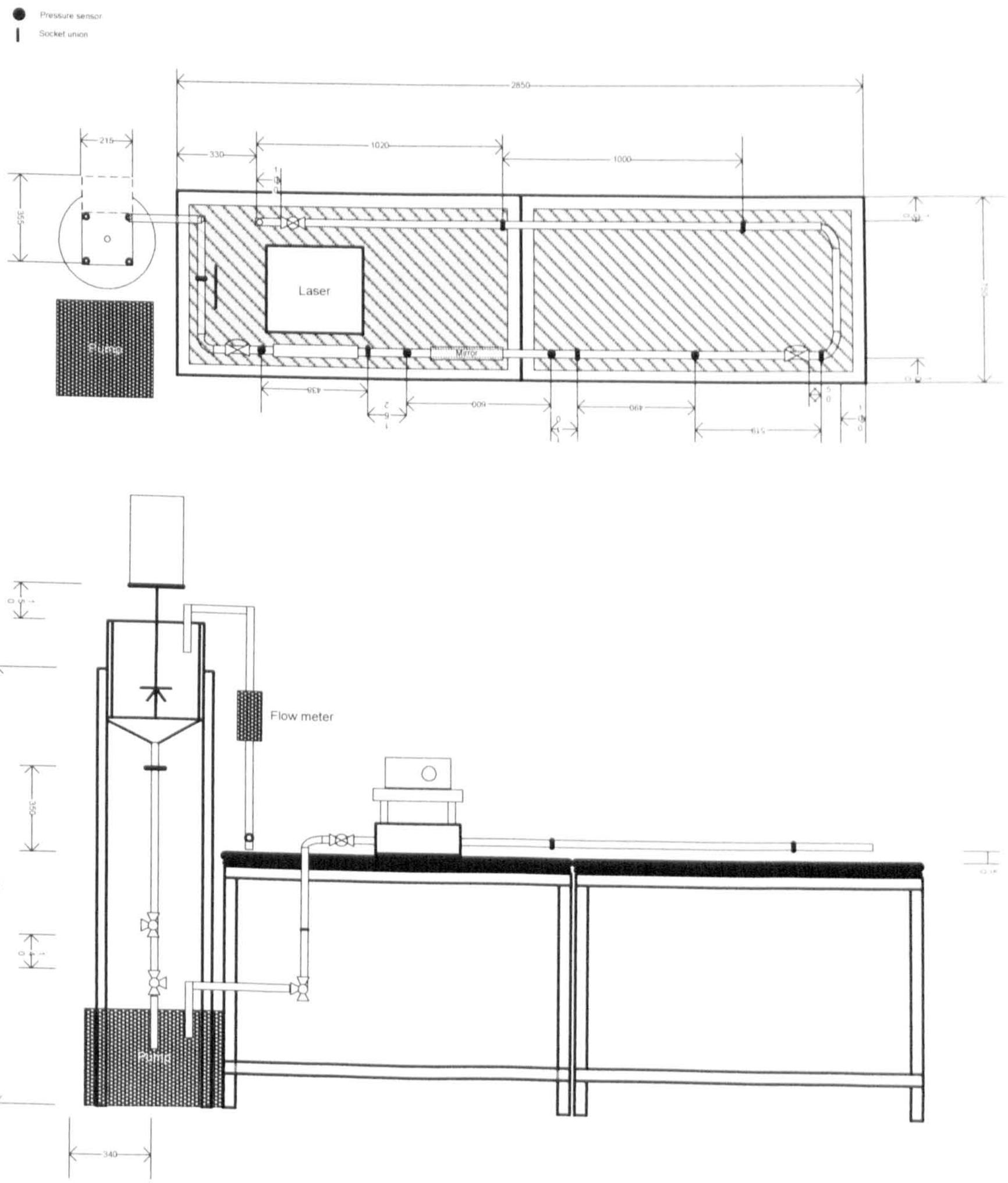

Figure D1. Pipe loop dimensions